Acoustical Physics, Vol. 48, No. 2, 2002, pp. 121–127. Translated from Akusticheskiĭ Zhurnal, Vol. 48, No. 2, 2002, pp. 149–155.

Application of Hydroacoustic Radiators for the Generation of Seismic Waves

V. S. Averbakh, B. N. Bogolyubov, Yu. A. Dubovo ĭ, Yu. M. Zaslavskiĭ, A. V. Lebedev, A. P. Maryshev, V. E. Nazarov, K. E. Pigalov, and V. I. Talanov

Institute of Applied Physics, Russian Academy of Sciences, ul. Ul'yanova 46, Nizhni Novgorod, 603950 Russia
e-mail: swan@hydro.appl.sci-nnov.ru

Received January 31, 2001

Abstract—To excite seismic waves with a high coherence, powerful hydroacoustic radiators placed in a natural reservoir were used. Theoretical estimates and the test data demonstrate a high efficiency of the proposed method of seismic wave excitation. The calculations are in good agreement with the results of measurements. The results of phasing the radiation with the use of two monopole sources separated by a quarter-wave distance are presented. It is shown that the use of the proposed scheme of excitation makes it possible to control the radiation pattern while obtaining a high coherence of seismic waves. *© 2002 MAIK "Nauka/Interperiodica".*

INTRODUCTION

In an earlier publication [1], the authors proposed using the powerful hydroacoustic radiator developed at the Institute of Applied Physics of the Russian Academy of Sciences [2] as a source of seismic waves. Owing to the relatively high frequency (about 200 Hz) and coherence of the radiation produced by such sources, they can be used for the investigation of near-surface layers with a high spatial resolution and for the detection of local inhomogeneities [3].

The cited paper [1] and the report at a Meeting of the Acoustical Society of America [4] were devoted to the theoretical evaluation of the efficiency of radiation of body seismic waves. It was shown that a radiator mounted in the upper part of a rigid tube filled with water and buried in the ground can provide a useful radiation power comparable with the acoustic power generated in a water medium. However, the suggested scheme of excitation has pronounced resonance properties, which leads to the necessity of matching its parameters. This causes problems in its practical realization. In this paper, an alternative scheme of excitation is theoretically studied, and the results of its field tests [5, 6] are compared with the theoretical estimates.

Seismically active regions are of most interest for seismology. These regions are often located near rivers and lakes. It is of interest to use these natural reservoirs for matching a hydroacoustic radiator with the ground. In this case, for an accurate calculation of the radiation efficiency, it is necessary to take into account a great number of details (the bottom profile, the contour of the shore, and so on), which strongly complicates such calculations. Therefore, it is necessary to use idealizations simplifying the task. Below, we consider a simple theoretical model. Then, in the next section, we compare the predicted and measured values of the velocity of vibration of the Earth's surface, which makes it possible to evaluate the efficiency of radiation. In the following section, the possibility of controlling the radiation of two phased sources is studied, and the last section summarizes the main results.

THE BASIC THEORETICAL MODEL

Let us consider the following problem. A monopole source is located in a layer of liquid. This layer is bounded by an air halfspace (an acoustically soft boundary) and by an elastic halfspace. It is necessary to find the displacements at large distances from the source and the power of the source radiation.

We combine the axis of symmetry of a cylindrical coordinate system with the gravity vector passing through the point where the source is positioned, the coordinates of this point being $(0, -h)$. We represent the displacements in the form of scalar (ϕ, φ) and vector ($\boldsymbol{\psi}$) potentials [7]:

$$\mathbf{U} = \begin{cases} \nabla\phi, & -H \le z \le 0 \quad \text{(liquid layer)} \\ \nabla\varphi + \nabla\times\boldsymbol{\psi}, & z > 0 \quad \text{(ground).} \end{cases} \tag{1}$$

Due to the axial symmetry of the problem, the potentials can be represented as the following integrals ($\boldsymbol{\psi}\times\mathbf{r} = \boldsymbol{\psi}\times\mathbf{z} = 0$):

$$\phi(r, z) = \frac{1}{4\pi}\int_C \hat{\phi}(\kappa, z) H_0^{(1)}(\kappa r)\kappa d\kappa,$$

$$\varphi(r, z) = \frac{1}{4\pi}\int_C \hat{\varphi}(\kappa, z) H_0^{(1)}(\kappa r)\kappa d\kappa, \tag{2}$$

1063-7710/02/4802-0121$22.00

$$\psi(r, z) = \frac{1}{4\pi}\int_C \hat{\psi}(\kappa, z) H_1^{(1)}(\kappa r)\kappa d\kappa,$$

where $H_j^{(1)}$ is a Hankel function of the first kind of order j (the time dependence of all quantities is assumed to be $\sim\exp(-i\omega t)$). The path of integration is chosen to satisfy the causality principle. The solution for the potentials is obtained by the method of sewing together partial domains by using the continuity of the displacement and stress fields. In the solution obtained, it is possible to identify the following terms [9]:

(i) body waves with a spherical divergence—the contribution of the points of stationary phase;

(ii) Rayleigh and Stoneley waves—the contribution of the poles; and

(iii) one or two lateral waves (for c_1 or $c_2 > c_0$)—the contribution of the branch points (c_1 and c_2 are the velocities of longitudinal and shear waves in the ground, and c_0 is the sound velocity in the liquid layer).

We will restrict our analysis to the body waves, because they are of most interest for tomography of the Earth's interior.[1]

The stationary points are determined by the conditions $\kappa = k_{1,2}\sin\theta$, where $k_1 = \omega/c_1$ and $k_2 = \omega/c_2$ are the wave numbers of longitudinal and transverse waves in the ground, the angle θ is counted from the z axis of symmetry of the coordinate system and corresponds to the direction of the radius vector from the source to the point of observation

$$\begin{aligned}\varphi(R, \theta) &= -i\frac{E(\gamma\sin\theta)k_1\cos\theta}{2\pi R}\exp(ik_1 R),\\ \psi(R, \theta) &= -\frac{F(\sin\theta)k_2\cos\theta}{2\pi R}\exp(ik_2 R),\end{aligned} \tag{3}$$

where R is the distance from the source. Equations (3) are valid on the condition that $k_{1,2}R \gg 1$. The functions $E(\cdot)$ and $F(\cdot)$ determining the spectral amplitudes of longitudinal and shear waves have the form

$$\begin{aligned}E(\tau) &= \frac{Q}{\omega k_2}(1-2\tau^2)\sin(y-x)/[\sqrt{\gamma^2-\tau^2}\sin(y)\\ &+ im\sqrt{p^2-\tau^2}((1-2\tau^2)^2\\ &+ 4\tau^2\sqrt{(1-\tau^2)(\gamma^2-\tau^2)})\cos(y)],\\ F(\tau) &= 2i\frac{\tau\sqrt{\gamma^2-\tau^2}}{1-2\tau^2}E(\tau),\end{aligned} \tag{4}$$

where $\tau = \kappa/k_2$, $\gamma = c_2/c_1$, $p = c_2/c_0$, $m = \rho/\rho_0$, $x = k_2 h\sqrt{p^2-\tau^2}$, and $y = k_2 H\sqrt{p^2-\tau^2}$.

We point out the following features of Eqs. (4):

1. The radiation of S-waves is absent in the direction $\theta_s = \arcsin\left(\frac{c_2}{c_1}\right)$, because $F(\theta) \sim \sqrt{\gamma^2-\sin^2\theta}$. This angle corresponds to a total reflection (without transformation of the type of wave) of the transverse wave arriving from the domain $z > 0$. Therefore, it is impossible to excite a shear wave in the solid by a sound wave propagating in the liquid layer and incident on the boundary between the two media at the angle corresponding to θ_s in the elastic halfspace.

2. The important kinematic relations should be noted:

2.1. If c_1 and c_2 are greater than c_0 (fast waves), the radiation of P- and S-waves is determined by the rays in the liquid within a cone with the apex angle $|\theta| \le \theta_* = \arcsin(c_0/c_{1,2})$. One can expect that, for $c_{1,2} > c_0$, only a small area bounded by the θ_*-rays will be responsible for the excitation of body waves (Fig. 1). This property can be used for suppressing a certain type of waves by using the directivity of the source.

2.2. For water-saturated rock, for which $c_2/c_0 \ll 1$, the radiation of S-waves is possible only in a narrow range of angles θ, and the longitudinal P-waves give the main contribution to the total power of the body wave radiation (Fig. 3).

(iii) The denominator of the first of Eqs. (4) determines the normal modes of the liquid layer

$$\begin{aligned}\sin(y)\sqrt{\gamma^2-\tau^2} + i\cos(y)m\sqrt{p^2-\tau^2}((1-2\tau^2)^2\\ + 4\tau^2\sqrt{(1-\tau^2)(\gamma^2-\tau^2)}) = 0.\end{aligned} \tag{5}$$

Solving Eq. (5), it is possible to determine the projections of the wave vector on the z axis (k_z) in the waveguide formed by the boundaries of the liquid layer. The following limiting cases can be distinguished: $m \longrightarrow 0$ (an acoustically soft boundary, soft rock) for which $k_z H = \pi + \pi n$, $n = 0, 1, \ldots$, and $m \longrightarrow \infty$ (a hard boundary, hard rock) for which $k_z H = \pi/2 + \pi n$. As is seen from Eqs. (4), the maximal radiation of P- and S-waves occurs in the vicinity of the critical frequencies of the waveguide. In the general case, when $0 < m < \infty$, the critical frequency of the lowest mode will be within $c_0/4H < f < c_0/2H$.

Now we evaluate the efficiency of excitation of seismic waves. The total power is determined by the expression

$$W = -\frac{1}{2}\mathrm{Re}\{\int \sigma_{ik} v_k^* ds_i\}, \tag{6}$$

[1] If the inverse reaction of radiation to the source characteristics is of little interest or weak, the near-field analysis is unnecessary. This is justified when the response is weakly frequency dependent and slight changes in the resonance frequency of the source do not lead to considerable changes in the characteristics of the whole radiating system. This situation takes place in many cases that can be of interest (Figs. 2b, 2c).

where σ_{ik} is the stress tensor, v is the particle velocity in a solid in the wave field, and $(\cdot)^*$ denotes complex conjugation.

By using Eq. (1) with the condition $k_1R, k_2R \gg 1$, we obtain

$$W = W_1 + W_2,$$

$$W_1 = \pi\rho\omega^3 \int_0^{\pi/2} k_1|\varphi|^2 R^2 \sin\theta d\theta, \quad (7)$$

$$W_2 = \pi\rho\omega^3 \int_0^{\pi/2} k_2|\psi|^2 R^2 \sin\theta d\theta,$$

where W_1 and W_2 are the powers of compressional and shear waves, respectively, with the potentials φ and ψ determined by Eqs. (3).

Figures 2a–2c show the dependences of W_1 and W_2 on the parameter k_0H. The values of W_1 and W_2 are normalized to $W_0 = \rho_0\omega k_0 Q^2/8\pi$ (the acoustic power of a monopole source in a boundless liquid). The calculations were performed for:

(a) granite with the parameters c_1 = 5000 m/s, c_2 = 2800 m/s, and m = 2.5;

(b) clay with the parameters c_1 = 2000 m/s, c_2 = 1000 m/s, and m = 2; and

(c) water-saturated loam with the parameters c_1 = 1800 m/s, c_2 = 200 m/s, and m = 2 [8].

In all cases, we used h/H = 0.5 and the sound velocity in liquid was assumed to be c_0 = 1500 m/s. The vertical dashed lines in Fig. 2a correspond to $k_0H = \pi/2, \pi$.

The total power $W_1 + W_2$ is less than W_0, because part of the radiation energy is transferred by the Rayleigh and Stoneley surface waves and, in addition, a sound propagation occurs in the liquid layer. Therefore, the maximums of the total power are reached near the critical frequencies of the waveguide. With an increase in frequency, an increasing number of modes is excited in the liquid layer, and the values of the radiation maximums in Fig. 2 decrease.

Thus, the proposed scheme of excitation of seismic waves by a powerful hydroacoustic radiator seems attractive, because it is possible to achieve a radiation level comparable with W_0 in the case of high coherence. Since sharp peaks in the frequency dependence of radiated power W_j are absent for soft rock with $c_2 < c_0$, it is not necessary to adjust the operating frequency. Only for hard rock, e.g., granite, such an optimization may be needed. However, in this case, the operating frequency is determined simply as $f = c_0/4H$.

It should be noted that, for moderate values of k_0H, the radiation pattern also does not have any sharp peaks, and the maximal level of radiation of longitudinal waves is reached in the direction $\theta = 0$ (Fig. 3). This property is very important for insonification with the use of longitudinal waves.

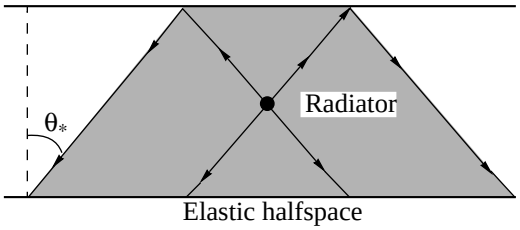

Fig. 1. Scheme of rays exciting fast seismic waves.

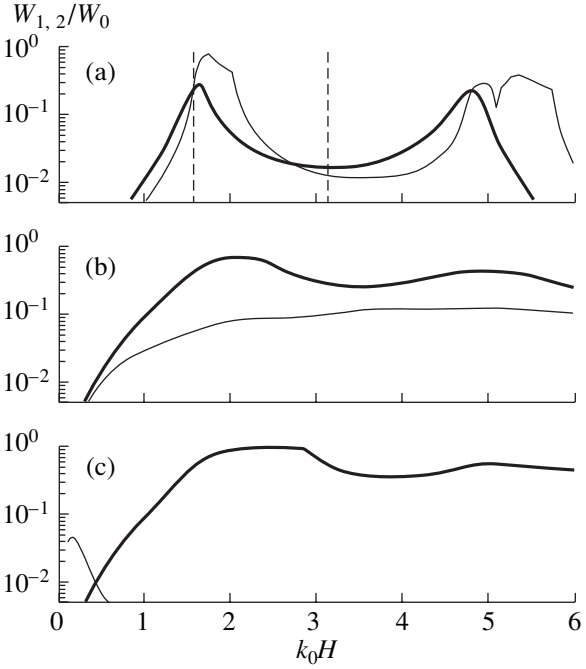

Fig. 2. Dependence of the power of body waves on the dimensionless frequency. The thick line corresponds to compressional waves and the thin line corresponds to shear waves. Additional comments are in the text.

ESTIMATION OF RADIATION EFFICIENCY. TEST DATA

The experiments were carried out on the bank of the Trotsa River (Nizhni Novgorod region, Russia). This minor forest river has a depth of 4–6 m near the bank (H = 4.5 m, h = 2 m) where the measurements were made. A detailed description of the measurements and the equipment can be found in papers [5, 6]. Figure 4 shows the schematic view of the measurements. The hydroacoustic transducer used in the experiments had an acoustic power of W_0 = 400 W [1, 2].

It was established [6] that the measured vertical velocity components are determined mainly by the reflected body waves (the amplitude of displacements is inversely proportional to the distance). The reflecting horizon was located at the depth H_b = 30 m and did not have any essential slope. The analysis of the times of arrival of radiated pulses as a function of distance

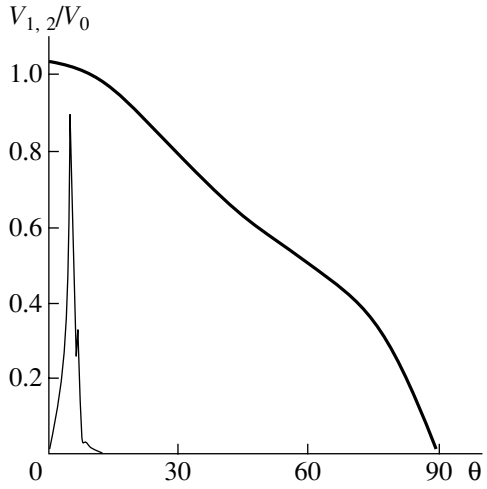

Fig. 3. Directivity of the body wave radiation for the frequency used in the measurements ($k_0H = 4.25$). The parameters m, c_1, and c_2 correspond to the data of Fig. 2c. The thick line corresponds to the angular distribution of the compressional wave amplitude and the thin line corresponds to the shear wave. The displacements are normalized to $U_0 = V_0/\omega$, where $V_0 = k_0Q/4\pi R$ is the particle velocity in a boundless liquid in the field of a monopole source with strength Q.

between the source and the receivers showed that c_1 = 1300–1400 and 1800–1950 m/s in the upper layer and at a depth of more than 30 m, respectively. The analysis by the SASW method [10] with the use of an additional shock exciter showed that the velocity of Rayleigh waves (measured with a good accuracy) was V_R = 190 m/s. The value obtained for V_R corresponds to $c_2 \simeq 200$ m/s in the upper layer.

Additional hydroacoustical measurements were performed for the determination of the bottom parameters. It was shown that the first waveguide mode was excited. The increase in pressure near the bottom at a distance of about 4 m from the source was observed. This allowed us to estimate the angle of total internal reflection $\theta^* = \arcsin(c_0/c_1)$ and the velocity of the longitudinal wave propagation in the bottom $c_1 \simeq 1700$ m/s.

By using the data presented above, we can estimate the efficiency of radiation. The acoustic power (W_0) of the transducer was 400 W at the operating frequency f = 226 Hz (the consumed electric power was 700 W [2]). The volume velocity Q is determined by the expression

$$Q = \frac{1}{f}\sqrt{\frac{2c_0W_0}{\pi\rho_0}} \simeq 0.09 \text{ m}^3/\text{s}. \quad (8)$$

The liquid particle velocity (see caption to Fig. 3) equals

$$|V_0| = \frac{fQ}{2c_0R} = \frac{1}{R}\sqrt{\frac{W_0}{2\pi\rho_0c_0}}, \quad (9)$$

where $R = \sqrt{d^2 + 4H^2}$ is the distance between the radiator and the receiver and $d = |SP|$ (the thin line in Fig. 4).

Figure 5 shows the dependence of the normal component (V_n) of the vibration velocity of the Earth's surface on the distance. The points correspond to the measured values of V_n, and the solid line corresponds to the computed values. The theoretical dependence was constructed in the following way:

(1) The angle of incidence on the boundary (H_b) was determined as

$$\theta = \arctan(d/2H_b). \quad (10)$$

(2) By using the data presented in Fig. 3 with $|V_0|$ determined by Eq. (9), we calculated the value of $V_1(\theta)$.

(3) This quantity was multiplied by the reflection coefficient $|\nu|$. The reflection coefficient was calculated for two liquid layers [11] (because of the absence of reliable data on the velocity of shear waves in a layer

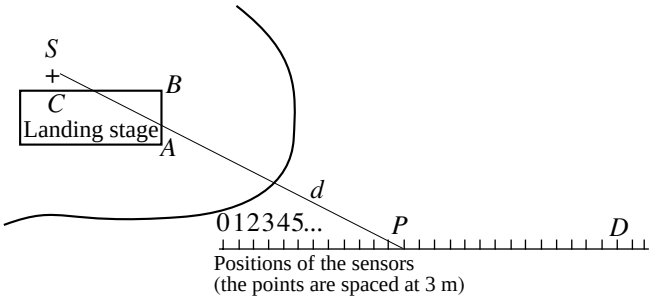

Fig. 4. Schematic view of the measurements at the Trotsa river. The point P is separated from the radiator by 42 m.

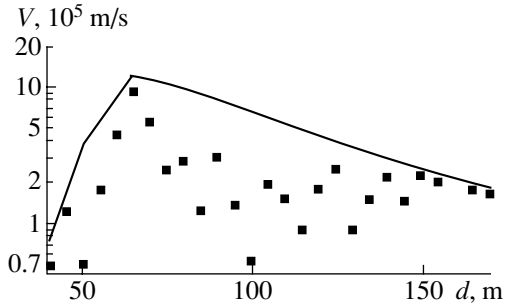

Fig. 5. Computed and measured amplitudes of the vertical projection of the velocity of surface vibrations along the measurement track.

below the 30-m horizon, it was impossible to make more accurate calculations):

$$\nu(\theta) = \frac{m\cos\theta - \sqrt{n^2 - \sin^2\theta}}{m\cos\theta + \sqrt{n^2 - \sin^2\theta}}, \quad (11)$$

where $m = \rho(H_b + 0)/\rho(H_b - 0)$ and $n = c_1(H_b - 0)/c_1(H_b + 0)$. The quantity ν was calculated for $m = 1$ and $n = 1350/1850$.

(4) The value of $|V_1(\theta)\nu(\theta)|$ was multiplied by $\cos\theta$ to find the normal component of the velocity near the free surface (V_n).

(5) Since the sensors detect also the waves reflected from the surface, the value of V_n was doubled. The factor "2" corresponds to the free boundary provided that $c_2 \ll c_1$ ($c_1 = 1350$ m/s, $c_2 = 200$ m/s).

(6) The measurements were performed using a set of eight sensors connected in phase. Therefore, the value of V_n should be multiplied by

$$S(\theta) = \frac{\sin[(\pi f L/c_1)\sin\theta]}{(\pi f L/c_1)\sin\theta}, \quad (12)$$

where $L = 10$ m, $f = 226$ Hz, and $c_1 = 1350$ m/s.

Thus, the solid line in Fig. 5 represents the product $|2V_0(\theta)\nu(\theta)S(\theta)\cos\theta|$.

As is seen from Fig. 5, a good qualitative agreement is observed between the calculated and measured data. The relatively wide scatter of experimental data is caused, on the one hand, by the superposition of multiply reflected pulses and, on the other hand, by the possible variations of the layer parameters ($z < H_b$ and $z > H_b$) along the measurement track (a change in the water saturation with increasing distance from the shore and so on). Thus, the theoretical model proposed in the previous section adequately describes the observed magnitudes of displacements, which allows one to reliably evaluate the power of radiation of P-waves. By using the plot shown in Fig. 2c, we obtain $W_1 = 0.4W_0 = 160$ W.

THE USE OF A SYSTEM OF PHASED RADIATORS

We used two radiators of the same type placed at the same point as in Fig. 4. The positions relative to the water surface differed in that the radiators were at the depth $H - h = 1.77$ m and were separated by 3.7 m in the direction parallel to the measurement track (Fig. 4). The receiver of the seismic signal was located at point D (Fig. 4), at a distance of 120 m from the bank.

The frequency of radiation was $f = 226$ Hz, and the pulse duration was $T \simeq 44.2$ ms (ten periods of the carrier frequency). The number of pulses used in the coherent summation was 50. The phase difference of the carrier frequency of the radiators was changed at 30° intervals from −180° to +180°. The normalized coherence function of the received seismic signal and

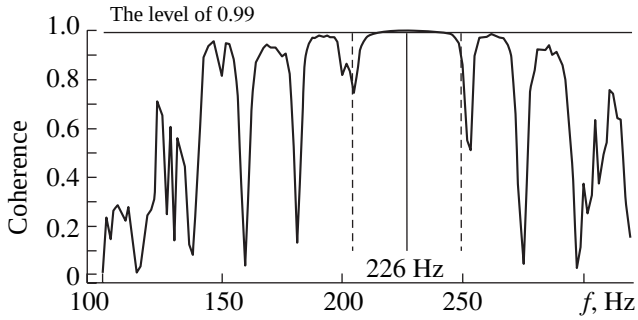

Fig. 6. Coherence of radiation. Averaging was made over 50 pulses of radiation. The dashed lines indicate the frequency band corresponding to 90% of the radiation power ($\Delta f = 2/T$).

the reference signal was more than 99% in the vicinity of the carrier frequency, which is seen clearly in Fig. 6. The received signal level as a function of the delay and phase difference of radiators is represented in Fig. 7. The calculations were made as follows. We assumed that the mutual influence of radiators is compensated and the field generated by each radiator is described by Eqs. (3). The phase factors $\exp(ik_1R)$ were brought to the midpoint of the system of two radiators. The synthesized temporal response was determined as a superposition of contributions of spectral components with the amplitudes proportional to expressions (3). The transfer functions of the radiators were also taken into account in the calculations. The inclusion of the transfer functions made it possible to describe the observed spreading of the radiated pulses and the absence of a sharp leading edge of the signal. In constructing the synthesized response, we took into account a single reflection of a compressional wave from the boundary $H_b = 30$ m (see above). The shear waves, converted waves, and multiple reflections were not considered. The scheme of calculations differed from the scheme used in constructing Fig. 5 only in the replacement of the factor $S(\theta)$ by unity, because, in the measurements with phased radiators, a compact group of receivers was used.

One can easily see the qualitative agreement between the results of measurements and the numerical modeling. The maximal level of the received signal observed in the experiment was reached for the phase difference equal to +90°. Along with the reflected compressional waves, which were taken into account in constructing the synthesized response, the shear waves, converted waves, and multiple reflections can also be observed. Presumably, the longer duration of the response in Fig. 7a can be determined by these factors.

Figure 8 shows the radiation patterns of the group of two sources. The unit level corresponds to the in-phase radiation in the direction $\theta = 0$. One can see that,

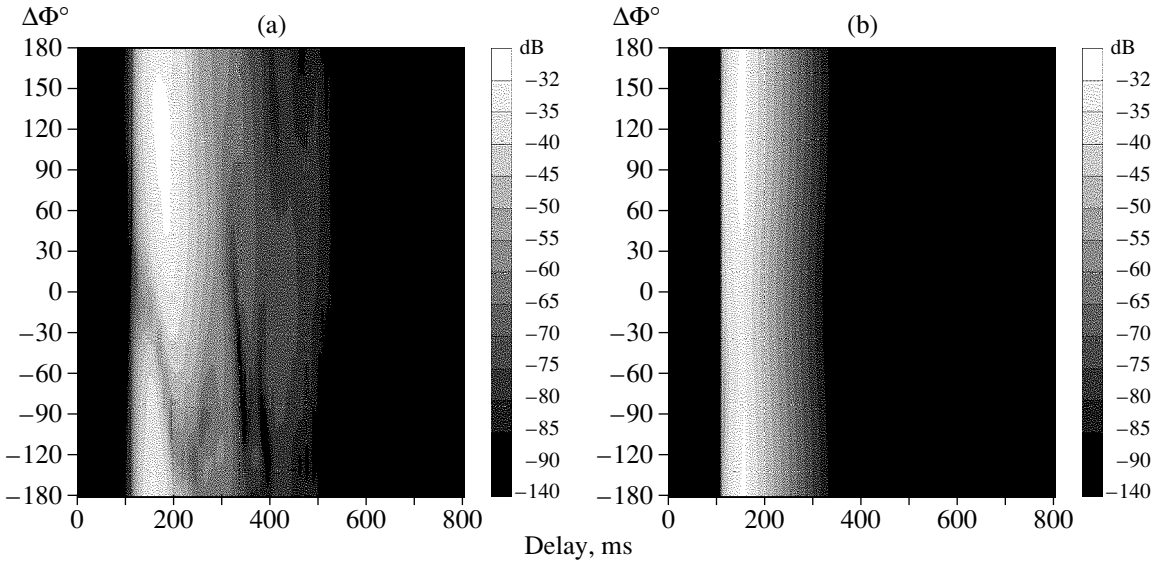

Fig. 7. Received signal level as a function of the propagation delay and the phase difference between the signals supplied to the two radiators: (a) measurements and (b) calculation.

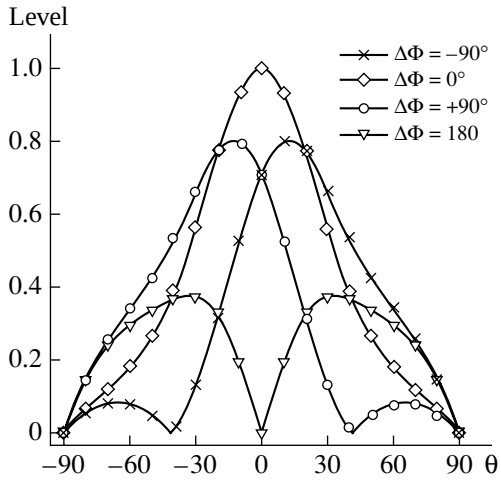

Fig. 8. Directivity of radiation for various phase relations between the sources in the group (calculation).

varying the phase difference between the sources, it is possible to control effectively the directivity of the radiation.

CONCLUSION

The analysis of the scheme of excitation of seismic waves by a hydroacoustic radiator is performed. The scheme is convenient for practical applications. Unlike the previous results [1], the proposed scheme of excitation makes it possible to reach high radiation levels in a wide frequency range. The maximal efficiency of radiation is reached in the vicinity of the critical frequency of the lowest mode of the liquid layer. This frequency changes from $k_0H = \pi/2$ (a soft bottom) to $k_0H = \pi$ (a hard bottom) and always can be determined experimentally. For the operating frequency $f \sim 100$ Hz, the optimal depth of a reservoir is from 3 to 6 m, depending on the bottom characteristics.

The measured values of the vertical displacements of the Earth's surface are in a good agreement with the results of calculations using the proposed computational model. This conclusion is important, because the experiment was carried out near the bank of a real natural reservoir with a variable depth, while, in the model, a boundless liquid layer of constant thickness is considered. The calculated value of the useful power is about 160 W and may be as high as 400 W in the case of the optimization of the operating frequency (Fig. 2). For comparison, we note that the Vibroseis seismic exciter,

which develops the force of 20 t, radiates approximately W_1 = 14 W and W_2 = 430 W at a frequency of 100 Hz [1]. The hydroacoustic transducer excites mainly compressional waves (for water-saturated rock), or compressional and shear waves of approximately equal powers for hard rock. At present, compressional waves are used in most applications, and the proposed scheme of excitation is best suited for the generation of waves of this type. Owing to the stability of the radiator operation and the constancy of the bottom parameters, it is possible to use long-term storage and coherent data processing [6].

The high degree of coherence of the radiation produced by the sources together with the simplicity of the electronic control of their excitation makes it possible to create phased sources on their basis with a desired directivity of radiation.

ACKNOWLEDGMENTS

This work was supported by the Russian Foundation for Basic Research, project nos. 00-15-96741 and 99-02-16957. We are grateful to Prof. A.M. Sutin for helpful discussions and to chief programmer A.V. Tsiberev for preliminary processing of the experimental data.

REFERENCES

1. A. V. Lebedev and A. M. Sutin, Akust. Zh. **42**, 812 (1996) [Acoust. Phys. **42**, 716 (1996)].
2. M. M. Slavinsky and B. N. Bogolubov, *Evaluation of Electromagnetic Source for Ocean Climate Acoustic Thermometry at Lake Seneca*, Technical Report (Woods Hole Oceanographic Institution, 1993).
3. C. H. Frazier, N. Cadalli, D. C. Munson, Jr., and W. D. O'Brien, Jr., J. Acoust. Soc. Am. **108**, 147 (2000).
4. A. V. Lebedev and A. M. Sutin, in *Proceedings of ASA 130th Meeting* (St. Louis, Missouri, USA, 1995).
5. B. N. Bogolyubov, Yu. A. Dubovoĭ, V. Yu. Zaĭtsev, *et al.*, Preprint No. 380, IPF RAN (Inst. of Applied Physics, Nizhni Novgorod, Russian Academy of Sciences, 1995).
6. V. S. Averbakh, B. N. Bogolyubov, Yu. M. Zaslavskiĭ, *et al.*, Akust. Zh. **45**, 1 (1999) [Acoust. Phys. **45**, 1 (1999)].
7. L. D. Landau and E. M. Lifshits, *Course of Theoretical Physics*, Vol. 7: *Theory of Elasticity*, 4th ed. (Nauka, Moscow, 1987; Pergamon, New York, 1986).
8. N. N. Goryainov and F. M. Lyakhovitskiĭ, *Seismic Methods in Engineering Geology* (Nedra, Moscow, 1979), Table 5.
9. K. Aki and P. G. Richards, *Quantitative Seismology, Theory and Methods* (Freeman, San Francisco, 1980; Mir, Moscow, 1983), Vols. 1, 2.
10. K. H. Stokoe, G. R. Rix, and S. Nazarian, in *Proceedings of the 12th International Conference on Soil Mechanics and Foundation Engineering* (Rio de Janeiro, 1989), Vol. 1, pp. 331–334.
11. L. M. Brekhovskikh and O. A. Godin, *Acoustics of Layered Media* (Nauka, Moscow, 1989; Springer, New York, 1990).

Translated by A. Svechnikov

Acoustical Physics, Vol. 48, No. 2, 2002, pp. 128–132. Translated from Akusticheskiĭ Zhurnal, Vol. 48, No. 2, 2002, pp. 156–161.

Factorization of Integro-Differential Equations of the Acoustics of Dispersive Viscoelastic Anisotropic Media and the Tensor Integral Operators of Wave Packet Velocities

L. M. Barkovsky and A. N. Furs

Belarussian State University, pr. F. Skoriny 4, Minsk, 220080 Belarus

e-mail: barkovsky@bsu.by

Received June 13, 2000

Abstract—Factorization of tensor integro-differential wave equations of the acoustics of dispersive viscoelastic anisotropic media is performed for the one-dimensional case. The resulting first-order partial differential equations include integral tensor functionals of the sound velocities of polarized plane wave pulses. The velocity operators $\hat{V}$ are expressed in a coordinate-free compact form. They are determined by the kernels of the integral representations and provide a general description of the kinematics and dynamics of wave packets for arbitrary propagation directions in anisotropic viscoelastic media. *© 2002 MAIK "Nauka/Interperiodica".*

In monograph [1], Whitham gave some examples of the factorization of several nonlinear partial differential wave equations. The factorization reduces the initial equations to the first-order equations, which can be solved by the existing methods of characteristics [2]. Various aspects of the factorization approach were also discussed in [3–6]. For systems of equations, the factorization is complicated because of the necessity to include the commutations of their matrix coefficients. The problem of factorization is still more complicated in the case of integro-differential equations [7, 8] when the polarization and dispersion of wave packets are taken into account. At the moment, the theory of sound beams and pulses is not sufficiently advanced to systematically describe their polarization and possible transformations, especially for spatially bounded plane and solid sound beams in inhomogeneous anisotropic complex media [9]. A finite-duration shear disturbance represented by a set of waves of different frequencies is characterized by a polarization-dependent velocity and can, to one or another measure, be transformed to a longitudinal or quasi-longitudinal wave in the presence of some inhomogeneities (e.g., interfaces) or external actions (as in parametric acoustics or electroacoustics). If the phase velocity of this disturbance depends on frequency, the medium is dispersive, and the velocity of the disturbance as a whole will differ from the velocities of its individual wave components. From the infinite set of wave states, only three states are stable (trirefringence in crystal acoustics). These states correspond to the eigenwaves (isonormal wave types). Any other polarization types that are allowed by the isotropic medium will be decomposed into eigenwaves when the wave is transmitted into the anisotropic medium, even if the propagation direction **n** remains intact, with the exception of some special directions **n** (the acoustic axes). The sets of eigenwaves are characterized by the spectra of three-dimensional evolution operators (also called Caushy operators or propagators) for the wave equations of crystal acoustics.

One of the methods simplifying the solution of wave equations consists in reducing the latter to first-order equations (the factorization method) [1], which can be solved using the known techniques [2]. In the first-order scalar equations for nondispersive media considered in [1, 10], the wave velocity appears as the factor of the spatial derivative. In the case of a system of equations, the matrix of the velocities (the velocity tensor) plays the role of this factor. The tensor dispersion relations are inherent in acoustic materials regardless of the complexity of their properties (such as linearity, nonlinearity, isotropy, anisotropy, and gyrotropy [11–14]).

Below, we consider polarized disturbances with the wave normals of all their components being parallel to a fixed direction **n**. We perform the factorization of the one-dimensional tensor differential wave equation that describes the behavior of such disturbances in linear anisotropic viscoelastic media. On the basis of the factorization of tensor wave equations, we propose an operator description of polarized acoustic packets. Malus was the first to show that nonpolarized light packets can become polarized at reflection. This fact is indicative of a limited applicability of the scalar approach. For acoustics, the importance of this inference follows from the existence of Brewster's angles for shear waves [15]. We consider the evolution tensor solutions, for which the field at the initial point at the initial moment is assumed to be given. In so doing, we simultaneously take into account the variations of the wave field in the longitudinal and transverse subspaces in the process of propagation. Below, we show how the

1063-7710/02/4802-0128$22.00

factorization method is used to reduce the second-order tensor wave equation of crystal acoustics of linear anisotropic viscoelastic media to a first-order integro-differential equation. This equation involves the second-rank velocity tensor $\hat{V}$, which is expressed as a function of the elasticity tensor, the viscosity tensor, and the wave normal vector **n**. From our consideration, it follows that the velocity tensor $\hat{V}$ is simply a mathematical consequence of the Christoffel equations [16].

Consider the factorization of the wave equation of acoustics of viscoelastic anisotropic media.

The equations of motion of an elastic medium have the form [16]

$$\rho\frac{\partial^2 u_i(\mathbf{r}, t)}{\partial t^2} = \frac{\partial \sigma_{ik}(\mathbf{r}, t)}{\partial x_k},$$

where $\mathbf{u}(\mathbf{r}, t) = (u_i(\mathbf{r}, t))$ is the displacement vector of points of the medium as a function of the radius vector of the observation point **r** and time t, σ_{ik} is the stress tensor, and ρ is the density of the medium. Summation is performed over repetitive indices from 1 to 3. Below, we consider anisotropic viscoelastic media with memory, for which the Hooke law can be written in the integral form:

$$\begin{aligned}\sigma_{ik} &= c_{iklm}\gamma_{lm} + \hat{C}_{iklm}\gamma_{lm} \\ &= c_{iklm}\gamma_{lm}(\mathbf{r}, t) + \int_{-\infty}^{t} dt' C_{iklm}(t-t')\gamma_{lm}(\mathbf{r}, t'),\end{aligned}$$

where c_{iklm} is the elasticity tensor characterizing the instantaneous response of the medium to an external action, $\hat{C}_{iklm}$ is the integral operator describing the aftereffect of the medium, $C_{iklm}(t - t')$ is the kernel of this operator, and γ_{lm} is the strain tensor. Note that, by virtue of causality, $C_{iklm}(t - t') = 0$ for negative arguments $t - t'$. Taking into account that the strain tensor $\gamma_{lm}(\mathbf{r}, t)$ can be expressed through the displacements $u_i(\mathbf{r}, t)$ as $\gamma_{lm} = (\partial u_l/\partial x_m + \partial u_m/\partial x_l)/2$ and using the symmetry of the tensors c_{iklm} and C_{iklm} with respect to the permutation of the second and fourth indices, we obtain

$$\begin{aligned}\rho\frac{\partial^2 u_i(\mathbf{r}, t)}{\partial t^2} &= c_{iklm}\frac{\partial^2 u_m(\mathbf{r}, t)}{\partial x_k \partial x_l} \\ &+ \int_{-\infty}^{t} dt' C_{iklm}(t-t')\frac{\partial^2 u_m(\mathbf{r}, t')}{\partial x_k \partial x_l}.\end{aligned} \tag{1}$$

Let a wave packet propagate in the direction specified by the unit vector **n**. Introducing the coordinate $\zeta = \mathbf{nr}$ along this direction and replacing the spatial derivatives $\partial/\partial x_k$ by $n_k\partial/\partial\zeta$, we represent Eq. (1) in the index-free form

$$\frac{\partial^2 \mathbf{u}(\zeta, t)}{\partial t^2} = \Lambda\frac{\partial^2 \mathbf{u}(\zeta, t)}{\partial \zeta^2} + \int_{-\infty}^{t} dt' \Phi(t-t')\frac{\partial^2 \mathbf{u}(\zeta, t')}{\partial \zeta^2}, \tag{2}$$

where the second-rank tensors Λ and Φ are determined according to the formulas

$$\Lambda_{im} = \frac{1}{\rho}c_{iklm}n_k n_l, \quad \Phi_{im} = \frac{1}{\rho}C_{iklm}n_k n_l. \tag{3}$$

To factorize the wave equation (2) of the acoustics of viscoelastic anisotropic media, we represent the vector field of the displacements of points of the medium $\mathbf{u}(\zeta, t)$ in the form of the Fourier expansion

$$\begin{aligned}\mathbf{u}(\zeta, t) &= \frac{1}{2\pi}\int_{-\infty}^{\infty} d\omega \mathbf{u}(\zeta, \omega)e^{-i\omega t}, \\ \mathbf{u}(\zeta, \omega) &= \int_{-\infty}^{\infty} dt \mathbf{u}(\zeta, t)e^{i\omega t},\end{aligned} \tag{4}$$

and substitute Eqs. (4) in Eq. (2):

$$\begin{aligned}\int_{-\infty}^{\infty} d\omega e^{-i\omega t}\Bigg\{-\omega^2\mathbf{u}(\zeta, \omega) - \Lambda\frac{\partial^2 \mathbf{u}(\zeta, \omega)}{\partial \zeta^2} \\ - \int_{0}^{\infty} dt' \Phi(t')\frac{\partial^2 \mathbf{u}(\zeta, \omega)}{\partial \zeta^2}e^{i\omega t'}\Bigg\} = 0.\end{aligned} \tag{5}$$

Introducing the tensor $\Phi(\omega)$ (the Fourier transform of the kernel $\Phi(t)$)

$$\Phi(\omega) = \int_{0}^{\infty} dt' \Phi(t')e^{i\omega t'} \equiv \int_{-\infty}^{\infty} dt' \Phi(t')e^{i\omega t'} \tag{6}$$

and equating the expression in braces in Eq. (5) to zero, we obtain

$$-\omega^2\mathbf{u}(\zeta, \omega) - [\Lambda + \Phi(\omega)]\frac{\partial^2 \mathbf{u}(\zeta, \omega)}{\partial \zeta^2} = 0.$$

Then, we have

$$\begin{aligned}\left[-i\omega + \sqrt{\Lambda + \Phi(\omega)}\frac{\partial}{\partial\zeta}\right]\left[-i\omega - \sqrt{\Lambda + \Phi(\omega)}\frac{\partial}{\partial\zeta}\right] \\ \times \mathbf{u}(\zeta, \omega) = \left[-i\omega - \sqrt{\Lambda + \Phi(\omega)}\frac{\partial}{\partial\zeta}\right] \\ \times\left[-i\omega + \sqrt{\Lambda + \Phi(\omega)}\frac{\partial}{\partial\zeta}\right]\mathbf{u}(\zeta, \omega) = 0,\end{aligned} \tag{7}$$

where $\sqrt{\Lambda + \Phi(\omega)}$ is the square root of the operator $\Lambda + \Phi(\omega)$ (about taking the root of operators, see, e.g., [17]). The tensor differential operators appearing in

square brackets in Eqs. (7) are commuting, which allows us to change from Eqs. (7) to the first-order differential equations for the vector field of displacements $\mathbf{u}(\zeta, \omega)$:

$$-i\omega\mathbf{u}(\zeta, \omega) \pm \sqrt{\Lambda + \Phi(\omega)}\frac{\partial\mathbf{u}(\zeta, \omega)}{\partial\zeta} = 0. \quad (8)$$

Now, we multiply Eq. (8) by $e^{-i\omega t}/(2\pi)$, integrate with respect to ω from $-\infty$ to $+\infty$, and use transformations (4) to change from the Fourier transform $\mathbf{u}(\zeta, \omega)$ to $\mathbf{u}(\zeta, t)$. As a result, we obtain the first-order tensor integro-differential equation in $\mathbf{u}(\zeta, t)$:

$$\frac{\partial\mathbf{u}}{\partial t} \pm \hat{V}\frac{\partial\mathbf{u}}{\partial\zeta} = 0, \quad (9)$$

or

$$\begin{aligned}\frac{\partial\mathbf{u}(\zeta, t)}{\partial t} &\pm \int_{-\infty}^{\infty} dt' V(t-t')\frac{\partial\mathbf{u}(\zeta, t')}{\partial\zeta} = 0,\\ \frac{\partial\mathbf{u}(\zeta, t)}{\partial t} &\pm \int_{-\infty}^{\infty} dt' V(t')\frac{\partial\mathbf{u}(\zeta, t-t')}{\partial\zeta} = 0,\end{aligned} \quad (10)$$

where the kernel $V(t)$ of the integral operator $\hat{V}$ is given by the formula

$$V(t) = \frac{1}{2\pi}\int_{-\infty}^{\infty} d\omega e^{-i\omega t}\sqrt{\Lambda + \Phi(\omega)}. \quad (11)$$

The operator $\hat{V}$ has the dimension of velocity, and we will call it the operator of phase velocities of elastic waves in viscoelastic media. The tensor nature of this operator follows from the anisotropy of the medium, and its integral nature is caused by the dispersion of waves, which is a consequence of the viscosity of the medium. Only when the viscosity vanishes, Eqs. (10) become local:

$$\frac{\partial\mathbf{u}(\zeta, t)}{\partial t} \pm \sqrt{\Lambda}\frac{\partial\mathbf{u}(\zeta, t)}{\partial\zeta} = 0. \quad (12)$$

From Eq. (6), it follows that the kernel $\Phi(t)$ is related to the Fourier transform $\Phi(\omega)$ by the formula

$$\Phi(t) = \frac{1}{2\pi}\int_{-\infty}^{\infty} d\omega e^{-i\omega t}\Phi(\omega).$$

Since $\Phi(t) = 0$ for negative t (due to causality), the tensor function $\Phi(\omega)$ has a regular analytic continuation to the upper half-plane of the complex plane ω [18]. The poles of the function $\Phi(\omega)$ always lie in the lower half-plane of the ω plane. The kernel $\Phi(t)$ appearing in Eq. (2) has the meaning of a response function. The general properties of the response functions, including those following from the causality requirements, were discussed in detail in the literature [19].

The wave equation of crystal acoustics, Eq. (2), generalizes the scalar equation

$$\varphi_{tt} - v^2\varphi_{xx} = 0, \quad (13)$$

which is encountered in different fields of physics [1]. Obvious complications in Eq. (2) are caused by the viscoelasticity of the medium and by the fact that different components of the displacement vector $\mathbf{u}$ are mutually related even in the boundary conditions, the tensor nature of Eq. (2) being essentially caused by polarization of the elastic waves.

It is obvious that Eq. (2) cannot be reduced to Eq. (13) in the case of isotropic nonviscous media as well; i.e., it has a tensor (nonscalar) structure even for isotropic media. We generalize the velocities of elastic waves to tensor quantities for reasons related to the contents of the known monographs by Whitham [1] and Lighthill [20], in which the problem on the velocities (especially, the group velocities) of linear and nonlinear waves of different nature occupies one of the most important places. The group velocity is used for constructing mathematical models of nonlinear equations for different complicated cases of anisotropic nonlinear dispersive media. Whitham (see Ch. 5 in monograph [1]) classified wave systems on the basis of linear, quasi-linear, and nonlinear first-order equations, as well as systems of such equations. The factorization of Eq. (13) leads to the equations

$$\varphi_t \pm v\varphi_x = 0, \quad (14)$$

whose solutions are

$$\varphi_+ = f(x - vt), \quad \varphi_- = g(x + vt), \quad (15)$$

where f and g are arbitrary functions. It is Eq. (14) rather than Eq. (13) that forms the basis for constructing nonlinear model equations, the simplest of which has the form

$$\varphi_t + v(\varphi)\varphi_x = 0, \quad (16)$$

where the propagation velocity $v(\varphi)$ is a function of the local disturbance φ. Equation (16) is called the quasi-linear equation, because it is nonlinear in φ, but linear in the derivatives φ_t and φ_x. A general-form nonlinear equation in the function $\varphi(x, t)$ allows an arbitrary functional relationship between φ, φ_t, and φ_x. The key to solving equations like Eq. (16) is the method of characteristics in the (x, t) plane. Along every characteristic, a partial differential equation is reduced to an ordinary differential equation. In certain cases, this fact offers an analytical solution; in other cases, the partial differential equation is reduced to a system of ordinary differential equations that can be solved using the procedures of step-by-step numerical integration [1].

For nonviscous anisotropic elastic media, the evolution of the vector field of displacements **u** in space and time is described by the formulas

$$\begin{aligned}\mathbf{u}_+(\zeta, t) &= F(\zeta - t\sqrt{\Lambda})\mathbf{u}_{0+},\\ \mathbf{u}_-(\zeta, t) &= G(\zeta + t\sqrt{\Lambda})\mathbf{u}_{0-},\end{aligned} \tag{17}$$

which are the solutions to Eqs. (12). Here, $\mathbf{u}_{0\pm}$ are the displacement vectors at the initial point ζ_0 at the initial moment t_0 and the functions F and G are arbitrary functions of the tensor arguments $\zeta - t\sqrt{\Lambda}$ and $\zeta + t\sqrt{\Lambda}$, which are linear functions of ζ and t. Evolution solutions (17) generalize the d'Alambert solutions (15). Solutions (17) are the evolution ones, because they imply that the operator-valued functions F and G are matrix-type operators (second-rank tensors) acting on the initial vectors $\mathbf{u}_{0\pm}$, which are assumed to be given. Each of solutions (17) corresponds to stable (retaining their envelope) polarized plane wave packets propagating along the ζ axis in either positive or negative direction.

In what follows, we apply the above factorization method to the wave equation with an exponential kernel $C_{iklm}(t)$ for a viscoelastic isotropic medium.

In an isotropic medium, the elasticity tensor has the form [16]

$$c_{iklm} = (c_{11} - 2c_{44})\delta_{ik}\delta_{lm} + c_{44}(\delta_{il}\delta_{km} + \delta_{im}\delta_{kl}),$$

where δ_{ik} is the Kronecker delta, $c_{11} = c_{1111}$, and $c_{44} = c_{2323}$. We assume that the response of the medium is described by an exponential function. The tensor $C_{iklm}(t)$ is symmetric with respect to permutations of the indices i, k and l, m and pairs of indices ik and lm. In the case under consideration, this tensor has the general form

$$\begin{aligned}C_{iklm}(t) &= [(C_{11} - 2C_{44})e^{-t/t_1}\delta_{ik}\delta_{lm}\\ &+ C_{44}e^{-t/t_2}(\delta_{il}\delta_{km} + \delta_{im}\delta_{kl})]\theta(t),\end{aligned}$$

where t_1 and t_2 are the relaxation times and $\theta(t)$ is the Heaviside step function ($\theta(t) = 1$ for $t > 0$ and $\theta(t) = 0$ for $t \le 0$). To simplify the calculations, we assume that the relaxation times are equal: $t_1 = t_2 \equiv t_0$. In this case, the tensors Λ and $\Phi(t)$ given by Eqs. (3) take the form

$$\Lambda = \sum_{j=1}^{2} a_j\tau_j, \quad \Phi(t) = \sum_{j=1}^{2} b_j\tau_j e^{-t/t_0}\theta(t). \tag{18}$$

Here, $a_1 = c_{11}/\rho$, $a_2 = c_{44}/\rho$, $b_1 = C_{11}/\rho$, $b_2 = C_{44}/\rho$, and τ_1 and τ_2 are the projective tensors (operators)

$$\tau_1 = \mathbf{n}\otimes\mathbf{n}, \quad \tau_2 = 1 - \mathbf{n}\otimes\mathbf{n} = -\mathbf{n}^{\times 2},$$

where $\mathbf{n}\otimes\mathbf{n}$ is the dyad (the direct product of vectors), $\mathbf{n}^\times$ is the tensor dual with the vector **n** [16], and 1 is the unit tensor. The tensors τ_1 and τ_2 satisfy the conditions

$$\tau_1^2 = \tau_1, \quad \tau_2^2 = \tau_2, \quad \tau_1\tau_2 = \tau_2\tau_1 = 0. \tag{19}$$

According to relationship (6), the Fourier transform of the kernel $\Phi(t)$ is

$$\Phi(\omega) = \sum_{j=1}^{2}\tau_j\frac{ib_j}{\omega + i/t_0}.$$

The function $\Phi(\omega)$ has the pole $\omega = -i/t_0$ in the lower half-plane of the complex ω plane.

Using Eq. (11), we determine the kernel $V(t)$ of the phase velocity integral operator $\hat{V}$. In view of properties (19) of the projective tensors τ_1 and τ_2, the square root of the tensor $\Lambda + \Phi(\omega)$ is

$$\sqrt{\Lambda + \Phi(\omega)} = \sum_{j=1}^{2}\tau_j\sqrt{a_j + \frac{ib_j}{\omega + i/t_0}}.$$

To calculate integral (11), we expand the integrand in the series

$$\sqrt{a_j + \frac{ib_j}{\omega + i/t_0}} = \sqrt{a_j}\left[1 - \sum_{n=1}^{\infty}\frac{(-i)^n(2n-3)!!}{n!(\omega + i/t_0)^n}\left(\frac{b_j}{2a_j}\right)^n\right],$$

where $n!! = 1\times 3\times 5\times\ldots\times n$ and $(-1)!! \equiv 1$. Closing the integration path by the semicircle of infinite radius in the lower half-plane of the complex plane ω for $t > 0$ and in the upper half-plane for $t < 0$, we obtain

$$\int_{-\infty}^{\infty}\frac{d\omega e^{-i\omega t}}{(\omega + i/t_0)^n} = 2\pi\frac{(-i)^n}{(n-1)!}t^{n-1}e^{-t/t_0}\theta(t), \quad n \ge 1.$$

In addition, it is known that

$$\int_{-\infty}^{\infty} d\omega e^{-i\omega t} = 2\pi\delta(t),$$

where $\delta(t)$ is the Dirac delta function. Then, the kernel $V(t)$ of the phase velocity operator is given by the formula

$$\begin{aligned}V(t) = \sum_{j=1}^{2}\sqrt{a_j}\Bigg[&\delta(t) + \theta(t)e^{-t/t_0}\frac{b_j}{2a_j}\\ &\times\sum_{n=1}^{\infty}\frac{(-1)^{n-1}(2n-3)!!}{(n-1)!n!}\left(\frac{b_j t}{2a_j}\right)^{n-1}\Bigg]\tau_j,\end{aligned}$$

and the factorized equation (9) takes the form

$$\begin{aligned}\frac{\partial\mathbf{u}(\zeta, t)}{\partial t} \pm \Bigg[&\sqrt{\Lambda}\frac{\partial\mathbf{u}(\zeta, t)}{\partial\zeta} + \sum_{j=1}^{2}\frac{b_j}{2\sqrt{a_j}}\int_0^{\infty}dt' e^{-t'/t_0}\\ &\times\sum_{n=1}^{\infty}\frac{(-1)^{n-1}(2n-3)!!}{(n-1)!n!}\left(\frac{b_j t'}{2a_j}\right)^{n-1}\tau_j\frac{\partial\mathbf{u}(\zeta, t-t')}{\partial\zeta}\Bigg] = 0.\end{aligned} \tag{20}$$

In the case of an isotropic medium with a small viscosity ($b_j t_0/a_j \ll 1$, $j = 1, 2$), we can neglect all terms of the series expansion in n in Eq. (20) except for the first term. As a result, we obtain the integro-differential equation

$$\frac{\partial \mathbf{u}(\zeta, t)}{\partial t} \pm \left[\sqrt{\Lambda} \frac{\partial \mathbf{u}(\zeta, t)}{\partial \zeta} + \sum_{j=1}^{2} \frac{b_j}{2\sqrt{a_j}} \int_0^\infty dt' e^{-t'/t_0} \tau_j \frac{\partial \mathbf{u}(\zeta, t-t')}{\partial \zeta} \right] = 0. \quad (21)$$

For nonviscous media, Eqs. (20) and (21) are reduced to Eq. (12) with tensor Λ given by Eq. (18).

In Eqs. (20) and (21), the projective operators τ_1 and τ_2 take into account the variations of the propagating wave field in the longitudinal and transverse subspaces; the operator τ_2 can be represented as $\tau_2 = \mathbf{e}_1 \otimes \mathbf{e}_1 + \mathbf{e}_2 \otimes \mathbf{e}_2$, where $\mathbf{e}_1$ and $\mathbf{e}_2$ are arbitrary, mutually perpendicular, unit vectors in the plane of the wave front. In the case of an anisotropic viscoelastic medium, the phase velocity operator $\hat{V}$ is represented as the expansion in three projective operators of the eigenwaves with a unit trace (see, e.g., [12]).

In conclusion, we note that modern acoustics brings into existence the problem of a high-precision description of tensor acoustic fields in space and time, as well as the determination and quantitative evaluation of the role of polarization in the focusing, transformation, and filtering of sound beams. The velocity tensors given by Eqs. (9)–(11) allow one to progress toward the tensor Fourier acoustics of wave beams in dispersive and viscoelastic anisotropic media. The initial scalarization of the problem on the ultrasonic propagation may lead to wrong results because of the possible transformations of longitudinal waves into transverse waves and vice versa and because of the existence of the Brewster angles [15]. In the actual propagation conditions, the beam of nonpolarized shear waves can become polarized, thus acquiring new physical properties that were neglected at the beginning. This fact and other circumstances should stimulate researchers to use the method of phase and velocity tensors, which are a direct consequence of the fundamental tensor equations of motion (Christoffel's equations).

The factorization of tensor wave equations opens the way to an extension of mathematical physics by the introduction of nonlinear tensor equations, which take into account the fact that a system can have spin degrees of freedom and generalize the known scalar equations (such as the Korteweg–de Vries and the Duffing equations). The derivation of the velocity tensors and their application to some nonlinear dynamic systems will be the subject of a separate paper.

REFERENCES

1. G. B. Whitham, *Linear and Nonlinear Waves* (Wiley, New York, 1974; Mir, Moscow, 1977).
2. E. Kamke, *Gewöhnliche Differentialgleichungen* (Academie, Leipzig, 1959; Nauka, Moscow, 1966).
3. P. M. Morse and H. Feshbach, *Methods of Theoretical Physics* (McGraw Hill, New York, 1953; Inostrannaya Literatura, Moscow, 1958, 1959), Vols. 1, 2.
4. S. P. Tsarev, Teor. Mat. Fiz. **122** (1), 144 (2000).
5. T. Grava, Teor. Mat. Fiz. **122** (1), 59 (2000).
6. L. Bers, F. Jonh, and M. Schechter, *Partial Differential Equations* (Interscience, New York, 1964; Mir, Moscow, 1966).
7. V. Volterra, *Theory of Functions and of Integral and Integro-Differential Equations* (Dover, New York, 1958; Nauka, Moscow, 1982).
8. Yu. N. Rabotnov, *Mechanics of a Deformed Solid* (Nauka, Moscow, 1988); Yu. N. Rabotnov, *Elements of Hereditary Mechanics of Solids* (Nauka, Moscow, 1977).
9. F. Meseguer, M. Holgado, D. Caballero, *et al.*, Phys. Rev. B **59** (19), 12169 (1999); M. Torres, F. R. Montero de Espinosa, D. Garcia-Pablos, and N. Garcia, Phys. Rev. Lett. **82** (15), 3054 (1999).
10. B. B. Kadomtsev and V. I. Karpman, Usp. Fiz. Nauk **103**, 193 (1971) [Sov. Phys. Usp. **14**, 40 (1971)].
11. L. M. Barkovsky and F. T. N. Khang, Akust. Zh. **36**, 550 (1990) [Sov. Phys. Acoust. **36**, 306 (1990)]; Akust. Zh. **37**, 222 (1991) [Sov. Phys. Acoust. **37**, 111 (1991)].
12. L. M. Barkovsky and F. I. Fedorov, Dokl. Akad. Nauk SSSR **218**, 1313 (1974) [Sov. Phys. Dokl. **19**, 688 (1974)]; Dokl. Akad. Nauk BSSR **19**, 1070 (1975); Izv. Akad. Nauk BSSR, Ser. Fiz.–Mat. Nauk, No. 2, 34 (1975); Izv. Akad. Nauk BSSR, Ser. Fiz.–Mat. Nauk, No. 2, 43 (1979).
13. L. M. Barkovsky and I. V. Mishenev, Akust. Zh. **40**, 24 (1994) [Acoust. Phys. **40**, 19 (1994)].
14. L. M. Barkovsky and A. N. Furs, J. Phys. A **33** (16), 3241 (2000).
15. K. S. Aleksandrov, in *Problems of Modern Crystallography*, Ed. by B. K. Vaĭnshteĭn and A. A. Chernov (Nauka, Moscow, 1975).
16. F. I. Fedorov, *Theory of Elastic Waves in Crystals* (Nauka, Moscow, 1965; Plenum, New York, 1968).
17. L. M. Barkovsky, G. N. Borzdov, and A. V. Lavrinenko, J. Phys. A **20**, 1095 (1987).
18. H. M. Nussenzveig, *Causality and Dispersion Relations* (Academic, New York, 1972; Mir, Moscow, 1976).
19. D. A. Kirzhnits, Usp. Fiz. Nauk **152** (3), 399 (1987) [Sov. Phys. Usp. **30**, 575 (1987)]; O. V. Dolgov and E. G. Maksimov, Usp. Fiz. Nauk **135** (3), 441 (1981).
20. J. Lighthill, *Waves in Fluids* (Cambridge Univ. Press, Cambridge, 1978; Mir, Moscow, 1981).

Translated by A. Vinogradov

Acoustical Physics, Vol. 48, No. 2, 2002, pp. 133–136. Translated from Akusticheskiĭ Zhurnal, Vol. 48, No. 2, 2002, pp. 162–165.

On the Utilization of Acoustic Diffraction in Monitoring Cetaceans

V. M. Bel'kovich*, V. A. Grigor'ev, B. G. Katsnel'son**, and V. G. Petnikov*****

** Shirshov Oceanology Institute, Russian Academy of Sciences, Nakhimovskiĭ pr. 36, Moscow, 117851 Russia*

*** Voronezh State University, Universitetskaya pl. 1, Voronezh, 394693 Russia*

**** Wave Research Center, General Physics Institute, Russian Academy of Sciences, ul. Vavilova 38, Moscow, 119991 Russia*

e-mail: petniko@kapella.gpi.ru

Received March 19, 2001

Abstract—An active acoustic technique for monitoring the whales is proposed. The technique allows one to monitor the whales' crossing of a conventional borderline extending for several tens of kilometers in a shallow-water area. The potentialities of the technique are demonstrated in the framework of a numerical experiment by solving the problem of diffraction by model scatterers in an acoustic waveguide. The scatterers are selected in the form of soft spheroids with dimensions characteristic of various kinds of cetaceans.

The necessity of remotely monitoring the migration of cetaceans arose in connection with the sharp decrease in the population of these large marine mammals in recent years (see, e.g., [1]). This problem is especially important for shallow-water regions at the sea shelf, where the existence of cetaceans is threatened by industrial activities. This paper proposes an active acoustic technique for monitoring cetaceans by way of monitoring their crossing a certain conventional borderline extending for several tens of kilometers through a shallow-water region. From the point of view of physical acoustics, such a monitoring implied the detection of the sound field perturbations caused by the diffraction of sound waves by the body of an animal that crosses a stationary acoustic track between a stationary sound source and a receiver. To demonstrate the feasibility of this technique, we present the results of a numerical experiment in the framework of which we solve the problem of the diffraction by spherical bodies in an oceanic-type waveguide. The dimensions of these bodies and their acoustic parameters (the sound velocity and the density) are close to the dimensions and parameters of various species of cetaceans [2, 3]. We note that the methods of solving the diffraction problems in a waveguide are well known (see, e.g., [4]). However, the existing results refer to perfectly rigid bodies of revolution or opaque screens, whereas in this paper, we consider a soft spheroid with the parameters close to the parameters of the medium in the waveguide (the seawater).

The scheme of the numerical experiment is shown in Fig. 1. It is assumed that a point source of sound with the radiation power $W_0 = 500$ W is located at the bottom of a waveguide with the constant depth $H = 40$ m, density $\rho = 1$ g/cm^3, and sound velocity $c = 1480$ m/s. The source emits a continuous tone signal at the frequency $f = 300$ Hz. The reception is performed by a vertical chain of three receivers positioned at a distance of 10 km from the source. The receiver depths are 5, 20, and 40 m. The waveguide is bounded from above by a free surface and from below, by an absorbing liquid bottom. The bottom parameters are as follows: the sound velocity $c_1 = 1780$ m/s; the density $\rho_1 = 1.8$ g/cm^3; and the wave number $k_1 = \frac{2\pi f}{c_1}(1 + i\frac{\alpha}{2})$, where $\alpha = 0.015$. The sound field perturbations ΔP produced by a soft spheroid crossing a stationary acoustic track at various angles $\hat{\gamma}$ were simulated. The intersection point was located in the middle between the sound source and the receiver. [We note that, in this case, the perturbations of the sound field are on the average minimal, and they increase when the intersection point moves closer to the source or to the receiver (for more details see [5]).] The

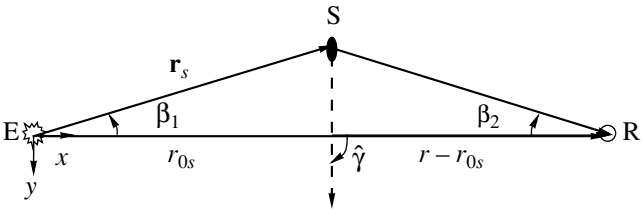

Fig. 1. Scheme of the numerical experiment. Letters E, R, and S indicate the positions of the source, the receiver, and the scatterer, respectively.

spheroid dimensions and its acoustic parameters were selected as follows:

(a) the large axis $L = 25$ m and the small axis $D = 3$ m [typical dimensions of blue whales (*Balaenoptera musculus*)];

(b) $L = 10$ m and $D = 3$ m [gray whales (*Eschrichtius*) and small rorquals (*B. acuto-rostrata*)];

(c) $L = 5$ m and $D = 1.2$ m [white and killer whales (*Delphinapterus leucas* and *Orcinus orca*)].

The sound velocity in a spheroid is $c_s = 1540$ m/s, the spheroid density is $\rho_s = 1.05$ g/cm^3, and the submersion depth is $z_s = 20$ m.

A mode description of the acoustic field was used to calculate the perturbations in a model waveguide. In this case, the sound pressure P_0 produced at the reception point with the coordinates $(\mathbf{r}, z)$ in the cylindrical coordinate system by a sound source located at the point $(0, z_0)$ can be written in the form

$$P_0(r, z) = A\sum_m \psi_m(z_0)\psi_m(z)\frac{\exp(iq_m r)}{\sqrt{q_m r}}\exp(-\gamma_m r/2). \quad (1)$$

Here, $\psi_m(z)$ and ξ_m are the eigenfunctions and eigenvalues of the Sturm–Liouville boundary-value problem ($\xi_m = q_m + i\gamma_m/2$), $r \equiv |\mathbf{r}|$, $A = \sqrt{\rho c W_0}e^{i\frac{\pi}{4}}$, and W_0 is the source power. In the presence of a scattering body, the complex amplitude of the sound field P at the reception point was represented as a sum of the direct P_0 and scattered P_s fields: $P = P_0 + P_s$. The sound field perturbations were calculated by the formula

$$\Delta P = |P| - |P_0|. \quad (2)$$

To determine the scattered field, we used the approach [5, 6] based on the representation of the scattering matrix of the waveguide modes with the help of the scattering amplitude of the body in a free space:

$$P_s(r, z) = A\sqrt{\frac{i}{8\pi}}\sum_{\mu, m} S_{\mu, m}\psi_m(z_0)\psi_m(z_s)\psi_\mu(z) \times \frac{\exp[i(q_m r_s + q_\mu|\mathbf{r} - \mathbf{r}_s|)]}{\sqrt{q_m r_s q_\mu|\mathbf{r} - \mathbf{r}_s|}}\exp\left[-\frac{\gamma_m r_s + \gamma_\mu|\mathbf{r} - \mathbf{r}_s|}{2}\right]. \quad (3)$$

Here, $(\mathbf{r}_s, z_s)$ are the coordinates of the scatterer position, $r_s \equiv |\mathbf{r}_s|$, and $S_{\mu m}$ is the scattering matrix

$$S_{\mu m} = 4\pi[a_m^+ a_\mu^+ F(\mathbf{k}_m^+, \mathbf{k}_\mu^-) + a_m^+ a_\mu^- F(\mathbf{k}_m^+, \mathbf{k}_\mu^+) + a_m^- a_\mu^+ F(\mathbf{k}_m^-, \mathbf{k}_\mu^-) + a_m^- a_\mu^- F(\mathbf{k}_m^-, \mathbf{k}_\mu^+)], \quad (4)$$

where $a_m^\pm = \frac{1}{2}\left[\psi_m(z) \pm \frac{d\psi_m/dz}{i\sigma_m}\right]_{z = z_s}$, $\sigma_m = \sqrt{k^2 - q_m^2}$, k is the wave number, $F(\mathbf{k}_m^\pm, \mathbf{k}_\mu^\pm)$ is the scattering amplitude of the body, and $\mathbf{k}_m^\pm$ and $\mathbf{k}_\mu^\pm$ are the wave vectors of the incident with the index m and scattered with the index μ waves corresponding to the waveguide modes.

The scattering amplitude is expressed through the angles θ and φ in a spherical coordinate system connected with the scatterer, and these angles determine the directions of the wave vectors of the incident and scattered plane waves, $F(\mathbf{k}_m^\pm, \mathbf{k}_s^\pm) \equiv F(\theta_m^\pm, \varphi_m^\pm, \theta_\mu^\pm, \varphi_\mu^\pm)$. In the case of the selected geometry of the numerical experiment (see Fig. 1), these angles are

$$\theta_m^+ = \theta_m^- = \arccos\left(\frac{q_m\cos(\hat{\gamma} + \beta_1)}{k}\right),$$
$$\theta_\mu^+ = \theta_\mu^- = \arccos\left(\frac{q_\mu\cos(\hat{\gamma} - \beta_2)}{k}\right),$$
$$\varphi_m^\pm = \pi \mp \arctan\left(\frac{\sigma_m}{q_m\sin(\hat{\gamma} + \beta_1)}\right), \quad (5)$$
$$\varphi_\mu^\pm = \pi \mp \arctan\left(\frac{\sigma_\mu}{q_\mu\sin(\hat{\gamma} - \beta_2)}\right),$$

where $\beta_{1, 2}$ are the azimuth angles determining the position of a scatterer with respect to the source and the receiver (Fig. 1). According to the formulas [7] for the selected model scatterer (a soft spheroid), the scattering amplitude can be written in the form

$$F(\mathbf{k}_m^\pm, \mathbf{k}_\mu^\pm) = \frac{2i}{k}\sum_{n=0}^{\infty}\sum_{l=n}^{\infty}\varepsilon_n S_{nl}(\chi, \cos\theta_m^\pm)S_{nl}(\chi, \cos\theta_\mu^\pm) \times \frac{m_s^{-1}R_{nl}^{(1)}(\chi, \vartheta)R_{nl}^{(1)'}(\chi_s, \vartheta) - R_{nl}^{(1)'}(\chi, \vartheta)R_{nl}^{(1)}(\chi_s, \vartheta)}{m_s^{-1}R_{nl}^{(1)'}(\chi_s, \vartheta)R_{nl}^{(3)}(\chi, \vartheta) - R_{nl}^{(3)'}(\chi, \vartheta)R_{nl}^{(1)}(\chi_s, \vartheta)} \times \cos[n(\varphi_m^\pm - \varphi_\mu^\pm)], \quad (6)$$

where $\varepsilon_n = \begin{cases}1, & n = 0\\ 2, & n \neq 0\end{cases}$ is the Neumann symbol; S_{nl}, $R_{nl}^{(1)}$, and $R_{nl}^{(3)}$ are the angular and radial prolate spheroidal functions of the first and third kinds (the primes marking the symbols of the radial functions means the derivatives with respect to ϑ); $\chi_s = \frac{k_s}{2}\sqrt{L^2 - D^2}$ ($k_s = 2\pi f/c_s$), $m_s = \rho_s/\rho$, $\chi = (k/2)\sqrt{L^2 - D^2}$; and $\vartheta = L/\sqrt{L^2 - D^2}$. The asymptotic formulas for spheroidal functions and the technique for calculating them numerically are given in [8].

The results of the numerical experiment for the velocity of a model scatterer $v_s = 1$ m/s are shown in Fig. 2. The moment $t = 0$ corresponds to the situation when a scatterer crosses the stationary acoustic track.

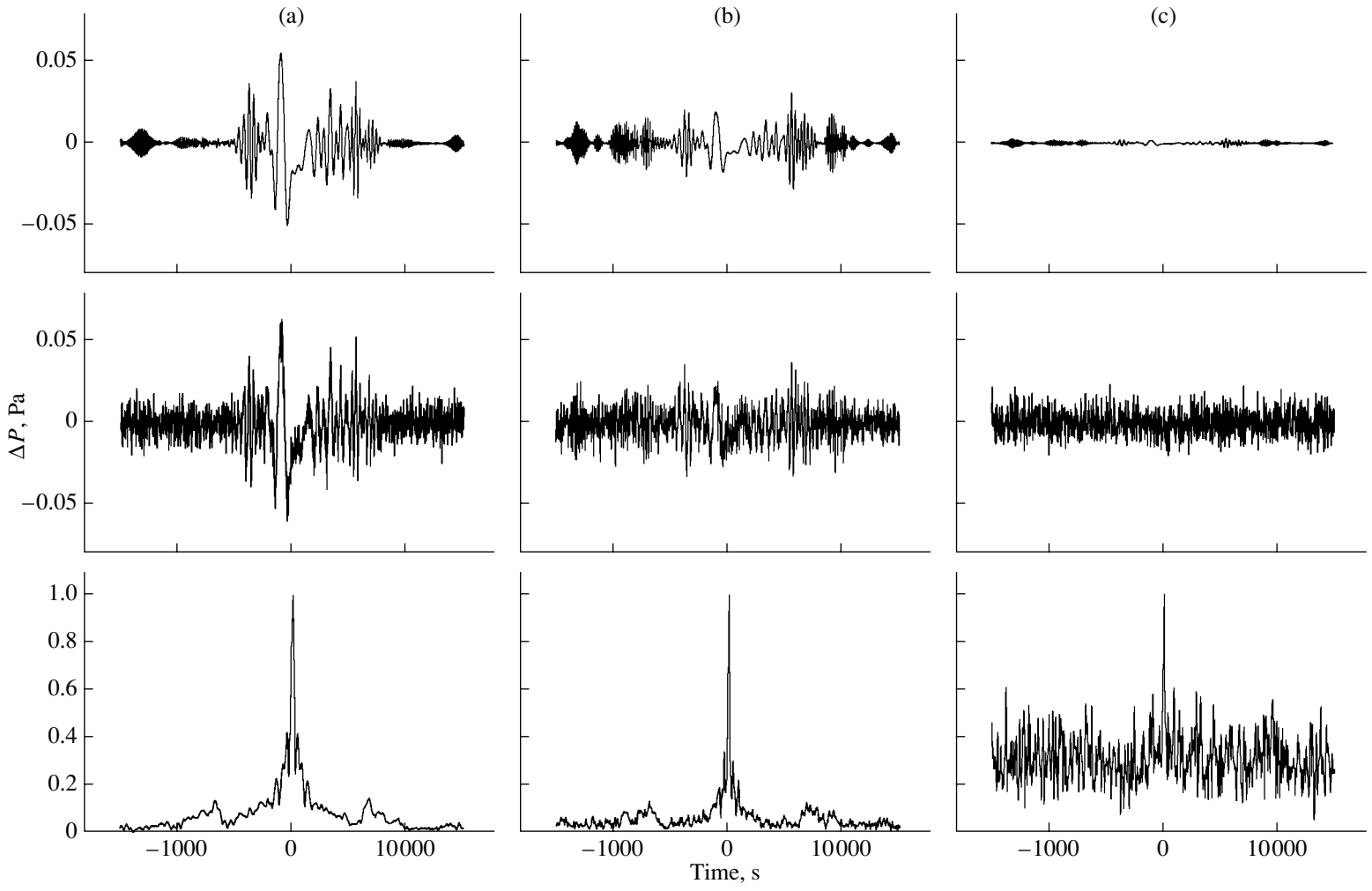

Fig. 2. Sound field perturbations ΔP at the reception point at a depth of 20 m in the case of the scatterer motion across the stationary acoustic track at the angle $\hat{\gamma} = 60°$ in the absence of acoustic noise (the upper series of plots) and in their presence (the middle series of plots). The result of quasi-optimal matched processing with a subsequent storage for three receivers at the depths 5, 20, and 40 m are given in the lower series of plots. The three columns of plots correspond to the scatterer dimensions (a) 25×3 m (blue whales), (b) 10×3 m (gray whales and small rorquals), and (c) 5×1.2 m (white and killer whales).

As one can see from the figures, the motion of a soft spheroid causes small characteristic perturbations of the acoustic field at the reception point. It is natural that the perturbation magnitude depends on the scatterer size. However this dependence is complex because of interference. We note that, in the general case, these perturbations are asymmetric with respect to the moment $t = 0$ when the stationary track is crossed at an arbitrary angle. The symmetry takes place when the track is crossed at a right angle or when a scatterer crosses the track exactly in the middle, while moving at an arbitrary angle, and the perturbations are detected at the same depth as the depth of the sound source ($z = z_0$). (See [9] for more details.)

In the actual conditions of a shallow sea, these perturbations can be concealed because of their smallness by the sound field fluctuations due to the ambient noise. Indeed, the inclusion of this noise with a typical radiation level of $\cong$80 dB (in a frequency band of 1 Hz) in the described numerical experiment makes these perturbations visually indistinguishable. (See the middle series of plots in Fig. 2.) In such a situation, it is necessary to use special methods of signal processing to detect the fact of crossing the stationary track. An example of the application of one such method [10], which is based on matched filtering of the indicated perturbations with subsequent storage for all receivers used in the numerical experiment, is given in Fig. 2. It is necessary to note that we used matched quasi-optimal filters for signals with an unknown initial phase. We also used the calculated perturbations shown in Fig. 2 (the upper series of plots) as reference signals. As one can see from Fig. 2 (the lower series of plots), the utilization of special methods of signal processing provides an opportunity to detect the moment of crossing the stationary track even by the smallest cetaceans (white and killer whales).

In conclusion, we note that the results obtained in this study demonstrate a possibility for designing the acoustic monitoring systems for various-size cetaceans with the use of relatively low-intensity and, therefore, ecologically safe sound sources. This is essential, because the acoustic characteristics of the bodies of these animals are close to the parameters of seawater and, therefore, their acoustic scattering cross-section is small. On the other hand, the required small radiation intensity provides an opportunity to design autonomous, long-lived, and relatively cheap sourses. Certainly, the possibility of detecting the signals scattered by cetaceans depends not only on the level of the ambient sea noise but also on the fluctuations of the "direct" signal detected by the receiver. These fluctuations are caused by the hydrodynamic variability of the water medium (internal and surface waves). However, these fluctuations, as well as the scattered signals, are directly proportional to the amplitude of emitted signals. The possibility of detecting the scattered signals against their background does not depend on the radiation intensity. We should also note that the hydrodynamic variability of the medium and, first of all, the field of internal waves have a considerable spatial anisotropy and pronounced geographic features, i.e., it depends on the vertical profile of the medium density, the bottom relief, and the amplitude of the tidal wave. [For example, in the absence of horizontal stratification, internal waves are completely absent (just this case was analyzed in the numerical experiment).] In this connection, a detailed analysis of the prospects of an acoustic monitoring in a specific region of a shallow sea must be conducted with allowance for the possible fluctuations of the "direct" signal and the acoustic noise, and both interfering factors included in the analysis must be typical of this region.

ACKNOWLEDGMENTS

This work was supported by the Russian Foundation for Basic Research, project no. 99-02-17671.

REFERENCES

1. J. Gedamke, D. Costa, and A. Dunstan, J. Acoust. Soc. Am. **109**, 3038 (2001).
2. V. M. Bel'kovich and A. V. Yablokov, *Whales and Dolphins* (Nauka, Moscow, 1972).
3. L. Bergmann, *Der Ultraschall und Seine Anwendung in Wissenschaft und Technik* (Hirzel, Zürich, 1954; Inostrannaya Literatura, Moscow, 1957).
4. S. M. Gorskiĭ, V. A. Zverev, and A. I. Khil'ko, in *Formation of Acoustic Fields in Oceanic Waveguides*, Ed. by V. A. Zverev (Inst. Prikl. Fiz., Akad. Nauk SSSR, Nizhni Novgorod, 1991), pp. 82–114.
5. V. A. Grigor'ev, B. G. Kantsel'son, V. M. Kuz'kin, and V. G. Petnikov, Akust. Zh. **47**, 44 (2001) [Acoust. Phys. **47**, 35 (2001)].
6. A. Sarkissian, J. Acoust. Soc. Am. **102**, 825 (1997).
7. É. P. Babaĭlov and V. A. Kanevskiĭ, Akust. Zh. **34**, 19 (1988) [Sov. Phys. Acoust. **34**, 11 (1988)].
8. I. V. Komarov, L. I. Ponomarev, and S. Yu. Slavyanov, *Spheroidal and Coulomb Spheroidal Functions* (Nauka, Moscow, 1976).
9. V. M. Kuz'kin, Akust. Zh. (in press).
10. V. A. Zverev, A. L. Matveev, and V. V. Mityugov, Akust. Zh. **41**, 591 (1995) [Acoust. Phys. **41**, 518 (1995)].

Translated by M. Lyamshev

Acoustical Physics, Vol. 48, No. 2, 2002, pp. 137–141. Translated from Akusticheskiĭ Zhurnal, Vol. 48, No. 2, 2002, pp. 167–171.

Effect of the Layer Inhomogeneity on the Particle Displacements in a Rayleigh-Type Wave

V. S. Borshchan, T. A. Viksne, and O. D. Sivkova

Novomoskovsk Institute of the Mendeleev University of Chemistry and Technology, ul. Druzhby 8, Novomoskovsk, Tula region, 301665 Russia

e-mail: rezvov@newmsk.tula.net

Received June 17, 1999

Abstract—The structure of the displacements in a Rayleigh-type wave that propagates in an isotropic solid covered with a liquid layer with exponentially varying density and sound velocity is investigated. *© 2002 MAIK "Nauka/Interperiodica".*

An inhomogeneous layer on the surface of a solid is widely encountered in practice. The layers formed on the surface of a metal in the processes of rolling and cold-work hardening are inhomogeneous [1]. On the surface of a solid exposed to the vapor of its solvent, a layer with inhomogeneous physical properties is formed due to sorption processes and dissolution [2]. Similar processes take place in gas sensors whose sensing element is a sorbent film deposited on a solid substrate [3]. Layers with vertical gradients of sound velocity exist in sea and ocean waters. In this case, the stratification of the sound velocity essentially affects the structure of the sound field generated by a point source [4–7], as well as the propagation of normal waves in the underwater sound channel [8–11]. In all cases, the inhomogeneity of a layer on the surface of a solid affects the characteristics of surface acoustic waves (SAW). This provides the possibility of obtaining the information on the gradients of the layer parameters from acoustic measurements [12].

However, in determining the parameters of a stratified layer, it is not sufficient to measure the phase and group velocities of SAW, because these quantities depend on the layer thickness, the laws governing the variations of the layer parameters (which, as a rule, are unknown), and the values of these parameters at one of the layer boundaries. In the simplest case of a liquid layer with a linear distribution of its parameters, it is necessary to determine five quantities: the thickness, the density, and the sound velocity at the layer boundary and two coefficients characterizing the stratification of these parameters. In this connection, for an unambiguous determination of the structure of the inhomogeneous layer, it is necessary either to measure the SAW velocities at several frequencies or to investigate the distribution of the displacement amplitudes in the layer by an optical probe [13]; then, solving the inverse problem, one can determine the layer parameters and their gradients. Therefore, the problem of the effect of the layer inhomogeneity on the particle displacements in the layer is urgent. The data on the distribution of the displacement amplitudes in depth are also needed, e.g., for calculating the integral of the Rayleigh wave energy flux over depth and for solving the problems on the excitation of Rayleigh and Stoneley–Scholte waves at the interface or on the Rayleigh wave scattering by surface and subsurface defects.

The problem on the distribution of the particle displacements in a SAW field for the case of a homogeneous layer overlying an elastic halfspace is considered in many papers, the main results of which are generalized in monographs [14, 15]. It is shown that the presence of a solid or liquid layer on the surface of an elastic halfspace leads to changes in the phase velocity and in the distribution of the amplitudes of particle displacements. For the case of a homogeneous liquid layer, the dispersion equation and the expressions for the displacement components in a Rayleigh-type wave (RTW) are given in [14]. It is shown that the displacement components vary in the layer by the cosine law, whereas, in the halfspace, they vary in the same way as in a Rayleigh wave, but the depth of the wave localization in the halfspace decreases with an increase in the layer thickness. The profiles of the amplitudes of the displacement components in a homogeneous solid layer and in a halfspace are presented in [15] for SAW with vertical and horizontal polarizations, for layers of various thickness. The case of a stratified layer can be theoretically investigated only for some specific laws of the parameter distribution, for which the wave equation of the inhomogeneous medium has analytical solutions [16]. The dispersion equations of SAW for some specific laws of the layer parameter variations are obtained in papers [12, 17, 18], and the effect of the layer inhomogeneity on the distribution of the particle displacements was not considered. The objective of this paper is to study the effect of the stratification of the layer parameters on the distribution of the displacement components in RTW.

1063-7710/02/4802-0137$22.00

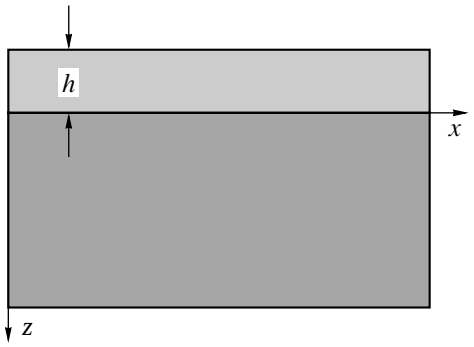

Fig. 1. Halfspace with a layer.

A stratified layer is supposed to be liquid with the density and sound velocity varying with depth according to the laws

$$\rho = \rho_0 \exp(\alpha z), \quad c = c_0 \exp(\beta z), \tag{1}$$

and the halfspace is supposed to be isotropic (Fig. 1). Let an RTW propagate in the positive direction along the x axis, the liquid layer occupying the domain $-h < z < 0$, and the halfspace occupying the domain $z > 0$. Then, in the case of a harmonic dependence on x and t for $\alpha \neq 0$ and $\beta \neq 0$, the expression for the sound pressure in the liquid has the form [18]

$$P = [C_1 J_\nu(Y) + C_2 N_\nu(Y)] \times \exp(-\alpha z/2) \exp i(\omega t - kx), \tag{2}$$

where $J_\nu(Y)$ and $N_\nu(Y)$ are the Bessel and Neumann functions, C_1 and C_2 are arbitrary constants, and

$$Y = \frac{k_0}{|\beta|} \exp(-\beta z), \quad k_0 = \frac{\omega}{c_0}. \tag{3}$$

The corresponding dispersion equation [18] relating the wave number k of the RTW to the layer thickness h can be written as

$$4k^2 qs - (k^2 + s^2)^2 = \frac{\rho_0 q k_t^4}{\rho D}, \tag{4}$$

where

$$D = \frac{\alpha}{2} + \nu\beta - \frac{\beta k_0}{|\beta|} \frac{N_\nu(Y_1) J_{\nu-1}(Y_0) - J_\nu(Y_1) N_{\nu-1}(Y_0)}{J_\nu(Y_0) N_\nu(Y_1) - J_\nu(Y_1) N_\nu(Y_0)}, \tag{5}$$

$$Y_0 = \frac{k_0}{|\beta|}, \quad Y_1 = Y_0 \exp(\beta h), \quad \nu = \sqrt{\frac{4k^2 + \alpha^2}{4\beta^2}}, \tag{6}$$

$q = \sqrt{k^2 - k_l^2}$, $s = \sqrt{k^2 - k_t^2}$, ρ and ρ_0 are the densities of the halfspace material and the liquid at the liquid–halfspace boundary, and k_l and k_t are the wave numbers of longitudinal and shear waves in the isotropic medium.

The horizontal and vertical displacement components in the liquid are determined by the expressions [19]

$$W_x = \frac{1}{\omega^2 \rho} \frac{\partial P}{\partial x} \quad \text{and} \quad W_z = \frac{1}{\omega^2 \rho} \frac{\partial P}{\partial z}, \tag{7}$$

respectively. Substituting Eq. (2) into Eqs. (7) and taking into account the relations between the arbitrary constants from [18], we perform some transformations to obtain

$$W_x = A \frac{k q k_t^2 D_1}{(k^2 + s^2) D} \times \exp(-\alpha z/2) \exp i(\omega t - kx - \pi/2), \tag{8}$$

$$W_z = A \frac{q k_t^2 D_2}{(k^2 + s^2) D} \exp(-\alpha z/2) \exp i(\omega t - kx), \tag{9}$$

where

$$D_1 = \frac{N_\nu(Y_1) J_\nu(Y) - J_\nu(Y_1) N_\nu(Y)}{J_\nu(Y_0) N_\nu(Y_1) - J_\nu(Y_1) N_\nu(Y_0)}, \tag{10}$$

$$D_2 = \left(\frac{\alpha}{2} + \beta\nu\right) D_1 + \beta Y \frac{J_\nu(Y_1) N_{\nu-1}(Y) - N_\nu(Y_1) J_{\nu-1}(Y)}{J_\nu(Y_0) N_\nu(Y_1) - J_\nu(Y_1) N_\nu(Y_0)}. \tag{11}$$

These expressions cannot be analyzed in analytical form. Therefore, their analysis was performed on the basis of the numerical calculations with the use of the following relations between the parameters of the solid and the layer: $\frac{\rho}{\rho_0} = 2.5$; $\frac{k_t}{k_0} = 1/3$; $\frac{k_l^2}{k_0^2} = 1/27$; and $\frac{|\alpha|}{k_0} = \frac{|\beta|}{k_0} = 1/6$. The chosen value of α corresponds to a change in the layer parameters by about a factor of three at the distance λ_0 (λ_0 is the wavelength in the liquid layer at the halfspace boundary). The dependences of the amplitudes of the vertical W_{z0} and horizontal W_{x0} displacement components in the layer and the halfspace on the z coordinate for various values of the layer thickness were calculated. For the layer, we used the amplitudes given by Eqs. (8) and (9) and for the halfspace, the relations derived in [14]

$$U_{x0} = Ak\left[\exp(-qz) - \frac{2qs}{k^2 + s^2} \exp(-sz)\right], \tag{12}$$

$$U_{z0} = -Aq\left[\exp(-qz) - \frac{2k^2}{k^2 + s^2} \exp(-sz)\right], \tag{13}$$

where the wave number k is determined from the dispersion equation (4).

For the comparison between the amplitudes of displacements with and without the layer, we introduced the relative amplitudes: $\overline{W}_{x0} = W_{x0}/U_{z0R}$, $\overline{U}_{x0} = U_{x0}/U_{z0R}$,

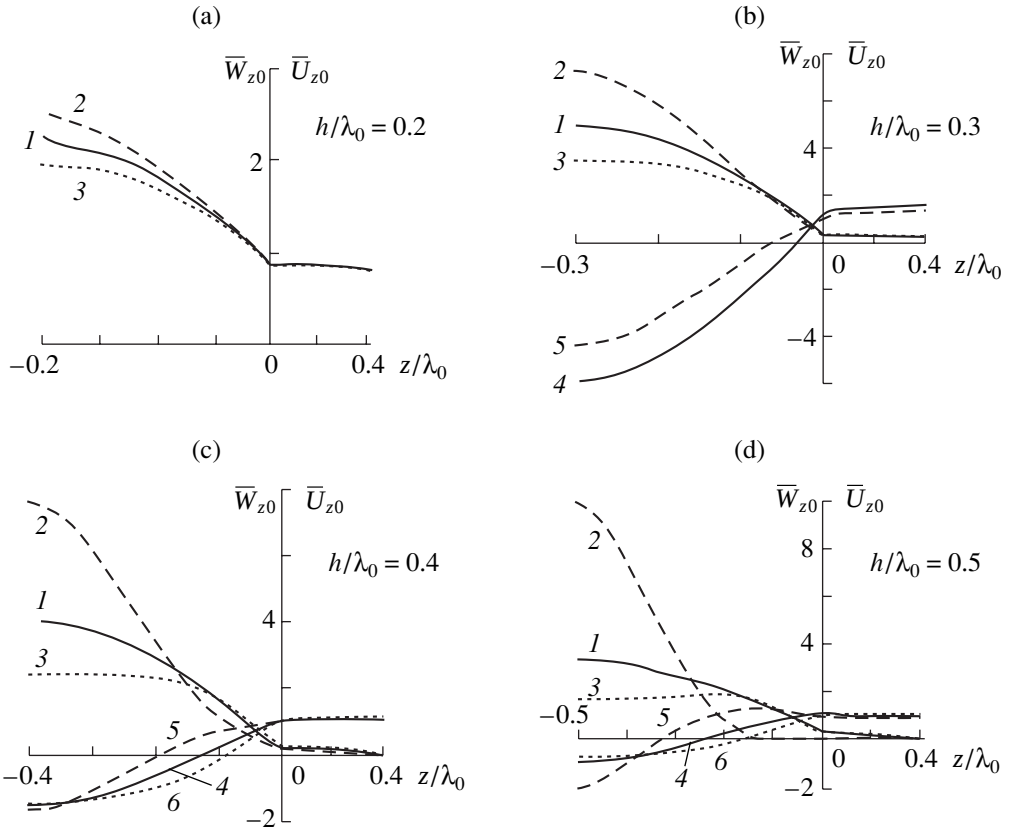

Fig. 2. Dependences of the relative amplitudes in the layer, $\overline{W}_{z0}$, and in the halfspace, $\overline{U}_{z0}$, on the relative coordinate z/λ_0 for various values of the layer thickness and for the cases (*1*, *4*) $\alpha = 0$, (*2*, *5*) $\alpha > 0$, and (*3*, *6*) $\alpha < 0$.

$\overline{W}_{z0} = W_{z0}/U_{z0R}$, and $\overline{U}_{z0} = U_{z0}/U_{z0R}$, where U_{z0R} are displacement amplitudes (12) and (13) in the Rayleigh wave in the plane $z = 0$ at $h = 0$ and $k = k_R$ (k_R is the solution to Eq. (4) with the right-hand side equal to zero). The vertical coordinate and the layer thickness were also expressed in relative units: z/λ_0 and h/λ_0. For comparison, we plotted the displacement profiles for the case of a homogeneous layer ($\alpha = \beta = 0$) with the density ρ_0 and the sound velocity c_0. The corresponding expressions for the displacement amplitudes take the form [14]

$$W_{x0} = Ak\frac{qk_t^2\sin[g(z+h)]}{g(k^2+s^2)\cos(gh)},$$
$$W_{z0} = Ak_t\frac{qk_t\cos[g(z+h)]}{(k^2+s^2)\cos(gh)}, \qquad (14)$$

where $g = \sqrt{k_0^2 - k^2}$.

Figure 2 shows the dependences of the relative amplitudes of the vertical displacement components in the layer $\overline{W}_{z0}$ and in the halfspace $\overline{U}_{z0}$ on the relative coordinate z/λ_0 for different values of the relative layer thickness h/λ_0. The profiles of the displacement amplitudes for greater layer thickness are not presented, because, in this case, according to Eqs. (1), the parameters of the liquid at the free layer boundary, reach values that are noncharacteristic for the liquid.

It is seen that, in the first normal wave (curves *1–3*), $\overline{W}_{z0}$ increases for $\alpha > 0$ (curve *2*), as compared to the homogeneous layer (curve *1*), and decreases for $\alpha < 0$ (curve *3*). This behavior of the amplitudes is caused by a change in the wave resistance (ρc) of the layer: for $\alpha > 0$, the wave resistance decreases in the direction of the free boundary of the layer, which leads to an increase in the amplitude, as compared to a homogeneous layer. In the case of $\alpha < 0$, an increase in ρc and a decrease in the amplitude takes place. Within the layer, the difference in the run of curves *1–3* increases as the free layer boundary is approached and reaches the maximal value $\overline{W}_{z0}(-h)$ at this boundary. The comparison of Figs. 2a–2d shows that, with the increase in the layer thickness, the value of $\overline{W}_{z0}(-h)$ increases, as compared to a homogeneous layer for $\alpha > 0$ and decreases for $\alpha < 0$, and further remains constant (Fig. 3). From Figs. 2a–2d, it is also seen that, for $\alpha > 0$, the wave energy concentrates near the free boundary of the layer: at $h/\lambda_0 = 0.5$ (Fig. 2d, curve *2*), $\overline{W}_{z0}$ is close to

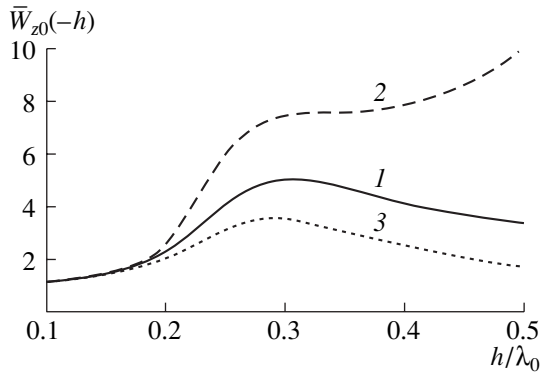

Fig. 3. Dependence of the relative amplitude $\bar{W}_{z0}(-h)$ at the free layer boundary on the relative thickness h/λ_0 for the cases (*1*) $\alpha = 0$, (*2*) $\alpha > 0$, and (*3*) $\alpha < 0$.

zero in the region $0.15 < z/\lambda_0 < 0$ and then rises sharply. This testifies to the fact that the inhomogeneity leads to a redistribution of the wave energy within the layer.

For $h/\lambda_0 \geq 0.3$, a second normal wave exists. Its displacement amplitudes $\bar{W}_{z0}$ are also shown in Figs. 2b–2d for $\alpha = 0$ (curve *4*), $\alpha > 0$ (curve *5*), and $\alpha < 0$ (curve *6*). Near the point of origination of this wave (Fig. 2b) in the case $\alpha > 0$, the displacement amplitudes in the layer are smaller than in the first normal wave, whereas, in half-space, they are greater. This character of displacements in the second normal wave results from the fact that the phase velocity of this wave lies between the velocities of the shear and Rayleigh waves in the elastic halfspace; i.e., the wave is close to a bulk wave and has a greater localization depth in the halfspace. Since, in this case, the effect of the layer on the propagation of SAW is weak, the inhomogeneity affects the value of $\bar{W}_{z0}$ to a lesser extent (the difference in the run of curves *4–6* is smaller than that of curves *1–3*).

As is seen from Fig. 4, the horizontal displacement components W_{x0} and U_{x0} vary, depending on the layer thickness and the sign of the parameter gradients, in the same way as the corresponding vertical components. The main difference is the zero value of W_{x0} at the free layer boundary and its discontinuity at the layer–halfspace boundary, which is determined by the boundary conditions and occurs for both a homogeneous and an inhomogeneous layer.

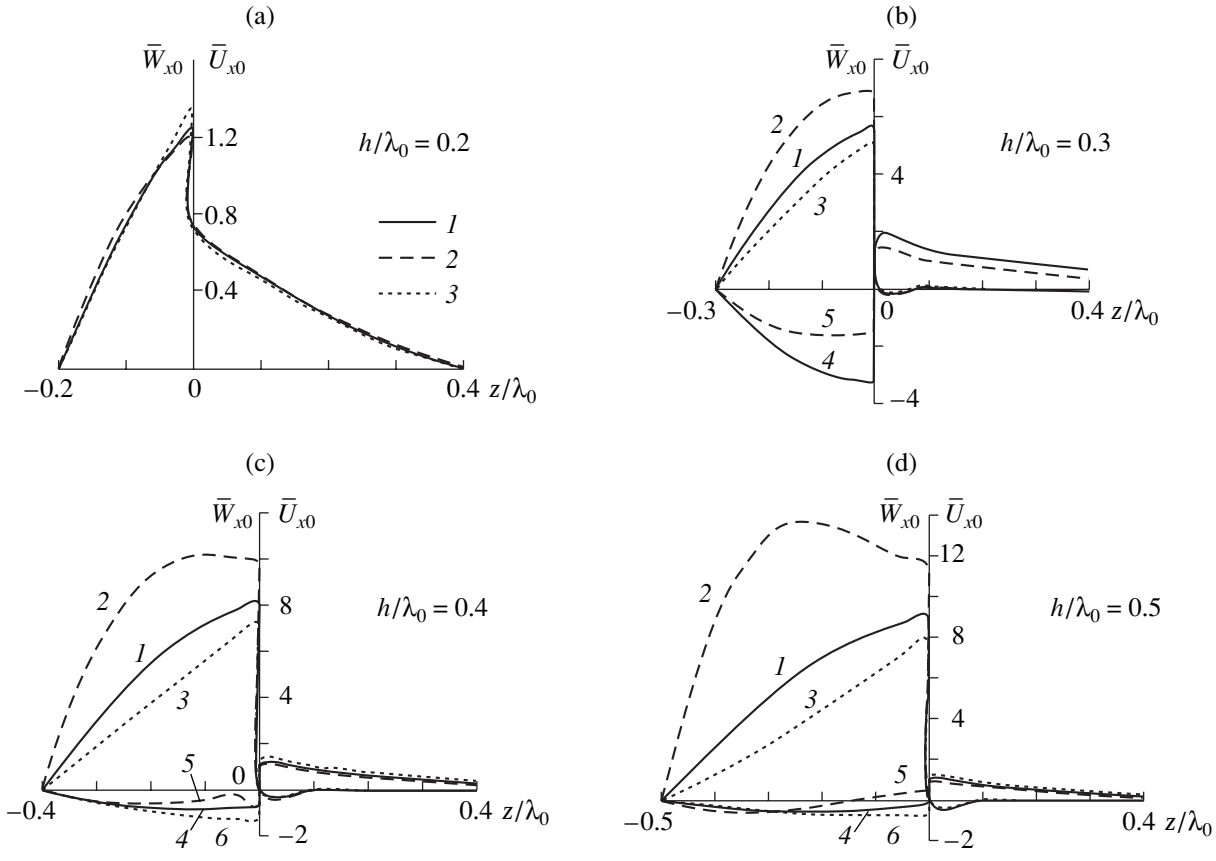

Fig. 4. Dependences of the relative amplitudes in the layer, $\bar{W}_{x0}$, and in the halfspace, $\bar{U}_{x0}$, on the relative coordinate z/λ_0 for various values of the layer thickness for the cases (*1*, *4*) $\alpha = 0$, (*2*, *5*) $\alpha > 0$, and (*3*, *6*) $\alpha < 0$.

As indicated by Figs. 2 and 4, the amplitudes $\bar{U}_{x0}$ and $\bar{U}_{z0}$ of the displacement components in the halfspace vary insignificantly due to the stratification of the layer. This results from the fact that the parameters of the liquid at the halfspace boundary have the same values in all cases considered above. The corresponding changes grow with the increase in the layer thickness and reach 20% for $h/\lambda_0 = 0.5$ in the plane $z = 0$. Consequently, the inhomogeneity of the layer leads to a redistribution of energy between the layer and the substrate. For $\alpha > 0$, the displacement components U_x and U_z decrease, as compared to a homogeneous layer (the energy is transferred from the substrate to the layer), and for $\alpha < 0$, these components increase (the energy is transferred from the layer to the substrate). The layer inhomogeneity practically does not affect the depth of the wave penetration into the substrate.

Thus, the inhomogeneity of a layer on the surface of a solid essentially affects the amplitudes of the components of particle displacements in an RTW. A redistribution of the wave energy takes place between the layer and the substrate, as well as within the layer, and this redistribution depends on the layer thickness and the magnitude and sign of the gradients of the layer parameters. By changing the layer thickness and the degree of its inhomogeneity, it is possible to control the velocity and the structure of surface waves. This result can find application in acoustoelectronic signal processors.

ACKNOWLEDGMENTS

We are grateful to O.Yu. Serdobol'skaya for discussing the purpose and the results of this study.

REFERENCES

1. B. P. Rykovskiĭ, V. A. Smirnov, and G. M. Shchetinin, *Local Hardening of Workpieces by Surface Cold-Work* (Mashinostroenie, Moscow, 1985).
2. E. V. Khamskiĭ, *Crystalline Materials and Products* (Khimiya, Moscow, 1986).
3. G. Fischerauer, F. L. Dickert, and R. Sikorsky, in *Proceedings of IEEE International Frequency Control Symposium* (Pasadena, USA, 1998), p. 608.
4. A. Maguer, Warren L. J. Fox, H. Schmidt, *et al.*, J. Acoust. Soc. Am. **107**, 1215 (2000).
5. C. W. Holland and J. Osler, J. Acoust. Soc. Am. **107**, 1263 (2000).
6. O. P. Galkin and S. D. Pankova, Akust. Zh. **44**, 57 (1998) [Acoust. Phys. **44**, 44 (1998)].
7. E. A. Borodina and Yu. V. Petukhov, Akust. Zh. **46**, 437 (2000) [Acoust. Phys. **46**, 373 (2000)].
8. T. C. Yang, J. Acoust. Soc. Am. **74**, 232 (1983).
9. Z. Ye, J. Appl. Phys. **78**, 6389 (1995).
10. R. A. Vadov, Akust. Zh. **44**, 749 (1998) [Acoust. Phys. **44**, 651 (1998)].
11. N. V. Studenichnik, Akust. Zh. **44**, 659 (1998) [Acoust. Phys. **44**, 571 (1998)].
12. P. Kielczynski and W. Pajewsky, Appl. Phys. A **48** (5), 423 (1989).
13. I. B. Yakovkin and D. V. Petrov, *Diffraction of Light by Acoustic Surface Waves* (Nauka, Novosibirsk, 1979).
14. I. A. Viktorov, *Acoustic Surface Waves in Solids* (Nauka, Moscow, 1981).
15. *Acoustic Surface Waves*, Ed. by A. A. Oliner (Springer, Berlin, 1978).
16. L. M. Brekhovskikh and O. A. Godin, *Acoustics of Layered Media* (Nauka, Moscow, 1989; Springer, New York, 1990).
17. V. Yu. Zavadskiĭ, *Calculation of Wave Fields in Open Spaces and in Waveguides* (Nauka, Moscow, 1972).
18. V. S. Borshchan and O. D. Sivkova, Akust. Zh. **40**, 139 (1994) [Acoust. Phys. **40**, 124 (1994)].
19. M. A. Isakovich, *General Acoustics* (Nauka, Moscow, 1973).

Translated by A. Svechnikov

Acoustical Physics, Vol. 48, No. 2, 2002, pp. 142–146. Translated from Akusticheskiĭ Zhurnal, Vol. 48, No. 2, 2002, pp. 172–177.

Long-Range Sound Propagation in the Shallow-Water Part of the Sea of Okhotsk

R. A. Vadov

Andreev Acoustics Institute, Russian Academy of Sciences, ul. Shvernika 4, Moscow, 117036 Russia

e-mail: vadov@akin.ru

Received February 14, 2001

Abstract—Experimental data on the long-range propagation of explosion-generated sound signals in the shallow-water northern part of the Sea of Okhotsk are analyzed. The propagation conditions in this region are characterized by a fully-developed underwater sound channel that captures the rays crossing the channel axis at angles lower than 3°. The experimental data reveal a small increase in the duration of the sound signal in proportion to the range with the proportionality factor lower than 0.00025 s/km. The frequency dependence of attenuation exhibits a pronounced minimum whose position on the frequency axis is close to the critical frequency of the first "water" mode (about 160 Hz). The increase in the attenuation coefficient at lower frequencies is confirmed by the field calculations performed with the wave-field computer code and is explained by the sound energy loss in the bottom sediments. At frequencies higher than 200 Hz, as in the Baltic Sea, the most probable reason for the attenuation to exceed the absorption in sea water is sound scattering by internal waves.

For years, the researchers of the Acoustics Institute have repeatedly studied long-range propagation of explosion-generated sound signals in the underwater sound channel (USC) of the Sea of Okhotsk. The experiments were carried out in both deep-water [1] and shallow-water (125–155 m) parts of the sea.

For the Sea of Okhotsk, a significant spatial variability of the oceanographic parameters is characteristic [2, 3]. The northern and north western parts of the sea are represented by shallow-water areas. The central part (about 70% of the total sea area) has typical depths of 800–1200 m. On the south, the Kuril Hollow is situated with sea depths of 3300–3400 m.

The bottom sediments of the Sea of Okhotsk are of a terrigenic nature. For the region of the experiment in the northern shallow-water part of the sea, aleurite diatomaceous clays and diatomaceous silts are typical [4].

The waters of the Sea of Okhotsk undergo a cyclonic circulation. Through the northern straits of the Kurile Island system, warm surface waters of the Pacific Ocean arrive, changing their properties as they pass into the interior areas of the sea. Through the southern straits, cold waters move from the sea to the ocean. The Tsushima current introduces warm salt waters through the La Perouse Strait.

Several stratification types of water masses can be distinguished in the northern part of the Sea of Okhotsk. The surface waters (the 30–60-m layer) are cooled in winter down to the temperature of freezing. In summer, the near-surface layer is heated up to 6–10°C, and, under the mixed layer, an undersurface water mass forms. In its core, the minimal temperature reaches –1.7 to –1.5°C. Near the bottom (at a sea depth of about 150 m), the temperature also remains negative (–1.4 to –1.6°C).

The experimental studies of long-range sound propagation were carried out in the shallow-water region of the Sea of Okhotsk in summertime (August). The propagation path was 335 km in length, with the sea depth changing from 125 to 155 m along the path. Prior to experimenting, six sets of hydrological measurements were performed at different distances from the receiving vessel. By continuously lowering and lifting the Istok-3 device, the following water parameters were measured every 1.5 s: the temperature, the electric conductivity (salinity), and the hydrostatic pressure. For each set of data, the values of these parameters were recalculated to the sound speeds according to the formula of Wilson [5].

Figure 1 shows the vertical sound speed profiles measured at both ends and at the middle of the path. At some fractions of the path, multilayer water structures were observed with different temperatures in individual layers. This phenomenon leads to "tongs" in the $c(z)$ profiles with the tong thickness less than 5–8 m and the differences in the sound speeds up to 0.4–0.6 m/s. The depth of the USC axis changed from 30 to 60 m along the path. The sound speed varied slightly at the axis depth. The difference in the sound speeds near the bottom and at the channel axis was about 1.5 m/s, and the corresponding difference between the surface and the axis reached 55 m/s. In the discontinuity layer, the sound speed gradient changed from 0.5 to 2 1/s. Below the USC axis (at depths greater than 50 m), the gradient was 0.02 1/s, which is close to the hydrostatic value. To

1063-7710/02/4802-0142$22.00 © 2002 MAIK "Nauka/Interperiodica"

make the profile $c(z)$ more evident, we choose different scales of the abscissa in Fig. 1 for undersurface waters and those at horizons deeper than 25–30 m.

To illustrate the variability of the hydrological parameters along the path at the depths 30–125 m (within the 100-m layer under the temperature discontinuity layer), we present the field of sound speeds (Fig. 2) calculated from the data of measurements. The step in the sound speed values is 0.2 m/s between the adjacent isospeed curves. The numbers near the curves indicate the excess of the sound speed above 1440 m/s. In this picture (at the bottom), the data obtained from echo-sounding performed during the experimentation are presented (the scales in distance and depth are the same as at the top of the picture). Up to a distance of 150–200 km along the path, a monotone bottom rise took place, and the sea depth decreased from 150 to 125 m. At longer ranges, the depth rather sharply increased to 155 m (in a region of about 50 km in length) and then decreased to 138 m.

Two vessels were used in the experiment. The receiving vessel drifted approximately 95 nautic miles south of Magadan. The transmitting vessel took a heading of 270° (in the western direction relative to the reception point) at 10–11 knots, along the 58° latitude. From the transmitting vessel, small explosive charges were dropped and exploded at a depth of 50 m (near the USC axis) with the use of pressure-sensitive detonators. A total of 50 charges were exploded. The time interval between successive explosions varied depending on the distance. At points nearest to the receiver, it changed from 2 to 10 min; at distances longer than 50 km, it was equal to 30 min. At the moment of each charge drop, the distance between the vessels was determined from the propagation time of the acoustic signal and then was refined according to observations periodically performed with the use of the satellite navigation systems of both vessels. The explosion-generated signals were received by omnidirectional hydrophones at depths 10, 50, and 120 m.

During experimenting, there was fog, swell of Beoufort 3, and wind of less than 6 m/s (at about 40°).

The explosion-generated signals that were received within the frequency band 10–20 Hz to 1–2 kHz from the distance 10–20 km or more were single-ray arrivals and had the shape of two short pulses of less than 1-ms duration. These pulses formed by the shock wave and the first gas-bubble oscillation were equal in their values and had the same signs. The time separation of the pulses corresponds to the period of the first bubble oscillation (T = 45 ms in our case).

In the case of a multiray reception, each ray in the time structure of the explosion-generated signal is represented by its own pair of pulses. The time structure of the sound field has a twofold nature: each pulse of the shock wave is followed by that of the gas-bubble oscillation. The first and second halves of the received multiray signal are identical. To confirm this fact, the cross-correlation function between the first and second parts

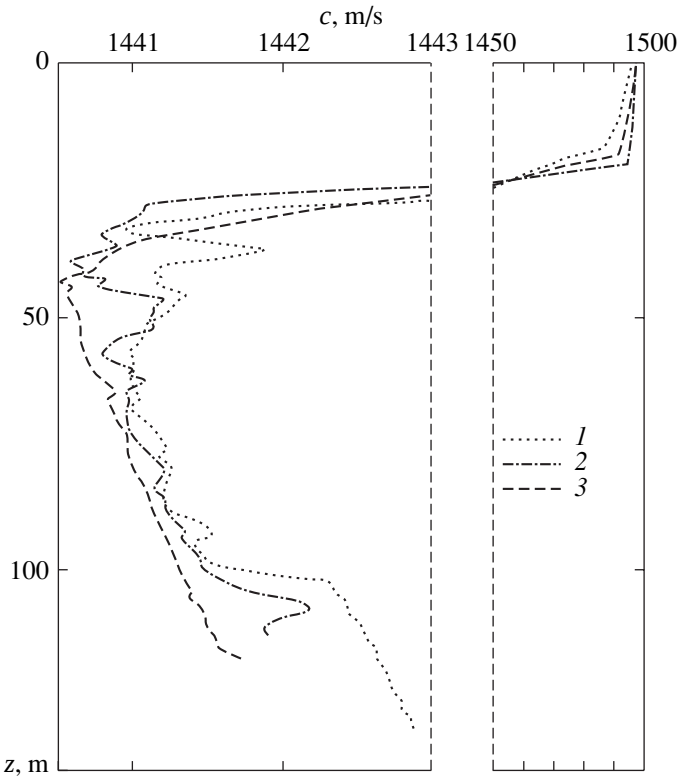

Fig. 1. Vertical profiles of the sound speed $c(z)$. Data of measurements supporting the acoustic experiment: (*1*) near the receiving vessel, (*2*) at a distance of 155 km, and (*3*) at a distance of 320 km.

of the explosion-generated signal can be used: the maximal value of this function is as high as 0.95–0.98.

At shorter distances, time delays between the signals separately arriving at the receiver are not longer than the period of the first oscillation (45 ms). At the distances 190–200 km from the source, they have the same order of magnitude as this period. Thus, for the temporal elongation of the signal in the region at hand, the proportionality factor does not exceed 0.00025 s/km, which is in a good agreement with the calculation performed with the simplified formulas [6] obtained for a bilinear $c(z)$ profile.

On the basis of the experimental data analyzed within a frequency band of 40–1000 Hz, the sound attenuation coefficients were estimated. These coefficients were determined by comparing the experimental decay of the sound field with the cylindrical law of geometrical spread. As a characteristic that is equivalent to the energy of the explosion-generated signal within the frequency band Δf, the following value was used:

$$E_f = \int_0^T p_f^2(t)dt,$$

where T is the duration of the explosion-generated signal and $p_f(t)$ is the signal sound pressure normalized to

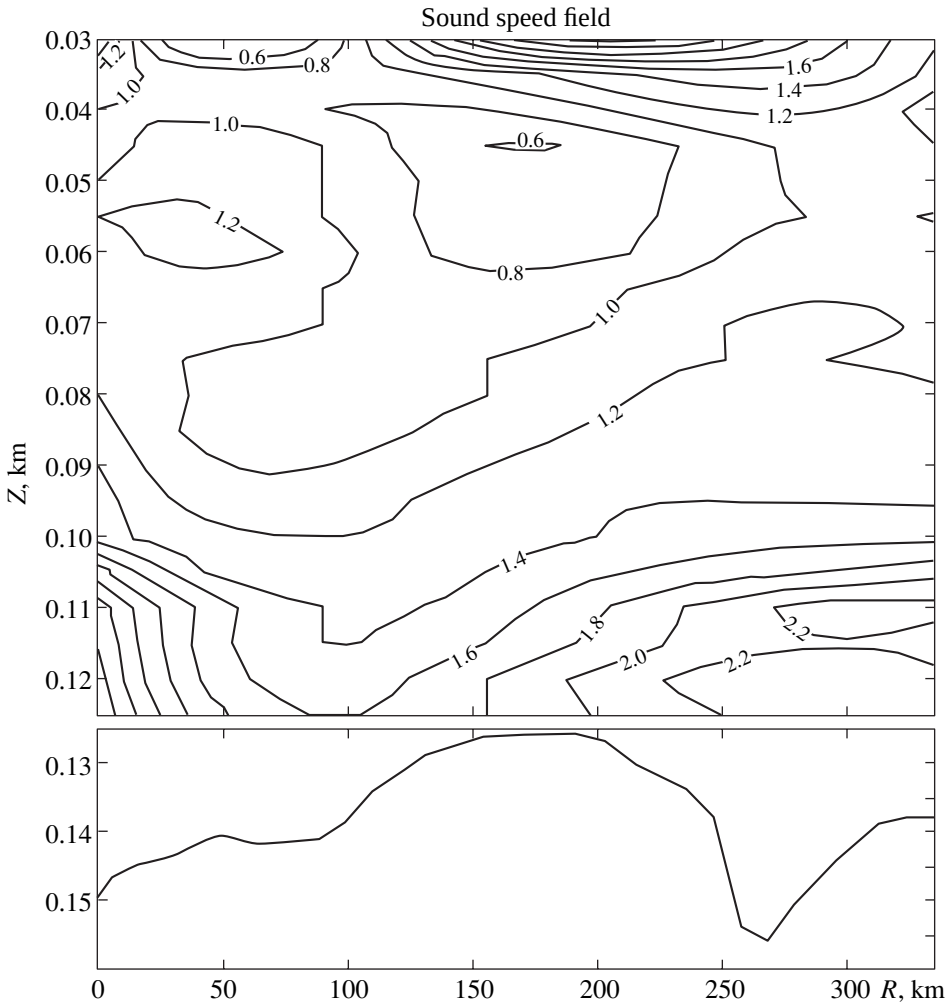

Fig. 2. Sound speed field along the path at depths of 30–125 m. Adjacent isospeed curves differ by 0.2 m/s, the numbers near the curves indicate the excess of the sound speed over 1440 m/s. The lower part of the figure presents the bottom relief measured by echo-sounding.

the frequency band Δf. To obtain the power spectrum of the explosion-generated signal, a computer code was used that was earlier developed to analyze the experimental decays of the sound field and to estimate the attenuation coefficients at individual frequencies.

At the reception depth of 20 m, the signals sufficiently exceeded the noise level at distances shorter than 17 km. For these signals, the loss die to bottom reflections is significant. At the two other reception horizons, all recorded signals are above the noise level within the frequency band 40–1000 Hz.

As a result of processing the signals received at depths of 50 and 120 m, the values of the attenuation coefficients were obtained (Fig. 3). There is nearly no difference in these values for depths of 50 and 120 m. The values obtained for the attenuation coefficients are much higher than the sound absorption coefficients in the sea water, which are presented in [1] for the Sea of Okhotsk.

At a frequency of about 200 Hz, a pronounced minimum can be noticed in the frequency dependence of attenuation. Earlier, in analyzing the data of similar studies [7] in the Baltic Sea, such a minimum was attributed to the critical frequency of the "water" modes. This conclusion was attained, because the Baltic-Sea studies were carried out in spring and summer when the conditions in the propagation channel considerably varied: the critical frequency of the first mode varied by a factor of two to three and the position of the minimum in the frequency dependence of attenuation also changed.

For the experiment in the Sea of Okhotsk, the calculated critical frequency of the first water mode is about 160 Hz, which does not significantly differ from the frequency of the attenuation minimum. To verify the concept of the relation between the attenuation minimum and the critical frequency of the water mode, we carried out a set of calculations with the use of the computer code by Avilov [8], which accounts for changes in the

propagation conditions along the path, namely: the changes in the sound speed profiles measured at different parts of the path and the data of echo-sounding. The calculations were performed for the frequency band 40–800 Hz, with the noise-like signals in 1/3-octave bands. A relatively simple model of the bottom was used: a liquid layer (with a sound speed of 1600 m/s, a loss factor of 0.015, and a density of 1.8 g/cm^3) overlying a liquid halfspace (2600 m/s, 0.001, and 4.0 g/cm^3, respectively). A good quantitative agreement was obtained between the calculated and observed low-frequency attenuation coefficients.

Figure 4 shows the results of calculations for the frequencies 50, 100, 200, and 400 Hz. At frequencies higher than 300–500 Hz, the calculated decays of the sound field (without the absorption in the water) follow the cylindrical law of the geometrical spread for the distances from the source, which exceed 50 km: the deviations of the average decay curves from the cylindrical law are no higher than 0.5 dB for the entire path. At frequencies lower than 300–500 Hz, the difference between the calculated and cylindrical decays increases as the frequency decreases: the additional loss caused by sound absorption in the bottom sediments becomes higher for lower frequencies and reaches 0.014 dB/km at 50 Hz. The latter value agrees well with the experimental data. It is worth mentioning that the objective of the calculations was not to develop a bottom model for the specific region. Instead, the calculations were performed to estimate the contribution of the bottom sediments to the sound attenuation at frequencies lower than the critical ones and to verify the existence of the proposed mechanism responsible for the formation of the minimum in the frequency dependence of attenuation.

At frequencies higher than 200 Hz, the frequency dependence of the sound attenuation in the shallow-water part of the Sea of Okhots can be expressed in the form:

$$\beta = 0.205 f^{1.13} \text{ dB/km},$$

where the frequency is specified in kilohertz. At such frequencies, the attenuation coefficients in the Sea of Okhotsk are, by a factor of 3–5, higher than those obtained in the Baltic Sea. The shapes of the decay curves are also somewhat different for these seas. In analyzing the experimental data of the Baltic Sea [7], a conclusion was made that the sound scattering by internal waves was the most probable factor responsible for the observed high attenuation in that region. The analysis included the data of the internal wave observation in the studies of sound attenuation in the Baltic Sea, as well as the results of modeling the off-channel sound scattering by internal waves.

During the experiments in the Sea of Okhotsk, no observations of internal waves were carried out. As far as the author knows, only publication [9] exists on measuring internal waves in a coastal zone of the Sea of Okhotsk. Specifically, the published data referred to the

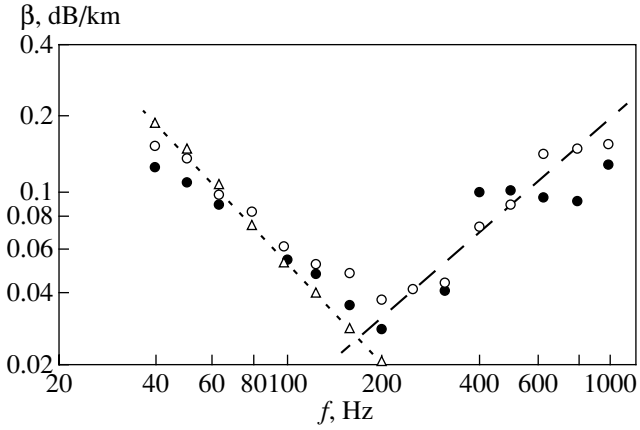

Fig. 3. Sound attenuation in the shallow-water (125–155 m) northern part of the Sea of Okhotsk: (○ ○ ○ ○) the experimental attenuation coefficients determined from the decay of the sound field at a depth of 50 m, (●●●●) similar values for a depth of 120 m, (△ △ △ △) the calculation with Avilov's computer code, and (_ _ _ _ _) the frequency dependence of attenuation obtained by the formula $\beta = 0.205 f^{1.13}$.

south western part of this sea (the measurements were performed in a narrow shelf patch near the south-western coast of Sakhalin) and, hence, cannot be extended to the large shelf zone of the northern part of the Sea of Okhotsk. At the same time, the Baltic Sea and the Sea of Okhotsk have a clearly defined layer of temperature discontinuity (at a depth of ~25 m) and comparable sea depths (80–100 m in the Baltic Sea and 125–155 m in the Sea of Okhotsk). These similarities allows one to assume that, in the experimental region of the Sea of Okhotsk, short-period internal waves also exist and their properties are similar to those of the Baltic Sea.

Using the known limiting angles, at which the water rays cross the USC axis, and the known full cycle lengths of these rays, and assuming a similarity of nature and amplitude of internal waves in the two seas, one can estimate the difference in attenuation, which is caused by the sound scattering from the internal waves. For the Baltic Sea, the angles at which the water rays cross the USC axis are $-(6°–8°) < \theta < +(6°–8°)$, and the lengh of the full cycle is D = 1.5–2.5 km for these rays. For the Sea of Okhotsk, the corresponding values are $-2.6° < \theta < +2.6°$ and D = 4–6 km. The loss caused by scattering is proportional to the cycle length of the water rays (the internal wave is associated with the temperature discontinuity layer, and the scattering takes place within the upper half-cycle) and to the squared limiting angle of their crossing the USC axis (see, e.g., [10, 11]). From these considerations, the ratio of the attenuation coefficients can be estimated for the Baltic Sea and the Sea of Okhotsk. The calculated ratio proves to be approximately equal to three, which well agrees with the experimental estimate (3–5). Of course, this agreement means nothing more than indirect evidence in favor of the hypothesis that the sound scattering by

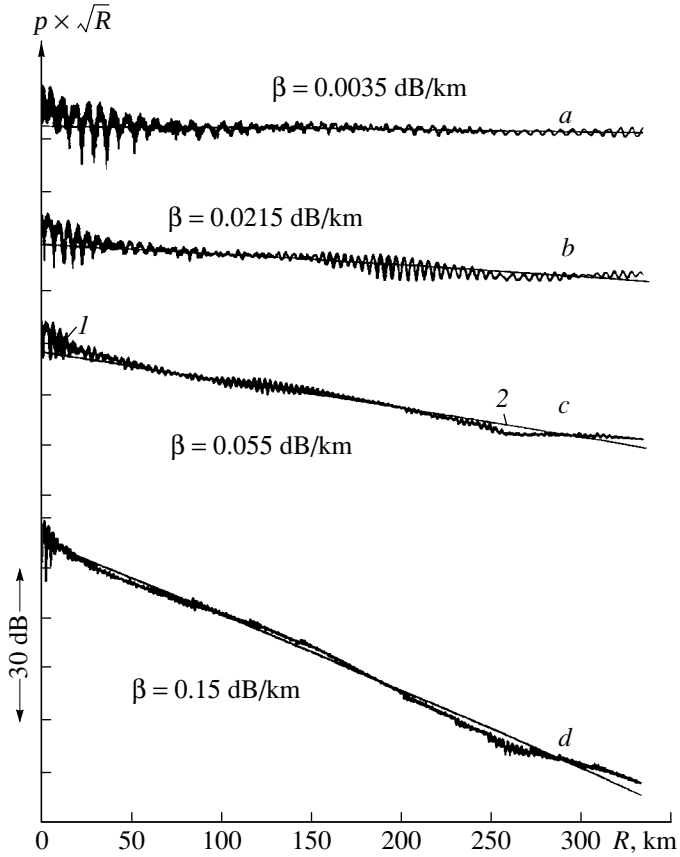

Fig. 4. Results of the sound field calculations by Avilov's computer code at the frequencies (*a*) 400, (*b*) 200, (*c*) 100, and (*d*) 50 Hz in 1/3-octave bands: (*1*) the range dependence of the sound level corrected for the cylindrical law of geometrical spread and (*2*) the linearly approximated decay of the sound level corrected for the cylindrical law (the linear approximation by the least-squares method for the part of the path 50–335 km). At each frequency, near the corresponding curve, the attenuation coefficient is indicated, as determined from the inclination of the line approximating the sound level decay corrected for the cylindrical law.

internal waves is the most probable attenuation mechanism (at frequencies higher than the critical one) for shallow-water sound channels. The real validation of this hypothesis requires the development of a rigorous theory of sound scattering by internal waves and a special-purpose acoustic experiment including the measurements of the internal waves.

In conclusion, we formulate the main results of the experiment on long-range propagation of the explosion-generated signals in the shallow-water (125–155 m) region of the Sea of Okhotsk with a fully-developed USC.

(i) In the time structure of the multiray explosion-generated signal received at the USC axis, at the distances up to 250–300 km, the pulses of the shock wave and the first gas-bubble oscillation are well resolved, each of them individually reproducing the time structure of the propagating sound field.

(ii) For the conditions of the experiment, a small increase in the duration of the explosion-generated signal is observed; the proportionality factor between the duration and the distance is about 0.00025 s/km (upon subtracting the period of the bubble oscillation).

(iii) The experimental data on the sound attenuation within the frequency band 40–1000 Hz are obtained. The attenuation is much higher than the sound absorption in the sea medium. The frequency dependence of attenuation has a minimum at a frequency of about 200 Hz, which is close to the critical frequency of the first water mode (about 160 Hz).

(iv) The mechanism responsible for the minimum in the frequency dependence of sound attenuation in the USC of a shallow sea is revealed. As the frequency decreases starting from the critical one (for the water modes), the sound attenuation increases because of the acoustic energy loss in the bottom sediments. At frequencies higher than the critical one, the most probable reason for the attenuation to exceed the absorption is the sound scattering by short-period internal waves.

REFERENCES

1. R. A. Vadov, Akust. Zh. **45**, 174 (1999) [Acoust. Phys. **45**, 143 (1999)].
2. V. F. Sukhoveĭ, *Seas of the Ocean* (Gidrometeoizdat, Leningrad, 1986).
3. T. A. Bernikova, *Hydrology and Industrial Oceanology* (Pishchevaya Promyshlennost', Moscow, 1980).
4. P. L. Bezrukov, Tr. Inst. Okeanolog. im. P. P. Shirshova, Akad. Nauk SSSR **32**, 15 (1960).
5. W. D. Wilson, J. Acoust. Soc. Am. **34**, 866 (1962).
6. L. M. Brekhovskikh and Yu. P. Lysanov, *Fundamentals of Ocean Acoustics* (Gidrometeoizdat, Leningrad, 1982; Springer, New York, 1991).
7. R. A. Vadov, Akust. Zh. **47**, 189 (2001) [Acoust. Phys. **47**, 150 (2001)].
8. K. V. Avilov, Akust. Zh. **41**, 5 (1995) [Acoust. Phys. **41**, 1 (1995)].
9. A. P. Nagovitsyn and E. N. Pelinovskiĭ, Meteorol. Gidrol. **4**, 124 (1988).
10. R. H. Mellen, D. G. Browning, and L. Goodman, J. Acoust. Soc. Am. **60**, 1053 (1976).
11. *Sound Transmission through a Fluctuating Ocean*, Ed. by S. Flatte (Cambridge Univ. Press, Cambridge, UK, 1979; Mir, Moscow, 1982).

Translated by E. Kopyl

Acoustical Physics, Vol. 48, No. 2, 2002, pp. 147–154. Translated from Akusticheskiĭ Zhurnal, Vol. 48, No. 2, 2002, pp. 178–186.

Effect of the Interaction of Spatial Modes on the Nonlinear Dynamics of Sound Beams

I. S. Vereshchagina* and A. A. Perelomova**

** Mathematical Faculty, Kaliningrad State University, ul. Aleksandra Nevskogo 14, Kaliningrad, 236041 Russia*
e-mail: verd@tphys.albertina.ru

*** Faculty of Engineering Physics and Applied Mathematics, Gdansk Technical University, Gdansk, 80952 Poland*
e-mail: anpe@mifgate.pg.gda.pl

Received July 31, 2000

Abstract—Propagation of an acoustic beam in a medium with a combined second- and third-order nonlinearity is studied. The derivation of the dynamics equations and the determination of modes is performed using the orthogonal-projection operator technique. The problem on the beam evolution considered with allowance for weak nonlinearity, diffraction, and dissipation leads to a set of equations describing the interaction of directed waves and a quasi-stationary (thermal) mode. In the conditions of a directed beam, the inclusion of the interaction leads to a modified Khokhlov–Zabolotskaya–Kuznetsov equation with quadratic and cubic nonlinearities. The solutions to the problem are obtained in the region near the beam axis, in the form of series expansions in the transverse coordinate up to the focal point. The results of calculations are represented in graphical form for different nonlinearity combinations. *© 2002 MAIK "Nauka/Interperiodica".*

One of the major problems of the theory of nonlinear acoustic waves is related to an adequate description of the distortions suffered by an acoustic signal in the course of its propagation in a medium. Any perturbation of a medium can be represented as a superposition of modes characteristic of a given problem, which determine the basic possible types of motion. Taking into account the nonlinearity of a beam leads to the interaction of modes and to their self-action. A correct consideration of the mode interaction is most simple when the separated modes are independent (i.e., they are separated by the projectors that are orthogonal in the linear approximation). The modes, as a basis, must describe all possible types of motion, i.e., the set of projection operators must be complete.

The basic equations of the theory describing the propagation of nonlinear acoustic beams are the Khokhlov–Zabolotskaya (KhZ) and Khokhlov–Zabolotskaya–Kuznetsov (KhZK) equations, which take into account the viscosity of the medium. These equations are obtained by the method of a slowly varying profile, when the evolution of the wave profile is studied in the x–ct coordinate system moving with the velocity of the wave propagation in the linear approximation [1–3].

The KhZ and KhZK equations do not take into account the effect of the other two modes: the stationary mode and the backward wave. The necessity to take into account the backward wave and the thermal mode in the one-dimensional dynamics is indicated in the review [4]. There, it is also demonstrated that the approximation of one directed acoustic mode leads to an incorrect value of the time-average flux of angular momentum. This points to the necessity of taking into account the mode interaction. In the cited review [4], attention is given to the generation of the thermal mode due to the dissipation of the acoustic mode related to the viscosity of the medium or the attenuation at the shock wave front. We note that the nonisentropic (thermal) mode must be taken into account even in the absence of viscosity and heat conductivity of the medium. This is essential for linear problems with nonisentropic initial conditions and in studying the nonlinear dynamics, because a nonlinear generation and the interaction of all modes take place. The thermal mode determined here as one of the principal modes is not necessarily the secondary mode caused by the attenuation of an acoustic wave. Traditionally, the thermal mode is treated as a secondary one [4], which evidently makes it impossible to consider the problems with essentially nonisentropic initial conditions.

In this paper, we consider the problem of the propagation and focusing of a nonlinear acoustic beam. For the derivation of the equations describing the wave dynamics, we propose the projection operator method. In the framework of the proposed approach, we obtain a set of coupled equations describing the interaction of two acoustic modes (the right and left beams) and the quasi-stationary thermal mode. These equations take into account the weak nonlinearity (quadratic and cubic) of the perturbation, the diffraction, and the dissipation of the beam. We note that, here, we do not use the assumption concerning the potential character of the flow. In particular, this approach provides a more accurate expression for the nonlinear constants in the

1063-7710/02/4802-0147$22.00 © 2002 MAIK "Nauka/Interperiodica"

KhZK equation (for example, for the right beam) for the terms with quadratic and cubic nonlinearities. The calculated coefficients take into account the nonlinear generation of other modes (the left beam and the stationary mode) and their inverse influence on the principal right wave.

Approximate solutions to the equation derived for the right beam are determined, including the solutions in the near-focal region, and the plots illustrating the beam behavior at different distances from the focus and the effect of the third-order nonlinearity on the profile dynamics are presented.

PROJECTION OPERATORS. MODE INTERACTION IN A ONE-DIMENSIONAL PROBLEM WITH VISCOSITY AND HEAT CONDUCTIVITY

Starting from the paper by Kovasznay and Boa The-Chu [5], in hydrodynamics it is common to single out three modes (the vortex mode, the sound pressure mode, and the entropy mode), which separate the types of possible perturbations according to the character of motion and dissipation, in studying perturbations in a viscous heat-conducting medium. In the linear approximation, these modes do not interact and a perturbation is generally represented as a sum of three modes. We also suggest the introduction of three modes in the linear approximation. However, in contrast to [5], we separate the perturbations according to the basic types of motion, which are determined by the dispersion relation in the linear approximation, rather than according to the character of motion and dissipation. This allows us to determine the modes using specific relations, namely, through the eigenvectors of the linear problem. Here, we restrict our consideration to a relatively simple case of a homogeneous medium in the absence of flows as a background. However, since it is easy to formulate the proposed method as an algorithm, it is also easy to consider stratified media with flows. It is important that the modes determined in this way are mutually orthogonal and form a complete set of basis vectors, and the relations obtained in the linear approximation are also valid for a nonlinear case. Let us briefly describe the idea of the proposed method of mode separation.

At the first stage, we consider the problem of the propagation of an acoustic beam in the linear approximation. As the initial equations, we take the system of hydrodynamic equations for the density ρ, mass velocity V along the x axis, and the internal energy of a unit mass e with the equation of motion in the Navier–Stokes form. In the equation of energy balance, we ignore the nonlinear viscous cross terms (which is a common approach in acoustics: see, e.g., [2, 4]). This approximation assumes the amplitude of the acoustic disturbance and the thermoviscosity to be small. In this case, the contribution of dissipative terms is (as usual [2]) much smaller than that of nonlinear terms.

$$\frac{\partial \rho}{\partial t} + \frac{\partial(\rho V)}{\partial x} = 0,$$

$$\rho\frac{\partial V}{\partial t} + \rho V\frac{\partial V}{\partial x} + \frac{\partial p}{\partial x} - \left(\frac{4}{3}\eta + \zeta\right)\frac{\partial^2 V}{\partial x^2} = 0, \qquad (1)$$

$$\rho\frac{\partial e}{\partial t} + \rho V\frac{\partial e}{\partial x} + p\frac{\partial V}{\partial x} - \chi\frac{\partial^2 T}{\partial x^2} = 0.$$

Here, p is pressure, T is temperature, ζ and η are the coefficients of volume and shear viscosities, respectively, and χ is the coefficient of heat conductivity. The coefficients of viscosity and heat conductivity are assumed to be constant, and the background is assumed to be homogeneous. To make system (1) complete, it is necessary to add two more equations. For this purpose, we take the caloric and thermal equations of state: $e = e(p, \rho)$ and $T = T(p, \rho)$. These equations have the following form for an ideal gas:

$$e = \frac{p}{\rho(\gamma - 1)}, \quad T = \frac{p}{\rho(\gamma - 1)C_v}, \qquad (2)$$

where C_v is the specific heat of the gas at constant volume and $\gamma = C_p/C_v$ is the adiabatic constant. Here, we consider the case of an ideal gas, although the caloric and thermal equations of state in the general form allow one to study the dynamics of any liquid or gas. To do this, it is necessary to expand the small perturbations of internal energy and temperature into a Taylor series in the vicinity of the background values of pressure and density with the required accuracy. Let us change to new variables:

$$p' = \frac{p - p_0}{\varepsilon c^2 \rho_0}, \quad \rho' = \frac{\rho - \rho_0}{\varepsilon \rho_0},$$

$$V' = \frac{V}{\varepsilon c}, \quad x' = \frac{x}{\lambda}, \quad \text{and} \quad t' = \frac{ct}{\lambda}.$$

Here, the background parameters are denoted by the index 0, λ is the characteristic wavelength, c is the adiabatic velocity of sound, and ε is the small amplitude parameter. Below, we omit the primes marking the dimensionless quantities. Eliminating T and e from the initial set of equations and ignoring the viscosity and heat conductivity, we represent Eqs. (1) in the linear approximation in the form

$$\frac{\partial \varphi}{\partial t} + L\varphi = 0,$$

$$\varphi = \begin{pmatrix} V \\ p \\ \rho \end{pmatrix}, \quad L = \begin{pmatrix} 0 & \frac{\partial}{\partial x} & 0 \\ \frac{\partial}{\partial x} & 0 & 0 \\ \frac{\partial}{\partial x} & 0 & 0 \end{pmatrix}. \qquad (3)$$

Let us consider plane waves representing the mass velocity as $V = V_k \exp(i\omega t - ikx)$ and the quantities p and ρ in an analogous form. The dispersion relation for Eqs. (3) has three roots $\omega_{1,2} = \pm k$ and $\omega_3 = 0$, which correspond to three independent branches of the dispersion relation. In this case, $\omega_1 = k$ describes the wave propagating to the right, $\omega_2 = -k$ describes the left wave, and $\omega_3 = 0$ describes the stationary addition to the background.

The eigenvectors corresponding to these three solutions have the forms $e_1 = (1, 1, 1)^T$, $e_2 = (-1, 1, 1)^T$, and $e_3 = (0, 0, 1)^T$, whence we have linearly independent solutions for each branch: $\varphi_1 = (V_1, p_1, \rho_1)^T$, $\varphi_2 = (-V_2, p_2, \rho_2)^T$, and $\varphi_3 = (0, 0, \rho_3)^T$. The corresponding operators of projection onto each branch can be represented in the explicit forms

$$P_{1,2} = \begin{pmatrix} 1/2 & \pm 1/2 & 0 \\ \pm 1/2 & 1/2 & 0 \\ \pm 1/2 & 1/2 & 0 \end{pmatrix}, \quad P_3 = \begin{pmatrix} 0 & 0 & 0 \\ 0 & 0 & 0 \\ 0 & -1 & 1 \end{pmatrix}. \quad (4)$$

It is very important that the projectors determined by Eqs. (4) are mutually orthogonal. This allows a correct separation of the initial disturbance into independent (in the linear approximation) modes. The components of the eigenvectors are evidently related as follows: $V_1 = \rho_1 = p_1$, $V_2 = -\rho_2 = -p_2$, and $p_3 = V_3 = 0$. The projection operators, as usual, satisfy the requirements of normalization and orthogonality: $P_1 + P_2 + P_3 = \hat{I}$, $P_k P_n = \hat{0}$, $k \neq n$, and $P_k P_k = P_k$, where $\hat{I}$ and $\hat{0}$ are the unit and null matrices, respectively.

The fact that it is possible to represent the projection operators in an explicit form provides an opportunity to separate any disturbance into the fields of the right and left waves and the stationary mode. For this purpose, it is sufficient to apply a corresponding projection operator to the vector $\varphi_k = P_{k\varphi}$.

It is important that the suggested separation into modes does not imply the separation of disturbances into vortex and vortex-free ones. Moreover, the stationary mode is not necessarily secondary, i.e., generated by an acoustic wave, as in [4]. This provides an opportunity to extend the class of the examined problems, e.g., to the problems with essentially nonisentropic initial conditions. According to our definition, the thermal mode is one of the basic types of motion even in media without viscosity and heat conductivity, in contrast to the secondary thermal mode caused by the attenuation of an acoustic wave [4]. It should also be noted that, in the case of a stratified medium, the elements of the projection operators are integro-differential operators [6].

The initial set of hydrodynamic equations (1) neglecting the viscosity and heat conductivity can be written in the form

$$\frac{\partial \varphi}{\partial t} + L\varphi = \tilde{\varphi}, \quad (5)$$

where the function $\tilde{\varphi}$ on the right-hand side of the equation takes into account the nonlinear terms and has the form

$$\tilde{\varphi} = \varepsilon \begin{pmatrix} -V\dfrac{\partial V}{\partial x} + \rho\dfrac{\partial p}{\partial x} \\ -V\dfrac{\partial p}{\partial x} - \gamma p\dfrac{\partial V}{\partial x} \\ -V\dfrac{\partial \rho}{\partial x} - \rho\dfrac{\partial V}{\partial x} \end{pmatrix} + O(\varepsilon^2).$$

Let us change to the new variables ρ_1, ρ_2, and ρ_3 and assume that, for the eigenvectors, the constraint equations that are determined by the linear problem are valid: $V = V_1 + V_2 = \rho_1 - \rho_2$, $p = p_1 + p_2 = \rho_1 + \rho_2$, and $\rho = \rho_1 + \rho_2 + \rho_3$. Applying the projection operators to both sides of Eq. (5), we obtain a set of nonlinearly coupled equations for the density perturbations of each mode:

$$\frac{\partial \rho_n}{\partial t} + c_n\frac{\partial \rho_n}{\partial x} + \frac{\varepsilon}{2}\sum_{i,m=1}^{3} Y^n_{i,m}\rho_i\frac{\partial}{\partial x}\rho_m + O(\varepsilon^2) = 0, \quad (6)$$

where $n = 1, 2, 3$; $c_{1,2} = \pm 1$, and $c_3 = 0$. The indices 1, 2, and 3 correspond to directed and stationary modes, which in the problem of nonlinear dynamics are appropriate to be called quasi-directed and quasi-stationary modes. The coefficients $Y^k_{i,m}$ are determined in the tables

$Y^1_{i,m}$	m	1	2	3
i				
1		$\gamma + 1$	$-(\gamma + 1)$	0
2		$\gamma - 3$	$-(\gamma + 1)$	0
3		-1	-1	0

$Y^2_{i,m}$	m	1	2	3
i				
1		$\gamma + 1$	$-(\gamma - 3)$	0
2		$\gamma + 1$	$-(\gamma + 1)$	0
3		1	1	0

$Y^3_{i,m}$	m	1	2	3
i				
1		$-2(\gamma - 1)$	$2(\gamma - 1)$	2
2		$-2(\gamma - 1)$	$2(\gamma - 1)$	-2
3		2	-2	0

In particular, for the right-propagating wave with allowance for self-action, from Eqs. (6) we obtain the known evolution equation [1, 2]:

$$\frac{\partial \rho_1}{\partial t} + \frac{\partial \rho_1}{\partial x} + \varepsilon \frac{\gamma + 1}{2} \rho_1 \frac{\partial}{\partial x} \rho_1 + O(\varepsilon^2) = 0. \quad (7)$$

Assuming the terms connected with viscosity and heat conductivity in Eqs. (1) to be small, as well as the nonlinear terms, we represent Eqs. (1) in terms of dimensionless variables in the form of Eq. (5) with a new vector on the right-hand side:

$$\tilde{\varphi} = \varepsilon \begin{pmatrix} -V\frac{\partial V}{\partial x} + \rho \frac{\partial p}{\partial x} \\ -V\frac{\partial p}{\partial x} - \gamma p \frac{\partial V}{\partial x} \\ -V\frac{\partial \rho}{\partial x} - \rho \frac{\partial V}{\partial x} \end{pmatrix} + \varepsilon^2 \begin{pmatrix} -\rho^2 \frac{\partial p}{\partial x} \\ 0 \\ 0 \end{pmatrix} + \begin{pmatrix} \delta_1 \frac{\partial^2 V}{\partial x^2} \\ \frac{\delta_2}{\gamma - 1} \frac{\partial^2 (\gamma p - \rho)}{\partial x^2} \\ 0 \end{pmatrix} + O(\varepsilon^3, \varepsilon\delta). \quad (8)$$

Here,

$$\delta_1 = \left(\zeta + \frac{4\eta}{3}\right)\frac{1}{\rho_0 c \lambda}, \quad \delta_2 = \chi\left(\frac{1}{C_v} - \frac{1}{C_p}\right)\frac{1}{\rho_0 c \lambda},$$

$$\text{and} \quad \delta = \delta_1 + \delta_2$$

are the small dimensionless parameters taking into account the contributions of viscosity and heat conductivity. Applying the operator P_1 to Eq. (5) with the right-hand side in the form of Eq. (8), we obtain the Burgers equation for the right mode with allowance for the self-action:

$$\frac{\partial \rho_1}{\partial t} + \frac{\partial \rho_1}{\partial x} + \varepsilon \frac{\gamma + 1}{2} \rho_1 \frac{\partial}{\partial x} \rho_1 - \frac{\delta}{2} \frac{\partial^2}{\partial x^2} \rho_1 + O(\varepsilon^2, \varepsilon\delta) = 0. \quad (9)$$

It is necessary to note that, in Eq. (8), the coefficients before the terms that correspond to the quadratic nonlinearity and thermoviscosity differ from the expressions given in [1–3, 7], where the stationary mode is not considered and the constraint equations correspond only to the acoustic modes: $p = \rho$. It is evident that, with such a description, the derived equations are unsuitable for investigating the complete nonlinear dynamics, because they lead to an incorrect determination of the matrix elements $Y^k_{i,m}$, which are responsible for the mode interaction.

NONLINEAR DYNAMICS OF SOUND BEAMS INTERACTING WITH THE THERMAL MODE

Let us consider the problem of the propagation of a three-dimensional acoustic beam with a weak divergence along the y and z directions, which are orthogonal to the propagation direction. As earlier, we assume the dissipative and nonlinear terms to be small. As above, at the first stage we consider the linear problem without taking into account the heat conductivity and viscosity:

$$\frac{\partial \varphi_1}{\partial t} + L_1 \varphi_1 = 0. \quad (10)$$

Here, $\varphi_1 = (V_x, V_y, V_z, p, \rho)^T$ and V_x, V_y, and V_z are the velocity components. Following the concept of a slowly varying profile (the transverse velocities change slower) [1, 2, 7], we introduce the dimensionless variables: $V'_x = V_x/\varepsilon c$, $V'_y = V_y/\varepsilon c$, $V'_z = V_z/\varepsilon c$, $y' = y\sqrt{\beta}/\lambda$, and $z' = z\sqrt{\beta}/\lambda$, where β is the small parameter characterizing the beam divergence. Below, we omit the primes marking the dimensionless variables. The matrix in Eq. (10) is of the fifth order:

$$L_1 = \begin{pmatrix} 0 & 0 & 0 & \frac{\partial}{\partial x} & 0 \\ 0 & 0 & 0 & \sqrt{\beta}\frac{\partial}{\partial y} & 0 \\ 0 & 0 & 0 & \sqrt{\beta}\frac{\partial}{\partial z} & 0 \\ \frac{\partial}{\partial x} & \sqrt{\beta}\frac{\partial}{\partial y} & \sqrt{\beta}\frac{\partial}{\partial z} & 0 & 0 \\ \frac{\partial}{\partial x} & \sqrt{\beta}\frac{\partial}{\partial y} & \sqrt{\beta}\frac{\partial}{\partial z} & 0 & 0 \end{pmatrix}.$$

The corresponding dispersion relation has five roots. One of the roots $\omega = 0$ corresponds to the stationary mode. Four other roots correspond to acoustic modes and are determined by the independent combinations of ω, k_x, k_y, and k_z with different signs, which satisfy the condition $\omega^2 = (k_x)^2 + \beta[(k_y)^2 + (k_z)^2]$. Two roots correspond to the right acoustic mode and two roots, to the left one. We assume that the motion is quasi-plane and weakly linear, which allows us to treat the corresponding terms in the initial set of equations as small additions. Taking into account the small nonlinear and thermoviscous terms leads to the following set of equations:

$$\frac{\partial}{\partial t}\left(\frac{\partial}{\partial t} + L\right)\varphi = \beta\left(\frac{\partial^2}{\partial z^2} + \frac{\partial^2}{\partial y^2}\right)\begin{pmatrix} 0 \\ p \\ \rho \end{pmatrix} + \tilde{\varphi}_1. \quad (11)$$

The operators L and φ have the same form as in the case of the one-dimensional problem, $\tilde{\varphi}_1 = \partial\tilde{\varphi}/\partial t$. Applying

one-dimensional projection operators to both parts of the set of equations (11), we obtain coupled equations

$$\frac{\partial}{\partial t}\Bigg(\frac{\partial \rho_n}{\partial t} + c_n\frac{\partial \rho_n}{\partial x} + \frac{\varepsilon}{2}\sum_{i,m=1}^{3} Y^n_{i,m}\rho_i\frac{\partial}{\partial x}\rho_m + \frac{\varepsilon^2}{2}\sum_{i,m=1}^{3} T^n_{i,m}\rho_i\rho_m\frac{\partial}{\partial x}(\rho_1-\rho_2) + \frac{1}{2}\sum_{i=1}^{3} B^n_i\frac{\partial^2}{\partial x^2}\rho_i\Bigg) - \frac{\beta}{2}\Big(\frac{\partial^2}{\partial y^2}+\frac{\partial^2}{\partial z^2}\Big)\sum_{i=1}^{3}\Theta^n_i\rho_i + O(\varepsilon^3, \varepsilon\beta, \varepsilon\delta) = 0. \quad (12)$$

Here, as before, $c_{1,2} = \pm 1$; $c_3 = 0$; and the coefficients $Y^n_{i,m}$, which take into account the quadratic nonlinearity, are determined earlier in the tables of Eq. (6). The coefficients Θ^n_i, B^n_i, and $T^n_{i,m}$, which determine the contributions of the beam divergence, thermal conductivity, and cubic nonlinearity, respectively, are given in the tables:

B^n_i	n 1	2	3
i			
1	$-\delta$	$\delta_1-\delta_2$	$\delta_2/(\gamma-1)$
2	$\delta_1-\delta_2$	$-\delta$	$\delta_2/(\gamma-1)$
3	$2\delta_2$	$2\delta_2$	$-2\delta_2/(\gamma-1)$

Θ^n_i	n 1	2	3
i			
1	1	1	0
2	1	1	0
3	0	0	0

$T^1_{i,m} = T^2_{i,m} = 1$, and $T^3_{i,m} = 0$ for all i, m.

The set of equations (12) describes the interaction of three independent modes, i.e., the right, left, and thermal modes. In particular, Eq. (12) yields the known KhZK equation taking into account the propagation of only the right wave:

$$\frac{\partial}{\partial\tau}\Bigg(\frac{\partial\rho_1}{\partial x} + \varepsilon\frac{\gamma+1}{2}\rho_1\frac{\partial}{\partial\tau}\rho_1 - \frac{\delta}{2}\frac{\partial^2}{\partial\tau^2}\rho_1\Bigg) - \frac{\beta}{2}\Big(\frac{\partial^2}{\partial y^2}+\frac{\partial^2}{\partial z^2}\Big)\rho_1 + O(\varepsilon^2, \varepsilon\delta, \varepsilon\beta) = 0. \quad (13)$$

The latter equation is transformed into the KhZ equation when $\delta = 0$.

THE MODIFIED KHOKHLOV–ZABOLOTSKAYA–KUZNETSOV EQUATION

Let us assume that one of the modes, the right one for definiteness, prevails, i.e., it is generated predominantly. This corresponds to the realization of linear relations (probably, approximate) for this mode. Problems with initial conditions and boundary-value problems can be considered in the framework of the indicated approximation (in this case, the correspondence must exist at the boundary). It is possible to demonstrate that a linear boundary-value problem in a semi-infinite space $x > 0$ (initially unperturbed) corresponds to a strict realization of the relations for the right mode at the boundary and in the whole semi-infinite space. The generation of other modes by the principal mode and their evolution is described by Eqs. (12). We use the nonsingular theory of perturbations to study the generation of two other modes and their reciprocal effect on the first one, as in [8, 9]. We assume that the nonlinearity prevails over the viscosity and beam divergence. We also assume that $\delta, \beta \sim \varepsilon^2$. The evolution of the density disturbance of the first mode with allowance for self-action is determined by the equation

$$\frac{\partial}{\partial t}\Bigg(\frac{\partial\rho_1^{(0)}}{\partial t} + \frac{\partial\rho_1^{(0)}}{\partial x} + \frac{\varepsilon}{2}(\gamma+1)\rho_1^{(0)}\frac{\partial\rho_1^{(0)}}{\partial x} + \frac{\varepsilon^2}{2}\rho_1^{(0)2}\frac{\partial\rho_1^{(0)}}{\partial x} - \frac{\delta}{2}\frac{\partial^2\rho_1^{(0)}}{\partial x^2}\Bigg) - \frac{\beta}{2}\Big(\frac{\partial^2}{\partial y^2}+\frac{\partial^2}{\partial z^2}\Big)\rho_1^{(0)} = 0. \quad (14)$$

For the second and third modes in the first approximation with allowance for their nonlinear generation, we have

$$\rho_2^{(1)}(x, y, z, t) = \rho_2^{(0)} - \frac{\varepsilon}{2}(\gamma+1)\times\int_0^t \rho_1^{(0)}(x+t-\tau, y, z, \tau)\frac{\partial}{\partial x}\rho_1^{(0)}(x+t-\tau, y, z, \tau)d\tau,$$

$$\rho_3^{(1)}(x, y, z, t) = \rho_3^{(0)} + \varepsilon(\gamma-1)\times\int_0^t \rho_1^{(0)}(x, y, z, \tau)\frac{\partial}{\partial x}\rho_1^{(0)}(x, y, z, \tau)d\tau.$$

The solutions to the equations for $\rho_2^{(0)}(x, y, z, t)$ and $\rho_3^{(0)}(x, y, z, t)$ are evidently zero: $\rho_2^{(0)}(x, y, z, t) = 0$ and $\rho_3^{(0)}(x, y, z, t) = 0$. Integrating Eq. (14) with respect to time, we obtain

$$\frac{\partial}{\partial t}\rho_1^{(0)}(x, y, z, t) + \frac{\partial}{\partial x}\rho_1^{(0)}(x, y, z, t) = O(\varepsilon). \quad (15)$$

Taking this equation into account, we can write for the next approximation:

$$\rho_2^{(1)}(x, y, z, t) = \frac{\varepsilon(\gamma+1)}{8}[(\rho_1^{(0)}(x, y, z, t))^2 - (\rho_1^{(0)}(x+t, y, z, 0))^2], \quad (16)$$

$$\rho_3^{(1)}(x, y, z, t) = -\frac{\varepsilon(\gamma-1)}{2}[(\rho_1^{(0)}(x, y, z, t))^2 - (\rho_1^{(0)}(x, y, z, 0))^2]. \quad (17)$$

Taking into account the reciprocal effect of the second and third modes, according to Eqs. (12), (16), and (17)

we obtain an evolution equation of the next order for the first mode:

$$\frac{\partial}{\partial t}\Bigg[\frac{\partial \rho_1^{(1)}}{\partial t} + \frac{\partial \rho_1^{(1)}}{\partial x} + \frac{\varepsilon}{2}\rho_1^{(1)}\Bigg((\gamma+1)\frac{\partial \rho_1^{(1)}}{\partial x} + \varepsilon(A_1+1)\rho_1^{(1)}\frac{\partial \rho_1^{(1)}}{\partial x}\Bigg) - \frac{1}{2}\delta\frac{\partial^2 \rho_1^{(1)}}{\partial x^2}\Bigg] - \frac{\beta}{2}\Big(\frac{\partial^2}{\partial y^2} + \frac{\partial^2}{\partial z^2}\Big)\rho_1^{(1)} = 0, \quad (18)$$

where

$$A_1 = \frac{1}{2}\sum_{m=2,3}(Y^1_{m,1}/2 + Y^1_{1,m})Y^m_{1,1}/(c_1 - c_m) = -\frac{1}{8}(\gamma+1)^2 - 1.$$

The new coefficient A_1 before the cubic term corresponds to the correction that takes into account the reciprocal influence of two other modes on the first one, while $T^1_{1,1} = 1$ in the same term takes into account the self-action of the order of ε^2 for the principal mode.

THE MODIFIED KHOKHLOV–ZABOLOTSKAYA EQUATION. AN ANALYTICAL SOLUTION

The set of equations (12) and the approximate evolution equation (18) are too complicated to obtain a general solution, even if we ignore the thermoviscous terms. Equation (18) differs from the KhZK equation in the cubic nonlinear term taking into account the effect of the left beam and quasi-stationary mode (which are generated in the course of the propagation of the right acoustic beam) on the right wave.

Let us recall briefly the advances in the study of the KhZK equation within the last few years. The study of the KhZ and KhZK equations started in the 1970s. The method of nonlinear geometric acoustics for high-frequency sources, $\lambda/a \ll 1$ (a is the characteristic size of the source), was used at that time [3]. The method allows one to describe the evolution up to the focal region, but not within the region itself, because the expressions become singular. Simultaneously, in optics, the paraxial approximation was successfully used. This approximation provided excellent results in nonlinear optics and laser physics for describing the self-focusing of a light beam. The successful application of the paraxial approach is related to the consideration of narrow-band quasi-harmonic signals and, therefore, with the possibility of an independent separation of the amplitude and the eikonal [3]. However, as applied to nonlinear acoustics, the approach imposes restrictions on the domain of applicability of the results obtained with its help: the solution is adequately described near the beam axis only at small distances from the source, $x \ll \omega a^2/2c$. Here, ω is the fundamental frequency of the source, a is the beam radius, and c is the sound velocity. A signal cannot be treated as a quasi-harmonic one, and it is necessary to expand the total field of acoustic pressure as a power series in a small parameter. The inclusion of higher-order corrections leads to incorrect results, which makes it impossible in the framework of this approach to describe the most interesting region where the focusing of a finite-amplitude sound beam takes place. In acoustics, the paraxial approach was first used by Rudenko, Soluyan, and Khokhlov [10].

An analytical method for describing a beam in the paraxial region was developed recently [11, 12]. This method makes it possible to study also the motion in the focal plane. There are also efficient numerical methods for solving the KhZ equation [13].

We follow the basic concepts [11, 12] in the analytical description of the beam evolution. We assume the problem to be cylindrically symmetric and represent Eq. (18) in cylindrical coordinates:

$$\frac{\partial}{\partial \tau}\Big[\frac{\partial P}{\partial \sigma} - NP\frac{\partial P}{\partial \tau} - \varepsilon\alpha MNP^2\frac{\partial P}{\partial \tau}\Big] = \frac{1}{4G}\Big[\frac{\partial^2 P}{\partial R^2} + \frac{1}{R}\frac{\partial P}{\partial R}\Big], \quad (19)$$

where $P = p/p_p$. Here, p is the dimensional pressure, p_p is the peak value of the sound pressure at the source, $\sigma = x/d$, $\tau = \omega(t - x/c)$, $R = r/a$, x is the axial coordinate, d is the focal length, and r is the transverse coordinate. The quantities r, x, t, c, and ω are dimensional; $G = x_0/d$ is the dimensionless constant; $\tilde{x} = 2c^3\rho_0/\varepsilon(\gamma+1)\omega p_p$ is the characteristic distance within which the shock wave is formed; and $x_0 = \omega a^2/2\beta c$ is the characteristic average diffraction length for an acoustic beam with the frequency ω. The quantity $N = d/\tilde{x}$ characterizes the quadratic nonlinearity of the beam, and G characterizes the beam focusing.

This equation differs from the classical KhZ equation by the presence of the term corresponding to cubic nonlinearity with the coefficients

$$M = \frac{p_p}{c^2\rho_0}, \quad \alpha = \frac{A_1 + T^1_{1,1}}{Y^1_{1,1}} = -\frac{(\gamma+1)}{8}.$$

Note that the sign of α calculated for an ideal gas with allowance for the reciprocal effect of modes differs from the sign of the parameter $\alpha_0 = T^1_{1,1}/Y^1_{1,1} = 1/(\gamma+1)$ when the calculation takes into account only the self-action of the right beam. This fact demonstrates the importance of taking into account the resonance interaction of all modes.

We try the a solution to the evolution equation (19) (as in [11, 12]) in the form of a series expansion in powers of the parameter $R = r/a$:

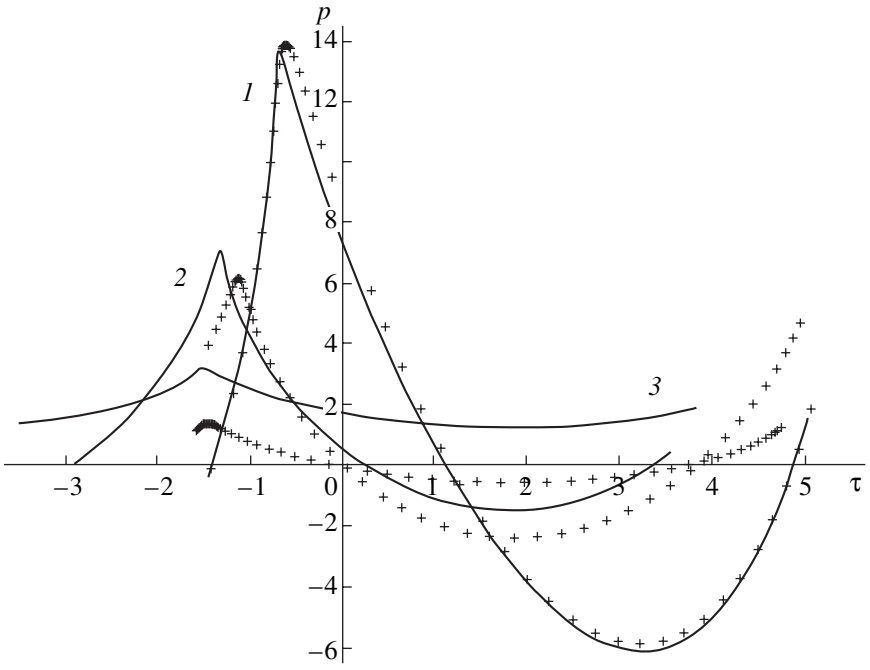

Fig. 1. Evolution of the disturbance profile for $\alpha = -0.3$ and $\sigma = (1)$ 1.01, (2) 1.2, and (3) 2.0 (the solid lines); the crosses represent the case without the cubic nonlinearity.

$$P(R, \sigma, \theta) = P_0(\sigma, \theta) + \frac{R^2}{2}P_2(\sigma, \theta) + \frac{R^4}{4}P_4(\sigma, \theta) + \ldots. \quad (20)$$

Then, performing calculations analogous to [11, 12], but taking into account the contribution of the cubic term, we obtain a solution for P_0 in the form

$$P_0(\eta, \tau) = \frac{1}{f(\eta)}\sin(\eta - \theta_0) + \frac{g(\eta)}{2f(\eta)}\sin(\eta - \zeta(\eta)) - \frac{\alpha NMG}{2}\int_0^\eta \frac{g(\eta')}{f(\eta')}\sin(\eta' - \zeta(\eta'))\sin(\eta - \eta')d\eta' \quad (21)$$

(here, we use the same notations as in [11]). In contrast to the solutions given in [11, 12], the solution given by Eq. (21) takes into account the contributions of both quadratic and cubic nonlinearities and also the interaction between different modes. If necessary, it is possible to obtain a solution for P_2 [the next order relative to Eq. (21)] with the help of the relations similar to those in [11, 12].

Here, $\theta_0(\tau, \eta)$ is determined from the solution of a transcendental equation:

$$\tau = \theta_0 - g(\eta)\sin(\theta_0 + \zeta(\eta)) - \alpha NMG \times \int_0^\eta \left[\sin(\theta_0 + \eta') + \frac{1}{2}g(\eta')\sin(\eta' - \zeta(\eta'))\right]^2 d\eta' - \delta(\eta). \quad (22)$$

The following notations are introduced in Eqs. (21) and (22):

$$f(\eta) = (\cos(\eta) + G\sin(\eta))^{-1},$$

$$g(\eta) = N\left(\frac{\eta^2 + \ln^2 f(\eta)}{1 + G^{-2}}\right)^{1/2},$$

$$\zeta(\eta) = \arctan\left(\frac{G\eta + \ln f(\eta)}{\eta - G\ln f(\eta)}\right),$$

$$\delta(\eta) = \frac{N^2G^2}{2(1 + G^2)}\eta\ln(\cos\eta + G\sin\eta).$$

Now, at $\varepsilon = 0$ (ignoring the cubic nonlinearity), it is easy to plot the signal profiles for different values of the parameters N and G characterizing the focusing and the diffraction, respectively. The simplest way to do this is to treat Eqs. (21) and (22) as a system of equations in the form $P_0 = P_0(\theta_0, \eta)$, $\tau = \tau(\theta_0, \eta)$, which determines (at a fixed value of η) the function $P_0 = P_0(\tau)$ in a parametric form. In this case, θ_0 plays the role of a parameter.

To plot a signal profile at $\varepsilon \neq 0$, it is necessary first to calculate the integral on the right-hand side of Eq. (22). Regretfully, it is impossible to calculate it analytically in the general form suitable for analysis. However, at fixed values of N, G, and η, it can be calculated as a function of θ_0, e.g., with the help of the MAPLE software package. In this case, it is possible to obtain the perturbation profiles in a parametric form with the help of the same software.

Figure 1 demonstrates the profiles of the beam at various distances from the source σ with allowance for the contribution of the cubic nonlinearity. The values of other parameters determining the contribution of non-

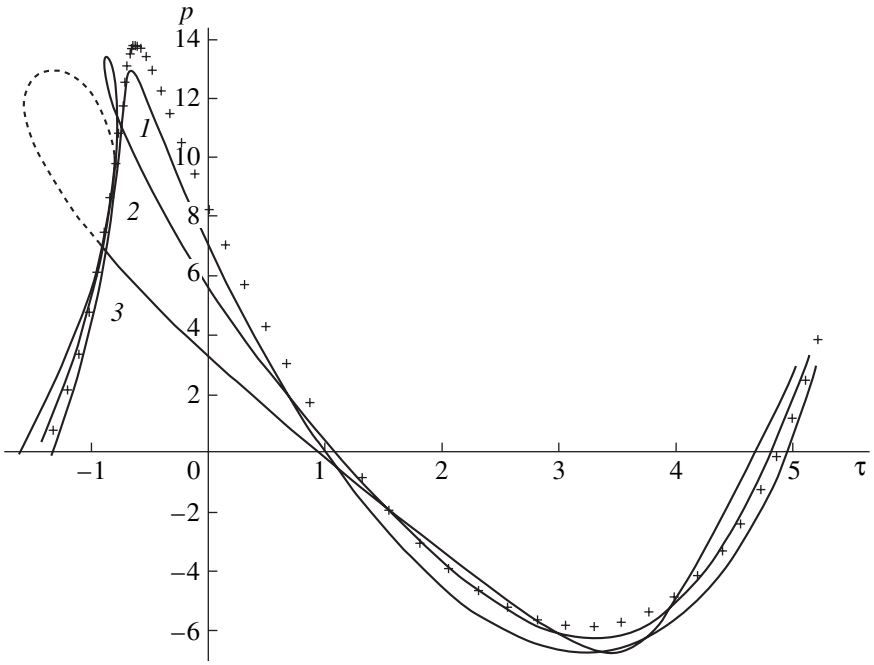

Fig. 2. Evolution of the disturbance profile for $\alpha = 0.3$ and $M = (1)$ 0.05, (2) 0.5, and (3) 1.0 (the solid lines); the crosses represent the case without the cubic nonlinearity.

linearity are selected as follows: $N = 0.3$ and $G = 10$. The value of the parameter α for an ideal diatomic gas is $\alpha = -0.3$. The profiles obtained without taking into account the cubic contribution are shown in the same figure by crosses, and they closely coincide with the plots presented in [11, 12].

Figure 2 shows the profiles of the beam at $\alpha = -0.3$, $N = 0.3$, and $G = 10$ for different values of the nonlinearity parameter: $M = 0.05$, 0.35, and 1.0. The profile obtained without taking into account the contribution of the cubic nonlinear term is represented by crosses (it coincides with the calculations from [10, 11]).

In Fig. 2, the plots obtained with allowance for the cubic nonlinearity lie below the plots taking into account only the quadratic term and have sharper peaks. As the nonlinearity parameter M grows, the wave amplitude decreases, the peak is shifted to the left, and a loop-type singularity is formed in the vicinity of the pressure peak. In the figure, the loops are marked with dots. Basically, the loop-type singularity can be eliminated analogously to the "backlash" singularity in the Riemann wave in the theory of weak shock waves [2].

ACKNOWLEDGMENTS

We are grateful to Professor S.B. Leble for the interest taken in our work and for valuable comments.

REFERENCES

1. E. A. Zabolotskaya and R. V. Khokhlov, Akust. Zh. **15**, 40 (1969) [Sov. Phys. Acoust. **15**, 35 (1969)].
2. O. V. Rudenko and S. I. Soluyan, *Theoretical Foundations of Nonlinear Acoustics* (Nauka, Moscow, 1975; Consultants Bureau, New York, 1977).
3. M. B. Vinogradova, O. V. Rudenko, and A. P. Sukhorukov, *The Theory of Waves*, 2nd ed. (Nauka, Moscow, 1990).
4. S. Makarov and M. Ochmann, Acustica **82**, 579 (1996).
5. Boa Teh-Chu and L. S. Kovasznay, J. Fluid Mech. **3**, 494 (1958).
6. A. A. Perelomova, Acta Acust. (China) **84** (6), 1002 (1998).
7. V. P. Kuznetsov, Akust. Zh. **16**, 548 (1970) [Sov. Phys. Acoust. **16**, 467 (1971)].
8. S. B. Leble, *Nonlinear Waves in Waveguides with Stratification* (Springer, Berlin, 1990).
9. S. P. Kshevetskiĭ and S. B. Leble, Izv. Akad. Nauk SSSR, Mekh. Zhidk. Gaza **3**, 1169 (1988).
10. O. V. Rudenko, S. I. Soluyan, and R. V. Khokhlov, Dokl. Akad. Nauk SSSR **225** (5), 1053 (1975) [Sov. Phys. Dokl. **20**, 836 (1975)].
11. M. F. Hamilton, V. A. Khokhlova, and O. V. Rudenko, J. Acoust. Soc. Am. **101**, 1298 (1997).
12. M. F. Hamilton, O. V. Rudenko, and V. A. Khokhlova, Akust. Zh. **43**, 48 (1997) [Acoust. Phys. **43**, 39 (1997)].
13. J. N. Tjotta, S. Tjotta, and E. H. Vefring, J. Acoust. Soc. Am. **88**, 2859 (1990).

Translated by M. Lyamshev

Acoustical Physics, Vol. 48, No. 2, 2002, pp. 155–161. Translated from Akusticheskiĭ Zhurnal, Vol. 48, No. 2, 2002, pp. 187–194.

Transfer Constant of a Multilayer Acoustic Transducer at the Direct and Inverse Transformation

M. A. Grigor'ev, A. V. Tolstikov, and Yu. N. Navrotskaya

Chernyshevski State University, ul. Astrakhanskaya 83, Saratov, 410026 Russia

e-mail: magrig@sgu.ssu.runnet.ru

Received May 28, 2001

Abstract—The algorithms for calculating the direct and inverse transfer constants of an acoustic transducer with an arbitrary number of intermediate layers between the piezoelectric layer, the acoustic duct, and the rear acoustic load are described. The results of a numerical analysis are presented and discussed. As an illustration, a 100-MHz transducer formed by a (Y + 36°)-cut $LiNbO_3$ plate fixed on a fused-quartz acoustic duct with the help of five metal layers is considered. The other side of the plate carries two metal layers and a rear load. The phase–frequency characteristics and the transformation loss as a function of frequency are analyzed for the cases of direct and inverse transformation under the assumption that the signal is supplied and retrieved by a two-wire line. *© 2002 MAIK "Nauka/Interperiodica".*

The well-known works (e.g., [1–7]) on the analysis of acoustic transducers for volume waves considered the direct transformation of the electromagnetic energy to the acoustic one. The sought-for quantity was the ratio of powers of the transformed waves, which is usually called the conversion coefficient. The phase–frequency characteristic was not considered in the above-mentioned works. It is useful to find out, what the phase–frequency and the amplitude–frequency characteristics of a complex multilayer piezotransducer are and how can they be controlled. This information is important, e.g., for the formation of an optimal impulse response of a transducer operating in the mode of emission and reception of short videopulses in a pulsed acoustic microscope [8, 9]. The means that influence to some extent the phase–frequency and amplitude–frequency properties of a transducer could be intermediate layers introduced between the piezoelectric, the acoustic duct, and the rear acoustic load. The latter can also be considered as a structure component intended for correcting the above-mentioned characteristics.

The quantity that most fully characterizes a transducer is the transfer function or transfer constant, which is the ratio of the complex amplitudes of the transformed waves. Knowing this constant allows one to determine the above-mentioned conversion coefficient and the phase difference between the output and input signals.

It is well known that the reciprocity theorem holds for a piezoelectric transducer [10]. However, it would be interesting to compare the direct and the inverse transfer constant for a specific example of a complex multilayer piezoelectric element used at high and microwave frequencies.

The purpose of this paper is to develop the algorithms and the programs for calculating both the direct and the inverse transfer constants of an acoustic transducer for volume waves with an arbitrary number of intermediate layers and with a rear acoustic load. The electromagnetic signal is supplied to or retrieved from the transducer by a two-wire line with a given wave resistance. A parasitic shunt capacitance and a connecting-wire inductance with an active loss resistance are also assumed to be connected with the piezoelectric element in parallel and in series, respectively.

THE MODEL UNDER ANALYSIS AND THE ASSUMPTIONS

Figure 1 demonstrates schematically the transducer under analysis. Between the piezoelectric layer *1* and the acoustic duct *2* there are M intermediate layers (sub-

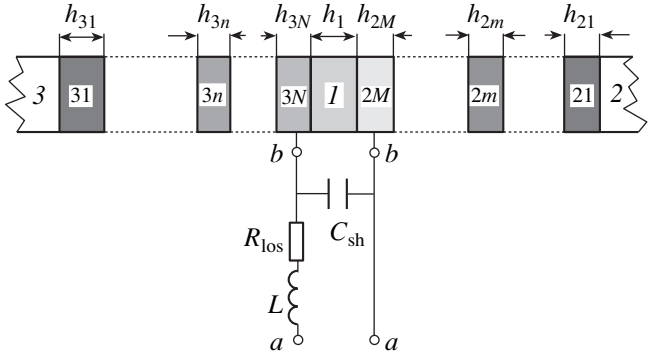

Fig. 1. The model of a piezoelectric transducer: (*1*) piezoelectric, (*2*) acoustic duct, and (*3*) rear acoustic load; the indices 2m and 3n represent the sublayer and superlayer numbers, respectively; C_{sh} is the parasitic shunt capacitance and R_{los} and L are the active resistance and the inductance of the conductor connecting the transducer with the transmission line.

1063-7710/02/4802-0155$22.00 © 2002 MAIK "Nauka/Interperiodica"

layers) with the common index 2 and individual numbers m increasing from 1 to M towards the piezoelectric layer. On the other side, between the piezoelectric and the rear load *3*, there are also N media (superlayers) with the common index 3 and numbers n changing from 1 to N in the direction from the rear load to the piezoelectric. The sublayers and superlayers are short acoustic waveguides with given lengths h_{2m} and h_{3n}, acoustic velocities v_{2m} and v_{3n}, and acoustic wave resistances Z_{2m0} and Z_{3n0}. We take that the acoustic duct and the rear load have infinite lengths and the given acoustic wave resistances Z_{20} and Z_{30}, respectively. The sublayer and the superlayer with the numbers $2M$ and $3N$, respectively, are metal electrodes. In the diagram, they are connected with the terminals *bb*, which in their turn are connected with the parasitic shunt capacitance C_{sh}. The two-wire transmission line with the wave resistance Z_0 is connected with the terminals *aa*. The latter, in their turn, are linked up to the terminals *bb* through the inductance L and the loss resistance R_{los}.

In the case of direct transformation, the direct electromagnetic (EM) wave arrives at the electric side of the transducer through the transmission line. The EM wave creates a complex voltage amplitude V_{aa+} across the terminals *aa*, which we take to be the input one. In the case of the inverse transformation, a voltage appears across the same terminals, and the complex amplitude of this voltage V_{aa+} is taken to be the output one. In the first case, the generator producing the signal is assumed to be matched with the transmission line, i.e., its internal resistance is equal to Z_0. In the second case, the line is loaded by the matched resistance Z_0.

On the acoustic side, it is the acoustic duct cross section at the boundary with the first sublayer ($m = 1$) that is taken as the output or input, depending on the transformation direction. The output signal or the input one is assumed to be the elastic stress of the acoustic wave outgoing or incoming through the duct with the complex amplitude T_{2+} at the aforesaid boundary.

The desired transfer constants can be defined as follows:

$$K_+ = \sqrt{Z_0 s/Z_{20}}(T_{2+}/V_{aa+}) \quad (1)$$

in the case of the direct transformation, and

$$K_- = \sqrt{Z_{20}/(Z_0 s)}(V_{aa+}/T_{2+}) \quad (2)$$

in the case of the inverse one.

Here, s is the area of the piezoelectric element. Defined in this way, the aforesaid coefficients are dimensionless quantities, and their absolute values squared are equal to the well-known transformation coefficients $\eta_+ = P_{ac}/P_{EM+}$ and $\eta_- = P_{EM}/P_{ac+}$, where P_{ac} and P_{EM} are the acoustic and electromagnetic powers, respectively.

The problem will be solved in the one-dimensional approximation ($\partial/\partial x = \partial/\partial y = 0$) on the assumption that the attenuation and diffraction of waves, as well as the conductivity of the piezoelectric, are negligibly small; in addition, all sublayers, superlayers, and the rear load are assumed to be isotropic; and the piezoelectric and the acoustic duct are oriented in such a way that the tensor equations describing the electromechanical processes in the media under consideration are reduced to scalar equations.

GENERAL RELATIONS

The equations relating the electric and mechanical quantities in the piezoelectric have the form

$$T_1 = c_1 \partial u_1/\partial z - eE, \quad (3)$$

$$D = e\partial u_1/\partial z + \varepsilon E, \quad (4)$$

$$\partial D/\partial z = 0, \quad (5)$$

where T_1 is elastic stress; u_1 is the elastic strain; D is the electric displacement (induction); E is the alternating electric field strength; c_1, e, and ε are the elastic constant, the piezoelectric modulus, and the dielectric constant, respectively.

As follows from Eq. (5), D is coordinate independent and, consequently, is a function of time only and has the form $D = D_0 e^{j\omega t}$, where the amplitude D_0 can generally be considered a complex quantity.

In the piezoelectric layer, both the direct and inverse waves of the elastic strain exist simultaneously:

$$u_1 = u_{1+}\exp(-j\beta_1 z) + u_{1-}\exp(j\beta_1 z). \quad (6)$$

Here, β_1, u_{1+}, and u_{1-} are the propagation constant and the complex amplitudes of these waves, respectively; z is the coordinate with the positive direction from the power source to the load. The coordinate origin is at the piezoelectric layer boundary closest to the aforementioned source.

To determine the voltage across the piezoelectric layer (see the terminals *bb* in Fig. 1) in the quasistatic approximation ($\mathrm{rot} E = 0$), we use Eq. (4) and obtain

$$V_{bb} = \int_0^{h_1} E_1 dz = \frac{D_0 h_1}{\varepsilon} - \frac{e}{\varepsilon}[u_{1+}(e^{-j\beta_1 h_1} - 1) + u_{1-}(e^{j\beta_1 h_1} - 1)]. \quad (7)$$

The complex quantities D_0, u_{1+}, and u_{1-} are determined by the continuity conditions for the acoustic stress and the current (or impedance) at the piezoelectric boundaries and also by the parameters of the electric circuit connected to the terminals *bb*.

The electric current I_e flowing in the external circuit equals the displacement current in the piezoelectric:

$$I_e = J_e s = (\partial D/\partial t)s = j\omega D s, \quad (8)$$

where J_e is the displacement current density.

Using Eqs. (3) and (6), we represent the acoustic stress and the acoustic current in the piezoelectric layer as

$$T_1(z) = c^*(-j\beta_1 u_{1+}e^{-j\beta_1 z} + j\beta_1 u_{1-}e^{j\beta_1 z}) - \frac{e}{\varepsilon}D_0, \quad (9)$$

$$I_1(z) = -(\partial u_1/\partial t)s = -j\omega s(u_{1+}e^{-j\beta_1 z} + u_{1-}e^{j\beta_1 z}). \quad (10)$$

Here, $c^* = c_1(1 + k^2)$ is the elastic constant renormalized due to the piezoelectric effect, $k^2 = e^2/c_1\varepsilon$ is the electromechanical coupling factor squared.

The sublayers connecting the piezoelectric layer with the acoustic duct are a cascade connection of acoustic waveguide sections. Each of them is a linear two-port network connecting the input acoustic stress $T_{m,\text{in}}$ and current $I_{m,\text{in}}$ with the output ones $T_{m,\text{out}}$ and $I_{m,\text{out}}$. The transfer matrix for a section of the uniform waveguide has the form [11]

$$[a] = \begin{bmatrix} \cos\theta_{2m} & j(Z_{2m0}/s)\sin\theta_{2m} \\ j(s\sin\theta_{2m})/Z_{2m0} & \cos\theta_{2m} \end{bmatrix}, \quad (11)$$

where m is the layer number; $\theta_m = \omega h_{2m}/v_{2m}$.

The acoustic wave resistance of the rear load Z_{30} is transformed by the series of N superlayers into some impedance Z_N in the input plane of the superlayer immediately adjacent to the piezoelectric. The value of Z_N can be found by applying the well-known expression

$$Z_{3n} = Z_{3n0}\frac{Z_{3,n-1}\cos(\omega h_{3n}/v_{3n}) + jZ_{3n0}\sin(\omega h_{3n}/v_{3n})}{Z_{3n0}\cos(\omega h_{3n}/v_{3n}) + jZ_{3,n-1}\sin(\omega h_{3n}/v_{3n})} \quad (12)$$

to each superlayer in turn, from $n = 1$ to $n = N$, by taking $Z_{3,n-1} = Z_{30}$ at $n = 1$. Here, Z_{3n} and $Z_{3,n-1}$ are the acoustic impedances at the input boundaries of the superlayers with numbers n and $(n - 1)$.

DIRECT TRANSFORMATION

Let the input signal be the voltage with a complex amplitude V_{aa+} induced across the terminals *aa* by the direct wave in the transmission line. The piezoelectric element is electrically characterized (at the terminals *bb*) by the so-called radiation impedance Z_{rad}. Taking into account the shunt capacitance C_{sh} along with the series inductance L and resistance R_{los}, we obtain the impedance across the terminals *aa*:

$$Z_{aa} = R_{\text{los}} + j\omega L + Z_{\text{rad}}/(1 + j\omega C_{\text{sh}}Z_{\text{rad}}). \quad (13)$$

This impedance loads the transmission line with the wave resistance Z_0. The reflection coefficient for the wave of voltage across the aforesaid terminals is

$$\Gamma_E = (Z_{aa} - Z_0)/(Z_{aa} + Z_0). \quad (14)$$

Evidently,

$$V_{aa+} = V_{aa}/(1 + \Gamma_E), \quad (15)$$

where V_{aa} is the complex amplitude of the total voltage across the terminals *aa*, $V_{aa} = V_{aa+} + V_{aa-}$, and V_{aa-} is its part corresponding to the reflected wave.

The voltage V_{aa} induced by the source of the signal causes the appearance of voltage across the piezoelectric element (the *bb* terminals). As a consequence, a stationary wave of elastic strain with complex amplitudes u_{1+} and u_{1-} is excited in the piezoelectric. The waves of acoustic stress and acoustic current appear. The latter two have complex amplitudes $T_1(h_1)$ and $I_1(h_1)$ at the sublayer boundary and are calculated according to Eqs. (9) and (10), if u_{1+}, u_{1-}, and D_0 are known. The values found are the input values for the sublayer chain. Using the transfer matrix (11) and applying it in turn to all sublayers, from $m = M$ to $m = 1$, one can find the acoustic stress and current at the output boundary of the last sublayer. The resulting value $T_{21,\text{out}} = T_{2+}$ is just the desired acoustic stress at the output of the transducer (at the input of the acoustic duct). One has but to find the transfer constant according to definition (1).

To put the above algorithm into effect, it is useful to introduce the dimensionless displacements $u'_{1\pm} = u_{1\pm}/N_0$, where N_0 is a norm defined by the formula

$$N_0 = eD_0/Z_{10}\varepsilon\omega.$$

Then, the continuity conditions for the acoustic impedances at the piezoelectric boundaries take the form

$$u'_{1+}e^{-j\beta_1 h_1}\left(\frac{Z_M}{Z_{10}} - 1\right) + u'_{1-}e^{j\beta_1 h_1}\left(\frac{Z_M}{Z_{10}} + 1\right) = -j, \quad (16)$$

$$u'_{1+}\left(\frac{Z_N}{Z_{10}} + 1\right) + u'_{1-}\left(\frac{Z_N}{Z_{10}} - 1\right) = j. \quad (17)$$

Here, Z_N and Z_M are the acoustic impedances in the superlayer at $n = N$ and in the sublayer at $m = M$ at the piezoelectric boundaries. The first impedance is calculated by a successive application of formula (12), by varying n from 1 to N. The second impedance is found by the same formula, replacing n by m and varying m from $m = 1$ to $m = M$ with taking $Z_{2,m-1} = Z_{20}$ at $m = 1$. The solution of the system of Eqs. (16), (17) gives the complex dimensionless strain amplitudes u'_{1+} and u'_{1-}.

The electric radiation impedance of the piezoelectric element can be found by dividing voltage (7) by

current (8). Changing to the dimensionless quantities, we obtain

$$\frac{Z_{\text{rad}}}{X_0} = -j + j\frac{k^2}{(1+k^2)(\beta_1 h_1)} \times [u'_{1+}(e^{-j\beta_1 h_1} - 1) + u'_{1-}(e^{j\beta_1 h_1} - 1)], \quad (18)$$

where $X_0 = 1/\omega C_0$ is the capacitive resistance of the piezoelectric element and $C_0 = \varepsilon s/h_1$ is its static capacitance.

The electric impedance Z_{aa} across the terminals *aa* and the reflection coefficient Γ_E are determined by Eqs. (13) and (14), respectively. Taking that the electric displacement D is predetermined and using the Kirchhoff rules for the electric circuit containing the piezoelectric element with the impedance Z_{rad}, the shunt capacitance C_{sh}, the inductance L, and the resistance R_{los}, one easily obtains

$$V_{aa} = j\omega D_0 s(1 + j\omega C_{\text{sh}} Z_{\text{rad}}) Z_{aa}.$$

Substituting this formula into Eq. (15) and expressing D_0 through the norm N_0, we obtain the complex amplitude of the voltage at the input of the transducer:

$$\frac{V_{aa+}}{N_0} = j\omega^2 s\sqrt{\frac{(1+k^2)\varepsilon_0\varepsilon_r Z_{10}}{v_1}} \times (1 + j\omega C_{\text{sh}} Z_{\text{rad}})\frac{Z_{aa}}{(1+\Gamma_E)}. \quad (19)$$

Introducing the dimensionless strains in Eqs. (9) and (10) and taking $z = h_1$, we find the complex amplitudes of acoustic stress and current at the output of the piezoelectric to the sublayer with the number M:

$$\frac{T_1(z=h_1)}{N_0} = jZ_{10}\omega[-u'_{1+}e^{-j\beta_1 h_1} + u'_{1-}e^{j\beta_1 h_1} + j], \quad (20)$$

$$\frac{I_1(z=h_1)}{N_0} = -j\omega s(u'_{1+}e^{-j\beta_1 h_1} + u'_{1-}e^{j\beta_1 h_1}). \quad (21)$$

The values obtained are the input ones for the cascade connection of the two-port networks represented by the media between the piezoelectric and the acoustic duct. Using the transfer matrix (11), one can write the equations that provide the output stress and current amplitudes for each layer, if the input ones are given:

$$T_{2m,\text{ out}} = (\cos\theta_{2m})T_{2m,\text{ in}} - j\frac{Z_{2m0}}{s}(\sin\theta_{2m})I_{2m,\text{ in}}, \quad (22)$$

$$I_{2m,\text{ out}} = -j\frac{s\sin\theta_{2m}}{Z_{2m0}}T_{2m,\text{ in}} + (\cos\theta_{2m})I_{2m,\text{ in}}. \quad (23)$$

The output values, $T_{2m,\text{ out}}$ and $I_{2m,\text{ out}}$, for the layer with the number $2m$ are the input ones, $T_{2(m-1),\text{ in}}$ and $I_{2(m-1),\text{ in}}$, for the layer $2(m-1)$. Performing the calculations by Eqs. (22) and (23) with m changing from M to 1, we obtain the complex amplitude T_{2+} of acoustic stress at the transducer output. Then the sought-for transfer constant K_+ can be determined by Eq. (1). The transformation coefficient is

$$\eta_+ = |K_+|^2, \quad (24)$$

and the phase difference between the excited acoustic wave and the direct EM wave supplied to the transducer is

$$\varphi_+ = \arctan\frac{\text{Im}(K_+)}{\text{Re}(K_+)}. \quad (25)$$

INVERSE TRANSFORMATION

Let an acoustic wave be supplied through the acoustic duct to the transducer and let this wave have a given complex strain amplitude u_{2+} at the boundary with the first sublayer. Then, at this boundary, the acoustic stress and current of the wave have the amplitudes

$$T_{2+} = -jZ_{20}\omega u_{2+}, \quad (26)$$

$$I_{2+} = -j\omega u_{2+}s. \quad (27)$$

The reflected waves are combined with the incident ones and give rise to the complex amplitudes of acoustic stress and current at the boundary:

$$T_2 = -jZ_{20}\omega u_{2+}(1 + \Gamma_T), \quad (28)$$

$$I_2 = -j\omega u_{2+}s(1 - \Gamma_T), \quad (29)$$

where Γ_T is the reflection coefficient of the elastic-stress wave, which can be easily found, if the acoustic impedance of the piezoelectric element Z_2 is known. In the case of the inverse transformation, this impedance characterizes the load of the acoustic duct. A technique for calculating Z_2 and then Γ_T will be shown below [see Eq. (42)].

Suppose that we found T_2 and I_2, which are the input quantities $T_{21,\text{ in}}$ and $I_{21,\text{ in}}$ for the series of sublayers. Considering the system of sublayers as a cascade connection of linear two-port networks characterized by the transfer matrix (11), one can determine the corresponding amplitudes $T_{2M,\text{ out}}$ and $I_{2M,\text{ out}}$ at the output of the entire system. The calculations are performed by Eqs. (22) and (23). After their M-fold application, we obtain the acoustic stress and current amplitudes T_1 and I_1 at the input of the piezoelectric at $z = 0$. In the piezoelectric, we have the strain waves with the amplitudes u_{1+} and u_{1-} and the current density J_e, which are related to the values of T_1 and I_1 determined above by the formulas

$$-jZ_{10}\omega(u_{1+} - u_{1-}) + jJ_e\frac{1}{\omega}\sqrt{\frac{k^2}{1+k^2}\frac{Z_{10}v_1}{\varepsilon}} = T_1, \quad (30)$$

$$-j\omega s(u_{1+} + u_{1-}) = I_1. \quad (31)$$

Knowing J_e, one can also easily calculate the voltage amplitude V_{aa+} at the output of the transducer (the terminals *aa*).

Equations (30) and (31) involve three unknown interrelated quantities u_{1+}, u_{1-}, and J_e. To find the last one, it is necessary to obtain one more equation. For this purpose, one can use the condition for the existence of stationary oscillations at the terminals *bb*:

$$Z_{\text{piez}} + Z_L = 0, \tag{32}$$

where Z_{piez} is the electric impedance of the piezoelectric element in the case of inverse transformation, and Z_L is the load impedance at the terminals *bb*. The first quantity can be calculated by dividing voltage (7) across the piezoelectric element by current (8). The second quantity can be found by the formula

$$Z_L = \frac{Z_0 + R_{\text{los}} + j\omega L}{1 + j\omega C_{\text{sh}}(Z_0 + R_{\text{los}} + j\omega L)}. \tag{33}$$

As a result, we obtain from Eq. (32):

$$u_{1+}(1 - e^{-j\beta_1 h_1}) + u_{1-}(1 - e^{j\beta_1 h_1}) + J_e s(Z_L - jX_0)\sqrt{\frac{1+k^2}{k^2}}\sqrt{\frac{\varepsilon}{Z_{10}v_1}} = 0. \tag{34}$$

From Eqs. (30), (31), and (34), one can easily determine numerically the complex amplitude of the density J_e of electric current flowing through the piezoelectric element and, then, calculate the amplitude of the voltage across the terminals *aa*:

$$V_{aa+} = \frac{J_e s Z_L Z_0}{Z_0 + R_{\text{los}} + j\omega L}. \tag{35}$$

Turn now to the beginning of this section and demonstrate how the reflection coefficient Γ_T is found. Outline first the way of solving this problem. First, it is necessary to calculate the dimensionless amplitudes of the direct and inverse waves u'_{1+} and u'_{1-} in the piezoelectric. Then, we find the amplitudes of the normalized acoustic stress T_1/N_0 and current I_1/N_0 in the piezoelectric at the sublayer boundary $z = h_1$. Further, using the transfer matrix (11), these quantities should be recalculated to the acoustic duct output, i.e., $T_{21,\text{in}}/N_0$ and $I_{21,\text{in}}/N_0$ should be found, their ratio being the acoustic impedance Z_2 in the output plane of the acoustic duct. It is the latter quantity that determines the sought-for reflection coefficient Γ_T.

The continuity condition for the impedance at the boundary $z = h_1$ between the piezoelectric and the adjacent superlayer, when written for the dimensionless displacement amplitudes, has the form

$$u'_{1+}\left(\frac{Z_{3N}}{Z_{10}} - 1\right)e^{-j\beta_1 h_1} + u'_{1-}\left(\frac{Z_{3N}}{Z_{10}} + 1\right)e^{j\beta_1 h_1} = -j. \tag{36}$$

Here, Z_{3N} is calculated by Eq. (12).

At the other boundary, at $z = 0$, we cannot write a similar condition, because, in this case, the acoustic impedance at this boundary is the sought-for quantity depending on the electric load of the piezoelectric element. Therefore, as the second equation, we use the condition of the existence of stationary oscillations written for the terminals *bb*. Using the dimensionless strain amplitudes, we obtain

$$u'_{1+}(e^{-j\beta_1 h_1} - 1) + u'_{1-}(e^{j\beta_1 h_1} - 1) = \frac{(\beta_1 h_1)(1+k^2)}{k^2}\left(j\frac{Z_L}{X_0} + 1\right). \tag{37}$$

The normalized acoustic strain and current in the piezoelectric at the boundary $z = 0$ (i.e., at the output of the sublayer $2M$) are

$$T_{2M,\text{out}}/N_0 = Z_{10}\omega[j(-u'_{1+} + u'_{1-}) - 1], \tag{38}$$

$$I_{2M,\text{out}}/N_0 = -j\omega(u'_{1+} + u'_{1-})s. \tag{39}$$

Using the transfer matrix (11), we can write the equations allowing one to determine the input stress and current amplitudes for each sublayer, if the output ones are known:

$$T_{2m,\text{in}} = (\cos\theta_{2m})T_{2m,\text{out}} + j\frac{Z_{2m,0}}{s}(\sin\theta_{2m})I_{2m,\text{out}}, \tag{40}$$

$$I_{2m,\text{in}} = j\frac{s\sin\theta_{2m}}{Z_{2m,0}}T_{2m,\text{out}} + (\cos\theta_{2m})I_{2m,\text{out}}. \tag{41}$$

Taking the stress and the current at the $2M$-sublayer output to be equal to the values from Eqs. (38) and (39) and then applying successively Eqs. (40) and (41) for m varying from M to 1, one can calculate $T_{21,\text{in}}$ and $I_{21,\text{in}}$, whose ratio gives the acoustic impedance Z_2. Then, the sought-for reflection coefficient will be

$$\Gamma_T = \frac{Z_2 - Z_{20}}{Z_2 + Z_{20}}. \tag{42}$$

It is this value Γ_T that should be substituted into Eqs. (28) and (29).

The transfer constant K_- is calculated according to definition (2). In this case, the amplitude of the output voltage V_{aa+} is determined by Eq. (33), and the amplitude of the input elastic stress T_{2+} is found by Eq. (26).

The coefficient for the inverse (acoustoelectric) transformation is calculated by Eq. (24), and the phase difference between the output and input signals is calculated by Eq. (25) with a change of indices from + to –.

COMPARISON OF THE DIRECT AND INVERSE TRANSFER CONSTANTS

On the basis of the above algorithms, two independent PC programs with the outer frequency loop were developed.

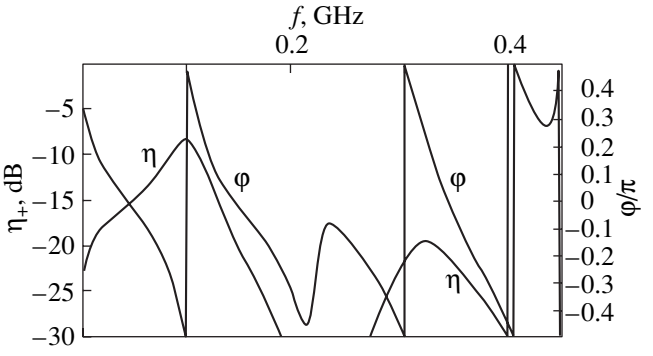

Fig. 2. Frequency dependences of the transformation coefficient $\eta(f)$ and the phase shift $\varphi(f)$ between the output and input signals. The piezoelectric is $(Y + 36°)$-cut lithium niobate (32 μm). The acoustic duct is fused quartz. The rear load is epoxy resin. The sublayers (beginning from the piezoelectric layer) are chromium (0.04 μm), copper (0.2 μm), indium (1 μm), copper (0.2 μm), and chromium (0.04 μm). The superlayers are (in the same order) chromium (0.04 μm) and copper (0.2 μm). L = 6 nH, R_{los} = 0.5 Ω, C_{sh} = 0, Z_0 = 50 Ω. The diameter of the transducer is 5 mm.

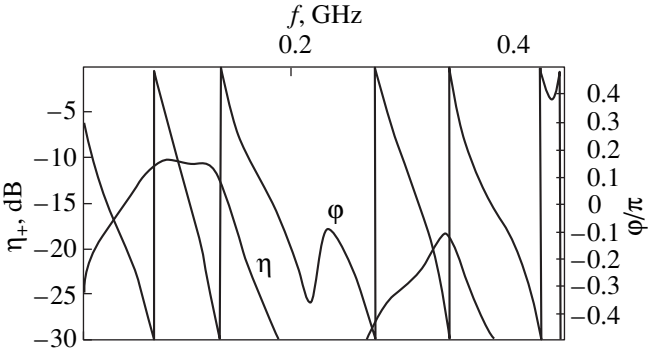

Fig. 3. The same as in Fig. 2 for the thickness of the indium layer 6.5 μm.

For the case of the direct transformation, the program successively executes the inner loops of calculating the values of Z_M and Z_N by Eq. (12); the simultaneous solution of Eqs. (16) and (17); the calculations by Eqs. (18), (13), (14), and (19)–(21); the inner loop of calculation by Eqs. (22) and (23); and, finally, the calculation of K_+, η_+, and φ_+ by Eqs. (1), (24), and (25).

For the inverse transformation, the program successively executes the inner loop of calculating Z_N by Eq. (12); the simultaneous solution of Eqs. (36) and (37); calculations by Eqs. (38) and (39); the inner loop of calculation by Eqs. (40) and (41); calculations by Eqs. (28), (29), and (42); the M-fold loop of calculation by Eqs. (22) and (23); calculations by Eq. (33); the simultaneous solution of Eqs. (30), (31), and (34); calculations by Eq. (35); and, finally, the calculation of K_-, η_-, and φ_- by Eqs. (2), (24), and (25) after changing the indices + to – in Eqs. (24) and (25).

The model analyzed was the structure shown in Fig. 1. The piezoelectric layer was taken to be connected with the acoustic duct by five intermediate metal sublayers, and the other side of the piezoelectric was loaded with a rear absorbing load with the help of two metal superlayers. It was assumed that, depending on the transformation direction, the line was either matched with the generator or loaded by a matched load. The transformation coefficient and the phase difference between the output and the input signals were calculated by Eqs. (24) and (25).

The analysis included wide-range variations of the layers thickness, the acoustic wave resistance of layers and the sound velocity in them, the inductance and the active resistance of the connecting wire, the wave resistance of the transmission line, the acoustic wave resistances of the acoustic duct and the rear absorbing load, the parasitic shunt capacitance, and the area and thickness of the piezoelectric element.

In all cases, the direct and the inverse transfer constants differed only in sign: $K_+ = -K_-$, while $\tan\varphi$ and, consequently, the angle φ were the same. The frequency dependences of the angles φ_+ and φ_- were almost linear with negative derivatives $\partial\varphi/\partial f$ in the vicinity of the maximal values of η_+ or η_-. It is well known that the linear frequency dependence of the output–input phase shift takes place but in the case of the transmission line section without dispersion.

Figures 2 and 3 illustrate the results of calculating η_+ and φ_+ as functions of frequency for two specific transducers. Similar curves are obtained in the case of the inverse transformation. The transducers in question were structures consisting of a $(Y + 36°)$-cut lithium niobate plate, an acoustic duct made of fused quartz, a rear acoustic load of epoxy resin, five sublayers, and two superlayers. The materials and the thicknesses of the sublayers and superlayers, as well as the necessary geometric and electric parameters of the transducers, are indicated in the cutline of Fig. 2. The results presented in Figs. 2 and 3 were obtained for the 10–450 MHz frequency range. The dependence $\eta(f)$ has two maximums in the aforementioned range. One is near 100 MHz, and the other is at about 320 MHz. The second maximum relates to the excitation of the so-called third harmonic. The calculation at higher frequencies reveals other maximums at frequencies of ~560 MHz (the fifth harmonic), ~790 MHz (the seventh harmonic), and so on. The effectiveness of excitation decreases compared to the previous maximum by ~10, ~5, ~3 dB, etc., respectively. The nonsymmetric nature of the curves is caused by the influence of intermediate layers. Variations of their thickness can lead to a considerable change in the curves' shapes. It can be seen that, for a thin indium layer (1 μm), the dependence $\eta(f)$ (see Fig. 2) is narrower, though higher, than for a thick layer (6.5 μm) (see Fig. 3). As for the phase shift φ, its frequency dependence obtained for the thin indium layer is less steep and deviates more widely from a linear one. The

observed jumps of the phase angle are exactly equal to π, and the derivative $\partial\varphi/\partial f$ at the jump points remains continuous.

It should be noted that, in the frequency interval from ~0.18 to ~0.25 GHz, the phase angle exhibits a smooth curve similar to an upturned letter *N* with a region where the derivative is $\partial\varphi/\partial f > 0$. This is observed near the point, where the transformation coefficient drops to zero.

CONCLUSION

In this paper, on the basis of the wave approach, we developed algorithms for calculating the direct and inverse transfer constants of a piezoelectric transducer with an arbitrary number of intermediate layers and with a rear load. We also developed the programs for a PC and applied them to diverse variants of transducers, which allowed us to demonstrate that the direct and the inverse transfer constants differ only in sign. The amplitude–frequency and phase–frequency characteristics obtained for the direct transformation and the inverse one fully coincide. The algorithms developed for calculating the transfer constants can be used in the analysis of the pulse responses of complex multilayer piezoelectric transducers.

REFERENCES

1. N. F. Foster, G. A. Coquin, G. A. Rozgonyi, and F. A. Vannata, IEEE Trans. Sonics Ultrason. **15** (1), 28 (1968).
2. T. M. Reeder and D. K. Winslow, IEEE Trans. Microwave Theory Tech. **17** (11), 927 (1969).
3. J. D. Larson, T. M. Reeder, and D. K. Winslow, IEEE Trans. Microwave Theory Tech. **18** (9), 602 (1970).
4. Yu. A. Zyuryukin, V. I. Nayanov, and V. A. Polotnyagin, Radiotekh. Élektron. (Moscow) **15**, 797 (1970); *ibid.* **15**, 1059 (1970).
5. V. A. Polotnyagin and V. N. Shevchik, Radiotekh. Élektron. (Moscow) **17**, 1260 (1972).
6. M. A. Grigor'ev, S. S. Kuryshov, and A. V. Tolstikov, Akust. Zh. **36**, 255 (1990) [Sov. Phys. Acoust. **36**, 139 (1990)].
7. M. A. Grigor'ev, V. V. Petrov, and A. V. Tolstikov, Radiotekh. Élektron. (Moscow) **35**, 1977 (1990).
8. Isao Ishikawa, Kageyoshi Katakura, and Yukio Ogura, IEEE Trans. Ultrason. Ferroelectr. Freq. Control **46**, 41 (1999).
9. D. A. Knapik, B. Starkoski, Ch. J. Pavlin, and F. S. Foster, IEEE Trans. Ultrason. Ferroelectr. Freq. Control **47**, 1540 (2000).
10. V. V. Furduev, *The Reciprocal Theorems in Mechanical, Acoustic, and Electromechanical Quadripoles* (GITTL, Moscow, 1948).
11. A. L. Fel'dshteĭn, L. R. Yavich, and V. P. Smirnov, *Components of Waveguide Technology: A Handbook* (Sovetskoe Radio, Moscow, 1967).

Translated by A. Kruglov

Acoustical Physics, Vol. 48, No. 2, 2002, pp. 162–165. Translated from Akusticheskiĭ Zhurnal, Vol. 48, No. 2, 2002, pp. 195–199.

Reflection of Normal Acoustic Waves in Thin Plates from a Grating with a Periodically Distributed Mechanical Load

S. G. Joshi*, B. D. Zaĭtsev, and I. E. Kuznetsova****

** Department of Electrical and Computer Engineering, Marquette University, Milwaukee, WI 53201-1881, USA*

*** Institute of Radio Engineering and Electronics, Russian Academy of Sciences, Saratov Branch, ul. Zelenaya 38, Saratov, 410019 Russia*

e-mail: zaitsev@ire.san.ru

Received December 29, 1999

Abstract—Reflection of zero-order normal acoustic waves excited in a thin piezoelectric plate from a set of conducting strips of a finite thickness is studied both theoretically and experimentally. The analysis shows that the effects produced by the short-circuiting of the plate surface and by the elastic load on the impedance ratio of adjacent plate segments are in opposition to each other. These effects can be commensurable, and, hence, for each wave type, there is a certain value of the strip thickness at which the reflection coefficient becomes equal to zero. The experimental results obtained for a shear horizontal normal wave (an SH_0 wave) propagating in a lithium niobate plate are in good agreement with the theory and justify the use of the equivalent-circuit model in analyzing the properties of reflectors of the type under study. *© 2002 MAIK "Nauka/Interperiodica".*

A reflector for normal acoustic waves is a useful, and often indispensable, component for many practical applications [1, 2]. Such reflectors are used in resonators, unilateral SAW transducers, delay lines with low-level spurious signals, directional couplers, various kinds of filters, etc. Several types of reflection gratings based on the use of electric and mechanical loads, as well as etched grooves on a substrate surface, have been successfully implemented in the design of SAW reflectors.

Recently, normal acoustic waves in thin plates have attracted considerable interest because of their unique properties, which are promising for designing new sensors and data processing devices and also for studying the properties of materials [3]. Evidently, the aforementioned types of SAW reflectors can also be used for the reflection of acoustic waves in plates. The reflection of a zero-order normal acoustic wave with the shear horizontal polarization (an SH_0 wave) from a set of thin conducting strips arranged on the *Y–X* surface of lithium niobate was studied in [4]. The results of this study showed that the reflection of normal acoustic waves in plates was more efficient than the reflection of SAW propagating in the same material. This result is explained by the stronger electromechanical coupling of waves in plates, as compared to SAW. From physical considerations, one would expect that gratings with a periodic mechanical load must also be more effective for waves in plates. In this paper, we present the first results obtained by studying the reflection of zero-order normal acoustic waves from a grating with a periodic mechanical load.

To calculate the characteristics of such a reflector, we used an equivalent circuit consisting of alternating segments of sound channels with different wave impedances. The theoretical analysis showed that an efficient reflection of zero-order normal acoustic waves can be achieved by using a grating with a relatively small number of elements. The experimental study of an SH_0 wave reflector that was made on the basis of silver strips deposited on a thin lithium niobate plate showed a good agreement with the theoretical results. This fact justified the use of the equivalent-circuit model in analyzing the reflection of acoustic waves in piezoelectric plates under the effect of a purely mechanical load.

Let us consider the theoretical model of a reflector with a mechanical load. The structure of such a reflector is shown in Fig. 1. It consists of a grating formed by finite-thickness strips deposited on the surface of a plate. Adjacent plate segments have different acoustic impedances, and, therefore, a propagating wave is reflected from every strip and gives rise to a resulting reflected wave. The operation of this reflector with allowance for multiple internal reflections can be analyzed with the help of the equivalent circuit conventionally used for SAW [5]. The circuit was modified for describing the reflection of acoustic waves in plates from a set of thin conducting electrodes [4]. The modified circuit contains no electromechanical transducers, because the aforementioned electrodes are not connected with each other. The modified circuit used in our study is shown in Fig. 2. Each grating element is repre-

1063-7710/02/4802-0162$22.00

sented by a T-section, and the elements of the circuit are characterized by the quantities

$$Z_1 = iZ\tan(kb/2), \quad (1)$$

$$Z_2 = -iZ/\sin(kb), \quad (2)$$

$$Z_{1m} = iZ_m\tan(k_m a/2), \quad (3)$$

$$Z_{2m} = -iZ_m/\sin(k_m a). \quad (4)$$

Here, a and b are the lengths of the reflector segments with and without mechanical load, respectively (see Fig. 1), and $Z = v\rho S$ and k are the total mechanical impedance and the wave number in the plate without load, where ρ is the density, v is the wave velocity, and S is the cross-sectional area of the acoustic waveguide. The quantities $Z_m = v_m\rho_m S_m$ and k_m are the mechanical impedances and the wave numbers for the mechanically loaded segments, where ρ_m and S_m are the effective densities and cross-sectional areas of the two-layer waveguide. The meaning of these two quantities will be explained below. The total reflection coefficient R of the whole grating can be determined from the relation $R = (Z - Z_{in})/(Z + Z_{in})$, where Z_{in} is the total input impedance of the whole reflector. The equivalent circuit shown in Fig. 2 allows one to calculate the reflection coefficient as a function of the frequency and the number of reflecting elements for different values of the impedance ratio of adjacent segments Z_m/Z. Evidently, the reflection of the acoustic wave is caused by a jump in the wave parameters of the grating elements, namely, when $Z_m/Z \neq 1$. The wider the ratio Z_m/Z differs from unity, the greater the reflection coefficient is. Figure 3 shows the characteristic dependences of the reflection coefficient on the ratio Z_m/Z at the central frequency for different numbers of strips in the grating.

Now, let us estimate the impedance ratio Z_m/Z for a reflector with a mechanical load. In the case of thin conducting electrodes whose mass is neglected, we have $Z_m/Z = v_m/v$ [4]. In the case of a grating with a periodic mechanical load, the situation becomes more complicated, because the adjacent segments differ not only in velocity, but also in density and in cross-sectional area. As the effective density for a mechanically loaded segment of the grating, we used the density value averaged over the cross section of the waveguide; i.e., the density ratio was determined by the formula $\rho_m/\rho = [\rho h + \rho_1 d)]/\rho(h + d)$, where ρ_1 and d are the density and the thickness of the layer, respectively. The ratio of the cross-sectional areas was determined as $S_m/S = (h + d)/h$.

To determine the velocities v and v_m, we performed a rigorous analysis of zero-order normal acoustic waves propagating in single-layer and two-layer waveguides based on lithium niobate. We assumed that the substrate thickness was much smaller than the wavelength λ, i.e., $h/\lambda \ll 1$. In this case, only three types of waves can propagate in the plate: two Lamb normal waves (the antisymmetric A_0 wave and the symmetric S_0 wave) and one shear horizontal normal wave (the SH_0 wave). For each of these waves, the cut of the plate, the propagation direction, and the plate thickness were selected so as to obtain the maximal coefficient of electromechanical coupling K. For lithium niobate, the corresponding parameters for each of the aforementioned modes are as follows [6]: for the A_0 wave, the $Y + 128°$ cut, the X direction of propagation, and $h/\lambda = 0.25$; for the S_0 wave, the Y cut, the $X + 50°$ direction of propagation, and $h/\lambda = 0.1$; and for the SH_0 wave, the Y cut, the X direction of propagation, and $h/\lambda = 0.1$.

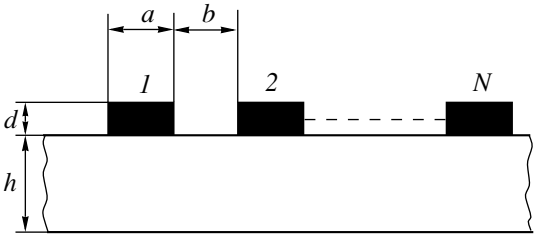

Fig. 1. Structure of a reflector for waves in a plate. The reflector contains N reflecting elements.

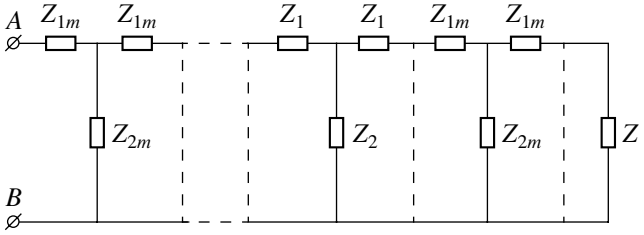

Fig. 2. Equivalent circuit of a reflector with a mechanical load.

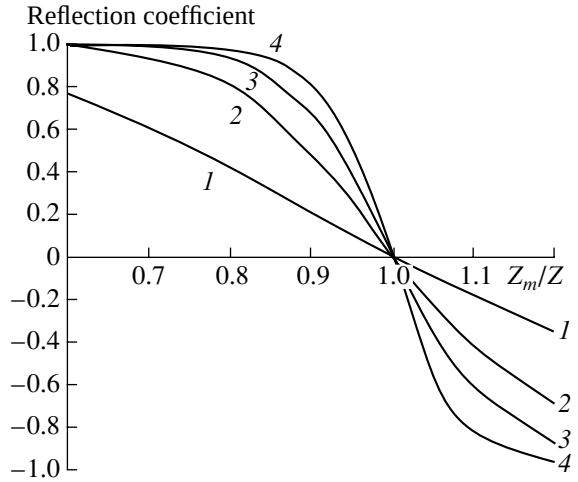

Fig. 3. Dependence of the reflection coefficient on the impedance ratio Z_m/Z at the central frequency for different numbers of strips in the reflection grating: N = (*1*) 2, (*2*) 5, (*3*) 8, and (*4*) 12.

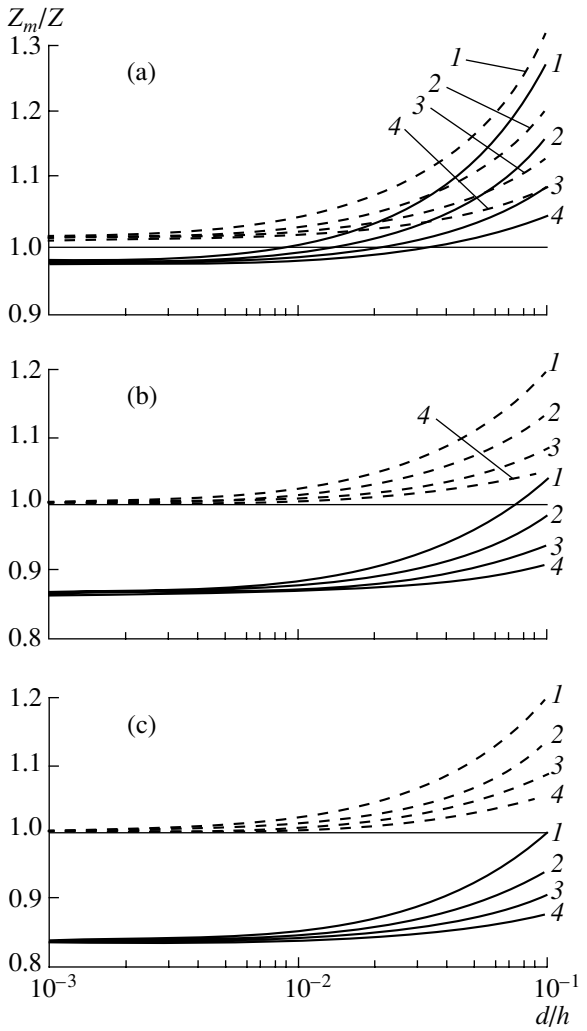

Fig. 4. Dependence of the impedance ratio Z_m/Z on d/h for the (a) A_0, (b) S_0, and (c) SH_0 waves. The layers are made of (*1*) gold, (*2*) silver, (*3*) titanium, and (*4*) aluminum. The surface areas between the strips are electrically free (the solid lines) and short-circuited by a thin conducting film (the dashed lines).

The mechanical loads were metal layers, which were easy to deposit and allowed a choice of acoustic impedance in a wide range of values. At first, we determined the wave velocity v for a given plate thickness h/λ. For this purpose, we used the method described in [7]. To determine the velocity v_m, we analyzed the propagation of acoustic waves in a two-layer structure containing a piezoelectric substrate and a perfectly conducting elastic layer of finite thickness. We used the standard equations of motion for both elastic media, the Laplace equation for the piezoelectric plate and the vacuum, and the corresponding equations of state. The mechanical and electric boundary conditions were as follows: (i) the stress and displacement continuity and the zero value of the electric potential at the boundary between the two elastic media; (ii) the continuity of both the electric potential and the normal component of the electric displacement and the zero stress value at the piezoelectric–vacuum boundary; and (iii) the zero stress value at the layer–vacuum boundary. From the theoretical analysis, we determined the dependence of the velocity on the normalized thickness h/λ_m for a given ratio d/h. Then, to determine the velocity v_m and the normalized plate thickness h/λ_m, we used the condition

$$(h/\lambda_m)\,v_m = (h_1/\lambda_1)\,v, \tag{5}$$

which meant that the frequency of the propagating wave was the same within loaded and unloaded segments.

The calculated dependences of the impedance ratio on d/h are shown in Figs. 4a–4c for the A_0, S_0, and SH_0 waves, respectively. The mechanical load was made of the following materials: gold, silver, titanium, and aluminum with the densities 19.31, 10.5, 4.5, and 2.7 g/cm^3, respectively. The density of lithium niobate was 4.628 g/cm^3. Figure 4 presents the results for two situations: the regions between the strips are electrically free (the solid lines) and short-circuited by a thin conducting film (the dashed lines).

In the first case, two factors are present: a mechanical load on the surface and the short-circuiting of the surface. The latter factor reduces the acoustic impedance, whereas the mechanical load causes an increase in the acoustic impedance with increasing layer thickness. Thus, the aforementioned factors "work" in opposite directions; i.e., for certain values of d/h, the acoustic impedance ratio becomes equal to unity. This occurs when the electric and mechanical effects compensate each other and the total reflection coefficient is equal to zero.

When the regions between the strips are short-circuited, the jump in the electric boundary conditions is absent, and the reflection is caused by the mechanical load only.

The aforementioned dependences allow one to optimize the situation when the impedance ratio is sufficient to obtain an efficient reflector governed exclusively by the mechanical load.

In line with the results presented above, we performed an experimental study of the reflection of an SH_0 wave from a grating with a purely mechanical load. The acoustic waveguide was made on the basis of a *Y*-cut lithium niobate plate with the direction of propagation along the *X* axis. To excite an acoustic wave at an operating frequency of 3 MHz, we used an interdigital transducer with a period of 1.2 mm and with two finger pairs. To reduce the reflection of the acoustic wave from the transducer and to reduce the level of the multiple reflection signal, the transducer was made on the basis of split electrodes. The capacitance of the transducer was compensated by a corresponding inductance, and the transducer was matched with the transmission line through a matching transformer. The reflector consisted

of five silver strips 10 μm thick, which were vacuum deposited with a period of 0.6 mm on the plate surface. To obtain a good adhesion of the reflecting strips, we first deposited a thin chromium film. This film short-circuited the tangential components of the electric field accompanying the wave within the unloaded segments, and, thus, the reflection occurred due to the mechanical load only. The amplitudes of the incident and reflected waves, A_i and A_r, were measured in a pulsed mode using an electrostatic probe [4]. The latter was a piece of a coaxial line whose central lead ended in a thin tungsten needle 100 μm in diameter. The opposite end of the coaxial line was cable-connected with the measuring oscilloscope. The tungsten needle of the probe touched the surface of the piezoelectric and could be moved smoothly from the transducer to the reflector by a precision mechanism. With the propagation of an acoustic wave pulse, an electric signal proportional to the strength of the piezoelectric field accompanying the wave appeared at the probe output. By changing the probe position, it was possible to separate in time the pulses corresponding to the incident and reflected waves on the screen of the oscilloscope. After the amplitudes of these waves were measured, the reflection coefficient R was calculated as $R = A_r/A_i$. To study the reflection of acoustic waves at different values of d/h, the plate thickness was decreased by polishing the back side of the plate. For this purpose, we used a special glass unit intended for fastening the plate, as described in [8]. This method allowed us to reduce the plate thickness from its initial value of 500 μm to a terminal value of 100 μm and to measure the characteristics of the reflector for several intermediate values of d/h. Figure 5 shows the reflection coefficient obtained from the experiment as a function of the plate thickness along with the corresponding theoretical dependence calculated with allowance for the short-circuiting of the surface. One can see a good agreement between the experimental data and the theoretical curve.

Thus, the theoretical analysis shows that, for a reflector based on a set of conducting strips of finite thickness, the effect of short-circuiting of the plate surface and the effect of an elastic load on the impedance ratio of adjacent plate segments are in opposition to each other. For the efficiency of a reflector of acoustic waves in plates, the effects of a mechanical load and the short-circuiting of the plate surface are commensurable. Therefore, for each type of waves, there exists a certain value of the strip thickness at which the reflection coefficient becomes zero. This conclusion is of practical importance for the development of a reflector with a controlled reflection coefficient. The experimental results presented above are in good agreement with the theory and testify that the use of the model based on equivalent circuits is suitable for analyzing the reflectors under discussion.

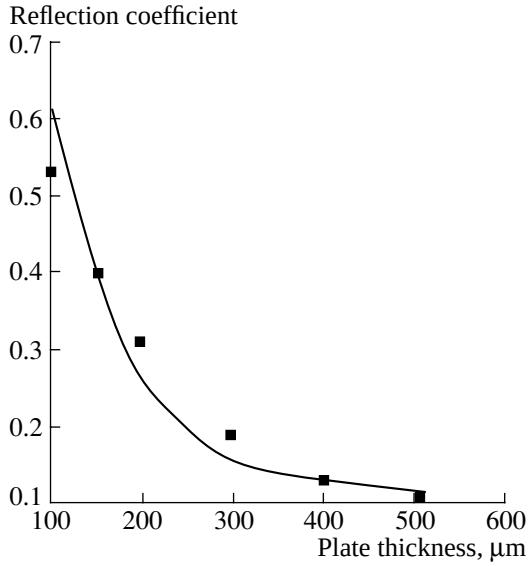

Fig. 5. Dependence of the reflection coefficient on the plate thickness for an SH_0 wave propagating in a *Y*-cut lithium niobate plate along the *X* axis: the theoretical dependence (the solid line) and the experimental data (the squares).

ACKNOWLEDGMENTS

This work was supported by the US National Science Foundation.

REFERENCES

1. C. K. Campbell, *Surface Acoustic Wave Devices for Mobile and Wireless Communications* (Academic, San Diego, 1998).
2. R. C. Williamson, in *Surface Wave Filters*, Ed. by H. Matthews (Wiley, New York, 1977).
3. D. S. Ballantine, R. M. White, S. J. Martin, A. J. Ricco, E. T. Zellers, G. C. Frye, and H. Wohltjen, *Acoustic Wave Sensors* (Academic, San Diego, 1997).
4. B. D. Zaitsev and S. G. Joshi, IEEE Trans. Ultrason. Ferroelectr. Freq. Control **46** (6), 1539 (1999).
5. W. R. Smith, in *Physical Acoustics*, Ed. by W. P. Mason (Academic, New York, 1981), Vol. 15.
6. I. A. Borodina, S. G. Joshi, B. D. Zaĭtsev, and I. E. Kuznetsova, Akust. Zh. **46**, 42 (2000) [Acoust. Phys. **46**, 33 (2000)].
7. S. G. Joshi and Y. Jin, J. Appl. Phys. **70**, 4113 (1991).
8. B. D. Zaitsev, S. G. Joshi, and I. E. Kuznetsova, IEEE Trans. Ultrason. Ferroelectr. Freq. Control **46** (5), 1298 (1999).

Translated by E. Golyamina

Acoustical Physics, Vol. 48, No. 2, 2002, pp. 166–170. Translated from Akusticheskiĭ Zhurnal, Vol. 48, No. 2, 2002, pp. 200–204.

Sound Scattering from Small Compact Inhomogeneities in a Sea Waveguide: The Inverse Problem

A. D. Zakharenko

Pacific Oceanological Institute, Russian Academy of Sciences, Far East Division, ul. Baltiĭskaya 43, Vladivostok, 690041 Russia

e-mail: zakharenko@poi.dvo.ru

Received April 4, 2001

Abstract—An approach based on the redistribution of acoustic energy between waveguide modes is used to state the inverse problem of sound scattering from small compact inhomogeneities in a shallow-water waveguide. Numerical results are presented. © *2002 MAIK "Nauka/Interperiodica".*

As shown in earlier publications [1, 2], three-dimensional problems of sound scattering in a shallow-water waveguide can be successfully approached from the point of view of the energy redistribution between waveguide modes. Weston and Fawcett [2] considered the sound scattering by the bottom inhomogeneities and derived simple formulas for the mode conversion coefficients, S_{mn}, which determine the amount of the acoustic energy scattered into the nth mode from the mth mode of the incident field. Fawcett [3] applied these formulas to reconstruct the form of axially symmetric inhomogeneities of the bottom by remote sensing. Similar formulas were derived by Fawcett [4] for acoustic scattering by three-dimensional axially symmetric inhomogeneities of the density and sound velocity. The representation of the sound field as the superposition of modes was used to state inverse problems of scattering and minimization [5].

In the previous paper [6], we obtained new formulas for the mode conversion coefficients, S_{mn}, from small compact inhomogeneities of the density, the sound velocity, and the internal boundaries of the sea bottom. In these formulas, the inhomogeneities are represented as the Fourier and Fourier–Bessel series in angular and radial coordinates, respectively. This leads to a more detailed analytical description of acoustic scattering.

In this paper, on the basis of these formulas, we state the problem of the reconstruction of an inhomogeneity from the observation data obtained in the far field. The problem is formulated as a linear operator equation of the first kind, which can be solved by the method of singular value decomposition. Cutting off the series representing inhomogeneities gives a regularizing effect, which complements the mechanism of the regularization on the basis of the selection of singular vectors with small singular values. Such a statement, contrary to that used in [5], allows one to solve problems of higher dimension with a smaller amount of computation. For simplicity, we consider only the case of a surface inhomogeneity of the sea bottom. The efficiency of the approach is illustrated by the results of model calculations.

STATEMENT OF THE INVERSE PROBLEM

We consider a stationary sound field of circular frequency ω, which is described by the complex sound pressure u in the region $-H \le z \le 0$, where z is the vertical coordinate. The horizontal coordinates are denoted by x and y.

We assume that the density ρ and the sound velocity c are piecewise continuous functions with discontinuities at the surface $z = h(x, y)$, at which the following conditions are fulfilled

$$u_+ = u_-, \quad \left(\frac{1}{\rho}\frac{\partial u}{\partial n}\right)_+ = \left(\frac{1}{\rho}\frac{\partial u}{\partial n}\right)_-,$$

where the symbols + and – denote the limits of the variables at a considered point $z = z_0$ from above, i.e., at $z > z_0$, and from below, respectively, and $\partial/\partial n$ denotes the derivative with respect to the normal.

Next, we assume that the sound velocity and the density above and below the interface depend only on z, and a function describing this interface can be represented as $h(x, y) = h_0 + h_1(x, y)$, where h_0 is a constant and h_1 is a small quantity, as compared to the typical wavelength $L = 2\pi c_0/\omega$ (c_0 is the typical sound velocity), and is zero outside a limited region Ω.

In the Born approximation, the acoustic pressure is represented by $u = u^{inc} + u^{sc}$, where u^{inc} is the incident field and u^{sc} is the principal term of the scattered field. As the incident field, we consider the field of a vertically distributed source (a vertical array) located at the point with the horizontal coordinates x_0, y_0. Such a field can be rep-

1063-7710/02/4802-0166$22.00

resented as a linear combination of modes: $u^{inc} = \sum a_j H_0^{(1)}(k_j\xi)\phi_j(z)$, where $\xi = \sqrt{(x-x_0)^2 + (y-y_0)^2}$ and ϕ_j and k_j are determined by the eigenvalue problem

$$\rho\frac{d}{dz}\left(\frac{1}{\rho}\frac{d\phi_j}{dz}\right) + \frac{\omega^2}{c^2}\phi_j = k_j^2\phi_j, \quad \phi_j|_{z=0} = 0,$$

$$\left.\frac{d\phi_j}{dz}\right|_{z=-H} = 0,$$

with the internal boundary conditions

$$\phi_{j+} = \phi_{j-}, \quad \left(\frac{1}{\rho}\frac{d\phi_j}{dz}\right)_+ = \left(\frac{1}{\rho}\frac{d\phi_j}{dz}\right)_-$$

at $z = h_0$ and with the eigenfunction normalization

$$\int_{-H}^{0}\frac{1}{\rho}\phi_j^2 dz = 1.$$

The scattered field can also be represented as a linear combination of the functions ϕ_j with range-dependent coefficients. In particular, if the incident field consists of a single mode $u^{inc} = H_0^{(1)}(k_j\xi)\phi_j(z)$, the scattered field can be represented as

$$u^{sc} = \sum S_{jn}(x, y; x_0, y_0)\phi_n(z),$$

where the coefficients S_{jn}, which are called the mode conversion coefficients, describe the scattering from the jth mode of the incident field to the nth scattering mode. In practice, these coefficients are easily obtained from the analysis of the mode composition of the sound field measured by vertical or horizontal arrays.

The expressions for the mode conversion coefficients S_{jn} derived in [6] are used to represent h_1 as a double Fourier and Fourier–Bessel series (see, e.g., [8]) in angular and radial coordinates, respectively, in the cylindrical coordinate system (r, α, z):

$$h_1(r, \alpha) = \sum_{m=-\infty}^{\infty}\sum_{p=1}^{\infty}\exp(im\alpha)\tilde{h}_{1mp}J_m(r\gamma_p/L),$$

where L is such that the region Ω is within the circle of radius L with the center at the coordinate origin, γ_p are the positive roots of the equation $J_m(r) = 0$, and J_m are the Bessel functions. Denoting the horizontal coordinates of the receiver and the source by (r_r, α_r) and (r_0, α_0), respectively, we write the expressions for S_{jn} from [6] as the Fourier series

$$S_{jn}(r_r, \alpha_r; r_0, \alpha_0) = \sum_{s=-\infty}^{\infty}\hat{S}_{jns}(r_r; r_0, \alpha_0)\exp(is\alpha_r), \quad (1)$$

where the coefficients $\hat{S}_{jns}$ are given by the formula

$$\hat{S}_{jns} = \sum_{m=-\infty}^{\infty}\sum_{p=1}^{\infty}\hat{A}_{jns}^{mp}\tilde{h}_{1mp}, \quad (2)$$

where

$$\hat{A}_{jns}^{mp} = -\frac{i\sqrt{2\pi}}{4}\frac{\exp(ik_n r_r - i\pi/4)}{\sqrt{k_n r_r}}e^{i(m-s)\alpha_0}\cdot$$

$$\{2G_1 H_{m-s}^{(1)}(k_j r_0)F_s^{mp} + ik_j k_n G_2$$

$$\times[H_{m-s+2}^{(1)}(k_j r_0) + e^{2i\alpha_0}H_{m-s}^{(1)}(k_j r_0)]F_{s-1}^{mp}\},$$

$$F_s^{mp} = \int_0^L J_m\left(\frac{\gamma_p^m}{L}r\right)J_{m-s}(k_j r)J_s(k_n r)r dr, \quad (3)$$

$$G_1 = \left(\frac{(\rho_- - \rho_+)}{\rho_+^2}\left(\frac{d\phi_n}{dz}\right)_+\left(\frac{d\phi_j}{dz}\right)_+\right.$$

$$\left. + \omega^2\left(\frac{1}{\rho_+ c_+^2} - \frac{1}{\rho_- c_-^2}\right)\phi_n\phi_j\right)\Bigg|_{z=h_0},$$

$$G_2 = \phi_n\phi_j\left(\frac{1}{\rho_+} - \frac{1}{\rho_-}\right)\Bigg|_{z=h_0}.$$

In these formulas, it is assumed that r_r is large enough to replace the Hankel functions $H_\mu^{(1)}(k_n r_r)$ by the principle terms of their asymptotics at $r_r \longrightarrow \infty$. We note that no similar limitations are imposed on the source coordinates.

Formulas (1) and (2) determine the linear transformations from the data specifying the inhomogeneity to the scattering data:

$$\hat{A}: \{\tilde{h}_{1mp}\} \longrightarrow \{\tilde{S}_{jns}(r_r; r_0, \alpha_0)\},$$

$$A: \{\tilde{h}_{1mp}\} \longrightarrow \{S_{jn}(r_r, \alpha_r; r_0, \alpha_0)\},$$

where $-\infty < m < \infty$, $1 \le p < \infty$, $-\infty < s < \infty$, and $0 < j, n \le M$, where M is the number of the modes under consideration; $(r_r, \alpha_r) \in E^r$ and $(r_0, \alpha_0) \in E^s$; E^r and E^s are the sets of the horizontal coordinates of the points where the sources and receivers are located. The matrix elements of the operator $\hat{A}$ in the key case of a single source and a single receiver are given by Eq. (3).

The inverse problem consists in the inversion of these operators on the measured scattering data, i.e., in solving the operator equations of the first kind. The use of the scattering data $\{\hat{S}_{jns}(r_r; r_0, \alpha_0)\}$ is natural, if measurements were carried out on the circles of sufficiently large radius. The typical finite-dimension approximation of this problem is obtained by limiting the number of the reconstructed coefficients $\tilde{h}_{1mp}$ and the number of the Fourier harmonics in the mode conversion coefficients and by presetting the finite sets E^r and E^s. In this case, we do not require that the number of the reconstructed coefficients coincide with the dimension of the space of scattering data. In this situation, we deal with a pseudoinversion of the operator A, and in this paper, we suggest using the method of

pseudoinversion based on the singular value decomposition [7]. This method includes the regularization procedure, which consists in projecting the solution on the halfspace that is orthogonal to singular vectors with singular values lying in the interval $(-\epsilon, \epsilon)$, where ϵ is the regularization parameter.

NUMERICAL RESULTS

Calculations were carried out for a two-layered medium (water/bottom) with a constant density and a constant velocity for each layer. For the water layer with a thickness of 200 m, the density and the sound velocity were taken to be 1000 kg/m^3 and 1470 m/s, respectively; for the bottom layer with a thickness of 500 m, these parameters were 1150 kg/m^3 and 2000 m/s. The sound frequency was 20 Hz. For these conditions, there are four propagating modes, which persist when the thickness of the bottom layer tends to infinity. Only these four modes were used in the calculations.

The test inhomogeneities of the sea bottom were given by the functions

$$h_1(r, \alpha) = A_M r^M \cos(M\alpha)\exp(-r^2/\sigma^2), \quad M = 0, 1, 2, 3. \tag{4}$$

The parameter σ was taken equal to 30, $A_0 = 1$, $A_1 = 8 \times 10^{-2}$, $A_2 = 3 \times 10^{-3}$, and $A_3 = 1 \times 10^{-4}$. Thus, each inhomogeneity was described by only one angular cosine Fourier harmonic $\mathrm{Re}\,\hat{h}_{1M}(r) = A_M r^M \exp(-r^2/\sigma^2)$. In the argument r, the functions (4) are well approximated by the Fourier–Bessel series of eight terms. These data were used for calculating the scattering coefficients S_{jn}, where $j, n = 1, \ldots, 4$, for the sources with the coordinates $r_0 = 500$ m, $\alpha_0 = 0°$, 90°, 180°, and 270°.

In this case, for the values of r_0 that are large enough to replace the Hankel function $H_s^{(1)}(k_j r_0)$ by its asymptotics, the coefficients S_{jn} have closed expressions

$$S_{jn} = -\frac{\exp(i(k_n r_r + k_j r_0))}{\sqrt{k_n r_r}\sqrt{k_j r_0}} e^{-iM\pi/2} \times \cos(M(\psi - \alpha_r)) A_M (G_1 + k_j k_n G_2 \cos(\alpha_0 - \alpha_r)) \times \frac{\kappa^M \sigma^{2(M+1)}}{2^{M+1}} \exp\left(-\frac{\kappa^2\sigma^2}{4}\right),$$

where

$$\kappa = \sqrt{k_j^2 + k_n^2 + 2k_j k_n \cos(\alpha_0 - \alpha_r)},$$

$$\psi = \arctan\left(\frac{-k_j \sin(\alpha_0 - \alpha_r)}{k_n + k_j \cos(\alpha_0 - \alpha_r)}\right).$$

These expressions were used for testing the accuracy of the representations of the functions of inhomogeneities by their Fourier–Bessel series.

The inverse problem was solved with the use of the scattering data $\{\hat{S}_{jns}(r_r; r_0, \alpha_0)\}$. The calculations were carried out in the MATLAB system. In this system, the method of pseudoinversion on the basis of the singular value decomposition was represented by the *pinv* procedure. For the calculations, the scattering data were prepared in the following way: the exact values $\hat{S}_{jns}$ were supplemented by a Gaussian white noise with a normal deviation of 3% from the mean value of $\hat{S}_{jns}$. The calculations were carried out for several realizations of noise, with two and four sources [in Figs. 1–3, versions (a) and (b), respectively]. Because of symmetry, we used only the mode conversion coefficients S_{jn} that satisfy the condition $n \geq j$, so that their number was equal to 10, and the number of angular harmonics in each coefficient was 21. The number of the Fourier–Bessel coefficients in the reconstructed function h_1 was eight, the number of the angular Fourier harmonics varied.

Figures 1–4 show the results of calculations for $M = 2$. In Figs. 1–3, the exact harmonic $A_M r^M \exp(-r^2/\sigma^2)$ is compared with the functions $\mathrm{Re}\,\hat{h}_{1M}(r)$ reconstructed using eight terms in the Fourier–Bessel series whose coefficients were obtained by the pseudoinversion of the operator $\hat{A}$ for three different realizations of random noise.

Figures 1 and 2 show the effect of the method of the pseudoinversion based on the singular value decomposition on the results of calculating the regularization parameter. The regularizing effect of cutting off the series representing the inhomogeneities is shown in Fig. 3. In all calculations, the mean square deviations of the harmonics that are not shown in the figures from zero in terms of the mean-square norm are the same as the deviations of the reconstructed fundamental harmonic from the exact one. This is clearly seen in Fig. 4, which exhibits the form of the surface of the initial function and the surface reconstructed by 17 Fourier harmonics with the regularization parameter 5×10^{-6} for four sources (see Fig. 1b).

The calculations carried out for all remaining functions of the form of Eq. (4) for $M = 0, 1, 3$ provide, in general, the same results.

The amount of computation, which can be estimated as a moderate one, is mainly related to constructing the matrix of the operator $\hat{A}$. Note that, in this case, the basic properties of the sound waveguide are also encoded in the matrix. The amount of calculation related to the solution of the operator equation (the pseudoinversion) is relatively insignificant.

Thus, the model calculations show that the statement of the inverse problem as a linear operator equation on the basis of the formulas for solving the direct problem from the previous paper [6] provides the necessary regularization and allows an efficient solution of

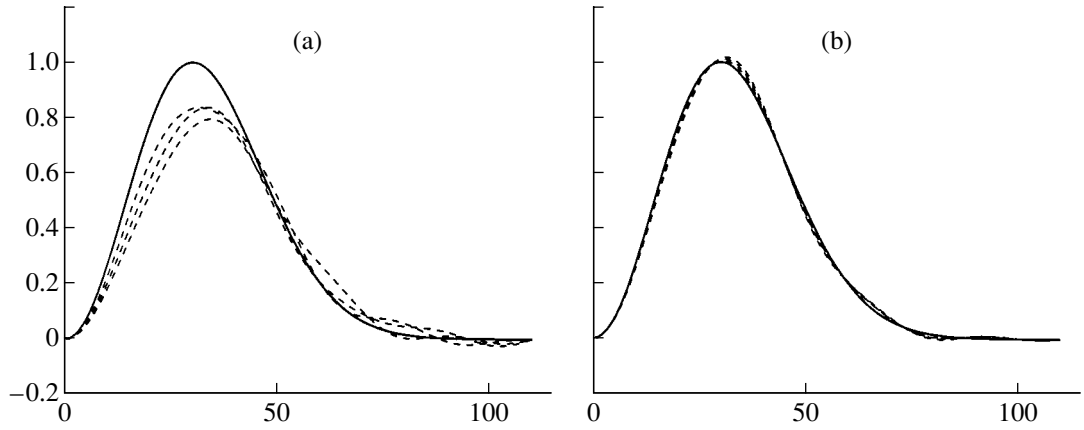

Fig. 1. Reconstruction of the inhomogeneity function (3) for $M = 2$ with allowance for 17 angular Fourier harmonics: the initial function (the solid line) and the solutions to the inverse problem (the dashed lines) for three realizations of 3% noise. (a) Two sources at the angles $\alpha_0 = 0°$ and 90°; (b) four sources at the angles $\alpha_0 = 0°$, 90°, 180°, and 270°. The regularization parameter is $\epsilon = 5 \times 10^{-6}$.

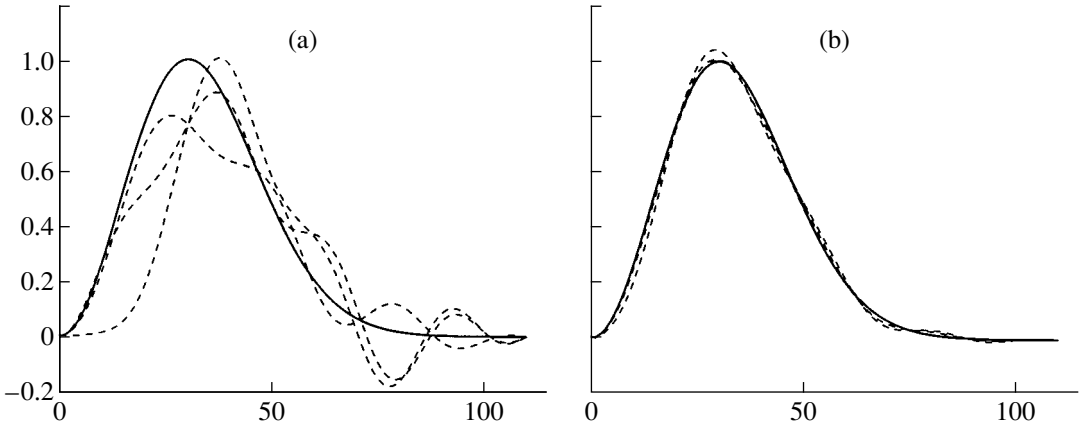

Fig. 2. Reconstruction of the inhomogeneity function (4) for $M = 2$ with allowance for 17 angular Fourier harmonics: the initial function (the solid line) and the solutions to the inverse problem (the dashed lines) for three realizations of 3% noise. Versions (a) and (b) are the same as in Fig. 1. The regularization parameter is $\epsilon = 1 \times 10^{-6}$.

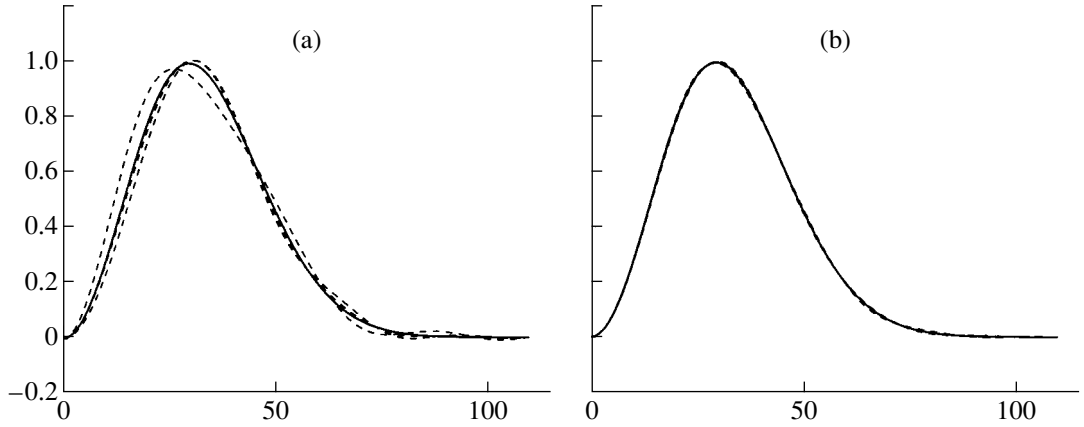

Fig. 3. Reconstruction of the inhomogeneity function (4) for $M = 2$ with allowance for seven angular Fourier harmonics: the initial function (the solid line) and the solutions to the inverse problem (the dashed lines) for three realizations of 3% noise. Versions (a) and (b) are the same as in Fig. 1. The regularization parameter is $\epsilon = 5 \times 10^{-6}$.

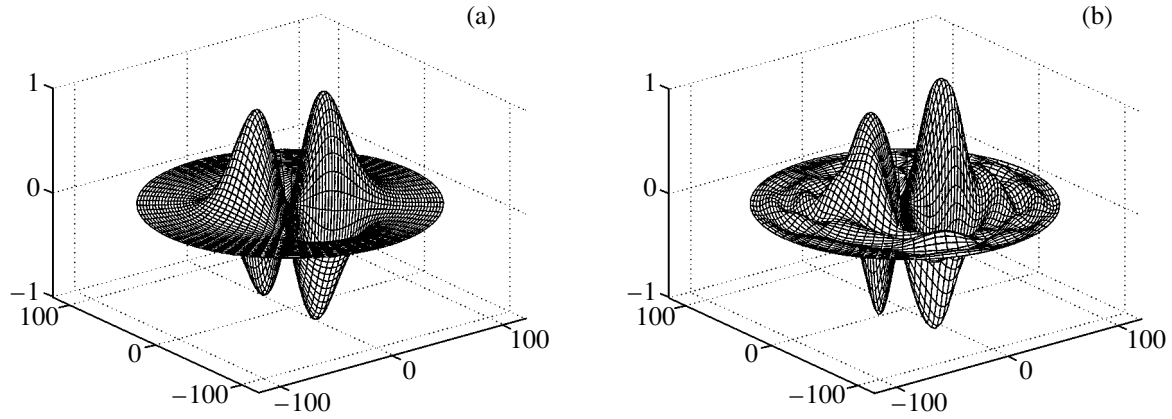

Fig. 4. Surface of the sea bottom inhomogeneities described by function (4) for $M = 2$: (a) the initial surface and (b) the surface reconstructed on the basis of the data obtained from four sources (Fig. 1b).

the inverse problem by conventional means. This makes the proposed approach suitable for use in practice for field experiments.

The reviewer of this paper pointed to significant coherent effects that accompany the backscattering of sound [9]. These effects cannot be taken into account in the Born approximation used in this paper. To include them in the consideration, the formalism must be extended, which will be the subject of the following studies.

REFERENCES

1. F. Ingenito, J. Acoust. Soc. Am. **82**, 2051 (1987).
2. B. T. R. Wetton and J. A. Fawcett, J. Acoust. Soc. Am. **85**, 1482 (1989).
3. J. A. Fawcett, Inverse Probl. **6**, 185 (1990).
4. J. A. Fawcett, J. Acoust. Soc. Am. **102**, 3387 (1997).
5. R. P. Gilbert, T. Scotti, A. Wirgin, and Y. S. Xu, J. Acoust. Soc. Am. **103**, 1320 (1998).
6. A. D. Zakharenko, Akust. Zh. **46**, 200 (2000) [Acoust. Phys. **46**, 160 (2000)].
7. A. E. Albert, *Regression and the Moore–Penrose Pseudoinverse* (Academic, New York, 1971; Nauka, Moscow, 1977).
8. H. Bateman and A. Erdélyi, *Higher Transcendental Functions* (McGraw-Hill, New York, 1953; Nauka, Moscow, 1966), Vol. 2.
9. Yu. A. Kravtsov and A. I. Saichev, Usp. Fiz. Nauk **137** (3), 501 (1982) [Sov. Phys. Usp. **25**, 494 (1982)].

Translated by Yu. Lysanov

Acoustical Physics, Vol. 48, No. 2, 2002, pp. 171–175. Translated from Akusticheskiĭ Zhurnal, Vol. 48, No. 2, 2002, pp. 205–210.

Konenkov's Waves in Anisotropic Layered Plates

D. D. Zakharov

Institute for Problems of Mechanics, Russian Academy of Sciences, pr. Vernadskogo 101-1, Moscow, 117526 Russia
e-mail: dd_zakh@mail.ru

Received April 11, 2001

Abstract—Rayleigh-type flexural waves localized near the edge of a thin anisotropic layered plate are investigated. The following effects are revealed: a wave attenuation with oscillations, a change of sign of the energy flux for certain types of anisotropy, and the appearance of stationary waves. © *2002 MAIK "Nauka/Interperiodica".*

To all appearance, flexural waves of the Rayleigh type were first investigated in [1] for the case of anisotropic media. Such waves must be taken into account at the excitation of a free edge, of the edge contact of different materials, etc. [2–4]. However, unlike plane Rayleigh waves, which are basic in a number of technologies used for nondestructive testing, seismic monitoring, and the like (the bibliography for the case of anisotropic media is presented, e.g., in [5, 6]), flexural waves are not so famous. The reason is the comparatively small damping coefficient of a flexural wave (of the order of ν^4, where ν is the Poisson ratio) in an isotropic medium. The appearance and widespread use of promising composite materials raises the following natural questions:

(i) do the Rayleigh flexural waves exist in media with a rather general type of anisotropy;

(ii) if so, what are their properties (the energy, the damping factors, etc.);

(iii) how are these properties affected by the stacking asymmetry in layered media (the correlation between flexure and the plane strained state).

In spite of the interest manifested by some authors [4], no detailed investigations of this problem were published. This paper gives the answers to the first two questions.

Consider a thin packet with a symmetric structure, which consists of anisotropic elastic layers. Denote the total thickness of the packet by $2h$, use the dimensionless orthogonal coordinates x_1, x_2 normalized to h, and take the internal stress-strained state of the layered packet to be a long-wave one, i.e., satisfying the classical relations of the theory of layered plates [7]. The interlayer contact is supposed to be an ideal one. All the elastic constants below are taken to be normalized to the maximal value (out of the packet layers) of the Young modulus, and the densities are normalized similarly.

Consider now harmonic oscillations of a semi-infinite packet characterized by the flexural stiffness matrix $\mathbf{D} = \|d^3_{pq}\|$ and occupying the region Ω: $x_2 \geq 0$, $-\infty < x_1 < \infty$. The packet edge $x_2 = 0$ is taken to be stress-free. Then, the normal deflection $w = w_*(x_1, x_2)\exp(i\omega t)$, normalized to the half-thickness h, satisfies the equation

$$\{L_3(\partial_1, \partial_2) - \rho\omega^2\}w_* = 0,$$

$$L_3(\partial_1, \partial_2) \equiv d^3_{11}\partial_1^4 + 4d^3_{16}\partial_1^3\partial_2 \tag{1}$$

$$+ 2(d^3_{12} + 2d^3_{66})\partial_1^2\partial_2^2 + 4d^3_{26}\partial_1\partial_2^3 + d^3_{22}\partial_2^4,$$

and the free-edge boundary conditions

$$M(\partial_1, \partial_2)w_* = 0, \quad F(\partial_1, \partial_2)w_* = 0, \tag{2}$$

$$\begin{bmatrix} M \\ F \end{bmatrix} = -\begin{bmatrix} d^3_{12}\partial_1^2 + d^3_{26}\partial_1\partial_2 + d^3_{22}\partial_2^2 \\ 2d^3_{16}\partial_1^3 + (d^3_{12} + 4d^3_{66})\partial_1^2\partial_2 + 4d^3_{26}\partial_1\partial_2^2 + d^3_{22}\partial_2^3 \end{bmatrix},$$

where ω is the cyclic frequency, ρ is the dimensionless integral density, and M and F are operators corresponding to the normal moment M_{22} and the normal intersecting Kirchhoff force $P_{2z} = 2\partial_1 M_{12} + \partial_2 M_{22}$.

1063-7710/02/4802-0171$22.00 © 2002 MAIK "Nauka/Interperiodica"

Let us analyze the possibilities for the existence of wave solutions propagating along the edge and exponentially decaying inside the packet, i.e., the Rayleigh-type solutions

$$w_* = Ae^{i(k_1x_1 + k_2x_2)}, \quad A = \text{const}, \quad \operatorname{Im} k_2 < 0.$$

We use the designations

$$d_{pq} = \frac{d^3_{pq}}{d}, \quad s^4 = \frac{\rho\omega^2}{dk_1^4}, \quad \xi = \frac{k_2}{k_1},$$

where d is some stiffness value chosen for the normalization. Taking for definiteness $k_1 > 0$, we obtain from Eq. (1) a characteristic equation with constant coefficients for the parameter ξ:

$$L(1, \xi) - s^4 \equiv d_{11} + 4d_{16}\xi + 2(d_{12} + 2d_{66})\xi^2 + 4d_{26}\xi^3 + d_{22}\xi^4 - s^4 = 0. \tag{3}$$

The following statements are evident.

Statement 1. In the absence of mixed stiffness constants ($d_{16} = d_{26} = 0$), Eq. (3) can have purely imaginary roots ξ: $\operatorname{Re}\xi = 0$; otherwise, the roots are real or complex ones.

Statement 2. All the complex roots of Eq. (3) are conjugate; two pairs of complex conjugate roots (along with the flexural wave of the Rayleigh type) can exist only in the range $s < s_*$, $s_*^4 = \inf_{\xi \in R} L(1, \xi)$.

Indeed, the fourth-order characteristic polynomial $L(1, \xi)$ is positive definite in the space of real numbers ξ. At $s = s_*$, due to the polynomial smoothness, Eq. (3) has at least one real root with a twofold multiplicity. For $s > s_*$, the number of real roots is no less than two. Thus, for $s \geq s_*$, there is no more than one pair of complex conjugate roots, which is insufficient to satisfy two boundary conditions (2) with a simultaneous exponential decay along the x_2 axis.

Statement 3. The phase velocity V_R of the Rayleigh-type flexural wave is bounded from above

$$V_R < V_*, \quad V_* = s_*^2 k_1 \sqrt{d/\rho}.$$

Denote the sought-for pair of complex roots by $\xi_{1,2}$ ($\operatorname{Im}\xi_{1,2} > 0$). The edge conditions (2) take the form

$$\det\Delta(s) = 0,$$

$$\Delta(s) = \begin{bmatrix} d_{12} + 2d_{26}\xi_1 + d_{22}\xi_1^2 & d_{12} + 2d_{26}\xi_2 + d_{22}\xi_2^2 \\ 2d_{16} + (d_{12} + 4d_{66})\xi_1 + 4d_{26}\xi_1^2 + d_{22}\xi_1^3 & 2d_{16} + (d_{12} + 4d_{66})\xi_2 + 4d_{26}\xi_2^2 + d_{22}\xi_2^3 \end{bmatrix}, \tag{4}$$

$$\frac{A_2}{A_1} = -\frac{d_{12} + 2d_{26}\xi_1 + d_{22}\xi_1^2}{d_{12} + 2d_{26}\xi_2 + d_{22}\xi_2^2}, \quad w_*(x_1, x_2) = \{A_1 e^{i\xi_1 k_1 x_2} + A_2 e^{i\xi_2 k_1 x_2}\}e^{ik_1 x_1}, \tag{5}$$

i.e., the problem of the existence of the desired waves is reduced to analyzing the roots s of Eq. (4) on the branches $\xi_1(s)$ and $\xi_2(s)$.

In the specific case of an orthotropic medium with the main axes coinciding with x_1 and x_2, the situation is considerably simplified. The mixed stiffness constants are $d_{16} = d_{26} = 0$, and the characteristic equation (3) has purely imaginary branches of the roots $\xi_1(s)$ and $\xi_2(s)$. Choosing the normalizing coefficient $d = d_{22}$, we obtain

$$\xi_{1,2} = i\{C \mp \sqrt{D + s^4}\}^{1/2}, \quad D = C^2 - \frac{d_{11}}{d_{22}},$$

$$C = \frac{d_{12} + 2d_{66}}{d_{22}}, \quad E = \frac{2d_{66}}{d_{22}},$$

$$f(s) = \left\{\frac{E + \sqrt{D + s^4}}{E - \sqrt{D + s^4}}\right\}^2 \left\{\frac{C - \sqrt{D + s^4}}{C + \sqrt{D + s^4}}\right\}^{1/2} = 1, \tag{6}$$

$$f(s) = 1 \Leftrightarrow \det\Delta(s) = 0.$$

When $s^4 \in [E^2 - D, C^2 - D]$, the function $f(s)$ varies from 0 to $+\infty$, i.e., the real root s of Eq. (6) always exists and is expressed as

$$s = \left\{-D + CE\left(2 - 3a^2 + 2\sqrt{2\left(a^2 - \frac{1}{2}\right)^2 + \frac{1}{2}}\right)\right\}^{1/4}, \tag{7}$$

$$a^2 = \frac{E}{C},$$

where the positive definiteness of the radicals follows from that of the elastic constants tensor. It is easily seen that the amplitude ratio (5) is also real. It is the real part of the solution $\operatorname{Re}\{w_*(x_1, x_2)e^{i\omega t}\}$ that has a physical meaning, and the angular displacements of cross sections θ_1, θ_2 and the longitudinal displacements u_1, u_2 are given by the formulas

$$\theta_\alpha = -\partial_\alpha \operatorname{Re}\{w_*(x_1, x_2)e^{i\omega t}\}, \quad u_\alpha = z\theta_\alpha \quad (\alpha = 1, 2)$$

$$u_1 = -z\operatorname{Re}\left\{ik_1A_1\left[e^{-k_1|\xi_1|x_2} + \frac{A_2}{A_1}e^{-k_1|\xi_2|x_2}\right]e^{i(\omega t + k_1x_1)}\right\},$$

$$u_2 = z\operatorname{Re}\left\{k_1A_1\left[|\xi_1|e^{-k_1|\xi_1|x_2} + |\xi_2|\frac{A_2}{A_1}e^{-k_1|\xi_2|x_2}\right]e^{i(\omega t + k_1x_1)}\right\}.$$

Hence, at the real amplitude A_1, the displacements u_1, u_2 (and the angles θ_1, θ_2) follow the harmonic law with a phase difference of $-\pi/2$. In one period of oscillations, an arbitrary point (x_1, x_2) describes an ellipse by moving in the positive direction, and the semi-axes of the ellipse exponentially decrease with distance from the free edge.

In the specific case of an isotropic (and transversely isotropic) medium, Eq. (7) leads to the well-known relation derived by Yu.K. Konenkov [1]:

$$s = \{(1-\nu)(3\nu - 1 + 2\sqrt{1-2\nu+2\nu^2})\}^{1/4},$$

where ν is the Poisson ratio.

It is also of interest to analyze the qualitative behavior of the phase velocity V_R (its ratio to the velocity V_B of a common flexural wave with the wave vector $\mathbf{k}$) and the period-average value of the power flow $\Im$

$$V_B = \frac{\omega}{|\mathbf{k}|} = \left[\frac{\omega^2 L_3(\cos\varphi, \sin\varphi)}{\rho}\right]^{1/4},$$

$$V_R = \frac{\omega}{k_1} = s\left[\frac{\omega^2 d_{22}^3}{\rho}\right]^{1/4},$$

$$r(\varphi) = \frac{V_R}{V_B} = s\left\{\frac{d_{22}^3}{L_3(\cos\varphi, \sin\varphi)}\right\}^{1/4},$$

$$\Im = -\frac{\omega}{2\pi}\int_0^{\frac{2\pi}{\omega}} dt \int_0^{+\infty} \{\mathrm{Re}\dot{\theta}_1 \mathrm{Re}M_{11} + \mathrm{Re}\dot{w}\mathrm{Re}P_{1z}\}dx_2,$$

where the dot means the time derivative and M_{11} and $P_{1z} = 2\partial_2 M_{12} + \partial_1 M_{11}$ are the normal moment and the intersecting Kirchhoff force in the packet cross section perpendicular to the x_1 axis.

With a view of a numerical illustration, we take two types of an orthotropic material: the carbon-filled plastic (CP) with the Young moduli $E_1 = 12800$ and $E_2 = 840$, the shear modulus $G_{12} = 460$ kg/mm^2, the Poisson ratio $\nu_{12} = 0.37$, and the density $\rho = 1.5$ g/cm^3; and the organic plastic (OP) with the respective constants $E_1 = 2600$, $E_2 = 1800$, $G_{12} = 230$, $\nu_{12} = 0.14$, and $\rho = 1.4$. The main orthotropic axes either coincide with the reference axes (CP/0) or are rotated through the right angle (CP/90); the thickness is taken to be $2h = 1$ mm and $d = \max(d_{11}, d_{22})$.

The typical values of s and the normalized values of the radiation power of the wave under study are as follows:

$s = 0.99982\pi$ (for CP/0) and 0.506225π (for CP/90),

$\min(\mathrm{Im}\xi_1, \mathrm{Im}\xi_2) = 0.0362$ (for CP/0) and 0.00949 (for CP/90),

$\Im/\omega d|k_1 A_1|^2 = -61.0861$ (for CP/0) and -15.38159 (for CP/90);

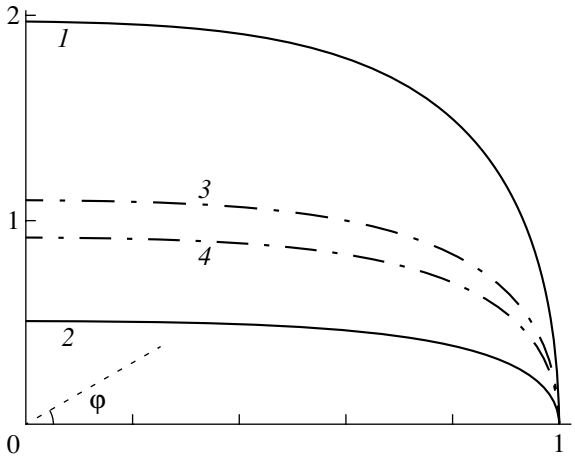

Fig. 1. Velocity ratio V_R/V_B in polar coordinates for the materials (*1*) CP/0, (*2*) CP/90, (*3*) OP/0, and (*4*) OP/90.

$s = 0.99769\pi$ (for OP/0) and 0.91085π (for OP/90),

$\min(\mathrm{Im}\xi_1, \mathrm{Im}\xi_2) = 0.0444$ (for OP/0) and 0.03616 (for OP/90),

$\Im/\omega d|k_1 A_1|^2 = -56.6055$ (for OP/0) and -48.26285 (for OP/90).

The curves for the velocity ratio are presented in Fig. 1.

Thus, for the case of orthotropic materials with standard orientation, we can make the following conclusions:

(i) the flexural wave of the Rayleigh type exists at all times;

(ii) the damping factor $\min(\mathrm{Im}\xi_1, \mathrm{Im}\xi_2)$ proves to be higher than that for an isotropic medium, where the corresponding value does not exceed 0.01;

(iii) the phase velocity of the Rayleigh flexural wave is not minimal among all possible flexural waves, as it is in the case of an isotropic medium.

In a more general case of anisotropy ($d_{16}, d_{26} \neq 0$), it is impossible to find analytical expressions for the roots $\xi_1(s)$, $\xi_2(s)$, and one has to resort to numerical analysis. The search procedure is as follows: the parameter s is specified, and two solutions $\xi_1(s)$ and $\xi_2(s)$ are determined from Eq. (3), then Eq. (4) is checked (the real and imaginary parts of $\det\Delta(s)$). Let us model the situation using the examples of the T material ($\rho = 1.58$ g/cm^3, $E_1 = 13000$, $E_2 = 975$, $G_{12} = 600$ kg/mm^2, and $\nu_{12} = 0.27$), and the E material ($\rho = 2$, $E_1 = 4500$, $E_2 = 1300$, $G_{12} = 440$, and $\nu_{12} = 0.29$) whose principal axes x_1', x_2' are rotated through the angle $0 < \psi < \pi/2$ with respect to the axes x_1 and x_2. The curves for the typical values of $s(\psi)$, the branches $\xi_1(\psi)$, $\xi_2(\psi)$, and the amplitude ratio (5) are presented in Figs. 2–5.

The behavior of the radiation power $\Im(\psi)$ is also of interest (the curves for the normalized values of this function are presented in Fig. 6). When $k_1 > 0$, the

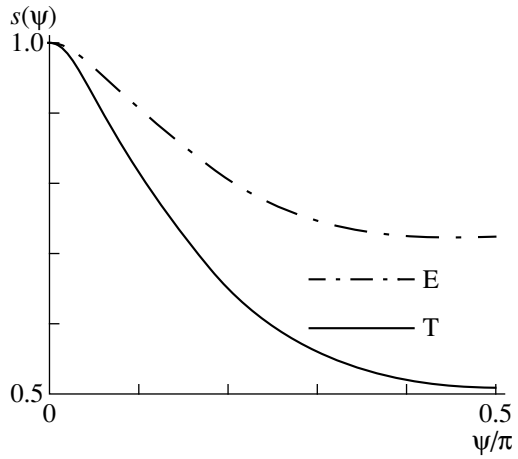

Fig. 2. Characteristic value curves for T and E.

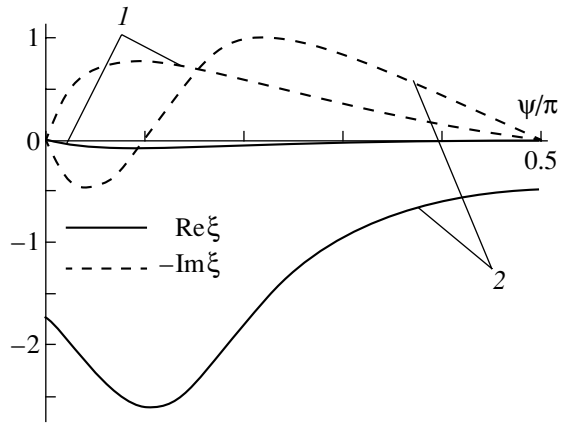

Fig. 3. Roots $\xi_1(\psi)$ and $\xi_2(\psi)$ for T.

power flux should seemingly be negative. For both materials, however, one can find the critical value of the orientation angle, $\psi_* = 0.07647\pi$ (T) and 0.10492π (E), when the sought-for wave turns into a stationary one, and then (at $\psi > \psi_*$) changes the direction of energy transfer. Further more, at the next critical angle, $\psi_{**} = 0.22862\pi$ (T) and 0.29861π (E), the wave again becomes stationary, and at $\psi > \psi_{**}$ the negative sign of the power flux is restored. This fact is new and peculiar exclusively to media with a sufficiently general anisotropy ($d_{16}, d_{26} \neq 0$). This fact was not noted earlier for the anisotropic media, and it is fundamentally absent in the case of isotropic media or conventionally oriented orthotropic ones.

To clarify the effect, consider the behavior of the generalized acoustic impedances

$$I_m^* = \frac{M_{11}}{\theta_1^{\cdot}} = \frac{I_m}{V_R}, \quad I_p^* = \frac{P_{1z}}{w^{\cdot}} = \frac{k_1^2 I_p}{V_R}, \quad I = I_m + I_p,$$

$$\theta_1 = -ik_1 w, \quad w^{\cdot} = i\omega w,$$

$$\Im = -\frac{\omega^2 k_1^2}{2V_R}\int_0^{+\infty} |w|^2 \mathrm{Re}(I_m + I_p)\,dx_2.$$

Following the elementary analogy for the damped harmonic oscillator

$$I^* = \frac{my^{\cdot\cdot} + by^{\cdot} + cy}{y^{\cdot}} = i\left(m\omega - \frac{c}{\omega}\right) + b, \qquad (8)$$

one can expect a positive value of $\mathrm{Re}(I_m + I_p)$ and a possible change of sign of the imaginary part. Figures 7–9 demonstrate the curves for the real and imaginary parts of the generalized impedances I_m, I_p, $I_m + I_p$ for three values of the angle ψ: beyond the interval $[\psi_*, \psi_{**}]$ (Figs. 7, 9) and within the interval (Fig. 8). It can be seen that, beyond the interval $[\psi_*, \psi_{**}]$, the qualitative analogy with Eq. (8) is valid, while at the intermediate value of ψ, an active edge zone with the opposite direction of the energy flow is present, which leads to the change of sign of the integral $\Im$. This situation takes place at any intermediate value of ψ. In particular, if one considers the value of $\mathrm{Re}(I_m + I_p)$ at one point $x_1 = 0$ as

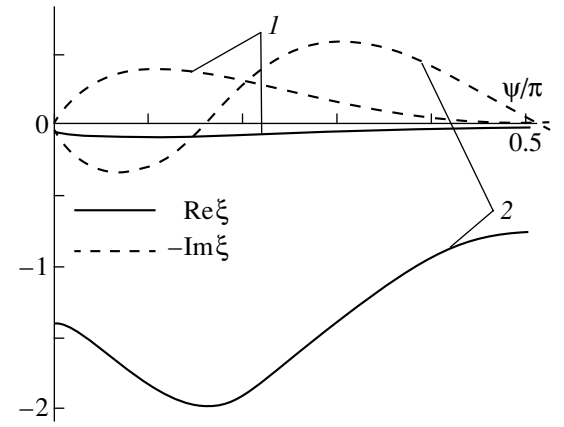

Fig. 4. Roots $\xi_1(\psi)$ and $\xi_2(\psi)$ for E.

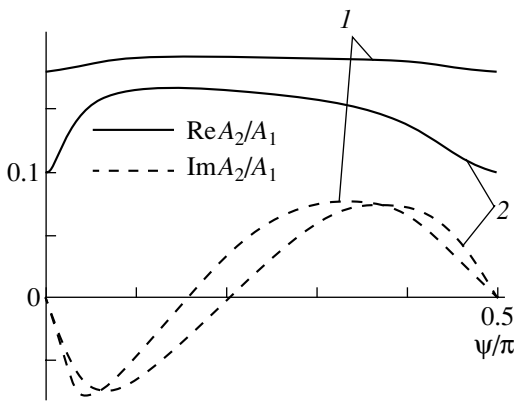

Fig. 5. Amplitude ratio A_2/A_1 as a function of ψ for the (*1*) T and (*2*) E materials.

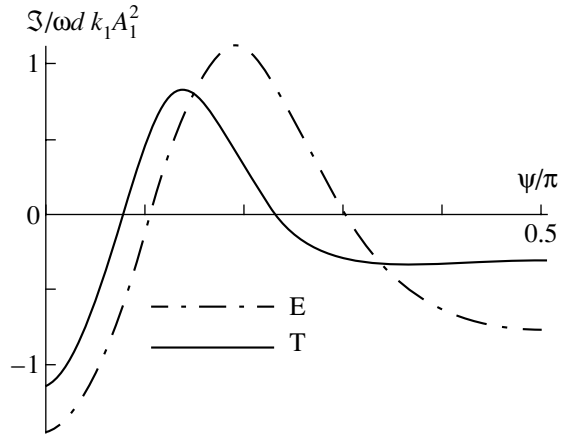

Fig. 6. Normalized radiation powers.

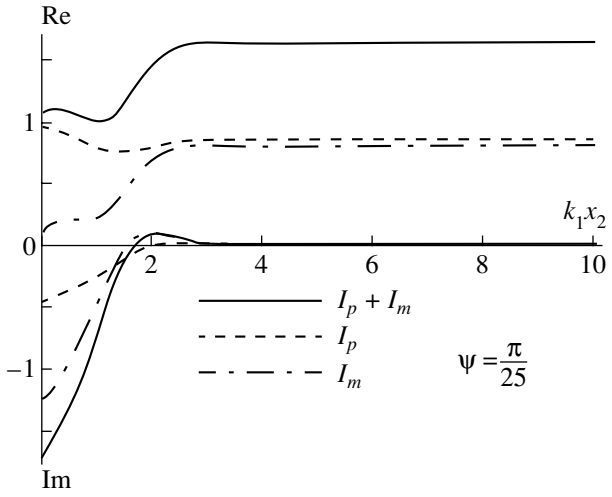

Fig. 7. Normalized impedances.

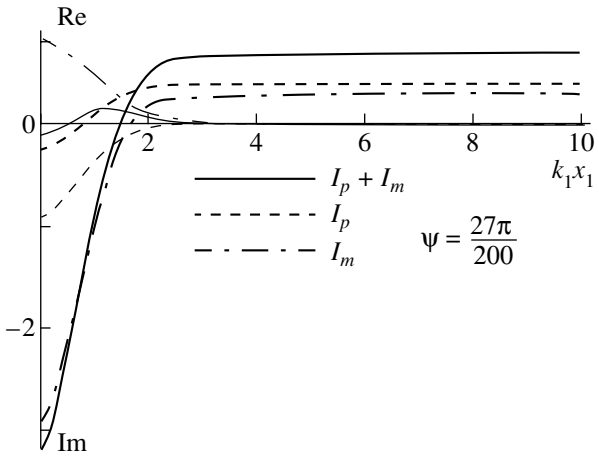

Fig. 8. Normalized impedances.

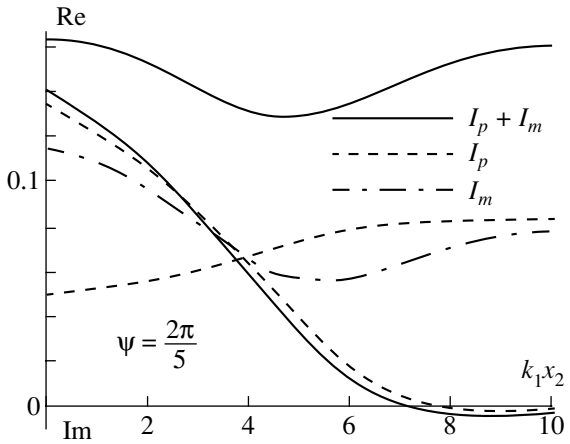

Fig. 9. Normalized impedances.

a function of ψ, this function will change its sign from positive to negative and back, at certain values to the left and to the right of the interval of critical angles, respectively. Between these values, the width of the opposite-energy-flow zone is finite, while between the critical angles it is this zone that dominates the radiation power integral.

Thus, we can state that the Rayleigh flexural waves in anisotropic media essentially and qualitatively differ from both Rayleigh compression-tension-shear waves [5, 6] and flexural waves in isotropic media.

ACKNOWLEDGMENTS

This work was partially supported by the INTAS, project no. 96-2306.

REFERENCES

1. Yu. K. Konenkov, Akust. Zh. **6**, 124 (1960) [Sov. Phys. Acoust. **6**, 122 (1960)].
2. Yu. I. Bobrovnitskiĭ, M. D. Genkin, V. P. Maslov, and A. V. Rimskiĭ-Korsakov, *Wave Propagation in Structures Made of Thin Rods and Plates* (Nauka, Moscow, 1974).
3. A. S. Zil'bergleĭt and I. B. Suslova, Akust. Zh. **29**, 186 (1983) [Sov. Phys. Acoust. **29**, 108 (1983)].
4. M. V. Belubekyan and I. A. Engibaryan, Izv. Ross. Akad. Nauk, Mekh. Tverd. Tela, No. 6, 139 (1996).
5. P. Chadwick and G. D. Smith, in *Advances in Applied Mechanics* (Academic, New York, 1977), Vol. 17, pp. 303–376.
6. S. A. Kaptsov and S. V. Kuznetsov, C. R. Acad. Sci. (Paris), Ser. IIb **327**, 1123 (1999).
7. S. G. Lekhnitskiĭ, *Anisotropic Plates* (Gostekhizdat, Moscow, 1957).

Translated by A. Kruglov

Acoustical Physics, Vol. 48, No. 2, 2002, pp. 176–179. Translated from Akusticheskiĭ Zhurnal, Vol. 48, No. 2, 2002, pp. 211–215.

Interference Immunity of a Focused Antenna

V. A. Zverev

Institute of Applied Physics, Russian Academy of Sciences, ul. Ul'yanova 46, Nizhni Novgorod, 603600 Russia
e-mail: zverev@hydro.appl.sci-nnov.ru

Received January 31, 2001

Abstract—The interference immunity of a focused antenna in the field of interference produced by discrete wideband sources is considered. It is shown that the focused antenna that processes the signal by the dark-field method provides a high interference immunity. Calculations show that this signal processing technique can provide acoustic monitoring in the presence of intense interference produced by ships. © *2002 MAIK "Nauka/Interperiodica".*

Interest in issues concerned with signal extraction in the presence of interferences persists (see, e.g., [1, 2]). These issues are topical in acoustics, because, in many applications, the interference is not a uniformly distributed noise, but exhibits a significant regularity. A classical example of such an interference is the noise produced by ships, which prevails at low frequencies (from 10 to 200–300 Hz) [3]. Such interferences can be rejected using long antennas with signal processing that is capable of eliminating or substantially suppressing the effect of noise produced by discrete sources. Among the methods that efficiently reject such interferences, adaptive methods [4] are most popular. However, in acoustic communications through a medium with a complex irregular structure, the efficiency of these methods diminishes [5, 6]. It should be noted that the requirements of regularity of the medium that provide the efficiency of the adaptive methods become much more stringent with an increase in the number of the antenna array elements and in the antenna length. Increasing the antenna aperture is useful and necessary for suppressing interferences produced by scattering from a rough water surface typical of acoustics.

The proven method referred to as the shadow or the dark-field method has long been known in optics [7]. This method is capable of rejecting (darkening) the interference sources in the presence of irregular aberrations produced by optical elements. A distinctive feature of this method is that, with an increase in lens aperture, it significantly relaxes the requirements imposed on the regularity of the wave field. A similar method can also be applied in acoustics [8]. As shown in [8], the acoustic dark-field method used for processing signals received by a sufficiently long (focused) antenna array basically differs from the signal processing in adaptive arrays. The dark-field method applied to the focused antenna is conceptually close to the cepstral analysis [9], which is widely used in acoustics.

A focused antenna operating with a monochromatic acoustic field has been considered in [8]. In this paper, we extend the dark-field method used with the focused antenna to the case of a wideband signal.

In solving this problem, we limit our consideration to the minimal number of sources—to just two sources, one of which is stronger than the other. We will show that, in this case, the coordinates and the intensity of the weaker source can be determined in the presence of the strong source, the only limiting factor being the distributed noise rather than the intensity of the strong source. The problem is solved by linear filtering. Therefore, if it can be solved in this simplified form, one can expect to succeed in the case of multiple sources. The supposition that there are only two sources does not present a fundamental limitation. It allows us to focus on the method and results, leaving the difficulties (mostly mathematical) associated with multiple sources to future analysis.

Let two sources (a strong source and a weak one) with a continuous spectrum be present. Let the sources be uncorrelated. This assumption is adopted only to make the problem definite. The problem is solved identically for uncorrelated and for correlated (completely or in part) sources. We emphasize that the adaptive methods use uncorrelated signals. The antenna consists of a number of hydrophones uniformly spaced a distance s apart in the horizontal direction. The antenna aperture is sufficient to be focused at all operating frequencies. These conditions are thoroughly studied in [8].

Let us determine the coordinates of the strong source with the help of the focused antenna. We assume that the signal produced by the strong source on the receiver antenna exceeds the signal produced by the weak source enough (in the numerical example, by 40 dB) for the radiation from the weak source to be neglected. The frequency spectrum of the spherical wave field produced by the wideband source and incident on the hydrophone number n of the linear antenna can be represented as

$$P(\omega, n) = G(\omega)\exp[i\omega T(n)]. \quad (1)$$

1063-7710/02/4802-0176$22.00

Here, $G(\omega)$ is the frequency spectrum of the field produced by the source, ω is the frequency, and $T(n)$ is the delay of the source signal incident on the hydrophone number n. If the wave is spherical and the source resides on the perpendicular erected to the antenna at its central element, we have

$$T(n) = \frac{s}{c}\sqrt{R^2 + (n-m)^2}, \quad (2)$$

where c is the light velocity, R is the distance to the source normalized by s, and m is the index of the central hydrophone.

The source coordinates can be found from the maximal response of the antenna, which occurs when the spherical wave front is compensated. This is a maximum of the following expression in the variables q and r:

$$U(q, r) = \int_\omega \left| \sum_n P(\omega, n) \exp[-i\omega M(q, r, n)] \right|^2 d\omega. \quad (3)$$

Here,

$$M(q, r) = \frac{s}{c}\sqrt{r^2 + (n-q)^2}. \quad (4)$$

Expression (3) reaches its maximum when the spherical wave front is compensated completely. This occurs when $r = R$ and $q = m$ in formula (4), which yields the source coordinates.

The above search procedure was simulated using the following parameters. The antenna consisted of 256 hydrophones. Both sources emitted uncorrelated Gaussian random signals with realizations being 32 elements long. In accordance with results obtained in [10, 11], the spectrum of the emitted signals was supplemented with zeroes to extend the length of the realization by a factor of eight. This operation was necessary, because, in numerical calculations, the delay given by Eqs. (2) and (4) can take only discrete values. A.A. Pavlenko showed that the additional zeroes in the spectrum significantly reduce the effect of delay quantization errors. The distance was $R = 128$ (half-length of the antenna), and $m = 128$.

The surface determined by Eq. (3) is illustrated in Fig. 1 by a function of r and q. This surface can be used to find the curvature of the incident wave front. Unfortunately, this processing procedure does not comply with the dark-field method. The radiation from the source can be screened in its most intense part, but this action will not extract the field of the weaker source, because Eq. (3) involves an irreversible operation (summation over frequencies).

To apply the dark-field method, we should eliminate the summation over frequencies, which makes Eq. (3) irreversible.

We write the spectrum of the stronger signal [let this be $P1(\omega, n)$] using Eq. (1) at $R = 256$ (the antenna length). The spectrum of the second signal should be written so as to take into account its shift by the angle ϑ from the normal to the antenna:

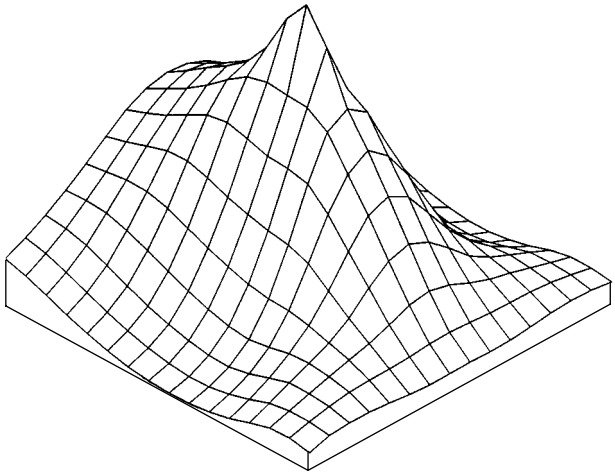

Fig. 1. Fragment of the field of view of the focused antenna. The axes represent the direction towards the source and the distance to it. The vertical axis represents the sum of intensities of the received signal over all frequencies of the antenna frequency range.

$$P2(\omega, n) = G2(\omega)\exp\{i\omega[T2(n) + hn]\}, \quad (5)$$

where $T2(n)$ is given by Eq. (2) at $R2 = 64$ and $h = \frac{s}{c}\sin(\vartheta)$. The spectrum of the signal at the hydrophones will be

$$PC(\omega, n) = P1(\omega, n) + 10^{-2}P2(\omega, n). \quad (6)$$

First of all, let us compensate the front curvature of the stronger wave. The parameters of this wave are obtained by the signal processing described above. To compensate the front curvature of the stronger wave, one should apply the following operation

$$W(\omega, n) = PC(\omega, n)\exp[-i\omega T1(n)]. \quad (7)$$

Then we should obtain the spatial spectrum of the signal at the antenna for each frequency ω by applying the Fourier transform to Eq. (7) with respect to n. Let us denote the spatial frequency corresponding to the variable n as ν. To visualize this spatial spectrum, we integrate its squared magnitude with respect to the frequency ω:

$$S(\nu) = \int_\omega |\Phi_n[W(\omega, n)]|^2 d\omega. \quad (8)$$

Here, $\Phi_x[Z(x)]$ means the Fourier transform of the function $Z(x)$ with respect to x.

The function $S(\nu)$ defined by Eq. (8) is illustrated in Fig. 2a. Both signals are seen in the figure: the strong one as a discrete spectral line and the weak one as a blurred curve, because the curvature of the weak sig-

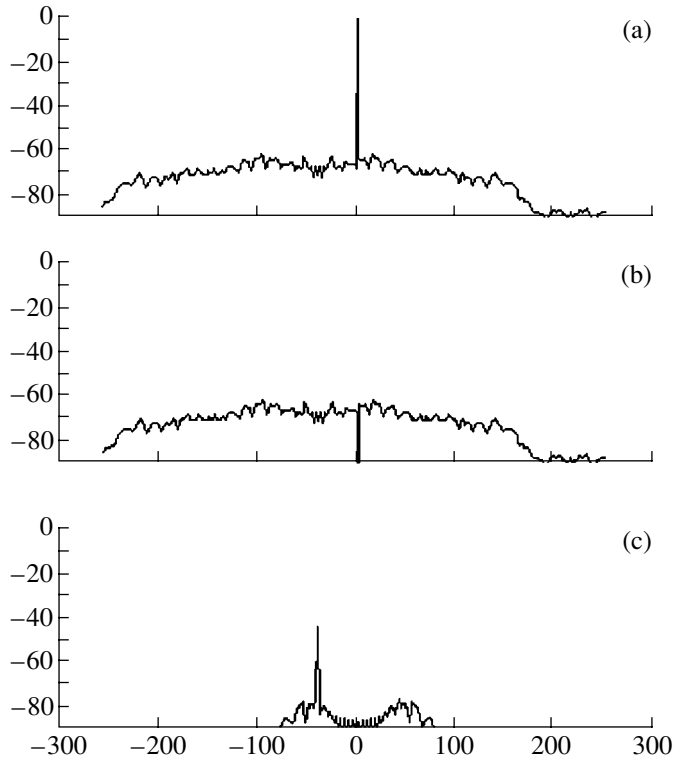

Fig. 2. The intensity integrated over all signal frequencies in decibels with respect to the maximum of the focused signal of the strong source versus the angle of arrival of the incident wave normalized by the antenna resolution. The antenna is focused at the strong source, and the source signal is (a) not darkened and (b) darkened. Figure 2c refers to the antenna focused at the weak source with the strong source darkened.

nal's front is greater, which considerably broadens its spatial spectrum.

To implement the dark-field method, one must block the domain (reduce the signal in it to zero) occupied by the spatial spectrum of the strong signal shown in Fig. 2a. This should be done necessarily and exclusively for the function $\Phi_n[W(\omega, n)]$ rather than for $S(\nu)$. After that, we integrate the result with respect to the frequency ω as in Eq. (8) to obtain the function shown in Fig. 2b.

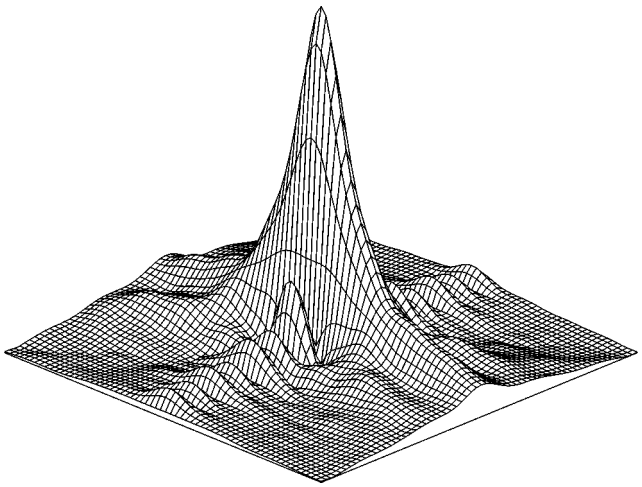

Fig. 3. Fragment of the field of view of the focused antenna near the weak source with the strong source darkened. The axes are labeled as in Fig. 1.

Now, only the weak signal is present. To find its parameters, it is necessary to compensate the curvature of its wave front. To this end, we go over from the spectrum to the signal by applying the inverse Fourier transform with respect to frequency ν and multiply the result by the factor

$$E(\omega, n) = \exp[i\omega T1(n)]\exp[-i\omega M(q, r)]. \quad (9)$$

The first exponential here is necessary for compensating the factor in the weak signal that removes the wave front curvature of the strong signal. The second exponential serves for removing the curvature of the wave front of the weak signal by choosing the appropriate q and r. The result of this procedure is shown in Fig. 2c. The process of fitting the parameters for removing the curvature of the small-signal wave front is illustrated in Fig. 3.

The effect of the dark-field method is clearly seen in Fig. 4. The field of the strong source is not darkened (the spatial spectrum in the corresponding domain is multiplied by unity rather than by zero). As a result, the field of the strong source covers the field of the weak source completely, although the antenna is focused at

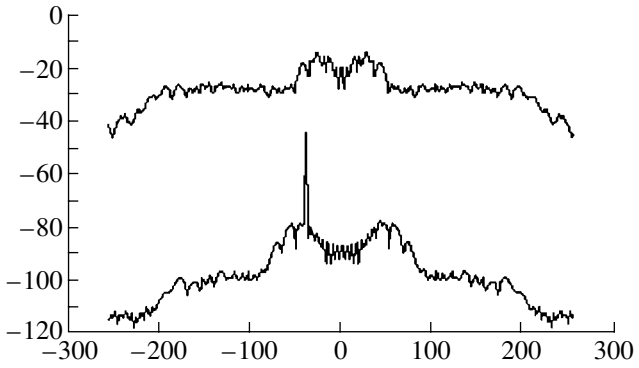

Fig. 4. Field of view of the antenna focused at the weak source with the field produced by the strong source not darkened (the upper curve) and darkened (the lower curve). The axes are labeled as in Fig. 2.

the weak source rather than at the strong one. The lower part of Fig. 4 shows the result when the field of the strong source is darkened. The difference in the residual background levels is almost 70 dB, which illustrates the interference immunity of the focused antenna in this example.

Basically, such a processing is applicable to the case of multiple sources. The number of sources that can effectively be darkened is determined by the number of array elements. The point is that the darkening of each element reduces the number of antenna elements.

In the above calculations, it is important that the antenna is ideal. Both the spread in the positions of individual antenna elements and the random variations of the amplitude and phase of the field incident on them are ignored. If the fact that the antenna is not ideal is taken into account, the result will change. The corresponding study requires additional calculations and, perhaps, experiments.

Here, we only note that the above method for processing the signals received by a focused antenna can give a similar interference immunity in the presence of multipath propagation and when the parameters of the antenna and the fluctuating medium are spread randomly. In the presence of multipath propagation, a long focused antenna may resolve or not resolve the virtual sources that appear in this case. If the antenna does not resolve such sources, its interference immunity remains the same as in a homogeneous unbounded space. If the antenna resolves these sources, they can be eliminated exactly as the real sources. This possibility has been demonstrated in [8], where it was shown that the effect of dispersion due to the propagation of sound in a waveguide can be compensated by increasing the darkened area of the focused antenna. The two most promising results were obtained in [11]. The first consists in the consideration of the dark-field method that works in the presence of high phase distortions in the antenna. The second consists in that it was demonstrated how to determine the phase distortions in the antenna from the field of the strong source alone in order to compensate them in the same way as the wave front curvature.

ACKNOWLEDGMENTS

I am grateful to the reviewer for comments which, being taken into account, improved the paper.

This work was supported by the Russian Foundation for Basic Research, project nos. 00-15-96741 and 99-02-164010.

REFERENCES

1. P. K. Willet, P. E. Swaszek, and R. S. Blum, IEEE Trans. Signal Process. **48** (12), 3266 (2000).
2. Z. Kang, C. Chatterjee, and V. P. Roychowdhary, IEEE Trans. Signal Process. **48** (12), 3328 (2000).
3. R. J. Urick, *Principles of Underwater Sound* (McGraw-Hill, New York, 1975; Sudostroenie, Leningrad, 1978).
4. R. A. Monzingo and T. W. Miller, *Introduction to Adaptive Arrays* (Wiley, New York, 1980; Radio i Svyaz', Moscow, 1986).
5. V. A. Zverev, Akust. Zh. **40**, 401 (1994) [Acoust. Phys. **40**, 360 (1994)].
6. A. B. Gershman, V. I. Turchin, and V. A. Zverev, IEEE Trans. Signal Process. **43** (10), 2249 (1995).
7. L. A. Vasil'ev, *Schlieren Methods* (Nauka, Moscow, 1968; Israel Program for Scientific Translations, Jerusalem, 1971).
8. V. A. Zverev, A. L. Matveev, M. M. Slavinskiĭ, and A. A. Stromkov, Akust. Zh. **43**, 501 (1997) [Acoust. Phys. **43**, 429 (1997)].
9. A. V. Oppenheim, R. W. Schafer, and T. G. Stockham, IEEE Trans. Audio Electroacoust. **16** (3), 437 (1968).
10. V. A. Zverev, A. A. Pavlenko, A. D. Sokolov, and G. A. Sharonov, Akust. Zh. **47**, 76 (2001) [Acoust. Phys. **47**, 62 (2001)].
11. V. A. Zverev and A. A. Pavlenko, Akust. Zh. **47**, 355 (2001) [Acoust. Phys. **47**, 297 (2001)].

Translated by A. Khzmalyan

Acoustical Physics, Vol. 48, No. 2, 2002, pp. 180–186. Translated from Akusticheskiĭ Zhurnal, Vol. 48, No. 2, 2002, pp. 216–223.

Application of a Noise Signal in Acoustic Tomography of the Arctic Basin

V. M. Kudryashov

Andreev Acoustics Institute, Russian Academy of Sciences, ul. Shvernika 4, Moscow, 117036 Russia

e-mail: bvp@akin.ru

Received April 4, 2001

Abstract—The time correlation function of a noise signal propagating in an arctic-type waveguide is considered. For a coherent signal, the time cross-correlation function is formed with the use of either the total signal, or a single selected mode, or a reference signal at one of the correlator inputs. The use of narrow-band signals is shown to be preferable, because the waveguide dispersion affects the waveguide response. It is demonstrated that, for tomographic investigations in a waveguide irregular along the path, it is expedient to correlate the signals received at two different points that are selected on the path so as to enclose the waveguide part the variability of whose parameters is the object of interest. *© 2002 MAIK "Nauka/Interperiodica".*

Acoustic tomography is determined as the method of reconstructing the local characteristics of an object from a set of its integral characteristics (projections) by subjecting them to special processing [1]. In a wider sense, tomography can be interpreted as a method for obtaining the information on the internal structure of the object of interest from the characteristics of the probing signal (see [1], p. 7). For example, in an inhomogeneous medium, one has to estimate the variation of the sound velocity profile within a part of the path. In this paper, the problem of determining the variations of the waveguide parameters from the characteristics of the received signal, i.e., the inverse problem, is not considered. This study is limited to a direct problem: we show that these variations can be revealed by the time correlation functions of a noise signal. In the cited publication [1], the authors consider deterministic signals including harmonic and pulsed ones. Below, we consider an acoustic signal formed by a noise source, which, within the observed realization, possesses statistically stationary and ergodic properties as a function of time.

The sound pressure produced by a narrow-band point source in a waveguide can be represented in terms of a mode expansion [2, 3]:

$$p(\mathbf{r}, z, t) = w\sqrt{\Delta f}\sum_m p_m(\mathbf{r})\Phi_m(z)F(t-t_m)\exp(-i\omega_0 t). \quad (1)$$

Here, the constant w is expressed in μPa and corresponds to a frequency band of 1 Hz: $20\log w = W$, where W characterizes the source power in decibels in a frequency band of 1 Hz at a distance of 1 m from the source; Δf is the frequency band of the signal. The summation over m is performed over all modes of the discrete spectrum [4]. The waves of the continuous spectrum (the continuum) are taken into account in the sound scattering from the bottom as a component (along the horizontal coordinate **r**) of the mode attenuation (damping). These waves affect the imaginary part of the longitudinal wave number $\varsigma_m(\mathbf{r})$ of a mode when the waveguide is irregular in **r**. We call a waveguide a plane-layered one, if its deterministic parameters do not depend on **r**. The function $\Phi_m(z)$ is the eigenfunction of the waveguide [2–5]. The z axis is directed downward, and the value $z = 0$ corresponds to the mean level of free water. The eigenfunctions are orthonormalized by the condition

$$\{\Phi_m(z)\Phi_n(z)\} = \begin{cases} 1 & \text{for } n = m \\ 0 & \text{for } n \neq m. \end{cases} \quad (2)$$

The braces denote the orthonormalization operation whose form depends on the parameters of the boundaries. In a liquid medium, this operation is reduced to an integral of the product of eigenfunctions with the weighting function $\rho(z)$, which is the density of the liquid, with respect to z. The integration is performed over the whole liquid column [4, 5].

In the narrow-band approximation, within the signal frequency band, no considerable variations occur in the eigenfunctions of the waveguide and in the group velocities v_m of modes determined by the relationship

$$v_m^{-1} = \left.\frac{\partial \varsigma_m}{\partial \omega}\right|_{\omega = \omega_0},$$

where $\omega = 2\pi f$, f is the frequency of sound, $\omega_0 = 2\pi f_0$, and f_0 is the central frequency of the signal in hertz.

1063-7710/02/4802-0180$22.00

The function $p_m(\mathbf{r})$ characterizes the spatial variability (in the distance $\mathbf{r}$) of the sound field. For a coherent field in a plane-layered waveguide, we have

$$p_m(\mathbf{r}) = i\pi\Phi_m(z_0)H_0^{(1)}(\varsigma_m r), \tag{3}$$

where z_0 is the depth of the sound source. Similarly, the quantity $p_m(\mathbf{r})$ is calculated for the central frequency in the case of a narrow-band signal.

Thus, we calculate the quantities $p_m(\mathbf{r})$, $\Phi_m(z)$, and ς_m by the program for calculating the harmonic sound field at the frequency f_0. Expression (1) describes a coherent field, if a stochastic scattering occurs in the waveguide along the sound propagation paths. If the waveguide parameters wary regularly with $\mathbf{r}$, i.e., the variability can be described by deterministic functions of $\mathbf{r}$, the quantity $p_m(\mathbf{r})$ can be calculated either in the adiabatic approximation [3, 4] neglecting the regular scattering or in the approximation taking into account the regular scattering (transformation) of modes [6–8]. The regular scattering is related to the variations of the eigenfunctions with $\mathbf{r}$, which results in the violation of the orthogonality condition for different-number modes calculated for different $\mathbf{r}$:

$$\{\Phi_m(z)|_{\mathbf{r}=\mathbf{r}_1}\Phi_n(z)|_{\mathbf{r}=\mathbf{r}_1+\Delta r}\} \neq 0 \quad \text{for } n \neq m.$$

In both approximations, the calculations are based on the Pierce scheme known as the vertical-mode and horizontal-ray approximation [1, 3, 4]. The sound field of a mode is calculated along the mode ray described in the horizontal plane by an eikonal-type equation whose right-hand side contains the longitudinal wave number of the mode instead of the wave number in water. The calculation of the mode rays can be performed by the well proven programs for a two-dimensional waveguide. The coefficients $p_m(\mathbf{r})$ are calculated along the mode rays by using a transport equation or another scheme, e.g., of the type used in [6, 7]. In these calculations, at each step along the distance, one has to take into account the mutual transformations of modes of the discrete spectrum.

In Eq. (1), t is time and t_m is the propagation time of the mth mode between the transmission and reception points spaced at a distance r. In a plane-layered waveguide, $t_m = r/v_m$. In the adiabatic approximation, $t_m = \int_0^r d\eta/v(\eta)$. In the regular scattering approximation, the calculation is more complicated, because new modes can be formed in the course of the propagation. In addition, $p_m(r)$ can be affected by the contributions made by other modes because of the scattering.

The noise character of the signal is determined by a random homogeneous ergodic function of time $F(t)$. We assume that $\overline{F(t)F(t-\tau)} = B(\tau)$, where $B(0) = 1$ and the overbar denotes averaging over time. Therefore, we have $\overline{p(\mathbf{r}, z)} = 0$. The time correlation function of the sound pressure is nonzero. This deterministic quantity corresponds to the second statistical moment [7].

The time cross-correlation function is determined by the expression

$$K_c(\mathbf{r}_1, \mathbf{r}_2, z_1, z_2; \tau) = \overline{p(\mathbf{r}_1, z_1, t)p^*(\mathbf{r}_2, z_2, t-\tau)}.$$

Substituting Eq. (1) in this expression, we obtain

$$K_c(\mathbf{r}_1, \mathbf{r}_2, z_1, z_2; \tau) = w^2\Delta f\sum_m\sum_n p_m(\mathbf{r}_1)p_m(\mathbf{r}_2) \times \Phi_m(z_1)\Phi_n(z_2)B(\tau - t_m + t_n)\exp(-i\omega_0\tau). \tag{4}$$

We assume that, at the point of observation, the signal is received by a vertical array with the sensitivity of its elements being determined according to the vertical variability of the Nth eigenfunction. Then, the Nth mode can be singled out of the sound field. For this purpose, we multiply Eq. (4) by $\Phi_N(z_2)$ and integrate the result with respect to z_2, at least over the layer of the concentration of the Nth mode. Applying the condition of orthogonality of modes, we obtain

$$K_N(\mathbf{r}_1, \mathbf{r}_2, z_1; \tau) = w^2\Delta f\, p_N^*(\mathbf{r}_2)\sum_m p_m(\mathbf{r}_1) \times \Phi_m(z_1)B(\tau - t_m + t_n)\exp(-i\omega_0\tau). \tag{5}$$

This expression is analogous in its structure to the pulsed waveguide response in which the role of the envelope of the transmitted signal is played by $B(\tau)$ and the time t is replaced by the delay τ. A similar result can be obtained when the Nth mode is separated in its arrival time t_N from the modes with $m \neq n$. Manipulating the delay at one of the correlator inputs, we can obtain a pulsed-response-type expression.

A widely used method [9, 10] is based on the correlation of the received signal with the reference one $F(t-\tau)\exp[i\omega_0(t-\tau)]$. Then, we obtain the expression

$$P_c(\mathbf{r}, z, \tau) = w\sqrt{\Delta f}\sum_m p_m(\mathbf{r})\Phi_m(z)B(\tau - t_m)\exp(-i\omega_0\tau). \tag{6}$$

This formula is analogous to the expression for the pulsed waveguide response in which the role of the pressure pulse is played by $P_c(\mathbf{r}, z, \tau)$. The advantage over the pulsed waveguide response caused by a pulsed signal is that one can obtain an analog of the pulse at the point of observation when the signal has a low power near the source. The required energy is accumulated because of the use of a signal of long duration. This way, one obtains a high signal-to-noise ratio due to the effect of a quasi-coherent accumulation. The disadvantage of this approach is its high sensitivity to the effects related to the movements of the transmission and reception points and to the variations of the waveguide parameters with time. An example is the Doppler effect, which less strongly affects the correlation function of

the type given by Eq. (5), if it produces approximately equal effects on all modes forming the pulsed response.

Expressions (4)–(6) correspond to a coherent field, i.e., a field averaged over an ensemble of realizations of stochastic scatterers. In calculating the variance of the sound pressure of the total field, we use the transport equation in the approximation of a multiple forward scattering and a single backward scattering [11, 12]. If the parameters of the waveguide vary regularly with **r** while the scale of these variations is (as usual) much greater than the horizontal correlation radii of stochastic scatterers, the calculation of the mean intensity of the total field is performed in the same way as the calculation for a plane-layered (on the average over an ensemble of scatterers) waveguide, but with allowance for the regular variability. If, in a plane-layered (on the average) waveguide, the mode transformation coefficients [7, 11–13] determined by the stochastic scattering are independent of **r**, then, in an irregular waveguide, one has to solve the differential transport equation with allowance for the variations of the average (over the ensemble of the scatterer realizations) mode transformation coefficients.

The expressions presented above for the time correlation functions describe these functions in the complex form. To adjust them to the real experiment, it is necessary to separate their real part, which, as a function of the delay τ, can be reduced to the form $A(\tau)\cos(w_0\tau)$. The information is carried by the envelope of the correlation function $A(\tau)$. Its structure depends on the form of the function $B(\tau)$, and the latter depends on the energy spectrum of the transmitted signal, as well as on the characteristics of the receiving filter and, especially on the frequency band Δf of the signal transmitted through the filter. In particular, the time correlation scale τ_0 of the function $B(\tau)$ is proportional to $1/\Delta f$. Hence, by increasing Δf, we reduce τ_0 and, as a result, obtain a narrower (in the delay) peak of the envelope of the time correlation function corresponding to a specific mode.

The peak of the envelope of the mth mode corresponds to the point $\tau = t_m$ on the delay axis. Since t_m is different for different modes, the received pulse is spread. For the water modes propagating in an arctic waveguide whose axis is adjacent to the ice cover, the minimal group velocity is characteristic of the modes that are captured by the near-ice layer lying between the ice cover and the Atlantic water layer. The thickness of the near-ice layer varies from 250 to 450 m with increasing distance from the Fram strait toward the coast of Canada. This is explained by the fact that the warm Atlantic waters arriving from the northern Atlantic become spread as they move further in the eastern direction. In the Atlantic waters, the sound velocity gradient is close to zero, whereas in the near-ice layer, the gradient of $c(z)$ is maximal, its average value being equal to 5–6 hydrostatic gradients. Under the Atlantic water layer, at depths greater than 750–10000 m, the arctic water layer is observed with the vertical sound velocity gradient close to the hydrostatic one. The waves refracted within this layer (the refraction is positive) have the maximal group velocities and, hence, the minimal propagation times t_m. These waves form the leading edge of the acoustic pulse. The waves captured by the near-ice channel are the last to arrive. Figure 1a shows the profile $c(z)$ for the central region of the Arctic basin. At a frequency of 20.1 Hz, for the free water surface, the group velocities of the first three modes are equal to 1439.168, 1451.375, and 1455.384 m/s. Let us consider an ice cover 65% of which is smooth ice and the rest is hummocky ice. The longitudinal wave velocity c_l in ice is $3500(1 - i0.004)$ m/s, the shear wave velocity is $c_t = 1800(1 - i0.04)$ m/s, and the ice density is 0.91 g/cm^3. According to the histogram of the lower surface of ice, the thickness of smooth ice is $h_1 = 2.6$ m, the square root of the variance of the ice draught is $\sigma_1 = 1.8$ m, and at the upper surface of the smooth ice, $\tilde{\sigma}_1 = 0.4$ m. For hummocky ice, we have $h_2 = 6.6$ m and $\sigma_2 = 3.3$ m. The horizontal correlation scales of roughness are 120 and 44 m for smooth and hummocky ice, respectively.

The coefficients of sound reflection from the ice cover were studied in [14, 15].

In the presence of the ice cover, the group velocities of the first three water modes are 1439.112, 1450.51, and 1455.211 m/s. From the comparison of these values with the corresponding values for a free water surface, one can see that the ice cover has almost no effect on the group velocities of normal waves.

The ice cover affects the attenuation coefficients of normal waves. For an acoustically soft boundary, at a frequency of 21 Hz, the attenuation coefficients of the first three water modes are equal to 0.000055 dB/km. This value is determined by the sound absorption in water. In the presence of the ice cover, we obtain 0.01801, 0.00735, and 0.00503 dB/km. The calculations were performed as in the previous publications [14, 15]. The maximal spatial attenuation is observed for the lowest-order modes. The first mode is captured by the near-ice channel and has its maximum at a depth of 160 m, although this mode partially penetrates the Atlantic water layer.

Within the narrow-band approximation, a broadening of the signal bandwidth Δf narrows the pulse peak of a mode. One would expect that the greater Δf, the easier the identification of modes separated by a delay time exceeding τ_0. However, this tendency is limited by the waveguide dispersion of modes, which leads to changes in t_m, $\Phi_m(z)$, and $p_m(\mathbf{r})$. For example, if t_m varies by more than $1/\Delta f$, the mode peak is destroyed becoming broader, and the form of the envelope of the time correlation function changes. The waveguide dispersion depends on the waveguide parameters.

To switch to the broadband approximation, we use the scheme described in [16]. We assume that, in the

frequency band Δf, the energy spectrum of the signal is described by the function $G(\omega)$ normalized so as to satisfy the condition

$$\int_{\omega_0 - \Delta\omega/2}^{\omega_0 + \Delta\omega/2} G(\omega) = 1,$$

where $\Delta\omega = 2\pi\Delta f$. We divide the frequency band Δf into intervals Δf_j:

$$\sum_{j=1}^{J} \Delta f_j = \Delta f.$$

We assume that, in the frequency band Δf_j, the signal is a narrow-band one with f_{0j} being the central frequency of the jth component; $\omega_{0j} = 2\pi f_{0j}$. We calculate the partial time correlation functions for each of the components in the frequency band Δf_j and combine them with allowance for the phases and with the weighting factors $G(\omega_{0j})$. As shown in [16], a broadband correlation function is characterized by changes in both its envelope and carrier, and the latter may not coincide with $\cos(\omega_0\tau)$.

Let us consider an example demonstrating the effect of the waveguide dispersion on the signal form. We assume that the sound velocity profile and the parameters of the bottom and the ice cover do not vary along the waveguide. The sound velocity profile is presented in Fig. 1a. The waveguide depth (corresponding to the water–ground boundary) is 3000 m. The bottom is modeled by a homogeneous elastic halfspace characterized by the longitudinal wave velocity $c_l = 1850(1 - i0.01)$ m/s, the shear wave velocity $c_t = 350(1 - i0.01)$ m/s, and density equal to 2 g/cm^3. According to the histogram obtained for the central Arctic region to the west of the Lomonosov ridge, 65% of the ice cover is smooth ice with an average thickness $h_1 = 2.6$ m, the average drought (the square root of the roughness variance) $\sigma_1 = 1.8$ m, and the average height of roughness at the upper boundary $\sigma_1/4.5$. For the hummocky part of the ice cover, the parameters are $h_2 = 6.6$ m and $\sigma_2 = 3.3$ m. The ratio of the hummock height to its drought in water is 1/4. The density of ice is 0.91 g/cm^3, and the wave velocities are $c_l = 3500(1 - i0.04)$ m/s and $c_t = 1800(1 - i0.04)$ m/s.

We consider the envelope of the pulsed response of the waveguide $P_c(\mathbf{r}, z, \tau)$ for $z = z_0 = 60$ m and $W = 100$ dB/Hz. The distance between the transmission and reception points is 900 km. The mean frequency of sound is $f_0 = 21$ Hz, and the signal bandwidth (resultant of the transmitted signal and the receiving filter) is 7.5 Hz.

The result of the calculation in the narrow-band approximation is shown in Fig. 2. Figure 3 presents the result obtained in the broadband approximation. In Fig. 2, one can notice the angular dispersion, i.e., the

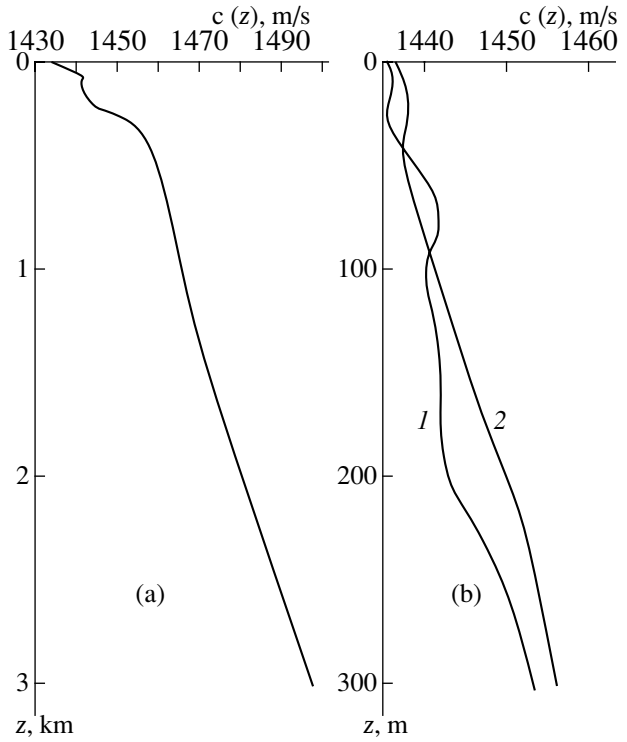

Fig. 1. Sound velocity profiles c(z).

mode dispersion. The higher-order water modes are the first to arrive. The contribution of the bottom-reflected waves is insignificant due to the high attenuation caused by the bottom reflection. The first water mode arrives last. In the narrow-band approximation, the width of each pulse corresponding to an individual mode is proportional to $1/\Delta f$. In the broadband approx-

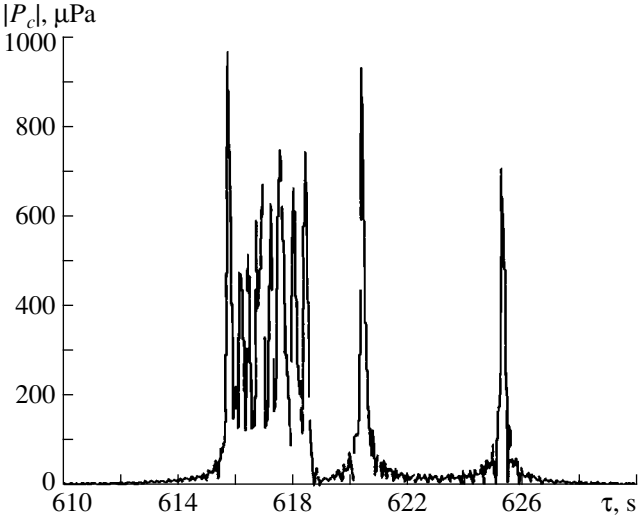

Fig. 2. Calculated envelope of the time correlation function $P_c(\mathbf{r}, z, \tau)$ in the narrow-band approximation for $f_0 = 21$ Hz, $\Delta f = 7.5$ Hz, $r = 900$ km, $z = z_0 = 60$ m, and $W = 100$ dB/Hz.

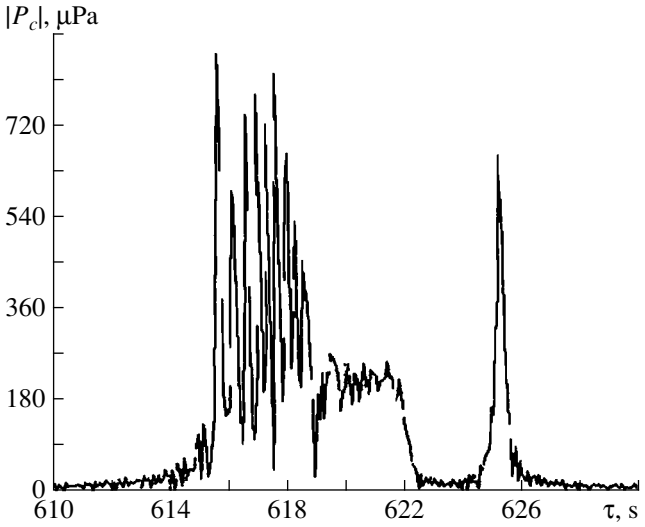

Fig. 3. Calculation for the same waveguide parameters as in Fig. 1 in the broadband approximation.

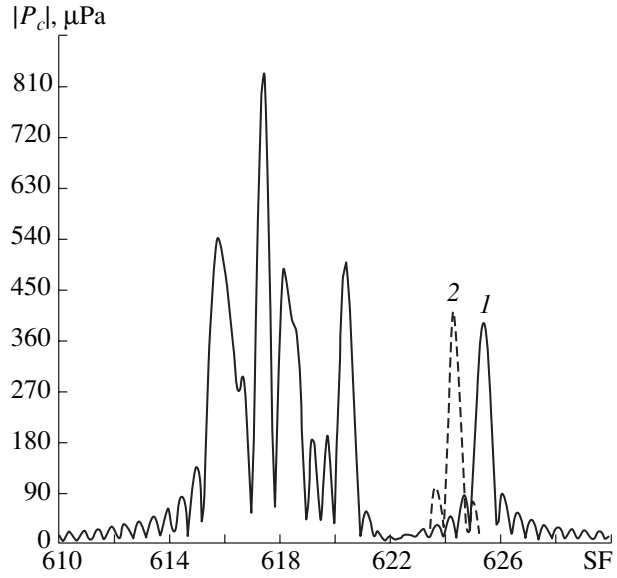

Fig. 4. (*1*) Same as in Fig. 2, but for Δf = 2 Hz; (*2*) the dashed curve corresponds to a 1.5 km shorter distance.

imation, the time of the mode propagation within the signal bandwidth varies considerably. This effect is most pronounced for the second water mode, which is transformed from a narrow pulse to a pulse spread in the arrival time. For the first water mode, the waveguide dispersion proves to be much weaker, although this mode exhibits a broadening of the peak of its envelope. However, the position of the top of this peak is the same in both approximations. When the signal bandwidth is Δf = 2 Hz, the signal remains narrow-band within the whole 900-km-long propagation path. The corresponding plot is shown in Fig. 4. It is similar to the plot presented in Fig. 2 with some deviations in the amplitudes and widths of the peaks.

In Fig. 4, peak *1* corresponds to the arrival of the first water mode at a distance of 900 km, and peak *2* corresponds to the arrival of the same mode at a 1.5 km shorter distance. The delay between these two peaks is approximately equal to 1 s, which should be expected taking into account the sound velocity in water. The supplement to the plot of the envelope of the signal correlation function is made for the following reasons. The expressions presented above for the time correlation functions imply the averaging over an infinite realization. In reality, the time interval T, over which the averaging is performed, is finite due to both technical factors and time variations of the waveguide parameters, which lead to the violation of the statistical stationary state and ergodicity of the noise signal. In addition, the spatial positions of the transmitter and the receiver can vary because of the drift of the ice fields to which the transmitter and the receiver are attached. It is possible that the transmitter and the receiver are objects independently moving in water. The motion of the objects leads to changes in the form of the correlation function, i.e., a deterministic quantity, which is used in solving the problems of monitoring where even the roll of the transmitting and receiving systems can deteriorate the measurement results. The finiteness of the averaging interval T leads to the appearance of a fluctuation component with a variance proportional to $(\Delta f T)^{-1}$ at the correlator output. The fluctuation component masks the deterministic component and imposes a limitation on the measurement accuracy and on the very possibility of detecting the deterministic component. Hence, the stability of the parameters of the experiment in time is of fundamental importance.

The above consideration may have another application. Let us assume that the transmitter–receiver distance is unknown, but the direction of the signal arrival is known. For example, the signal is received by a horizontal array or a set of receivers, which can be used to form a receiving system with spatial selectivity. By placing a test hydrophone at a known distance from the receiving system in the direction from which the signal arrives, or introducing simple geometric corrections, we determine the time delay between the signal arrivals at the receiver and at the test hydrophone. Knowing this delay and the delays in the signal propagation times to the points of observation from the transmitter, through simple calculations we determine the distance between the transmitting and receiving systems. In our case, the distance is about 900 km (which can be easily verified). More precisely, the calculation yields approximately 930 km with allowance for the accuracy of the determination of the peak positions on the delay axis. The position of a peak can be determined with higher accuracy, if the peak is made sharper by using, e.g., receiving filters whose frequency characteristic provides sharper peaks.

The problem of determining the distance becomes more complicated when the waveguide parameters vary along the sound propagation path, as well as in the presence of an additive noise caused by the medium and a multiplicative noise caused by the stochastic scattering of sound. In the case under consideration, the latter can be neglected, so that the signal is a coherent one.

As the second example, we consider a path that is irregular in the distance **r**. The parameters of the path are taken from the experiment carried out by researchers from the Acoustics Institute in the 1980s [17]. The path contains a shallow-water part whose parameters correspond to the Franz–Victoria trough. The length of the shallow-water part is 5 km. The slope of the bottom extends to a distance of 110 km where the depth reaches a value of 3 km. At distances from 110 to 200 km, a deep-water region was observed in the experiment. In the calculations, we assume that this region extends to a distance of 900 km in the direction of the general decline of the waveguide depth. In the deep-water region, the sound velocity profile c(*z*) corresponds to curve *2* in Fig. 1b. In the shallow-water region, the sound velocity takes the values 1440, 1450.2, 1451.4, and 1444.5 m/s at the depths 0, 50, 140, 170, and 400 m, respectively. Recall that the initial, i.e., zero, depth in the profiles c(*z*) corresponds to the free water level, although the water layer begins below the ice cover, and this fact is taken into account in the calculations by recalculating the sound velocity profile according to the position of the ice–water boundary. To describe the variation of the sound velocity profile from shallow-water to deep-water one within the irregular region, we use linear interpolation. The parameters of ice in the deep-water region are the same as in the preceding example. In the shallow-water region, the ice cover is smooth everywhere. Its thickness is 1 m, the average drought is $\sigma = 0.6$ m, and the correlation scale of the ice roughness is 40 m. The ground is considered as an elastic halfspace with $c_l = 1800(1 - i0.005)$ m/s and $c_t = 350(1 - i0.005)$ m/s. The ground density is 2 g/cm^3. These parameters approximately correspond to the shallow-water region and the initial part of the slope at low frequencies. We use the same parameters for the ground in the deep-water region, because, at a distance of 900 km, the contribution of the bottom reflections is insignificant, if the waves reflected from the bottom in the regular deep-water region of the waveguide are considered.

The source of sound generates a noise signal with the central frequency $f_0 = 21$ Hz and is observed in the frequency band $\Delta f = 2$ Hz. The transmission depth is 40 m, and the reception depth is 50 m.

The study of the sound propagation along a path that contains deep-water and shallow-water regions is not only of scientific interest, but also of practical value. Large and heavy transmitting and receiving systems intended for long-term operation are rather installed in shallow-water regions for technical reasons. In a coastal zone, such systems can be cable-connected with stationary coastal stations.

As for the observations (e.g., climate monitoring), they should be performed in the deep-water regions of the arctic ocean, because these regions are characterized by a relative stability of the water column parameters in depth. The coastal part of the slope and the shallow-water regions are characterized by unstable acoustic parameters of the water column because of such phenomena as tides, seasonal variability, and currents. The variations of the sound velocity profile that occur in the deep-water regions due to the variations of the salinity and temperature of the water layers are relatively small. Hence, the variations caused by these phenomena in the mode propagation times are also small. Therefore, the perturbations introduced by the shallow-water parts of the path can cause considerable variations of the pulse structure of the signal. For example, we note the following factor. In shallow-water regions at high frequencies, the group velocities of modes usually decrease with increasing mode number. In deep-water regions, the situation is reversed. As a result, the differences in the mode propagation times t_m can vanish [10]. As the zero time of the mode propagation over an irregular path, it is convenient to take the instant of the mode transition from a surface–bottom mode to the stage of its separation from the bottom reflection, i.e., to a water mode. For example, on the path under study, the first water mode, which is concentrated in a narrow layer near the sound channel axis, at low frequencies (20 Hz and higher) becomes separated from the bottom and passes to the adiabatic stage (for the coherent component of the sound pressure) starting approximately from a distance of 10 km and beyond, when the sound source is positioned in the shallow-water region. In the experiment on the time monitoring of this mode, it is expedient to construct the time correlation function by formula (5), where $N = 2$ (the first mode at frequencies of several tens of hertz is the flexural wave of the ice cover, which rapidly attenuates with increasing distance r); thus, $N = 2$ corresponds to the first water mode.

Figure 5 presents the envelope of the time correlation function (5) as a function of the delay for an irregular path on the condition that the total coherent noise signal received at a distance of 900 km correlates with the first water mode of the same signal received at a distance of 10 km. The envelope is similar in its shape to the pulse transmitted through a distance of 890 km. The higher-order modes arrive first, forming a kind of a single pulse. Then the pulse corresponding to the first water mode arrives; this mode is the only one captured by the near-ice water layer at a frequency of 21 Hz.

At the given transmitter and receiver depths, the first water mode prevails in the signal received at a distance of 10 km. Therefore, if we construct a time correlation function for the same conditions, but by formula (4), for $r_2 = 10$ km and $r_1 = 900$ km, the envelope of the cross-correlation function K_c will take the form shown in

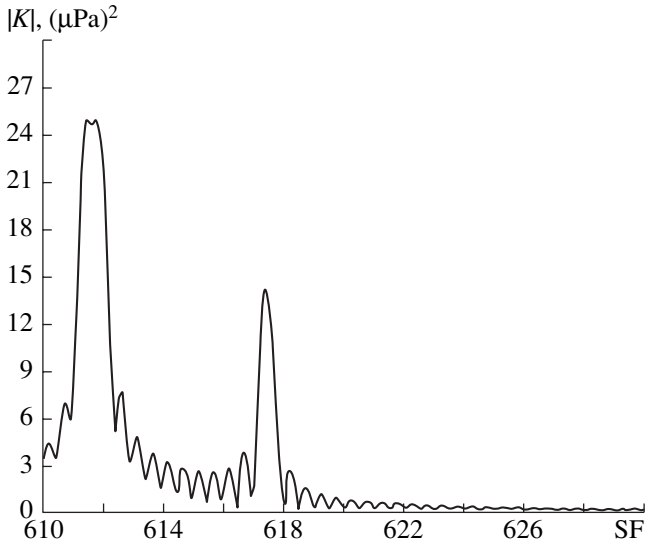

Fig. 5. Envelope of the time correlation function given by Eq. (5) for an irregular propagation path; r_1 = 900 km and r_2 = 10 km.

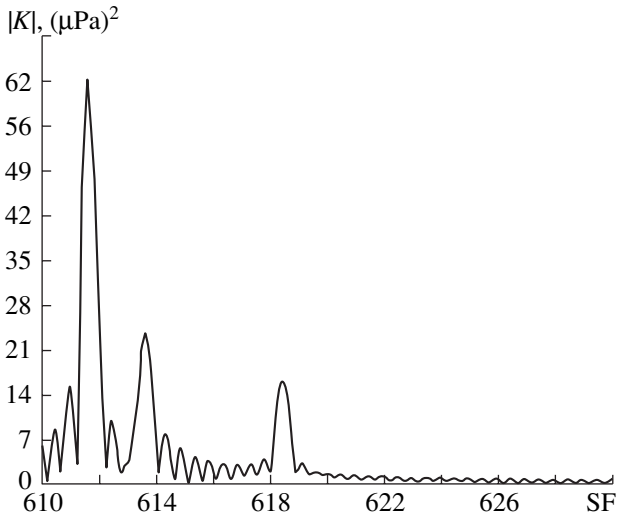

Fig. 6. Same as in Fig. 5, but for the sound velocity profile corresponding to curve *1* from Fig. 1b.

Fig. 5 with a rather small difference between the envelopes of the time cross-correlation functions: the peak positions on the time delay axis are identical, but the maximal values are somewhat smaller in the second case, because the magnitude of the eigenfunction of the first water mode is less than unity.

Figure 6 presents a plot for the case similar to that of Fig. 5. The only difference is that, for the deep-water region, we used the sound velocity profile given by curve *1* from Fig. 1b. The change in the sound velocity profile caused a noticeable change in the time (delay) structure of the envelope. The changes in the mode propagation times are most pronounced for the modes of the first numbers, which are concentrated in the water layers where the changes in the sound velocity profile are maximal.

Thus, with the above formulation of the problem, it is possible to reveal a change in the sound velocity profile within a given part of the sound propagation path, e.g., in the course of a long-term experiment, on condition that the path geometry and the transmitted signal are invariable.

ACKNOWLEDGMENTS

This work was supported by the Russian Foundation for Basic Research, project no. 01-02-16636.

REFERENCES

1. V. V. Goncharov, V. Yu. Zaĭtsev, V. M. Kurtepov, A. G. Nechaev, and A. I. Khil'ko, *Acoustic Tomography of the Ocean* (IPF RAN, Nizhni Novgorod, 1997).
2. L. M. Brekhovskikh, *Waves in Layered Media*, 2nd ed. (Nauka, Moscow, 1973; Academic, New York, 1960).
3. L. M. Brekhovskikh and Yu. P. Lysanov, *Fundamentals of Ocean Acoustics* (Gidrometeoizdat, Leningrad, 1982; Springer, New York, 1991).
4. B. G. Katsnel'son and V. G. Petnikov, *Acoustics of a Shallow Sea* (Nauka, Moscow, 1997).
5. V. D. Krupin, Akust. Zh. **46**, 789 (2000) [Acoust. Phys. **46**, 692 (2000)].
6. V. M. Kudryashov, Akust. Zh. **33**, 55 (1987) [Sov. Phys. Acoust. **33**, 32 (1987)].
7. V. M. Kudryashov, Akust. Zh. **34**, 117 (1988) [Sov. Phys. Acoust. **34**, 63 (1988)].
8. E. C. Shang and Y. Y. Wang, J. Acoust. Soc. Am. **105**, 1592 (1999).
9. P. N. Mikhalevsky, A. N. Gavrilov, and A. B. Baggeroer, IEEE J. Ocean Eng. **24** (2), 183 (1999).
10. P. N. Mikhalevsky, A. B. Baggeroer, A. Gavrilov, and M. Slavinsky, EOS Trans. Am. Geophys. Union **76** (27), 265, 268 (1995).
11. F. G. Bass and I. M. Fuks, *Wave Scattering from Statistically Rough Surfaces* (Nauka, Moscow, 1972; Pergamon, Oxford, 1978).
12. V. M. Kudryashov, Matem. Probl. Geofiz. (Novosibirsk), No. 4, 256 (1973).
13. V. M. Kudryashov, Akust. Zh. **42**, 438 (1996) [Acoust. Phys. **42**, 386 (1996)].
14. V. M. Kudryashov, Akust. Zh. **42**, 247 (1996) [Acoust. Phys. **42**, 215 (1996)].
15. V. M. Kudryashov, Akust. Zh. **45**, 529 (1999) [Acoust. Phys. **45**, 472 (1999)].
16. V. M. Kudryashov, Akust. Zh. **34**, 1081 (1988) [Sov. Phys. Acoust. **34**, 618 (1988)].
17. V. M. Kudryashov, in *Proceedings of All-Union Acoustical Conference* (Moscow, 1991), Section D, p. 35.

Translated by E. Golyamina

Acoustical Physics, Vol. 48, No. 2, 2002, pp. 187–200. Translated from Akusticheskiĭ Zhurnal, Vol. 48, No. 2, 2002, pp. 224–238.

Effect of a Mudcake on the Propagation of Stoneley Waves in a Borehole

G. A. Maximov and M. E. Merkulov

Moscow State Engineering Physics Institute (Technical University), Kashirskoe sh. 31, Moscow, 115409 Russia

e-mail: maximov@dpt39.mephi.ru

Received March 19, 2001

Abstract—The problem of detecting a permeable stratum blocked by a mudcake with the help of acoustic measurements inside a borehole is considered. Different physical models of the mudcake are compared: in the form of a highly viscous liquid layer, in the form of a soft elastic shell, and in the form of an elastic shell fixed in an arbitrary way to the borehole walls. Numerical calculations are presented for the wave field in a borehole. © *2002 MAIK "Nauka/Interperiodica".*

In view of the numerous predictions concerning the exhaustion of basic oil reserves, the problems of both prospecting for new deposits and efficient use of known oil supplies become increasingly important. For years, studies had been carried out to determine the relation between the properties of low-frequency Stoneley waves excited in a borehole and the permeability of the surrounding medium.

Laboratory experiments [1] showed that the properties of Stoneley waves in a borehole surrounded by a permeable medium are adequately described by the Biot theory [2, 3]. However, in actual conditions, the walls of the borehole can be covered with an almost impermeable layer, which considerably reduces the fluid flow from the reservoir to the well. The formation of such a layer, namely, a mudcake, can be caused, e.g., by the drilling mud that is deposited on the walls of the borehole or penetrates under hydrostatic pressure into the porous medium. On the other hand, experiments [4] showed that in the course of drilling, solid particles of rock can penetrate into the pores of the borehole walls and form a thin (<0.5 mm) barrier, which is 100 to 20000 times less permeable than the surrounding medium. It was shown that this process leads to a decrease in the average permeability of rock by a factor of 2–150. Thus, a mudcake considerably reduces the production of an oil pool and can even hinder its detection by a fluid flow.

Currently, none of the existing technologies is able to determine the position of a permeable stratum in the presence of a mudcake in a borehole. The first step in the development of such technologies is a theoretical study of the effect of a mudcake on the acoustic wave field inside a borehole. For this purpose, it is necessary to develop a model that adequately describes the mudcake. Active studies in this area of research are carried out in the United States [5, 6]. For example, some authors [5] represent a mudcake as an impermeable thin elastic membrane, and other authors [6] consider the mudcake as a layer of rock with a reduced permeability. In both cited publications, a complete wave problem for the Biot model was solved for an arbitrary frequency range, which considerably complicates the description and the physical interpretation of the results.

In this paper, we consider only the long-wave approximation, because, in acoustic measurements, the characteristic wavelengths observed in both the surrounding medium and the borehole fluid are usually much greater than the borehole diameter. Three different physical models of the mudcake are developed. In the first model, the mudcake is described as a highly viscous liquid layer formed in a permeable porous medium of the stratum. This representation can be easily reduced to the model of a low-permeability layer [6] and, from this point of view, it is more general. In the second model, the mudcake is considered as a free elastic shell situated near the wall of the borehole. The third model differs from the second in that the shell is fixed in an arbitrary way to the borehole walls. This model includes an additional assumption that the shell thickness is much smaller than the borehole diameter.

For each of the models, numerical calculations are performed to determine the wave field inside a borehole intersecting a permeable stratum that is blocked by a mudcake. The calculations make it possible to draw the conclusions concerning the possibility of detecting a permeable stratum in the case of a wave and a mudcake with characteristic parameters.

The frequency range used in vertical seismic profiling as a rule does not exceed several hundreds of hertz, and the borehole diameter does not exceed 20 cm. Hence, the characteristic wavelengths in both the borehole fluid and the surrounding medium far exceed the borehole diameter. Therefore, in deriving equations, we use the long-wave approximation $\lambda \gg b$ (b is the borehole radius).

1063-7710/02/4802-0187$22.00 © 2002 MAIK "Nauka/Interperiodica"

The propagation of small-amplitude waves in a liquid is described by the equations of motion, continuity, and state:

$$\begin{cases} \dfrac{\partial}{\partial t}\rho_f(r, z, t) + \rho_f^0 \nabla \mathbf{V}^{(f)}(r, z, t) = 0 \\ \rho_f^0 \dfrac{\partial}{\partial t}\mathbf{V}^{(f)} = -\nabla P_f(r, z, t) \\ P_f(r, z, t) = c_0^2 \rho_f. \end{cases} \quad (1)$$

Here, $P_f(r, z, t)$, $\rho_f(r, z, t)$, and $\mathbf{V}^{(f)} = \{V_r^{(f)}(r, z, t), 0, V_z^{(f)}(r, z, t)\}$ denote the deviations of the local pressure, density, and mass velocity, respectively, from their equilibrium values; ρ_f^0 and c_0 are the initial density of the liquid and the sound velocity in it.

In the long-wave approximation, it is natural to characterize the sound field in the borehole by the dynamical quantities averaged over the borehole cross section [7, 8]:

$$P_f(z, t) = \frac{2\pi}{\pi b^2}\int_0^b P_f(r, z, t) r dr,$$

$$\rho_f(z, t) = \frac{2\pi}{\pi b^2}\int_0^b \rho_f(r, z, t) r dr, \quad (2)$$

$$\mathbf{V}^{(f)}(z, t) = \frac{2\pi}{\pi b^2}\int_0^b \mathbf{V}^{(f)}(r, z, t) r dr.$$

Here, b is the radius of the borehole. In Eqs. (1) and (2), we took into account that, in the long-wave approximation, the distributions of the dynamical quantities in the borehole are axially symmetric, so that averaging over the angle yields the factor 2π.

According to Eqs. (2), after averaging the equation of continuity and the equation of motion (its projection on the borehole axis) over the borehole cross section, we obtain the relationships

$$\frac{\partial}{\partial z}V_z^{(f)}(z, t) = -\frac{1}{\rho_f^0}\frac{\partial}{\partial t}\rho_f(z, t) - \frac{2}{b}V_r^{(f)}(r = b, z, t), \quad (3)$$

$$\rho_f^0 \frac{\partial V_z^{(f)}(z, t)}{\partial t} = -\frac{\partial P_f}{\partial z}. \quad (4)$$

Combining Eqs. (3) and (4), we obtain an inhomogeneous wave equation for the pressure field in a fluid-filled borehole:

$$\frac{\partial^2 P_f}{\partial z^2} - \frac{1}{c_0^2}\frac{\partial^2 P_f}{\partial t^2} = \frac{2\rho_f^0}{b}\frac{\partial V_r^{(f)}(r = b, z, t)}{\partial t}, \quad (5)$$

or, in terms of the frequency representation,

$$\frac{\partial^2 \bar{P}_f}{\partial z^2} + \frac{\omega^2}{c_0^2}\bar{P}_f = i\omega\frac{2\rho_f^0}{b}\bar{V}_r^{(f)}(r = b, z, \omega). \quad (6)$$

When transverse filtration flows in the borehole–stratum system are absent, the fluid velocity near the borehole boundary coincides with the velocity characterizing the displacement of the borehole walls (or the inner surface of the mudcake). The fluid filtration through the mud is neglected in this case.

In the long-wave approximation, to obtain a closed equation for the pressure in the borehole, we can use the quasistatic relation between the applied pressure and the displacement of the borehole walls (the inner surface of the mudcake), which can be determined from the static equations of the theory of elasticity [7–9]. Since we limit our consideration to the linear approximation, this relation will also be linear:

$$V_r^{(f)}(r = b, z, \omega) = AP_f + B. \quad (7)$$

Then, the closed equation for the pressure will have the form

$$\frac{\partial^2 P_f}{\partial z^2} + K^2(\omega)P_f = i\omega\frac{2\rho_f^0}{b}B, \quad (8)$$

where the wave number is determined by the expression

$$K(\omega) = \left(\frac{\omega^2}{c_0^2} - i\omega\frac{2\rho_f^0}{b}A\right)^{\frac{1}{2}}. \quad (9)$$

This expression can also be represented in the form [5, 6]

$$K(\omega) = \omega S(\omega)\left[1 + \frac{i}{2Q}\right], \quad (10)$$

where $S(\omega) = c^{-1}(\omega)$ is the slowness, i.e., the reciprocal of the phase velocity of the tube wave, and Q is the Q-factor.

The coefficients A and B in Eq. (7) depend on the parameters of the borehole wall, the mud, and the fluid. For simple cases, these coefficients are well known. If the borehole is surrounded by a homogeneous elastic medium, these coefficients are $A = i\omega b/2\mu$ and $B = -P_{\text{ext}}A$, where μ is the shear modulus of the elastic medium and P_{ext} is the effective external stress. Then, the wave number will be determined by the expression

$$K^2(\omega) = \omega^2\left(\frac{1}{c_0^2} + \frac{\rho_f^0}{\mu}\right). \quad (11)$$

If the elastic medium under consideration is characterized by a nonzero permeability, the expression for the velocity will have an additional term associated with the transverse filtration flows in the borehole–stra-

tum system. In this case, the wave number will have the form [8]:

$$K^2(\omega) = \omega^2\left(\frac{1}{c_0^2} + \frac{\rho_f^0}{\mu} + 2\rho_f^0\frac{m_0}{K_f}\frac{1}{z}\frac{K_1(z)}{K_0(z)}\right), \qquad (12)$$

where the argument $z = \sqrt{i\omega\frac{\eta m_0}{k_0 K_f}}\,b$ is determined by both the frequency and the combination of the parameters characterizing the porosity m_0, the permeability k_0, and the dynamic viscosity of the fluid η; K_0 and K_1 are the Macdonald functions.

In this paper, we determine the coefficients of the quasistatic relation between the applied pressure and the displacement of the inner surface of the mudcake. For this purpose, we consider the following system: a borehole in a permeable homogeneous elastic medium blocked by a mudcake. The main problem is that the mudcake may exhibit different properties in different conditions. Therefore, we developed several models of the mudcake [10]. In fact, only two fundamentally different ways are possible in describing this object: the mudcake can be considered either as a highly viscous liquid or as a solid shell.

MODEL OF A MUDCAKE AS A HIGHLY VISCOUS LIQUID

This model represents the mudcake as a highly viscous liquid layer formed in the porous medium of a permeable stratum. In the framework of this model, the coefficients characterizing the relation between the velocity of the inner mud surface and the pressure have the form (see Appendix A):

$$A_1 = m_0\sqrt{i\omega}F(\gamma_1 R_0)\tilde{F}(\gamma_1 R_0)\frac{F(\gamma_2 R_1)\left[\frac{I_0(\gamma_1 R_1)}{I_1(\gamma_1 R_0)} + \frac{K_0(\gamma_1 R_1)}{K_1(\gamma_1 R_0)}\right] + \frac{a_1}{K_{f1}}\left[\frac{I_1(\gamma_1 R_1)}{I_1(\gamma_1 R_0)} - \frac{K_1(\gamma_1 R_1)}{K_1(\gamma_1 R_0)}\right]}{F(\gamma_2 R_1)\left[\frac{I_0(\gamma_1 R_1)}{I_0(\gamma_1 R_0)} - \frac{K_0(\gamma_1 R_1)}{K_0(\gamma_1 R_0)}\right] + \frac{a_1}{K_{f1}}\left[\frac{I_1(\gamma_1 R_1)}{I_0(\gamma_1 R_0)} + \frac{K_1(\gamma_1 R_1)}{K_0(\gamma_1 R_0)}\right]}, \qquad (13)$$

$$B_1 = -P^{\text{ext}}A_1, \qquad (14)$$

where R_0 is the inner radius of the mud layer (in this model, it coincides with the borehole radius b); R_1 is the outer radius of the mud layer; $a^2 = k_0 K_f/\eta m_0$; $\gamma_j = \sqrt{i\omega/a_j^2}$; $j = 1, 2$, where 1 corresponds to the mud and 2 to the fluid; K_0, I_0, K_1, and I_1 are zero-order and first-order modified Bessel functions;

$$F(\gamma_i R) = \frac{a_i}{K_{fi}}\frac{K_1(\gamma_i R)}{K_0(\gamma_i R)};\ \text{and}\ i = 1, 2;\quad \tilde{F}(z) = \frac{I_1(z)}{I_0(z)}.$$

Taking into account the elastic motion of the borehole walls, we obtain an expression for the wave number describing the wave propagation in the borehole:

$$K^2 = \omega^2\left[\frac{1}{c_0^2} + \frac{\rho_f^0}{\mu} - i\frac{2\rho_f^0}{b}\frac{A_1}{\omega}\right]. \qquad (15)$$

When the thickness of the mudcake is zero, i.e., $R_0 = R_1$, this expression is reduced to Eq. (12).

In [6], the authors described the mudcake in the framework of the Biot model as a thin layer of the surrounding elastic medium with a reduced permeability k_{imp}. Since permeability is involved in Eq. (13) only in combination with the viscosity, k/η, our model can be easily reduced to the model described in [6]. For this purpose, it is sufficient to assume that the compression modulus of the mud is equal to that of the fluid: $K_{f1} = K_{f2}$. Then, by varying the viscosity of the mud, we effectively vary the permeability of rock. The cited publication [6] presents the low-frequency approximation of the total result (see Eq. (13) in [6]):

$$K^2 = \omega^2\left[\frac{1}{c_0^2} + \frac{\rho_f^0}{\mu} + \frac{2\rho_f^0}{b}\frac{1}{W_i(\omega) + W_p(\omega)}\right], \qquad (16)$$

where

$$W_i(\omega) = -i\omega(R_1 - R_0)\frac{\eta}{k_{\text{imp}}},$$

$$W_p(\omega) = -\frac{\tilde{K}}{m_0}\frac{\tilde{z}}{b}\frac{H_0^{(1)}(\tilde{z})}{H_1^{(1)}(\tilde{z})},\quad \tilde{z} = \sqrt{\frac{i\omega m_0\eta}{k_0\tilde{K}}}\,b,$$

$H_0^{(1)}$ and $H_1^{(1)}$ are the zero-order and first-order Hankel functions of the first kind, and $\tilde{K}$ is a fairly complex combination of the porosity and the elastic moduli that characterize the skeleton of the porous medium and the fluid (detailed formulas can be found in [5]). Performing the numerical comparison, we took into account the difference between $\tilde{K}$ and K_f by introducing a correction factor close to unity.

Table 1. Parameters used in the calculations

Fluid-filled borehole	Fluid density	ρ_f^0, kg/m^3	1000
	Sound velocity in the fluid	c_0, m/s	1500
	Fluid viscosity	η, Pa s	0.001
	Borehole radius	b, cm	14.5
Porous medium	Longitudinal wave velocity	c_p, m/s	3735
	Transverse wave velocity	c_s, m/s	2080
	Density of rock	ρ_b, kg/m^3	2337
	Porosity	m_0	0.2
	Permeability	k_0, D	0.1
Mudcake	Sound velocity in the mud	c_{CL}, m/s	1500
	Mud viscosity	η_{CL}, Pa s	[0.001–0.1]
	Mud density	ρ_{CL}, kg/m^3	1000
	Mudcake thickness	$R_1 - R_0$, mm	1

When the thickness of the mudcake is zero, Eq. (16) is reduced to an expression equivalent to Eq. (12):

$$K^2 = \omega^2\left[\frac{1}{c_0^2} + \frac{\rho_f^0}{\mu} - 2\rho_f^0\frac{m_0}{\tilde{K}}\frac{1}{\tilde{z}}\frac{H_1^{(1)}(\tilde{z})}{H_0^{(1)}(\tilde{z})}\right]. \qquad (17)$$

It should be noted that, to change to the frequency representation, we used the Fourier transform with the core $e^{i\omega t}$, whereas in the aforementioned publications [5, 6], the core $e^{-i\omega t}$ was used. Therefore, to compare results, it is necessary to perform the substitution $\omega \longrightarrow -\omega$. Taking into account the relation between the Hankel and Macdonald functions, $K_\nu(z) = \frac{\pi}{2} i^{\nu+1} H_\nu^{(1)}(iz)$ [11], one can easily verify that Eqs. (12) and (17) are structurally identical.

To compare our model of a highly viscous liquid with the model of a low-permeability layer, we used Eq. (16) and the parameters from [6] (Table 1). The results of this comparison are presented in Fig. 1.

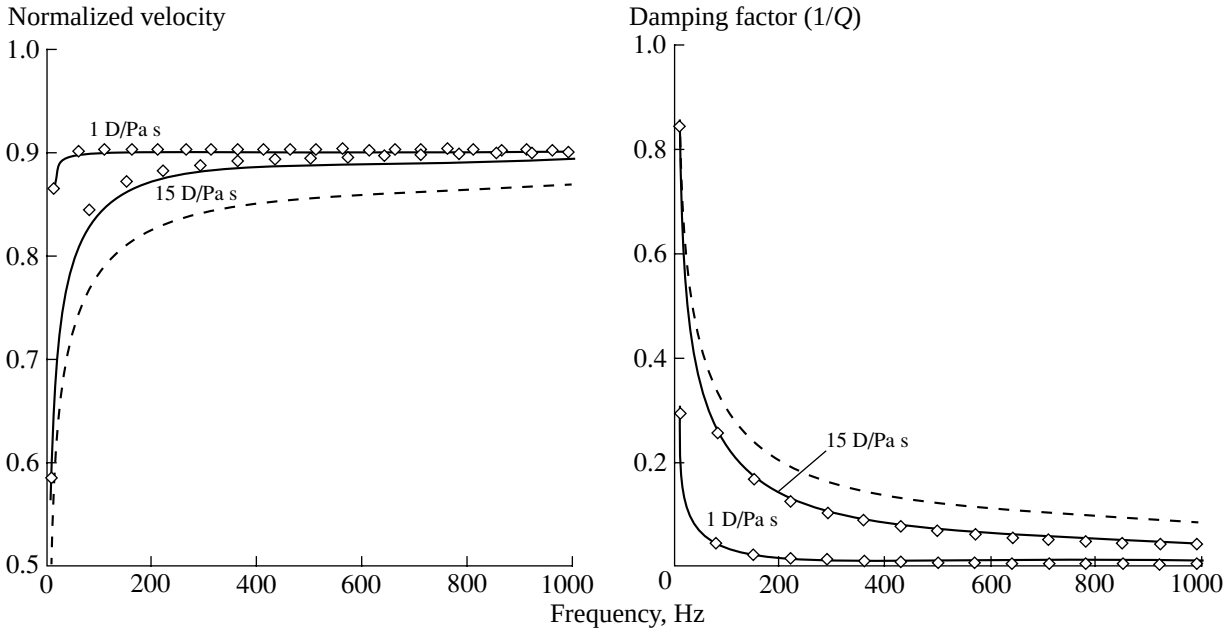

Fig. 1. Comparison of the frequency dependences of the phase velocity $c(\omega)/c_0$ (left) and the damping factor $1/Q$ (right) calculated using the model of a highly viscous liquid (the solid curves) for the parameters k_0/η_{CL} = 1 and 15 D/Pa s with the corresponding dependences obtained for the model of a low-permeability layer [5]. The dashed curves correspond to the calculations for an open borehole.

MODEL OF THE MUDCAKE AS AN ELASTIC CYLINDRICAL SHELL

In this model, the mudcake is represented as an elastic cylindrical shell, which has the inner radius R_0 and the outer radius R_1 and is situated near the inner surface of the borehole (see Appendix B). The coefficients characterizing the quasistatic relation between the velocity of the inner mud surface and the pressure have the form

$$A_2 = \frac{i\omega R_0}{2}\frac{[1+d_1]+\left(1-\left(\frac{R_0}{R_1}\right)^2\right)\left[\frac{\Psi(z)}{\mu_1}-1\right]}{d_1\mu_1\left(1-\left(\frac{R_0}{R_1}\right)^2\right)+\Psi(z)\left(1+d_1\left(\frac{R_0}{R_1}\right)^2\right)}, \quad (18)$$

$$B_2 = \frac{i\omega R_0}{2}\frac{-P_{\text{ext}}[1+d_1]}{d_1\mu_1\left(1-\left(\frac{R_0}{R_1}\right)^2\right)+\Psi(z)\left(1+d_1\left(\frac{R_0}{R_1}\right)^2\right)}, \quad (19)$$

where

$$\Psi(z) = \mu_2\frac{\tilde{\Phi}(z)}{2\mu_2+\tilde{\Phi}(z)}, \quad \tilde{\Phi}(z) = \frac{K_f}{m_0}\frac{zK_0(z)}{K_1(z)},$$

and the parameter d is determined by the following expressions depending on the type of the stressed state:

$d = \dfrac{3\lambda+2\mu}{\lambda+2\mu}$ when the shell ends are free ($\sigma_{zz}=0$) and

$d = \dfrac{\lambda+\mu}{\mu}$ when the shell ends are fixed ($u_{zz}=0$).

Index 1 corresponds to the mudcake, and index 2 to the porous elastic medium.

We note that, in this model, the coefficient B is not related to A by Eq. (14), so that the velocity characterizing the displacement of the inner mud surface is not proportional to the difference between the pressures inside the borehole and at infinity. This is a consequence of the fact that, under pressure, the mudcake is not only displaced as a whole, but it is also deformed, i.e., its thickness changes.

In [5], the mudcake was considered as an elastic membrane. The result obtained in this case in the low-frequency approximation is as follows (Eq. (58) from [5]):

$$K^2(\omega) = \omega^2\left(\frac{1}{c_0^2}+\frac{\rho_f^0}{M_f}+\frac{\rho_f^0}{[W_{MC}+W_p(\omega)]}\frac{2}{b}\frac{(1-f_c)\mu_2^2}{H^2}\right), \quad (20)$$

where

$$M_f = \frac{\mu_2[\lambda_1+2\mu_1]+f_c(\mu_1-\mu_2)(\lambda_1+\mu_1)}{\lambda_1+2\mu_1+f_c(\mu_2-\mu_1)};$$

$$f_c = 1-\left(\frac{R_0}{R_1}\right)^2; \; H = \mu_2 - f_c(\mu_2-\mu_1)(\lambda_1+\mu_1)/(\lambda_1+2\mu_1);$$

and W_{MC} is the membrane stiffness, this parameter being artificially introduced in the boundary condition between the porous medium and the mudcake: $\sigma_{rr1}(b) = P_2(b) + W_{MC}[U_{r2}(b) - u_{r2}(b)]$. Here, σ_{rr} is the radial component of the stress tensor at the surface of the mudcake; P_2 is the fluid pressure in the pores; and U_{r2} and u_{r2} are the displacements of the fluid and the skeleton of the porous medium, respectively. In the case $W_{MC} = \infty$, this condition is reduced to the zero difference between the displacements: $U_{r2}(b) - u_{r2}(b) = 0$. In the case $W_{MC} = 0$, we obtain the equality of pressures: $\sigma_{rr1}(b) = P_2(b)$.

In developing our model, we used the latter condition, i.e., the condition of equal pressures (see Appendix B). Therefore, to perform the comparison, we must set $W_{MC} = 0$ in Eq. (20).

Substituting A_2 into Eq. (9), we obtain the wave number of the tube wave in our model. If we separate the term ρ_f^0/M_f and use the formula $d_1 = (\lambda_1+\mu_1)/\mu_1$ corresponding to the case of fixed ends ($u_{zz}=0$), the wave number can be written in the form

$$K^2(\omega) = \omega^2\left(\frac{1}{c_0^2}+\frac{\rho_f^0}{M_f}+\frac{2\rho_f^0}{b}\frac{(1-f_c)\mu_2^2}{(X+W_p(\omega)H)H}\right), \quad (21)$$

where $X = 2\mu_2\mu_1 f_c\dfrac{\lambda_1+\mu_1}{\lambda_1+2\mu_1}$ is the term that distinguishes our result from Eq. (20) at $W_{MC}=0$.

When the membrane thickness is equal to zero, i.e., $R_1 - R_0 = 0$, we have $f_c = 0$, which yields $X = 0$, and the results coincide. In the other limiting case $k_0 \longrightarrow 0$, we have $W_p \longrightarrow \infty$, and both Eqs. (20) and (21) are reduced to the expression

$$K^2(\omega) = \omega^2\left(\frac{1}{c_0^2}+\frac{\rho_f^0}{M_f}\right). \quad (22)$$

Figure 2 shows the results of calculations by Eqs. (20) and (21) for the parameters presented in Table 2 (the values of the parameters are taken from [5]).

STATISTICAL MODEL

To compare the model of a highly viscous liquid with the cylindrical shell model, it is necessary to calculate the wave field inside the borehole. In the following section, we will show that the results obtained with these two models differ considerably. The calculations using the cylindrical shell model with the characteristic parameters show that the mudcake practically does not affect the wave field (this conclusion was also made in [5]), whereas the calculations performed in the framework of the model of a highly viscous liquid show considerable changes in the wave field structure due to the mudcake.

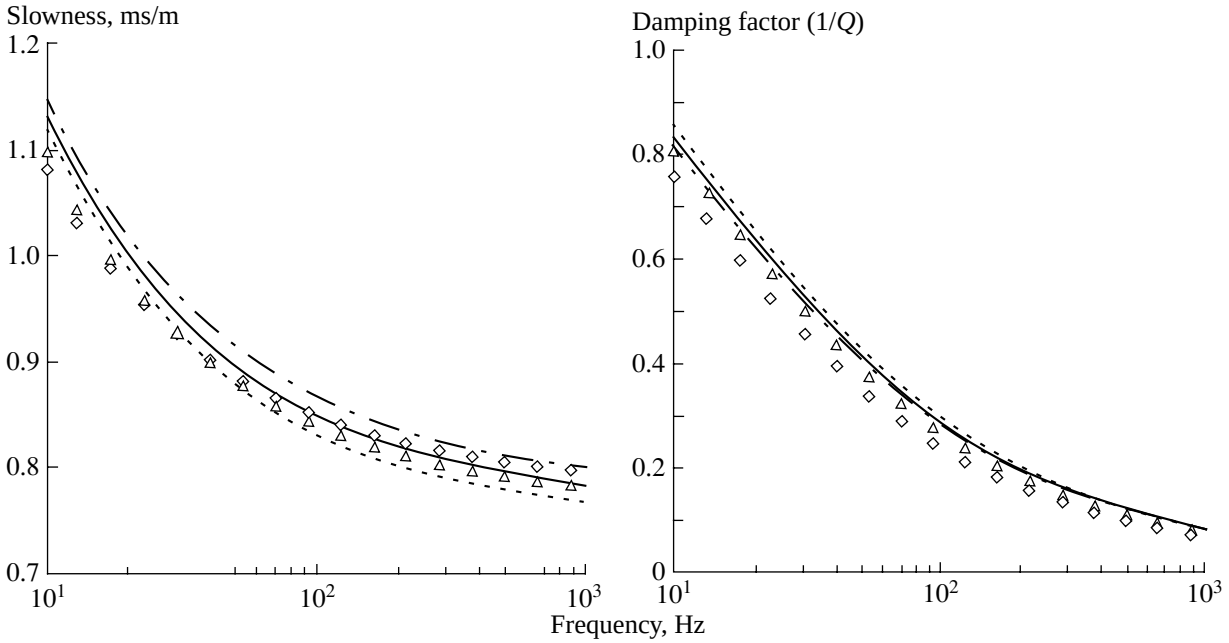

Fig. 2. Comparison of the frequency dependences of the Stoneley wave slowness $S(\omega)$ (left) and the damping factor $1/Q$ (right) calculated using the model of an elastic membrane for the parameters $h = 3$ mm (the solid curves) and 6 mm (the dot-and-dash curves) with the corresponding dependences obtained for the membrane model [5]. The triangles refer to $h = 3$ mm and the diamonds refer to $h = 6$ mm. The dashed curves represent the calculations for an open borehole.

This discrepancy between the results called for the development of a more realistic model in which the mudcake is considered as a thin cylindrical elastic shell fixed to the borehole walls in an arbitrary way (see Appendix C). This model contains a random parameter—the distance between the fixing points. Varying its average value, one can obtain the results similar to those derived from the two models considered above. In the case under consideration, the coefficients in Eq. (7) have the form

$$A_3 = \frac{i\omega b}{2\mu} + \frac{i\omega}{\tilde{W}_{MC} + K_f z K_0(z)/(m_0 b K_1(z))}, \qquad B_3 = -P_{\text{ext}} A_3, \tag{23}$$

Table 2. Parameters used in the calculations

Fluid-filled borehole	Fluid density	ρ_f^0, kg/m^3	1000
	Sound velocity in the fluid	c_0, m/s	1500
	Fluid viscosity	η, Pa s	0.001
	Borehole radius	b, cm	10.5
Porous medium	Longitudinal wave velocity	c_p, m/s	3360
	Transverse wave velocity	c_s, m/s	1675
	Density of rock	ρ_b, kg/m^3	2670
	Porosity	m_0	0.2
	Permeability	k_0, D	0.1
Mudcake	Longitudinal wave velocity in the mud	c_{CL}^p, m/s	1500
	Transverse wave velocity in the mud	c_{CL}^s, Pa s	320
	Mud density	ρ_{CL}, kg/m^3	1100
	Mudcake thickness	$R_1 - R_0$, mm	[0–6]

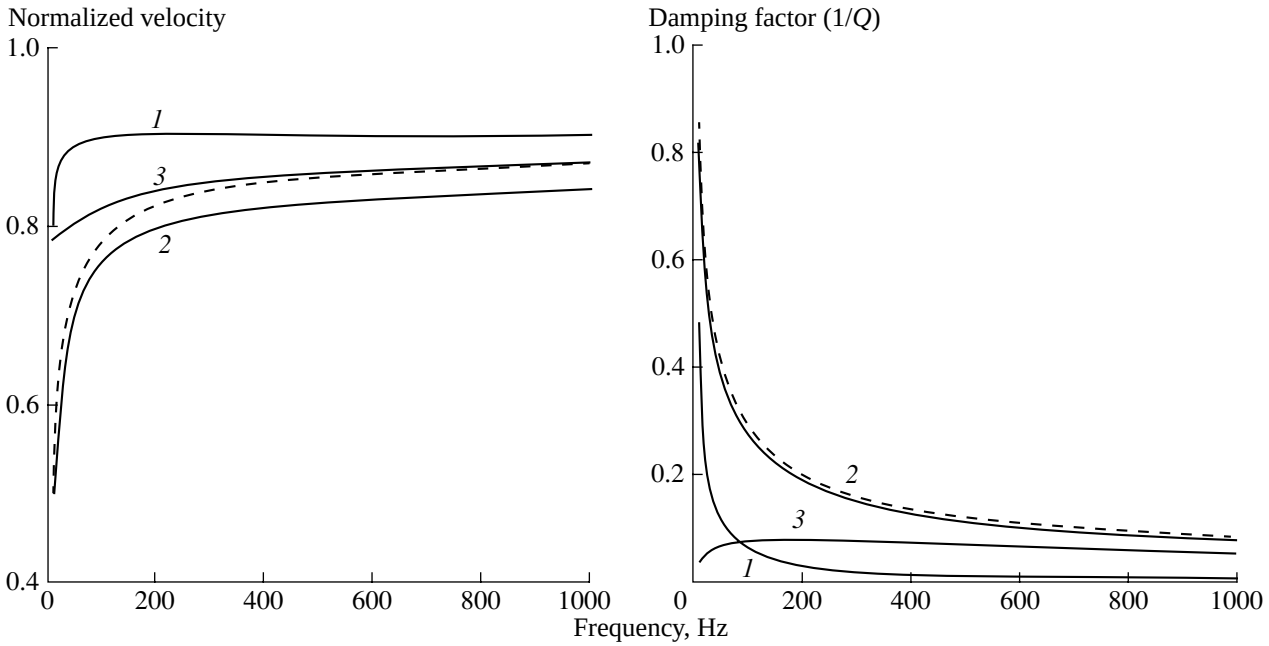

Fig. 3. Comparison of the frequency dependences of the phase velocity $c(\omega)/c_0$ (left) and the damping factor $1/Q$ (right) for different models of the mudcake: (*1*) the highly viscous liquid model, (*2*) the elastic shell model, and (*3*) the statistical model. The dashed curves correspond to an open borehole.

where

$$\tilde{W}_{MC} = \frac{Eh}{(1-\sigma^2)b^2} 2\left[e^{-\frac{2}{1+s}\left(\frac{\delta\sqrt{hb}}{\sqrt[4]{3\tau}}\right)} + e^{-\frac{25}{1+4s}\left(\frac{\delta\sqrt{hb}}{\sqrt[4]{3\tau}}\right)} \right]^{-1}$$

is the shell stiffness; h is the shell thickness; E and σ are the Young modulus and the Poisson ratio, respectively; $\tau = \frac{D}{\bar{L}}$; $s = \frac{\bar{L}^2}{D} - 1$; $\bar{L}$ is the average distance between the fixing points; and D is its variance. The wave number is expressed by the formula

$$K^2 = \omega^2\left(\frac{1}{c_0^2} + \frac{\rho_f^0}{\mu} + \frac{2\rho_0^f}{b}\frac{1}{\tilde{W}_{MC} + K_f z K_0(z)/(m_0 b K_1(z))}\right). \quad (24)$$

We note that, in this model, the velocity of the inner surface of the mudcake is proportional to the pressure difference $P_f - P_{\text{ext}}$ despite the fact that, as in the previous case, the mudcake is described as a solid body. This is a consequence of the thin shell approximation.

Figure 3 presents the comparison of the frequency dependences of the phase velocity and the damping factor of a tube wave for the model of a highly viscous liquid, the elastic shell model, and the statistical model. The calculations were performed using the parameters from Table 2. The mud viscosity was $\eta_{CL} = 0.1$ Pa s; the mudcake thickness was $h = 5$ mm; the average length and its variance in the statistical model were taken to be $\bar{L} = 4$ mm and $D = 13$ mm^2. These parameters were selected so as to demonstrate most clearly the intermediate position of the statistical model.

Below, we present examples of calculated seismograms that illustrate the effect of the mudcake on the acoustic wave field generated in a borehole by a pulsed source positioned inside the borehole. To obtain the seismograms, we used the TUBEWAVE software [7, 8], which allowed us to calculate the wave field in a borehole embedded in a stratified elastic medium.

Figure 4a shows the simplest case of a borehole in a homogeneous elastic medium. In this case, a wave propagates in the borehole without reflections. If a permeable stratum with the same elastic parameters as those of the surrounding medium is introduced in the system, a difference will appear in the fluid velocities near the borehole walls. Then, the wave numbers given by Eqs. (11) and (12) will differ by only the second term in Eq. (12), i.e., the term associated with the permeability. This may give rise to a reflected wave (Fig. 4b).

In our calculations, we used the following parameters: the initial fluid density $\rho_f^0 = 1000$ kg/m^3; the initial fluid velocity $c_f = 1500$ m/s; the fluid viscosity $\eta = 0.001$ Pa s; the borehole radius $b = 10$ cm; the density of the surrounding elastic medium $\rho = 2000$ kg/m^3; the longitudinal and transverse velocities of sound in this medium $c_p = 4500$ m/s and $c_s = 2500$ m/s, respectively; the thickness of the permeable stratum (for the case corresponding to Fig. 4b) $d = 4$ m; the porosity of the medium $m_0 = 15\%$; and the permeability of the medium

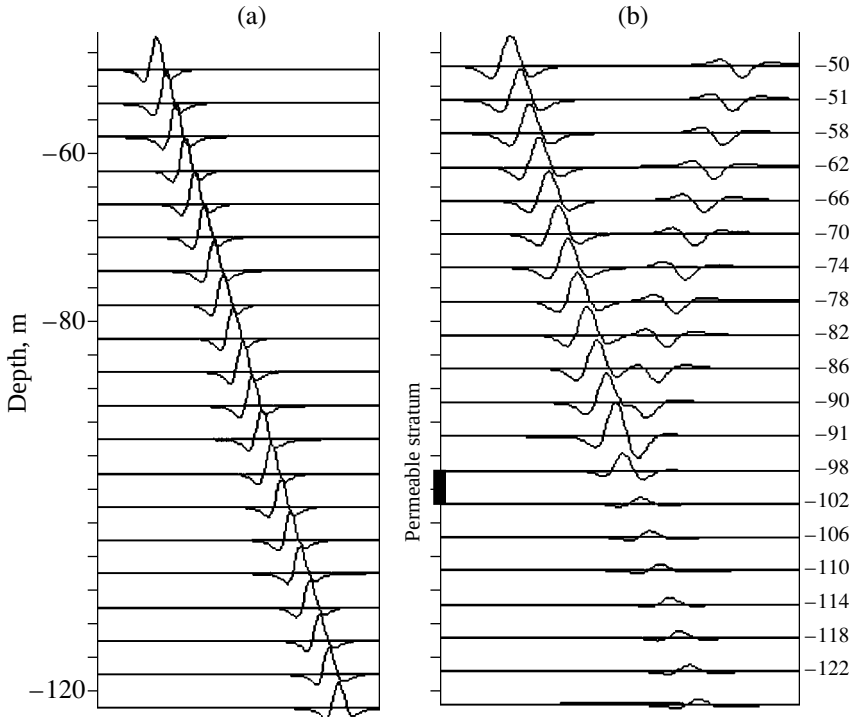

Fig. 4. Synthetic seismograms illustrating the propagation of Stoneley waves in a borehole (a) in the absence and (b) in the presence of a permeable stratum.

k_0 = 10 D. The permeability was chosen to be high to make the effect under investigation more pronounced.

Now, let us assume that the permeable stratum is blocked by mud. Depending on the mudcake and stratum parameters, three situations are possible:

(a) mud is amenable to varying pressure; then, the seismogram has the form shown in Fig. 4a, i.e., the stratum is clearly "visible";

(b) mud is resistant to varying pressure; then, the seismogram has the form shown in Fig. 4b, i.e., the stratum is "invisible";

(c) the intermediate situation.

Thus, the effect of the mudcake on the wave field should manifest itself as a change in the amplitude ratio of the reflected and transmitted waves. The stronger the mudcake blocks the permeable stratum, the smaller the amplitude of the reflected wave.

For each model of the mudcake and for a fixed mudcake thickness h = 1 cm and with fixed parameters for the borehole, we chose mud parameters that correspond to each of the three aforementioned situations (Fig. 5).

In the model of a highly viscous liquid, the permeable stratum is visible at $\frac{\eta_{CL}/K_{CL}}{\eta_f/K_f} = 1$ and invisible when $\frac{\eta_{CL}/K_{CL}}{\eta_f/K_f} \gg 1$, and the intermediate situation is realized when $\frac{\eta_{CL}/K_{CL}}{\eta_f/K_f} >\approx 1$. In the elastic shell model, the stratum is visible when $\mu_1/\mu_2 \ll 1$ and invisible when $\mu_1/\mu_2 \gg 1$, and the situation is intermediate when $\mu_1/\mu_2 \approx 1$. In the framework of the statistical model, the stratum is visible when $\frac{\mu_1}{\mu_2}\frac{\sqrt{hb}}{\bar{L}} \ll 1$ and invisible when $\frac{\mu_1}{\mu_2}\frac{\sqrt{hb}}{\bar{L}} \gg 1$, and the intermediate situation corresponds to $\frac{\mu_1}{\mu_2}\frac{\sqrt{hb}}{\bar{L}} \approx 1$.

Calculations performed for the characteristic parameters of both borehole and mud showed that, for the highly viscous liquid model, case (b) is realized (the stratum is invisible), and for the elastic shell model, case (a) takes place (the stratum is clearly visible). This is the discrepancy of the results that was mentioned above. In the calculations, we used the following characteristic parameters of mud: the density ρ_{CL} = 2000 kg/m^3, the longitudinal sound velocity c_{CL}^p = 1000 m/s, the transverse sound velocity (for the elastic shell model) c_{CL}^s = 500 m/s, and the viscosity η_{CL} = 1–100 Pa s. A similar calculation for the statistical model showed that case (a) is most likely to be realized.

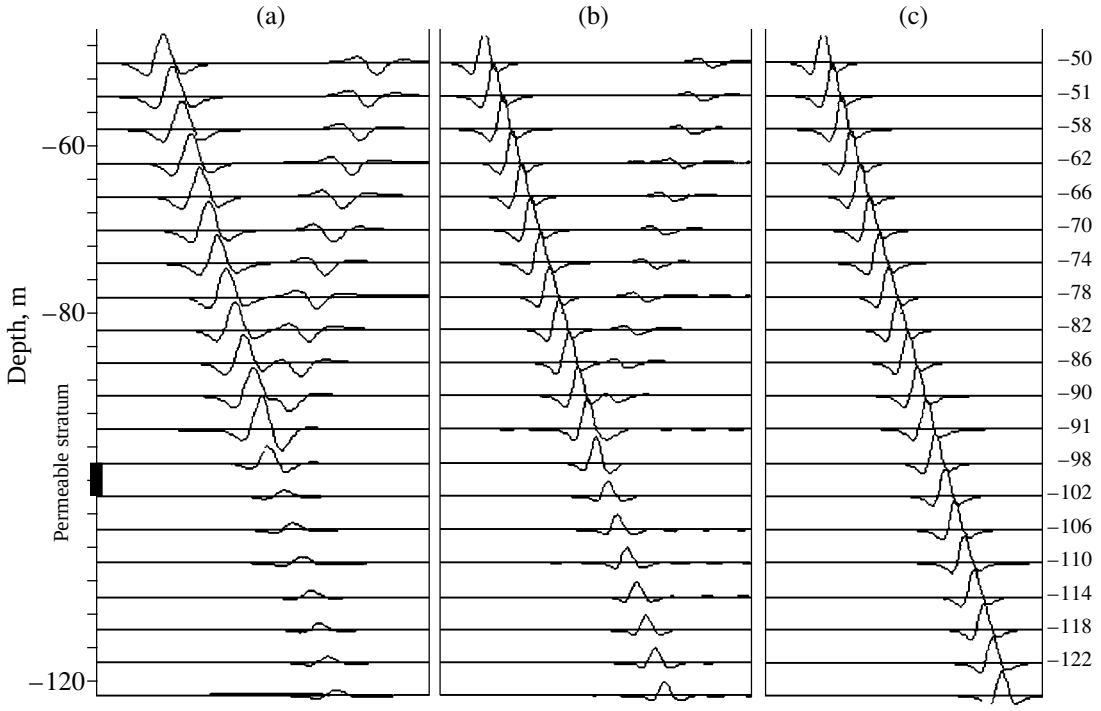

Fig. 5. Synthetic seismograms illustrating the effect of the mudcake on the reflection of Stoneley waves and their transmission through a blocked permeable interval for the cases of (a) a weak, (b) intermediate, and (c) strong blockage. The parameters corresponding to these cases for (1) the model of a highly viscous liquid, (2) the elastic shell model, and (3) the statistical model are as follows: case (a): (1) $\frac{\eta_{CL}/K_{CL}}{\eta_f/K_f} = 1$, (2) $\frac{\mu_1}{\mu_2} \ll 1$, (3) $\frac{\mu_1}{\mu_2}\frac{\sqrt{hb}}{L} \ll 1$; case (b): (1) $\frac{\eta_{CL}/K_{CL}}{\eta_f/K_f} \gtrsim 1$, (2) $\frac{\mu_1}{\mu_2} \approx 1$, (3) $\frac{\mu_1}{\mu_2}\frac{\sqrt{hb}}{L} \approx 1$; case (c): (1) $\frac{\eta_{CL}/K_{CL}}{\eta_f/K_f} \gg 1$, (2) $\frac{\mu_1}{\mu_2} \gg 1$, (3) $\frac{\mu_1}{\mu_2}\frac{\sqrt{hb}}{L} \gg 1$.

Thus, in this paper, we discussed the problem of detecting a blocked permeable stratum by means of acoustic measurements in a borehole. In this context, we studied the response of such an object as a mudcake to the effect of an acoustic wave field. Several ways of describing the mudcake were proposed, and it was found that its response to the effect of acoustic waves strongly depends on the mudcake model. The calculation performed in the framework of the model representing the mudcake as a highly viscous liquid layer showed that, in the case of a viscosity characteristic of a mud solution, a mudcake several millimeters thick completely blocks the permeable interval. A similar calculation using the elastic shell model yields the opposite result even for a one-centimeter-thick mudcake. A more realistic model representing the mudcake as an elastic membrane fixed in an arbitrary way to the borehole surface allowed us to combine the two previous results by averaging them with different weights. Formally, this procedure resulted in the introduction of the effective stiffness of the membrane $\tilde{W}_{MC}$. In [5], the membrane stiffness was introduced as a parameter, whereas, in this paper, we proposed a new method for its calculation. We showed that, in the low-frequency limit, the results obtained in [5, 6] in the framework of the Biot theory agree well with the results obtained by us. However, the results obtained in this paper are derived in a much simpler way and have a clearer physical interpretation.

In closing, we conclude that, currently, there exists a theoretical basis for the determination of mud-cake-blocked permeable intervals in a borehole from the character of the propagation of Stoneley waves. However, the choice of the most adequate model of a mudcake is hampered by the lack of experimental data.

APPENDIX A

(THE HIGHLY VISCOUS LIQUID MODEL)

In the framework of this model, a mudcake is considered as a highly viscous liquid layer formed in the porous medium of a permeable stratum and characterized by the inner radius R_0 and the outer radius R_1.

A laminar fluid flow in a porous medium is described by the continuity equation and the Darcy law:

$$\begin{aligned}\frac{\partial(m\rho_f)}{\partial t} + \mathrm{div}(m\rho_f \mathbf{V}^{(f)}) &= 0,\\ \mathrm{grad}P_{\mathrm{por}} &= -\frac{m_0\eta}{k_0}\mathbf{V}^{(f)},\end{aligned} \tag{A.1}$$

where m and m_0 are the current and initial porosities of the medium, respectively; ρ_f and ρ_f^0 are the current and initial densities of the fluid; $\mathbf{V}^{(f)}$ is the mass velocity of the fluid (the skeleton of the porous medium is assumed to be stationary); k_0 is the permeability of the medium; and η is the dynamic viscosity of the fluid.

Setting $m = m_0 = \mathrm{const}$ (i.e., neglecting in this way the contact compressibility) and taking into account the compressibility of the fluid according to the relationship $\rho_f = \rho_f^0\left(1 + \frac{P_{\mathrm{por}}}{K_f}\right)$, we linearize Eqs. (A.1):

$$\begin{aligned}\frac{\partial P_{\mathrm{por}}}{\partial t} + K_f \mathrm{div}\mathbf{V}^{(f)} &= 0,\\ \mathrm{grad}P_{\mathrm{por}} &= -\frac{m_0\eta}{k_0}\mathbf{V}^{(f)}.\end{aligned} \tag{A.2}$$

Here, K_f is the bulk modulus of the fluid. From Eqs. (A.2), we easily obtain the filtration equation

$$\frac{\partial P_{\mathrm{por}}}{\partial t} + a^2\Delta P_{\mathrm{por}} = 0, \tag{A.3}$$

where $a^2 = k_0K_f/\eta m_0$ and Δ is the Laplacian. We seek the solution in the form $P_{\mathrm{por}} = P_{\mathrm{ext}} + P(r, t)$.

In terms of the frequency representation with allowance for the cylindrical symmetry, the problem of filtration can be formulated as follows:

$$\begin{cases}\Delta_r P(r,\omega) - \dfrac{i\omega}{a_1^2}P(r,\omega) = 0 \quad \text{for} \quad R_0 < r < R_1\\ \Delta_r P(r,\omega) - \dfrac{i\omega}{a_2^2}P(r,\omega) = 0 \quad \text{for} \quad R_1 < r < \infty.\end{cases} \tag{A.4}$$

The general solution for $R_0 < r < R_1$ has the form

$$P(r,\omega) = C_1K_0\left(\sqrt{\frac{i\omega}{a_1^2}}r\right) + C_2I_0\left(\sqrt{\frac{i\omega}{a_1^2}}r\right)$$

for $R_0 < r < R_1$ and

$$P(r,\omega) = C_3K_0\left(\sqrt{\frac{i\omega}{a_2^2}}r\right) + C_4I_0\left(\sqrt{\frac{i\omega}{a_2^2}}r\right) \tag{A.5}$$

for $R_1 < r < \infty$,

where K_0, I_0, K_1, and I_1 are the zero-order and first-order modified Bessel functions [11]. The constants C_i are determined from the following boundary conditions: at long distances from the borehole, the deviation of the pressure from the equilibrium value should tend to zero, i.e., $P(r \longrightarrow \infty, \omega) \longrightarrow 0$. At the mud–fluid boundary in the porous medium, the conditions of equal pressures and equal velocities must be satisfied, and at the borehole boundary, the mud pressure should be equal to the fluid pressure in the borehole:

$$\begin{cases}P(R_1 - 0, \omega) = P(R_1 + 0, \omega)\\ v^{(f)}(R_1 - 0, \omega) = v^{(f)}(R_1 + 0, \omega)\\ P(R_0, \omega) = P_f(\omega).\end{cases} \tag{A.6}$$

Here, P_f represents the deviation of the pressure in the borehole from the equilibrium pressure.

Thus, substituting the general solutions (A.5) into Eqs. (A.6), we obtain a set of equations for the determination of the constants C_i. Using the solution of the filtration problem for $R_0 < r < R_1$ and Eqs. (A.2) relating $\mathbf{V}^{(f)}$ and P, we obtain (through cumbersome transformations, which are omitted here) an expression for the filtration velocity at the inner boundary of the borehole:

$$v^{(f)}(R_0,\omega) = P_f m_0\sqrt{i\omega}F(\gamma_1R_0)\tilde{F}(\gamma_1R_0)\frac{F(\gamma_2R_1)\left[\frac{I_0(\gamma_1R_1)}{I_1(\gamma_1R_0)} + \frac{K_0(\gamma_1R_1)}{K_1(\gamma_1R_0)}\right] + \frac{a_1}{K_{f1}}\left[\frac{I_1(\gamma_1R_1)}{I_1(\gamma_1R_0)} - \frac{K_1(\gamma_1R_1)}{K_1(\gamma_1R_0)}\right]}{F(\gamma_2R_1)\left[\frac{I_0(\gamma_1R_1)}{I_0(\gamma_1R_0)} - \frac{K_0(\gamma_1R_1)}{K_0(\gamma_1R_0)}\right] + \frac{a_1}{K_{f1}}\left[\frac{I_1(\gamma_1R_1)}{I_0(\gamma_1R_0)} + \frac{K_1(\gamma_1R_1)}{K_0(\gamma_1R_0)}\right]}, \tag{A.7}$$

where $\gamma_j = \sqrt{\frac{i\omega}{a_j^2}}$, $j = 1, 2$;

$$F(\gamma_iR) = \frac{a_i}{K_{fi}}\frac{K_1(\gamma_iR)}{K_0(\gamma_iR)}, \quad i = 1, 2; \quad \tilde{F}(z) = \frac{I_1(z)}{I_0(z)}.$$

One can easily verify that, at $R_0 = R_1$, i.e., when the mud layer thickness is equal to zero, Eq. (A.7) is reduced to the expression, which coincides with the result obtained in [5] by solving a simple filtration problem without the mud layer:

$$v^{(f)} = P_f m_0 \sqrt{i\omega} F(\gamma_2 R_0) = P_f m_0 \sqrt{i\omega} \frac{a_2}{K_{f2}} \frac{K_1(\gamma_2 R_0)}{K_0(\gamma_2 R_0)}. \quad \text{(A.8)}$$

One can also show that Eq. (A.7) transforms to Eq. (A.8) when the parameters of the fluid and the mud are equal, i.e., when $\gamma_1 = \gamma_2$.

APPENDIX B

(THE CYLINDRICAL ELASTIC SHELL MODEL)

In this model, the mudcake is represented as an elastic shell characterized by the inner radius R_0 and the outer radius R_1 and situated near the inner surface of the borehole with the radius R_2 (Fig. 6). We assume that only radial displacements take place. Then, from the conditions of equal pressures and displacements at the layer boundaries, we obtain an expression for the displacement velocity of the mudcake with allowance for the transverse flows in the borehole–stratum system.

The equilibrium equation for a solid under a surface force has the form [12]

$$2(1-\sigma)\mathrm{grad}(\mathrm{div}\mathbf{u}) - (1-2\sigma)\mathrm{curlcurl}\mathbf{u} = 0,$$

where σ is the Poisson ratio.

The deformation caused by a pressure that is uniform along the tube has the form of a radial displacement $u_r = u(r)$. In this case, we obtain

$$\mathrm{grad}(\mathrm{div}\mathbf{u}) = 0, \quad \mathrm{div}\mathbf{u} = \frac{1}{r}\frac{\partial(ru)}{\partial r} = \mathrm{const}, \quad u = ar + \frac{b}{r}. \quad \text{(B.1)}$$

Using the Hooke law, we derive an expression for the radial component of the stress tensor:

$$\sigma_{rr}(r) = 2a\mu d - 2\mu\frac{b}{r^2}, \quad \text{(B.2)}$$

where $d = \dfrac{3\lambda + 2\mu}{\lambda + 2\mu}$ when the ends of the shell are free ($\sigma_{zz} = 0$) and $d = \dfrac{\lambda + \mu}{\mu}$ when the ends are fixed ($u_{zz} = 0$).

We will first consider the fluid in layer III as a solid by formally introducing its shear modulus μ_f, and, in the final formula, we will set $\mu_f = 0$. Then, according to Eqs. (B.1), the displacement of the fluid has the form

$$u_r^{\mathrm{III}}(r) = a_f r + \frac{b_f}{r}. \quad \text{(B.3)}$$

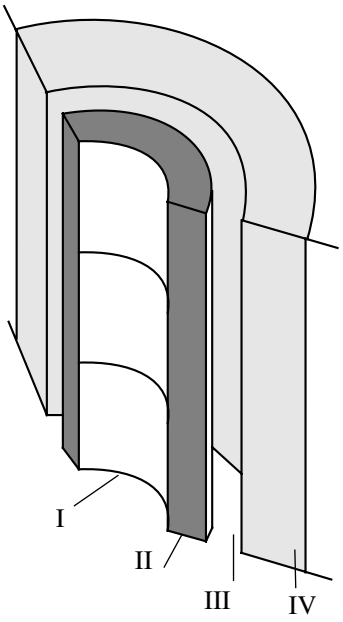

Fig. 6. Geometry of the problem for a borehole blocked by a mudcake: (I) the borehole fluid, (II) the mudcake, (III) the intermediate fluid layer, and (IV) the surrounding permeable porous medium.

Using Eqs. (A.1)–(A.5) from Appendix A, we obtain the expressions for the pressure and the fluid displacement in the porous medium:

$$P_{\mathrm{por}}^{\mathrm{IV}}(r) = P_{\mathrm{ext}} + CK_0(\sqrt{i\omega/a^2}\,r), \quad \text{(B.4)}$$

$$u_{\mathrm{por}}^{\mathrm{IV}}(r) = C\frac{1}{K_f}\frac{1}{\sqrt{i\omega/a^2}}K_1(\sqrt{i\omega/a^2}\,r). \quad \text{(B.5)}$$

Now, we formulate the conditions of the equality of pressures and displacements at the layer boundaries:

$$\sigma_{rr}^{\mathrm{II}}(R_0) = -P_f, \quad \sigma_{rr}^{\mathrm{II}}(R_1) = \sigma_{rr}^{\mathrm{III}}(R_1), \quad u_r^{\mathrm{II}}(R_1) = u_r^{\mathrm{III}}(R_1). \quad \text{(B.6)}$$

The displacement at the fluid–porous medium boundary ($r = R_2$) is determined by the filtration of the fluid and the elastic displacement of the porous medium:

$$u_r^{\mathrm{III}}(R_2) = u_r^{\mathrm{IV}}(R_2) + m_0 u_{r\mathrm{por}}^{\mathrm{IV}}(R_2), \quad \sigma_{rr}^{\mathrm{III}}(R_2) = \sigma_{rr}^{\mathrm{IV}}(R_2) = -P_{\mathrm{por}}^{\mathrm{IV}}(R_2). \quad \text{(B.7)}$$

The conditions at infinity have the form

$$\sigma_{rr}^{\mathrm{IV}}(\infty) = -P_{\mathrm{ext}}, \quad P_{\mathrm{por}}^{\mathrm{IV}}(\infty) = P_{\mathrm{ext}}. \quad \text{(B.8)}$$

Substituting Eqs. (B.1) and (B.2) into the boundary conditions (B.6)–(B.8), we obtain a set of linear equations in the unknowns a_1, b_1, b_f, b_2, and C:

$$\begin{cases} 2a_1\mu_1 d_1 - 2\mu_1\dfrac{b_1}{R_0^2} = -P_f \\ 2a_1\mu_1 d_1 - 2\mu_1\dfrac{b_1}{R_1^2} = 2a_f(\mu_f+\lambda_f) - 2\mu_f\dfrac{b_f}{R_1^2} \\ -P_{\text{ext}} - CK_0(\sqrt{i\omega/a^2}R_2) = 2a_f(\mu_f+\lambda_f) - 2\mu_f\dfrac{b_f}{R_2^2} \\ a_1R_1 + \dfrac{b_1}{R_1} = a_fR_1 + \dfrac{b_f}{R_1} \\ -P_{\text{ext}} - 2\mu_2\dfrac{b_2}{R_2^2} = -P_{\text{ext}} - CK_0(\sqrt{i\omega/a^2}R_2) \\ a_fR_2 + \dfrac{b_f}{R_2} = \dfrac{b_2}{R_2} + m_0C\dfrac{1}{K_f\sqrt{i\omega/a^2}}K_1(\sqrt{i\omega/a^2}R_2). \end{cases} \tag{B.9}$$

Solving this set of equations and setting $\mu_f = 0$, we derive an equation for the displacement of the mudcake:

$$u_r^{\text{II}}(R_0) = a_1R_0 + \frac{b_1}{R_0} = \frac{R_0}{2}\frac{P_f\left[\left(d_1+\left(\frac{R_0}{R_1}\right)^2\right)\left[1+\frac{\Psi(z)}{K_f}\left(1-\left(\frac{R_1}{R_2}\right)^2\right)\right]+\left(\frac{R_1}{R_2}\right)^2\frac{\Psi(z)}{\mu_1}\left(1-\left(\frac{R_0}{R_1}\right)^2\right)\right]-P_{\text{ext}}(d_1+1)}{\mu_1 d_1\left(1-\left(\frac{R_0}{R_1}\right)^2\right)\left[1+\frac{\Psi(z)}{K_f}\left(1-\left(\frac{R_1}{R_2}\right)^2\right)\right]+\Psi(z)\left(\frac{R_1}{R_2}\right)^2\left[1+d_1\left(\frac{R_0}{R_1}\right)^2\right]}, \tag{B.10}$$

$$\tilde{\Phi}(z) = \frac{K_f z K_0(z)}{m_0 K_1(z)}; \quad z = \sqrt{i\omega\frac{\eta m_0}{k_0 K_f}}R_2; \quad \Psi(z) = \mu_2\frac{\tilde{\Phi}(z)}{2\mu_2+\tilde{\Phi}(z)}.$$

The corresponding velocity in the frequency representation is related to displacement (B.10) by the factor $i\omega$: $v(\omega) = i\omega u(\omega)$. We limit our consideration to the case $R_1 = R_2$, i.e., to the case of a mud layer immediately adjacent to the borehole wall. Then, we have

$$v_{CL}(R_0,\omega) = \frac{i\omega R_0}{2} \times \frac{(P_f - P_{\text{ext}})[1+d_1] + P_f\left(1-\left(\frac{R_0}{R_1}\right)^2\right)\left[\frac{\Psi(z)}{\mu_1}-1\right]}{d_1\mu_1\left(1-\left(\frac{R_0}{R_1}\right)^2\right)+\Psi(z)\left(1+d_1\left(\frac{R_0}{R_1}\right)^2\right)}. \tag{B.11}$$

For a shell of zero thickness ($R_0 = R_1$), Eq. (B.11) takes the form

$$v_{CL}(R_0,\omega) = i\omega R_0\frac{P_f - P_{\text{ext}}}{2\Psi(z)} = i\omega R_0\Delta P\left[\frac{1}{2\mu_2}+\frac{m_0}{K_f z}\frac{K_1(z)}{K_0(z)}\right]. \tag{B.12}$$

Expression (B.12) coincides with Eq. (A.8) correct to the term $i\omega R_0\Delta P/2\mu_2$, which represents the velocity determined by the elastic motion of the borehole walls.

APPENDIX C

(THE STATISTICAL MODEL)

In the two preceding appendixes, we considered the model of a highly viscous liquid and the elastic shell model. These models yielded entirely different results. In the case of a highly viscous liquid, the filtration flows can be neglected. On the other hand, in the elastic shell model, a one-centimeter-thick mudcake practically does not affect the velocity of the fluid near the borehole walls.

This discrepancy between the results required the development of a more realistic model. In such a model, the mudcake is considered as a thin elastic cylindrical shell fixed in an arbitrary way to the borehole walls. For simplicity, we assume that the positions of the fixing points obey cylindrical symmetry. The distance between the neighboring fixing points L is a random value whose distribution is described by some probability density. The probability density function is unknown, but we can assume that its behavior is similar to the Gaussian distribution, because L depends on many parameters. Then, the probability density function should have a dome-like shape characterized by a mean value and a variance of L; it should be defined within the interval $0 < L < \infty$ and normalized to unity.

In this paper, for simplicity and convenience, we use the probability density function in the form

$$G(L) = \frac{1}{\tau^{s+1}s!}L^s\exp(-L/\tau), \tag{C.1}$$

where s is a positive integer.

Averaging of the Mudcake Displacement within a Single Cell

The equilibrium equation for a thin cylindrical plate in the absence of the dependence on the azimuth angle has the form [12]

$$\frac{\partial^4}{\partial x^4}\xi + \frac{12}{R^2h^2}\xi = \frac{\Delta P}{D},$$
$$D \equiv \frac{Eh^3}{12(1-\sigma^2)}, \tag{C.2}$$

where ξ is the radial displacement of the plate, E is the Young modulus, σ is the Poisson ratio, h is the plate thickness, R is the borehole radius, and ΔP is the difference between the pressures on the two sides of the plate: $\Delta P = P_f - P_{\text{out}}$.

The boundary conditions have the form

$$\xi(x) = 0 \text{ and } \frac{\partial}{\partial x}\xi(x) = 0 \text{ at } x = 0, L.$$

These boundary conditions allow us to consider the plate fixed at many different points as a set of individual cells, which are fixed at their ends and have different lengths. We introduce the notation

$$k^4 = \frac{12}{h^2R^2}. \tag{C.3}$$

Evidently, a particular solution to inhomogeneous equation (C.2) is $\xi_1 = \Delta P/Dk^4$, and the general solution to the homogeneous equation can be easily determined by applying the substitution $\xi = \exp(\lambda x)$. From the condition that the displacements be real and from the boundary conditions, we obtain the expression for the displacement ξ of a cylindrical shell fixed at the edges. Averaging this expression for ξ over x, we obtain

$$\bar{\xi} = \frac{1}{L}\int_0^L \xi(x)dx = \frac{\Delta P}{Dk^4}F(b), \tag{C.4}$$

where

$$F(b) = 1 - \frac{2}{b}\frac{\sinh(2b) + \sin(2b) - 2[\sin(b)\cosh(b) + \sinh(b)\cos(b)]}{\cosh(2b) + \cos(2b) - 2} \tag{C.5}$$

and $b = kL/\sqrt{2}$.

The function $F(b)$ has the following asymptotics: $F(b) \xrightarrow{b\to 0} b^4/180$ and $F(b) \xrightarrow{b\to\infty} 1 - 2/b$. Since the function $F(b)$ has a fairly complex form, we select an approximating function of a simpler form for the subsequent calculations:

$$f(b) = b^4/(b+\delta)^4. \tag{C.6}$$

When b is small, the function $f(b)$ behaves as $(b/\delta)^4$ and, when b is large, $f(b) \approx 1 - 4\delta/b$. By varying the parameter δ, it is possible to obtain a coincidence of the functions $F(b)$ and $f(b)$ for different values of b.

Averaging of the Mudcake Displacement over All Cells

Let the distribution of the cell length L be described by the probability density $G(L)$. Then, the procedure of averaging over L has the form

$$\langle\bar{\xi}\rangle = \int_0^\infty \bar{\xi}(L)G(L)dL = \frac{\Delta P}{Dk^4}\int_0^\infty G(L)F(b(L))dL. \tag{C.7}$$

Performing the integration in (C.7), we replace the function $F(b)$ in the integrand by the function $f(b)$ given by Eq. (C.6). The parameter δ is chosen so as to make the functions $F(b)$ and $f(b)$ as close as possible to each other near the maximum of the function $G(b(L))$ given by Eq. (C.1). In this case, we obtain

$$\langle\bar{\xi}\rangle = \frac{\Delta P}{Dk^4\tau^{s+1}s!}\int_0^\infty \frac{b^4L^s}{(b+\delta)^4}e^{-\frac{L}{\tau}}dL$$
$$= \frac{\Delta P\alpha^{s+1}}{Dk^4s!}\int_0^\infty \frac{b^{s+4}}{(b+\delta)^4}e^{-\alpha b}db, \tag{C.8}$$

where

$$\alpha = \sqrt{2}/\tau k. \tag{C.9}$$

This integral can be calculated. Then, the average displacement will have the form

$$\langle\bar{\xi}\rangle = \frac{\Delta P}{Dk^4}\Phi(\alpha\delta, s).$$

Here,

$$\Phi(\alpha\delta, s)$$
$$= \frac{(\alpha\delta)^{s+1}}{s!}(-1)^s\frac{\partial^{s+4}}{\partial(\alpha\delta)^{s+4}}\left(-\frac{(\alpha\delta)^3}{6}e^{\alpha\delta}\text{Ei}(\alpha\delta)\right),$$

where $\text{Ei}(x) = \int_1^\infty \frac{e^{-xt}}{t}dt$.

The analytical form of the function $\Phi(\alpha\delta, s)$ is rather complicated. Since our aim is to obtain the most simple

function that is convenient for calculations and adequately describes the main features of the behavior of the physical quantity, we again use an approximating function. It has the form

$$\Phi'(\alpha\delta, s) = \frac{1}{2}\left[\exp\left(-\frac{A_1}{1+B_2 s}\alpha\delta\right) + \exp\left(-\frac{A_2}{1+B_2 s}\alpha\delta\right)\right], \quad \text{(C.10)}$$

where the parameters A_1, A_2, B_1, and B_2 are chosen so as to obtain the closest approximation of the initial function. In the calculations, we used the values $A_1 = 2$, $A_2 = 25$, $B_1 = 1$, and $B_2 = 4$.

Substituting the initial parameters of the problem, we obtain

$$\langle\bar{\xi}\rangle = \frac{\Delta P(1-\sigma^2)}{Eh}R^2\frac{1}{2} \times\left[\exp\left(-\frac{2}{1+s}\frac{\delta\sqrt{hR}}{\sqrt[4]{3\tau}}\right) + \exp\left(-\frac{25}{1+4s}\frac{\delta\sqrt{hR}}{\sqrt[4]{3\tau}}\right)\right] \equiv \frac{\Delta P}{\tilde{W}_{MC}}. \quad \text{(C.11)}$$

In this formula, the displacement is expressed through the pressure difference between the two sides of the shell. Now, we introduce in our consideration the permeable stratum and the filtration flows from it (as in the previous model). Since we already averaged the displacement along the borehole, we now consider the mudcake as an ordinary (not fixed) shell. Then, by analogy with (B.1)–(B.8), we obtain the set of equations

$$\begin{cases} \langle\bar{\xi}\rangle \equiv u = (P_f - P_{\text{out}})/\tilde{W}_{MC} \\ P_{\text{out}} = P_{\text{ext}} + CK_0(z) \\ u = m_0 C\dfrac{R}{K_f z}K_1(z). \end{cases} \quad \text{(C.12)}$$

Solving this set, we obtain

$$u = \frac{(P_f - P_{\text{ext}})}{\tilde{W}_{MC} + K_f z K_0(z)/(m_0 R K_1(z))}. \quad \text{(C.13)}$$

The corresponding velocity in the frequency representation is related to displacement (C.13) by the factor $i\omega$: $v(\omega) = i\omega u(\omega)$. It is also necessary to take into account the elastic motion of the borehole walls. This is accomplished by introducing an additional term in the expression for the velocity. The final result has the form

$$\frac{v_{\text{tot}}}{i\omega R} = (P_f - P_{\text{ext}}) \times\left[\frac{1}{2\mu} + \frac{1}{R\tilde{W}_{MC} + K_f z K_0(z)/(m_0 K_1(z))}\right]. \quad \text{(C.14)}$$

When the thickness of the mudcake tends to zero, we have $\tilde{W}_{MC} \longrightarrow 0$, and Eq. (C.14) is reduced to Eq. (B.12).

REFERENCES

1. K. W. Winkler, H. Liu, and D. L. Johnson, Geophysics **54**, 66 (1989).
2. M. A. Biot, J. Acoust. Soc. Am. **28**, 168 (1956).
3. V. N. Nikolaevskiĭ, *Mechanics of Saturated Porous Media* (Nedra, Moscow, 1977).
4. P. A. Francis, M. R. P. Eigner, I. T. M. Patey, and I. S. C. Spark, in *Expanded Abstracts of the SPE European Formation Damage Conference* (Soc. Petrol. Eng., The Hague, 1995), p. 101.
5. H. Liu and D. L. Johnson, J. Acoust. Soc. Am. **101**, 3322 (1997).
6. B. W. Tichelaar, Hsui-Liu Liu, and D. L. Johnson, J. Acoust. Soc. Am. **105**, 601 (1999).
7. A. M. Ionov, O. V. Kozlov, and G. A. Maksimov, Akust. Zh. **41**, 603 (1995) [Acoust. Phys. **41**, 529 (1995)].
8. A. M. Ionov and G. A. Maximov, Geophys. J. Int. **124** (3), 888 (1996).
9. J. E. White, *Underground Sound. Application of Seismic Waves* (Elsevier, Amsterdam, 1983; Mir, Moscow, 1986).
10. G. A. Maksimov and M. E. Merkulov, in *Proceedings of Scientific Session MIFI-99* (MIFI, Moscow, 1999), Vol. 1, p. 159.
11. *Handbook of Mathematical Functions*, Ed. by M. Abramowitz and I. A. Stegun (Dover, New York, 1971; Nauka, Moscow, 1979).
12. L. D. Landau and E. M. Lifshits, *Course of Theoretical Physics*, Vol. 7: *Theory of Elasticity*, 4th ed. (Nauka, Moscow, 1987; Pergamon, New York, 1986).

Translated by E. Golyamina

Acoustical Physics, Vol. 48, No. 2, 2002, pp. 201–208. Translated from Akusticheskiĭ Zhurnal, Vol. 48, No. 2, 2002, pp. 239–247.

Fish Target Strength Estimation Using Multiple Echo Statistics[1]

M. Moszynski

Technical University of Gdansk, ul. Narutowicza 11/12, 80-952 Gdansk, Poland

e-mail: marmo@pg.gda.pl

Received June 26, 2001

Abstract—When fish strength is estimated indirectly from the sounder echo amplitudes, the inverse techniques of solving the so-called "single-beam integral equation" are quite satisfactorily used. This approach needs prior knowledge of the beam pattern PDF, as it represents the kernel of the integral equation to be solved and is usually calculated under the assumption of a uniform spatial distribution of fish. However, it may be shown that in some cases this assumption is not necessarily justified. For instance, when the density of fish increases, one receives multiple echoes from the same single fish in successive transmissions, which results in observing so-called fish echo traces. Typically used fish counting methods are either simple direct echo counting statistics or fish traces statistics [1]. Increased fish concentration is not only the reason of multiple echo formation resulting in the fish traces in consecutive pings. As it is easily seen from the geometry of the phenomenon, even a relatively low-density fish aggregation forms multiple echoes and, hence, fish traces if the vessel (or fish) relative speed is low enough and the beam pattern angular width (sampling volume) is large enough. In some situations, the uniform assumption works properly only for the cases of large numbers of samples. Taking into account this phenomenon, the accuracy of the solution can be improved by including the fish traces counting statistics in calculating the beam pattern PDF. In this paper, two different models of fish traces statistics are investigated: one assuming the vessel movement with stationary fish and the other with a stationary vessel and moving fish. Both approaches are modeled numerically and verified experimentally using the data obtained from a dual-beam system. The comparison of both approaches, i.e., for single echo traces and multiple echoes, is carried out using Windowed Singular Value Decomposition (WSVD) and Expectation Maximization and Smoothing (EMS) inverse techniques of fish target strength estimation in both the absolute domain (backscattering length estimation) and the logarithmic domain (target strength estimation). © *2002 MAIK "Nauka/Interperiodica".*

INTRODUCTION

Indirect methods of fish target strength estimation using single beam echosounder systems fall into the category of inverse problems in which the probability density function (PDF) of target strength is estimated from fish echoes. Due to hydroacoustics system characteristics, the reconstruction of the fish target strength PDF is based on incomplete data [2]. This kind of problem is an example of the statistical linear inverse problem, which is typically ill-conditioned and can be solved using direct inverse techniques, based on regularization or iterative techniques in which additional constraints are specified. In most cases, the observed data are restricted to the certain echo amplitude dynamic range limited by the side-lobe level. This approach allows omission of the problem of ambiguity of the beam pattern function [2]. However, to calculate this function, an additional assumption on the spatial distribution of fish in the beam pattern volume is to be made.

The statistics of the so-called fish traces, which are represented by multiple echoes received from the same fish in consecutive echosounder transmissions, and beam pattern probability density function (PDF) seem to be two absolutely separate and unrelated issues. The first one is used in the analysis of fish counts estimates [1], whereas the second one plays a crucial role in indirect fish target strength estimation [2]. However, it appears that these two seemingly separate problems are closely related when one considers the PDF of the beam pattern in the context of multiple echoes from individual fish.

The widely used assumption of a uniform spatial distribution of fish in the water column leads to a sine-law distribution of the angular position of the fish. This assumption is valid only for the case of single or non-multiple echoes received from individual fish in consecutive pings. However, when acquiring actual data from acoustic surveys, the multiple or correlated echoes may be collected from the same fish forming the fish traces.

In this paper, the analysis of two models of fish traces is presented and the PDF's of the number of multiple echoes occurring in fish traces and the angular position of the fish are also derived. Later on, the beam pattern PDF is calculated based on the same assumptions as in the case of the fish traces statistics. Finally, the beam pattern PDF is used as the kernel of the "single beam integral equation" for reconstructing the fish target strength estimate from the echo data.

[1] This article was submitted by the author in English.

1063-7710/02/4802-0201$22.00 © 2002 MAIK "Nauka/Interperiodica"

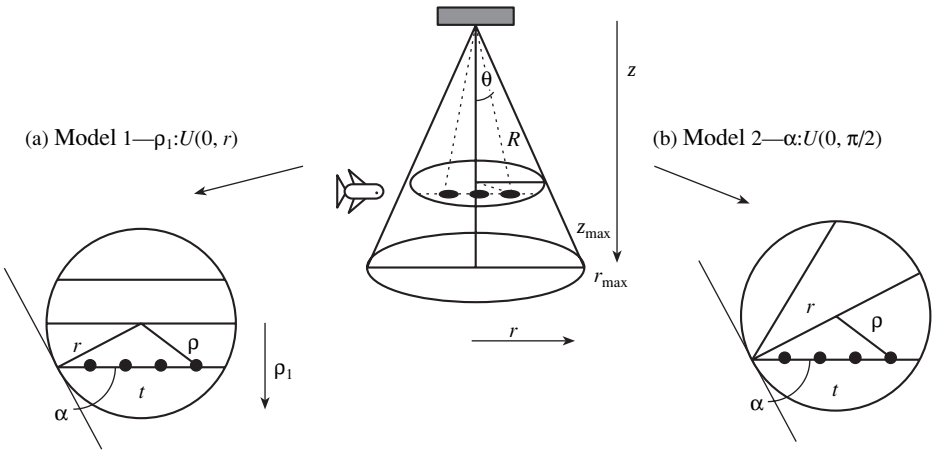

Fig. 1. Geometry of two models for the number of echoes in fish traces analysis.

FORMULATION OF THE PROBLEM

Two models of the fish traces statistics, the geometry of which is illustrated in Fig. 1, have been considered:

(1) a moving vessel model with stationary fish,

(2) a moving fish model with a stationary vessel.

In the first model, the uniform vessel movement with stationary fish is assumed as detailed in Fig. 1a. The second model assumes a fish movement along an arbitrary path in the transducer beam pattern cross-section, as shown in Fig. 1b.

Let us further assume that the distribution of the variable z representing the depth at which fish appears in the conical area defined by observation angle θ_{max} is uniform, i.e.,

$$p_z(z) = \frac{1}{z_{max}}, \tag{1}$$

where z_{max} represents the maximum depth. Due to the linear relation between depth and radius of a circular slice $z = r\tan\theta_{max}$, the distribution of the random variable r also becomes uniform, i.e.,

$$p_r(r) = \frac{1}{r_{max}}, \tag{2}$$

where $r_{max} = z_{max}/\tan\theta_{max}$ is the maximum possible radius of the circular cross-section of the beam pattern.

MOVING VESSEL AND STATIONARY FISH MODEL

In the first model, all fish traces represent parallel lines crossing every circular slice of the observation cone. Thus, the fish position in consecutive pings can be represented by equidistant points on parallel chords. The unknown statistics of the number of fish N_1 can be derived from the geometrical equation:

$$N_1 = \frac{2}{\Delta d}\sqrt{r^2 - \rho_1^2}, \tag{3}$$

where Δd represents the sampling distance between consecutive points. The random variable r represents the radius of a circle, and the random variable ρ_1 represents the distance between the center of that circle and the trace of the fish. In this model, one assumes that a fish may appear in the circle in such a way that the distance from the centre to the trace of the fish is equally probable, so that, in other words, the distribution of ρ_1 is uniform in a range interval $(0, r)$. This allows us to treat the random variable ρ_1 as a product of two random variables $\rho_1 = r\,u$, where the variable u is represented by a normalized uniform distribution. Substituting this relation into Eq. (3), we obtain:

$$N_1 = \frac{2}{\Delta d}\, r\sqrt{1 - u^2}. \tag{4}$$

Now we can treat again the number N of fish traces as a product of two random variables $x = 2r/\Delta d$ and $y = (1 - u^2)^{1/2}$ and calculate the probability distribution function as an integral equation $p_z(z) = \int p_x(x)p_y(z/x)/x\,dx$, which gives the PDF of N as

$$p_{N_1}(N) = \int\limits_{\frac{\Delta d N_1}{2r_{max}}}^{1} \frac{\Delta d}{2r_{max}} \frac{y}{\sqrt{1 - y^2}} \frac{du}{y}, \tag{5}$$

which, in its turn, yields

$$p_{N_1}(N) = \frac{\Delta d}{2r_{max}}\left(\frac{\pi}{2} - \arcsin\frac{\Delta d N}{2r_{max}}\right). \tag{6}$$

The expression $\Delta d/(2r_{max})$ in Eq. (6) may be treated as the parameter of the data measurement system and can

be calculated from the relation for the mean value of the random variable:

$$E\{N_1\} = \frac{\Delta d}{2r_{\max}}\frac{\pi}{8}. \quad (7)$$

The probability density function of the number of echoes in fish traces for this model is presented in Fig. 2.

MOVING FISH AND STATIONARY VESSEL MODEL

In the second model, one assumes that the fish crosses an arbitrary circular cross-section of the conical sampled volume with an equally probable angle α. From geometrical relations, the number of fish traces can be expressed as

$$N_2 = \frac{2}{\Delta d} r\sin\alpha, \quad (8)$$

where the random variable α represents the crossing angle. The unknown distribution of the number of fish echoes in the fish trace N_2 can be derived again from the equation determining the PDF of the product of two random variables $x = 2r/\Delta d$ and $y = \sin\alpha$. Assuming a uniform distribution of the angle α, we obtain:

$$p_{N_2}(N) = \int_{\frac{\Delta d N_2}{2r_{\max}}}^{1} \frac{\Delta d}{2r_{\max}}\frac{2}{\pi}\frac{1}{\sqrt{1-y^2}}\frac{dy}{y}, \quad (9)$$

which eventually leads to:

$$p_{N_2}(N) = \frac{\Delta d}{\pi r_{\max}}\operatorname{arctanh}\sqrt{1-\left(\frac{\Delta d}{2r_{\max}}N_2\right)^2}. \quad (10)$$

The mean value of the random variable N_2 with a PDF in the form of Eq. (10) is given by:

$$E\{N_2\} = \frac{\Delta d}{2r_{\max}}\frac{1}{\pi}. \quad (11)$$

The probability density function of the number of echoes in fish traces for this model is presented in Fig. 3.

STATISTICS OF THE ANGULAR POSITION OF FISH FOR MULTIPLE ECHO TRACES

Let us now consider the distribution of the angular position of fish θ in the transducer beam that is necessary for calculating the beam pattern PDF. The random variable θ can be expressed as (see Fig. 4):

$$\theta = \arccos\frac{z}{R} = \arccos\frac{1}{\sqrt{1+(\rho/z)^2}}, \quad (12)$$

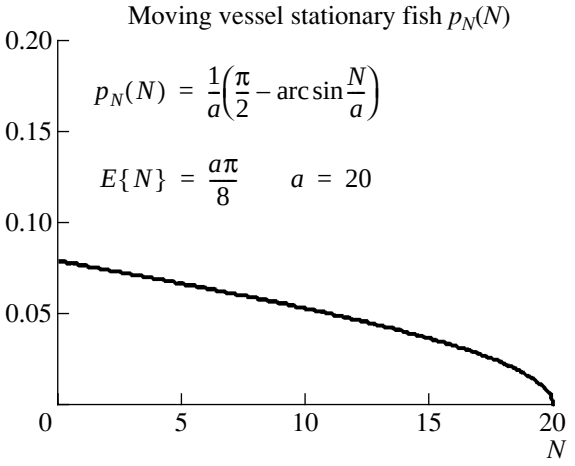

Fig. 2. Theoretical probability density function (PDF) of the number N of echoes in fish traces for moving vessel and stationary fish model.

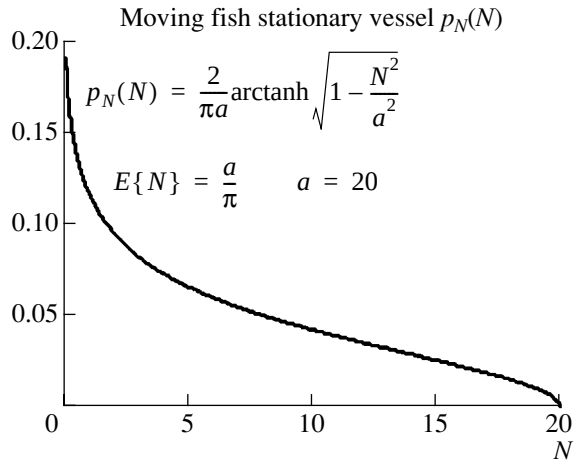

Fig. 3. Theoretical PDF of the number N of echoes in fish traces for moving fish and stationary vessel model.

where the random variable z represents the fish depth and the random variables R and ρ represent the fish position coordinates related by the equation $R^2 = \rho^2 + z^2$. Let us also consider the random variable t called the trace distance, which represents the distance of the fish from the crossing point of the circular slice. Assuming that the fish swims on the chord and is "sampled" uniformly in the consecutive pings, we can treat its PDF as uniform in a range $(0, 2r\sin\alpha)$. Thus, the trace distance random variable can be expressed as $t = 2r\sin\alpha\, u$, where u again has a normalized uniform distribution. Taking into account the cosine law in the nonright-angled triangle (Fig. 4) we obtain:

$$\begin{aligned}\rho^2 &= r^2 + t^2 - 2rt\sin\alpha \\ &= r^2(1-(2\sin\alpha)^2(u-u^2)).\end{aligned} \quad (13)$$

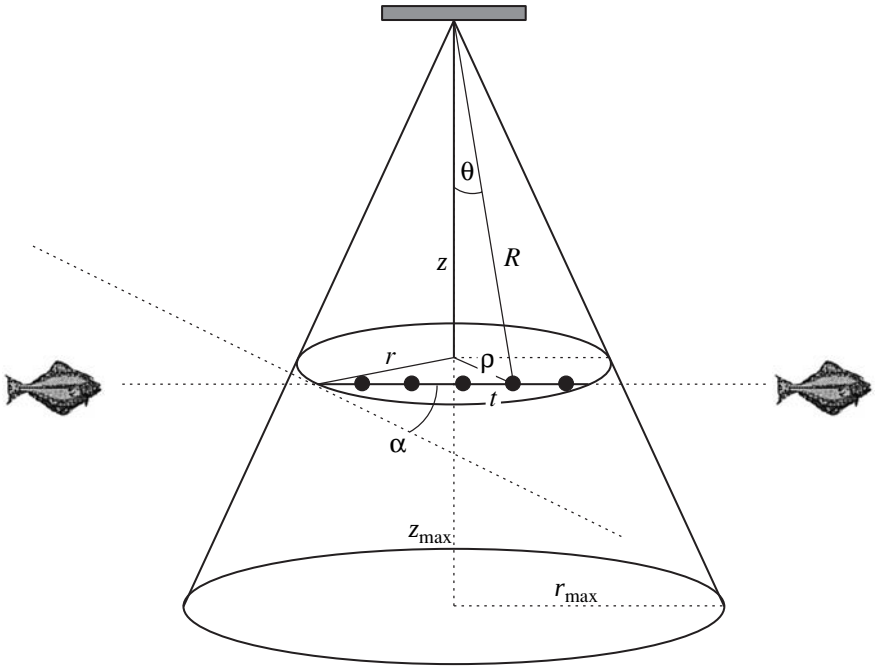

Fig. 4. Geometry of multiple echo traces of the fish.

Substituting $z = r\tan\theta_{max}$, which removes the z dependence from Eq. (5) and the r dependence in Eq. (6), we receive the equation for the angular position θ:

$$\theta = \arccos\frac{1}{\sqrt{2-(2\sin\alpha)^2(u-u^2)}}. \qquad (14)$$

Equation (7) shows that the distribution of the angular position θ depends only on the distribution of the crossing angle α as random variable u represents uniform distribution resulting in the PDF of variable $u - u^2$ expressed as $p_{u-u^2}(x) = (1/4 - x)^{-1/2}$. The distribution of the variable α depends on the angular relations between fish and vessel movement [2] and can change from sine-law, when the stationary fish model is used, to uniform distribution when the stationary vessel model is used. Both models give the distribution of the variable $4\sin^2\alpha$ as $p_{4\sin^2\alpha}(x) = (4x - x^2)^{-1/2}/\pi$ for the sine-law model or $p_{4\sin^2\alpha}(x) = (4 - x)^{-1/2}/4$ for the uniform distribution one. Finally, using the formulae for the PDF of the product of random variables and transforming according to Eq. (7), we receive for the first and the second model, respectively:

$$p_{\theta 1}(\theta) = \frac{1}{\tan^2\theta_{max}} K\left(\frac{\tan\theta}{\tan\theta_{max}}\right)\frac{\sin\theta}{\cos^3\theta}, \qquad (15)$$

$$p_{\theta 2}(\theta) = \frac{1}{\tan^2\theta_{max}}\frac{1}{\sqrt{1-\left(\frac{\tan\theta}{\tan\theta_{max}}\right)^2}}\frac{\sin\theta}{\cos^3\theta}, \qquad (16)$$

where $K(k) = \int_0^{\pi/2}(1 - k^2\sin^2\varphi)^{-1/2}d\varphi$ represents a complete elliptic integral of the first kind.

Both distributions are illustrated in Fig. 5. It is worth to note that, as one could expect, there are more echoes received from larger angles, which results in an increase in the distribution as compared to the sinelike distribution known for the case of nonmultiple echoes received from a single fish.

BEAM PATTERN PDF BASICS

To derive the beam pattern PDF, let us first consider an ideal circular piston transducer in an infinite baffle, for which the one-way beam pattern function b is given by

$$b(\theta) = \frac{2J_1(x)}{x}, \qquad (17)$$

where x is defined by $x = ka\sin\theta$, k is the wave number, a is the transducer radius, and J_n is the Bessel function of the first kind of order n. The logarithmic form of the two-way pattern in decibels is derived by the simple transform $B(\theta) = 10\log b(\theta)^2 = 20\log b(\theta)$.

The beam pattern PDF $p_B(B)$ represents the kernel function of the inverse problem for a two-way system and can be obtained from its absolute variable form

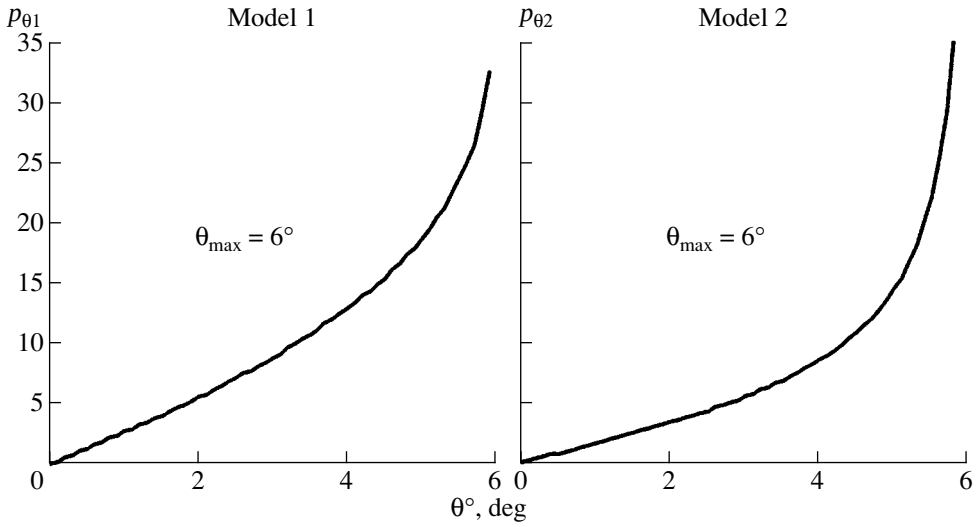

Fig. 5. Theoretical distribution of the angular position θ for the two analysed models.

p_b, which can be expressed as a parametric function $p_b(b) = (b^2(\theta), p_b(\theta))$ with the angle θ as a parameter:

$$p_b(b) = \left(\left(\frac{2J_1(x)}{x} \right)^2, \frac{p_\theta(\theta)\tan\theta}{\left| \frac{8J_1(x)J_2(x)}{x} \right|} \right), \qquad (18)$$

where p_θ is a probability density function of the random angular position of fish. Then, using a logarithmic transform of variables $B(b) = 20\log b$, its PDF relation can be written as

$$p_B(B) = \frac{\ln 10}{20} \left| 10^{\frac{B}{20}} \right| p_b\left(10^{\frac{B}{20}} \right). \qquad (19)$$

A typical approach in the PDF calculation of the angular fish position p_θ is based on the assumption of a uniform distribution of fish in the water column (further called nonmultiple echoes statistics), which gives the sine-law distribution of the angular position θ [1]:

$$p_\theta(\theta) = \frac{1}{1 - \cos\theta_{max}} \sin\theta, \qquad (20)$$

where θ_{max} is the maximum angle of the beam pattern involved in the calculation. However, as will be shown in the next section, for datasets obtained during a survey where several echoes from one fish are present in consecutive pings, a more accurate assumption should be made.

BEAM PATTERN PDF FOR AN ACTUAL SYSTEM

The way of calculating the beam pattern PDF for a Biosonics's dual-beam ESP (i.e., Echosounder Signal Processor) system is presented. The ESP system uses a dual-beam (6°/15°) digital echosounder of 420 kHz operating frequency and 0.4 ms pulse length. The calculation of the beam pattern is performed only for a narrow beam channel, as echo from this channel can be used for inverting the target strength of the fish. The beam pattern was fitted using the following approximation proposed in [1]:

$$b(\theta) = \left(1 - (1 - 2^{-\gamma}) \frac{(1 - \cos\theta)}{1 - \cos\theta_{3dB}} \right)^{\frac{1}{\gamma}}, \qquad (21)$$

where the exponential coefficient $\gamma = -0.1$ was fitted numerically to the actual pattern. The logarithmic transform and the inclusion of nonmultiple echo statistics, Eq. (20), leads to the equation

$$p_B(B) = \frac{\ln 10}{20} \frac{\gamma}{1 - 2^{-\gamma}} \frac{1 - \cos\theta_{3dB}}{1 - \cos\theta_{max}} 10^{\frac{\gamma B}{20}}, \qquad (22)$$

and the inclusion of multiple echo statistics, Eq. (15), leads to the equation

$$p_B(b) = \frac{\ln 10}{20} \frac{\gamma}{1 - 2^{-\gamma}} \times \frac{1 - \cos\theta_{3dB}}{\tan^2\theta_{max}} K\left(\frac{\tan\theta}{\tan\theta_{max}} \right) \frac{1}{\cos^3\theta} 10^{\frac{\gamma B}{20}}, \qquad (23)$$

where θ can be calculated as the inverse of $b(\theta)$ from Eq. (20):

$$\theta = \arccos(1 - (1 - 10^{0.05\gamma B})(1 - \cos\theta_{3dB})/(1 - 2^{-\gamma})).$$

Figure 6 illustrates the approximation of the actual beam pattern of a narrow beam channel and two PDF functions, one with nonmultiple echo assumption and the other with multiple echo assumption.

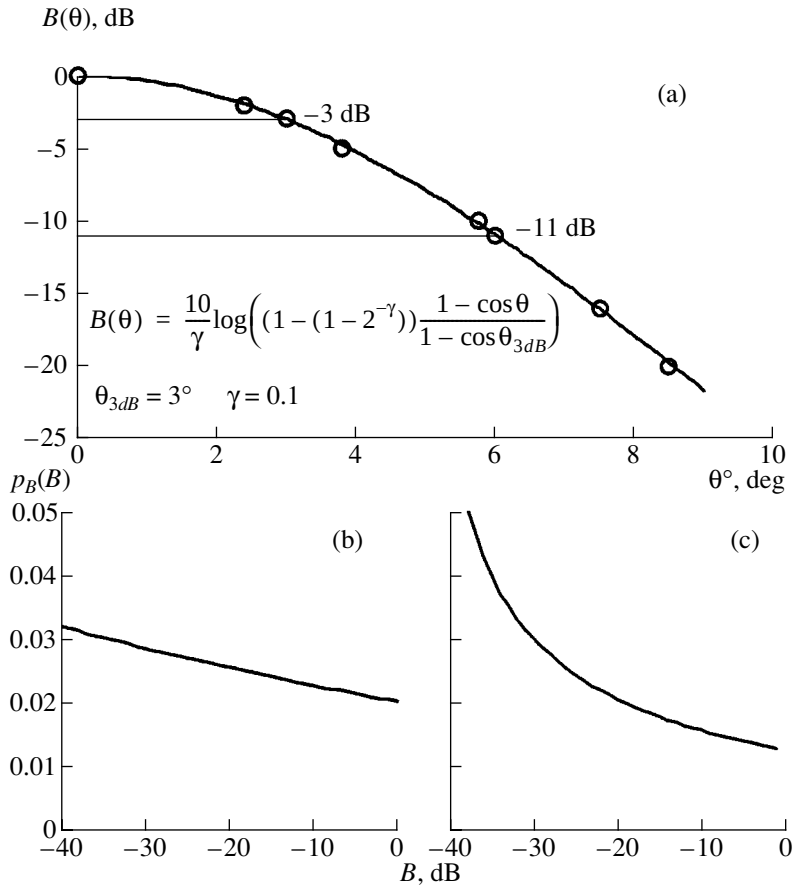

Fig. 6. (a) Beam pattern approximation, (b) beam pattern PDF for the nonmultiple echoes assumption, and (c) beam pattern PDF for the multiple echoes assumption.

SURVEY RESULTS

To justify the correctness of the presented analysis and validate its results, actual fish echo data was used. The data was acquired from an acoustic survey on pelagic fish populations (mostly salmon and trout) in Coeur d'Alene Lake, Idaho (provided by J.B. Hedgepeth, Biosonics Inc., Seattle and E. Parkinson, University of Vancouver, Canada) using a dual-beam digital echosounder of 420 kHz operating frequency and 0.4 ms pulse length. There were processed records of over 6500 pings from which over 10000 fish echoes were extracted for analysis and, using software algorithms, 2009 fish were counted. The distribution of the number N of multiple echoes in fish traces is shown in Fig. 7 in the form of a histogram. The results match Model 2 of distribution presented in Fig. 5. However, it is also possible that it matches Model 1 due to the border effect in obtaining the PDF estimate by the histogram technique (the range between $N = 0$ and $N = 1$ cumulates as only $N = 1$ has physical sense).

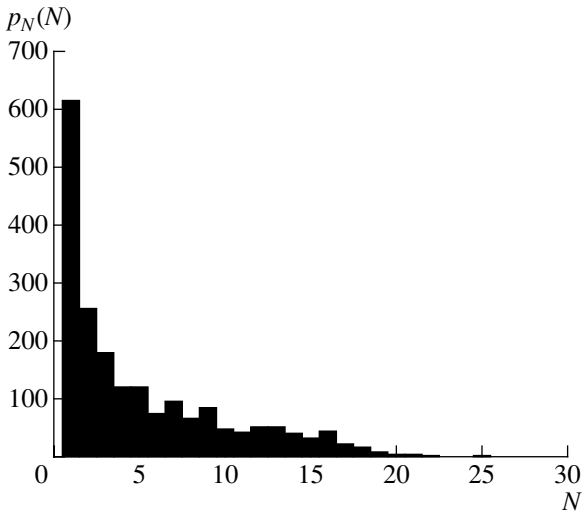

Fig. 7. Sample distribution of the number of multiple echoes in fish traces from survey.

Numerical experiments conducted on survey data show good agreement with the presented models of fish statistical behavior during measurements. The mean value of the distribution is equal to 5.3. It is worth noting that in practice it is possible that the complicated fish behavior can be modeled by a mixture of Model 1 and Model 2 due to the relative movement of the fish and the vessel. Model 2 with a uniform distribution of the crossing angle represents a more "random" case

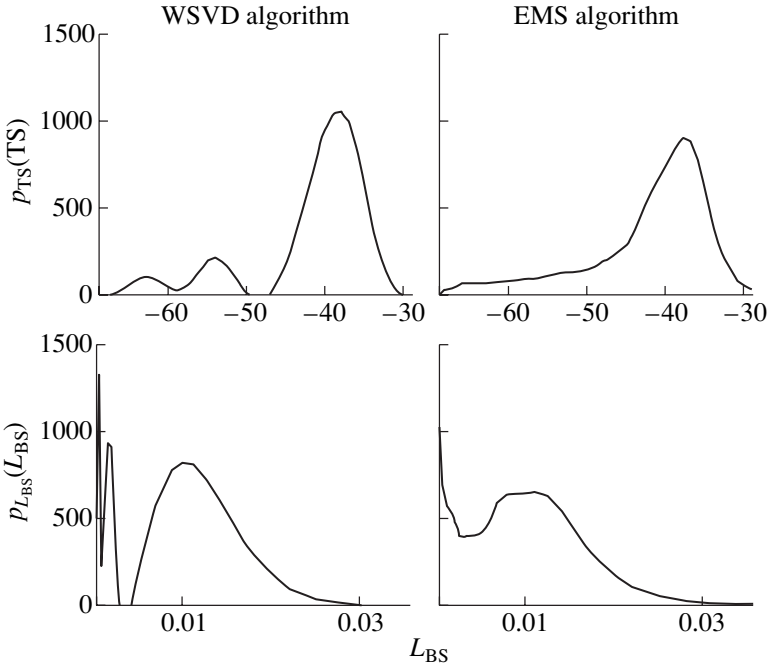

Fig. 8. Results of the fish target strength TS estimation and the backscattering length L_{BS} estimation using nonmultiple echo statistics.

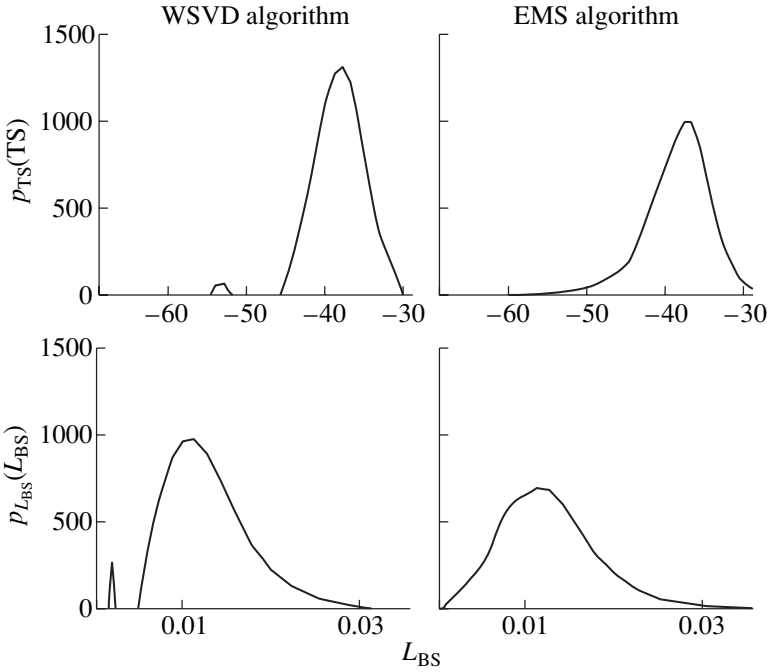

Fig. 9. Results of the fish target strength TS estimation and the backscattering length L_{BS} estimation using multiple echo statistics.

than Model 1 with its sine-law distribution of the crossing angle.

Two different inverse techniques were used to observe the difference in the results obtained by using both assumptions concerning multiple echoes cases. The first technique, Windowed Singular Value Decomposition with nonnegative constraint, as a direct method of calculation represents the classical approach to solving ill-conditioned integrals. The second technique is more sophisticated: Expectation, Maximization, and Smoothing based on an iterative algorithm with statistical constraints, which also seems to be the more robust inverse technique [3]. The results of the typically

used assumption of nonmultiple echoes statistics are presented in Fig. 8, and the results of using multiple echoes statistics are shown in Fig. 9.

CONCLUSION

Two different approaches to the statistics of fish echo traces in the calculation of the beam pattern PDF were analysed in this paper. When the data acquired during surveys contain multiple echoes from single fish, it appears that the typically used approach is not adequate. The presence of a multiple number of echoes in the fish traces can be verified numerically during data postprocessing, which may show that the more adequate approach needs to use the statistics of the number of multiple echoes in fish traces. The results presented in the paper allow use of multiple echo statistics for the beam pattern PDF calculation.

The results of using two different assumptions on the statistics of fish echo traces in the process of reconstructing the target strength and backscattering length of the fish population from single beam data are presented in the paper. When the data acquired during measurements contain multiple echoes from one fish, a more adequate approach is suggested. The presence of a multiple number of fish echo traces was verified numerically during data postprocessing resulting in a distribution of the number of multiple echoes in fish traces. The results allow one to use multiple echo statistics for the beam pattern calculation [4].

Figures 8 and 9 shows that both inverse techniques perform better when proper assumptions are made. It is worth noting that, when the kernel of the single-beam integral is properly chosen, the large artefacts in estimates disappear. It is especially observed in the case of reconstructing the backscattering length, which represents numerically a more ill-posed situation. The estimates presented in Fig. 8 suggested the existence of a large number of very small fishes, which after verification using the dual-beam data appeared to be incorrect. By contrast, the results presented in Fig. 9 clearly show the existence of one group of large fish with the other smaller group of smaller fish (using the WSVD method). Note also that the EMS method may oversmooth the PDF and create an impression of the existence of only one group of fish.

REFERENCES

1. R. Kieser and T. J. Mulligan, Can. J. Fish. Aquat. Sci. **41**, 451 (1984).
2. A. Stepnowski and M. Moszynski, J. Acoust. Soc. Am. **107**, 2554 (2000).
3. J. B. Hedgepeth, V. F. Gallucci, F. O'Sullivan, and R. E. Thorne, ICES J. Mar. Sci. **56** (1), 36 (1999).
4. M. Moszynski and A. Stepnowski, in *Proceedings of the Fifth European Conference on Underwater Acoustics* (Lyon, France, 2000).

Acoustical Physics, Vol. 48, No. 2, 2002, pp. 209–213. Translated from Akusticheskiĭ Zhurnal, Vol. 48, No. 2, 2002, pp. 248–252.

Nonstationary Self-Focusing of Sound Beams in a Vibrationally Excited Molecular Gas

N. E. Molevich

Korolev State Aerospace University, Samara, Moskovskoe sh. 34, Samara, 443086 Russia
e-mail: molevich@mb.ssau.ru

Received November 30, 1999

Abstract—Mechanisms of the self-action of sound in quasi-stationary gases with nonequilibrium-excited vibrational states of molecules are considered. It is demonstrated that the observation of a self-focusing of sound is possible in such media. Two mechanisms of the self-action of sound are responsible for the self-focusing in an acoustically active medium: the cooling of gas by sound and the excitation of acoustic streamings in opposite directions. © *2002 MAIK "Nauka/Interperiodica".*

Various mechanisms of the self-action of sound that lead to its defocusing or self-focusing in heat-conducting viscous media are considered in [1–11]. According to the estimates [4], it was demonstrated that the contribution to the self-action of a beam observed before the shock formation can be made only by the mechanisms related to the heating of the liquid because of the sound absorption and to the excitation of a longitudinal acoustic streaming. In liquids and gases in thermodynamic equilibrium the second mechanism always leads to the defocusing of sound, because the direction of the acoustic streaming coincides with the propagation direction of a sound beam. As for the thermal mechanism, it leads to a self-focusing in the case of the sound propagation in liquids (except for water) and to defocusing in the case of the sound propagation in a gaseous medium, because in the latter case, the sound velocity increases with temperature. Therefore, the sound propagates faster in the central, hotter, part of a beam than in the less heated peripheral region, and a diverging thermal lens is formed in the medium.

It was demonstrated in [12] that the situation changes in thermodynamically nonequilibrium media, e.g., in a vibrationally excited molecular gas. The dynamic properties of such a medium are determined by the second viscosity whose sign depends on the degree of nonequilibrium [13, 14]. In media with a negative second viscosity, the dissipated energy flux is directed from the medium to the wave, and such a medium acquires focusing properties. However, the strong inhomogeneity of nonequilibrium media prevents the observation of the self-focusing of sound. From this point of view, nonstationary nonequilibrium media are of interest. On the one hand, these media stay acoustically active, as was demonstrated in [15–17]. On the other hand, there is no need to provide for a special heat sink in them, and such a medium can be fairly homogeneous within the time $\Delta t < \tau_T = a^2/\chi$, where a is the characteristic dimension of the system and χ is the thermal diffusivity.

This paper considers both mechanisms of the self-action of sound propagating in a quasi-stationary, vibrationally excited gas.

The initial set of equations of gas dynamics has the form

$$\frac{d\rho}{dt} + \rho \mathrm{div}\mathbf{V} = 0,$$

$$\rho\frac{d\mathbf{V}}{dt} = -\nabla P + \eta\Delta\mathbf{V} + \left(\xi + \frac{\eta}{3}\right)\nabla\mathrm{div}\mathbf{V},$$

$$C_{V\infty}\frac{dT}{dt} + \frac{dE_v}{dt} - \frac{T}{\rho}\frac{d\rho}{dt} = C_{P\infty}\chi\Delta T \qquad (1)$$

$$+ \frac{\eta m}{\rho}\frac{\partial V_i}{\partial x_k}\left(\frac{\partial V_i}{\partial x_k} + \frac{\partial V_k}{\partial x_i} - \frac{2}{3}\delta_{ik}\frac{\partial V_i}{\partial x_i}\right) + Q,$$

$$\frac{dE_v}{dt} = \frac{E_e - E_v}{\tau_v(T,\rho)} + Q, \quad P = \frac{\rho T}{m}.$$

Here, $d/dt = \partial/\partial t + \mathbf{V}\nabla$; $\mathbf{V}$, ρ, P, and T are the velocity in the gas, its density, pressure, and temperature; η is the shear-viscosity coefficient; m is the molecular mass; E_v and E_e are the vibrational energy per molecule and its equilibrium value; τ_v is the vibrational relaxation time; and Q is the power of the energy source that maintains the excitation of vibrational states. For simplicity, we assume that Q, χ, and η are independent of T and ρ; $C_{V\infty}$ and $C_{P\infty}$ are the heat capacities of translational and rotational degrees of freedom (and also of equilibrium vibrational modes) at constant volume and pressure. The equations are written in terms of energy units. In the case of cylindrically symmetric beams, the

vector **V** has two components: the longitudinal component U and the transverse component W. The transverse velocity component W, which results from the divergence, is the quantity of a higher degree of smallness than U.

We try a solution to Eqs. (1) in the form

$$\begin{aligned} U &= U^{(0)}(r, x, t) \\ &+ \frac{U^{(1)}}{2}(r, x, t)\exp\left[-i\int\omega dt + ikx\right] + \text{c.c.}, \\ P &= P_0(t) + P^{(0)}(r, x, t) \\ &+ \frac{P^{(1)}}{2}(r, x, t)\exp\left[-i\int\omega dt + ikx\right] + \text{c.c.}, \end{aligned} \tag{2}$$

and analogously, for other components, where ω and k are the frequency and the wave vector of an acoustic wave. In a quasi-stationary approximation, the parameters of a nonequilibrium medium must change slowly in comparison with ω, i.e.,

$$\frac{1}{P_0}\frac{\partial P_0}{\partial t} = \frac{1}{T_0}\frac{\partial T_0}{\partial t} = \frac{S}{\tau_v C_{V\infty}} \ll \omega,$$
$$\frac{1}{\rho_0}\frac{\partial \rho_0}{\partial t} = 0,$$

where $S = (E_v^0 - E_e^0)/T_0$ is the degree of nonequilibrium in the medium and E_v^0 and E_e^0 are the unperturbed values of the vibrational energy and its equilibrium value. In addition, the length of an acoustic pulse must lie in the range $\omega^{-1} \ll t_i < \tau_T$.

The acoustic streaming $U^{(0)}$ caused by an acoustic wave of frequency ω is assumed to be incompressible. We use the geometric-acoustics approximation, in which $U^{(0)}$, $U^{(1)}$, $P^{(0)}$, $P^{(1)}$, and other complex amplitudes are assumed to be functions slowly varying with t, x, and r, which satisfy the condition

$$\frac{\partial}{\omega\partial t} \sim \frac{\partial}{k\partial x} \sim (\nabla_\perp)^2 k^{-2} \sim \varepsilon,$$

where ε is the smallness parameter.

The geometric-acoustics approximation is applicable when the beam width is $a > 2\pi/k$. The complex amplitudes for a high-frequency acoustic wave ($\omega\tau_v \gg 1$) are linearly related:

$$\begin{aligned} T^{(1)} &= U^{(1)}U_\infty m/C_{P\infty}, \quad P^{(1)} = U^{(1)}U_\infty\rho_0, \\ \rho^{(1)} &= U^{(1)}\rho_0/U_\infty, \quad W^{(1)} = U_\infty\nabla_\perp U^{(1)}/i\omega, \end{aligned} \tag{3}$$

where $\nabla_\perp$ is the transverse gradient, $U_\infty = \sqrt{\gamma_\infty T_0/m}$ is the velocity of high-frequency sound, and $\gamma_\infty = C_{P\infty}/C_{V\infty}$.

Substituting Eqs. (2) with the relations between the components given by Eqs. (3) into the set of equations (1), we obtain a system of three reduced equations describing the self-action of sound.

The equation that determines the sound amplitude variation has the form

$$\left(\frac{\partial}{\partial x} + \frac{1}{U_\infty}\frac{\partial}{\partial t} - \frac{i}{2k}\Delta_\perp + g\right)U^{(1)} = -\frac{ik}{2}U^{(1)}\left(\frac{2U^{(0)}}{U_\infty} + \frac{T^{(0)}}{T_0}\right). \tag{4}$$

This equation ignores the cubic terms $\sim U^{(1)}|U^{(1)}|^2$, which correspond to an inertialess change of state [7, 8] and, according to [4], make no significant contribution to the self-action of sound at distances $L < L_p$, where L_p is the distance of shock formation. If the characteristic length of self-focusing is $L_F > L_p$, self-focusing is also possible [5, 18, 19] but difficult to describe analytically, and this case is beyond our consideration. The terms on the right-hand side of Eq. (4) correspond to two mechanisms of self-action: the excitation of acoustic streaming and the heating of the medium by sound. The dissipation coefficient is $g = \delta + g_V$, where

$$\delta = \frac{\omega^2}{2U_\infty^3}\left(\frac{4}{3}\frac{\eta}{\rho_0} + \frac{\chi}{C_{V\infty}}\right)$$

is the coefficient of sound absorption in a heat-conducting viscous medium,

$$g_V = \alpha_\infty + \frac{(\gamma_\infty - 2)S}{4C_{P\infty}U_\infty\tau_v}$$

is the coefficient of the velocity perturbation growth in a quasi-stationary medium [15–17], and

$$\alpha_\infty = \frac{\omega^2\xi(\omega)}{2U_\infty^3\rho_0}$$

is the absorption (or amplification at $\xi < 0$) coefficient related to the presence of relaxation processes in the medium and to the second viscosity ξ formed by them.

The second-viscosity coefficient at $\omega\tau_v \gg 1$ has the form [14]

$$\xi = \frac{(U_\infty^2 - U_0^2)C_V^0\rho_0}{\omega^2\tau_v C_{V\infty}} = \frac{[C_V + S(\tau_{vT} - C_{V\infty})]U_\infty^2\rho_0}{\omega^2\tau_v C_{P\infty}C_{V\infty}}.$$

Here, $U_0 = \sqrt{C_P^0 T_0/C_V^0 m}$ is the velocity of low-frequency sound ($\omega\tau_v \ll 1$); $C_P^0 = C_{P\infty} + C_v + S(\tau_{vT} + 1)$ and $C_V^0 = C_{V\infty} + C_v + S\tau_{vT}$ are the low-frequency heat capacities at constant pressure and at constant volume, $\tau_{vT} = \partial\ln\tau_v/\partial\ln T_0$, and C_v is the equilibrium vibrational heat capacity.

The second viscosity (and α_∞) are negative when $C_v + S(\tau_{vT} - C_{V\infty}) < 0$. This condition corresponds to the presence of a positive feedback between the acoustic perturbation and the heat release from the nonequilibrium degrees of freedom and, hence, to a sound amplification.

It should be noted that, in stationary media with $\xi < 0$, the perturbations of the velocity, pressure, and density in an acoustic wave increase with the same increment α_∞, whereas in quasi-stationary media, the increments of these perturbations have different forms [15–17]. For example, the pressure perturbation increases with the increment

$$g_P = g_V - \frac{1}{1T_0U_\infty}\frac{\partial T_0}{\partial t} = \alpha_\infty - \frac{(2+\gamma_\infty)}{4C_{P\infty}U_\infty\tau_v}.$$

The second equation of the set describes the development of a longitudinal acoustic streaming:

$$\frac{\partial U^{(0)}}{\partial t} - \frac{\eta}{\rho_0}\Delta_\perp U^{(0)} + \frac{1}{\rho_0}\frac{\partial P^{(0)}}{\partial x} = g\left|U^{(1)}\right|^2. \qquad (5)$$

In this equation, we ignore the diffraction changes of the amplitude $U^{(0)}$. Moreover, in the following calculations, we ignore in Eq. (5) the value of the longitudinal pressure gradient, which is insignificant when $U^{(0)} \ll U_\infty$ [3, 4].

The right-hand side of Eq. (5) represents the driving force caused by the acoustic radiation pressure and determined by the change of the amplitude of an acoustic wave in a dissipative medium. Equation (5) coincides with the equation describing, e.g., an Eckart flow correct to the form of the absorption coefficient [20]. However, one should note that, for $g > 0$, this flow is always directed in the direction of the sound propagation, whereas in an amplifying medium with $g < 0$, the sign of the driving force changes and the acoustic streaming becomes opposite.

The third equation of the set describes the temperature change in a medium under the effect of intense sound:

$$\frac{\partial T^{(0)}}{\partial t} - \chi_0\Delta_\perp T^{(0)} = \frac{U_\infty g m}{C_P^0}\left|U^{(1)}\right|^2, \qquad (6)$$

where $\chi_0 = \chi C_{P\infty}/C_P^0$.

In Eq. (6), we ignore the term responsible for the adiabatic mechanism of heating and the value of $\partial P^{(0)}/\partial t$, which is admissible for $t_i > (4U_\infty g)^{-1}$ and a/U_∞ [4].

According to Eq. (6), an acoustically active medium in the field of an intense sound wave is not heated but, on the contrary, cooled.

We can further simplify the set of equations (4)–(6) with the help of the known methods of nonlinear geometric optics (acoustics) [21]. For this purpose, we represent the complex amplitude $U^{(1)}$ in the form

$$U^{(1)} = A(\zeta, r, t)\exp[ik\psi(\zeta, r, t)],$$

where A is the real wave amplitude, ψ is the eikonal, and $\zeta = x - U_\infty t$ is the "traveling" wave coordinate, and substitute it into Eq. (4). Ignoring the diffraction term, we finally obtain

$$\frac{\partial I}{\partial\zeta} + \theta\nabla_\perp I + I\nabla_\perp\theta + 2gI = 0, \qquad (7)$$

$$2\frac{\partial\theta}{\partial\zeta} + 2\theta\nabla_\perp\theta + \left[\frac{2}{U_\infty}\nabla_\perp U^{(0)} + \frac{\nabla_\perp T^{(0)}}{T_0}\right] = 0, \qquad (8)$$

where $I = A^2$ and $\theta = \nabla_\perp\psi$ is the inclination angle of a ray with respect to the x axis. In the case of a beam characterized by a radius a_0, an initial parabolic profile of intensity, and a plane wave front, the solutions to Eqs. (7) and (8) can be tried in the form

$$\theta = \beta(\zeta, t)r, \quad I = I_0\left(\frac{a_0}{a}\right)^2\left(1 - \frac{2r^2}{a^2}\right)e^{-2\int_0^\zeta g d\zeta},$$

where $I_0 = A_0^2$, A_0 is the initial amplitude of the beam at its axis, and $a(\zeta, t) = a_0\exp\int_0^\zeta\beta d\zeta$ is the beam width.

Then, in the case of a dimensionless beam width $f = a/a_0$, Eq. (8) can be reduced to the form

$$\frac{\partial^2 f}{\partial\zeta^2} = -\frac{1}{2r}\left[\frac{2}{U_\infty}\nabla_\perp U^{(0)} + \frac{\nabla_\perp T^{(0)}}{T_0}\right]. \qquad (9)$$

We assume the dependences of $T^{(0)}$ and $U^{(0)}$ on r to also be parabolic, which is a good approximation of an exact solution to Eqs. (5) and (6) for $t_i < \tau_T$, $\rho_0 a^2/\eta$ [6]:

$$T^{(0)} = F_1 + r^2F_2,$$
$$U^{(0)} = B_1 + r^2B_2. \qquad (10)$$

Substituting Eqs. (10) into Eqs. (5), (6), and (9), we obtain

$$\frac{1}{f}\frac{\partial^2 f}{\partial \zeta^2} = -\left[\frac{2}{U_\infty}B_2 + \frac{F_2}{T_0}\right], \quad (11)$$

$$\frac{\partial F_2}{\partial t} = -\frac{2U_\infty g I_0 m e^{-2\int g d\zeta}}{C_P^0 a_0^2 f^4}, \quad (12)$$

$$\frac{\partial B_2}{\partial t} = -\frac{2g I_0 e^{-2\int g d\zeta}}{a_0^2 f^4}. \quad (13)$$

If the background values of temperature change insignificantly within the characteristic time of the sound beam focusing τ_F ($\tau_F \partial T_0/\partial t \ll T_0$), the set of equations (11)–(13) can be reduced to a single equation after differentiating Eq. (11) with respect to time:

$$\frac{\partial}{\partial t}\left(\frac{1}{f}\frac{\partial^2 f}{\partial \zeta^2}\right) = -\frac{\alpha N}{f^4} e^{-2\int g d\zeta}, \quad (14)$$

where $N = \pi a_0^2 \rho_0 U_\infty I_0/2$ is the total power of the sound beam and

$$\alpha = -\frac{4g}{\pi a_0^4 U_\infty^2 \rho_0}\left(2 + \frac{\gamma_\infty}{C_P^0}\right).$$

The exponential factor on the right-hand side of Eq. (14) enhances the nonlinear refraction in an amplifying medium ($g < 0$) and reduces it in an absorbing medium ($g > 0$). We can ignore this factor in the approximation of a thick lens ($|g|L_F < 1$). In this case, Eq. (14) coincides with the corresponding equation from [6], correct to the form of the quantity α.

According to [6], when $\alpha > 0$, one can observe the self-focusing of sound with the characteristic focusing length $L_F \approx (4.7/\alpha E)^{1/2}$, where $E = \int_0^t N dt$ is the energy of the sound beam.

The quantity α is always positive, e.g., in liquids (apart from water), when thermal self-action prevails over the streaming one. In equilibrium gaseous media, both mechanisms of the self-action always lead to a defocusing of sound ($\alpha < 0$). On the contrary, in an acoustically active nonequilibrium medium, both mechanisms make a positive contribution to the coefficient α. Exceptions are strongly nonequilibrium media, in which $C_P^0 < 0$.

Now, we present the estimates of the characteristic quantities for a typical laser medium $CO_2 : N_2 : He = 1 : 2 : 3$ with $P_0 = 1$ atm, $T_0 = 300$ K, $\tau_v \approx 10^{-5}$ s, and $\tau_{VT} \approx -3.4$ [14].

In the case of a specific energy contribution to the vibrational degrees of freedom $W = 50$ mJ/cm^3, the value of S is $S \approx 0.5$. Then, for a sound beam with the radius $a_0 = 1$ cm and the frequency $\omega = 5 \times 10^5$ Hz, the absorption coefficient is $\delta \approx 10^{-3}$ cm^{-1} and the amplification coefficient is $g_V \approx 0.5$ cm^{-1}. We obtain the value of the critical energy E_{cr} necessary for the observation of the self-focusing from the condition $L_F = L_d$, where $L_d = ka_0^2/2$ is the characteristic diffraction length:

$$E_{cr} \approx \frac{18.8}{k^2 a_0^4 \alpha} = 12 \text{ mJ}.$$

The condition $L_F < L_d$ must be satisfied for the observation of self-focusing. For example, at $E = 9E_{cr}$ and $t_i = 1$ s, we have $L_F = L_d/3 \leqslant 2$ cm. In this case, the distance at which a shock is formed, is equal to [20]

$$L_p = 2U_\infty^2/\omega(\gamma_\infty + 1)A_0 \approx 22 \text{ cm} \gg L_F.$$

Such a pulse also satisfies the condition $t_i < \tau_T \approx 1.5$ s.

Thus, this paper demonstrates the fundamental possibility to observe the self-focusing of sound in a quasistationary, vibrationally excited gas. Two mechanisms of self-action cause the self-focusing of sound in an acoustically active medium: the cooling of gas by sound and the excitation of acoustic streamings in opposite directions.

REFERENCES

1. G. A. Askar'yan, Pis'ma Zh. Éksp. Teor. Fiz. **4**, 144 (1966) [JETP Lett. **4**, 99 (1966)].
2. E. A. Zabolotskaya and R. V. Khokhlov, Akust. Zh. **22**, 28 (1976) [Sov. Phys. Acoust. **22**, 15 (1976)].
3. E. A. Zabolotskaya, Akust. Zh. **22**, 222 (1976) [Sov. Phys. Acoust. **22**, 124 (1976)].
4. F. V. Bunkin, K. I. Volyak, and G. A. Lyakhov, Zh. Éksp. Teor. Fiz. **83**, 575 (1982) [Sov. Phys. JETP **56**, 316 (1982)].
5. N. S. Bakhvalov, Ya. M. Zhileĭkin, and E. A. Zabolotskaya, *Nonlinear Theory of Sound Beams* (Nauka, Moscow, 1982; AIP, New York, 1987).
6. M. Yu. Romanovskiĭ, Akust. Zh. **33**, 331 (1987) [Sov. Phys. Acoust. **33**, 192 (1987)].
7. O. V. Rudenko and O. A. Sapozhnikov, Zh. Éksp. Teor. Fiz. **106**, 395 (1994) [JETP **79**, 220 (1994)].
8. O. V. Rudenko and A. A. Sukhorukov, Akust. Zh. **41**, 822 (1995) [Acoust. Phys. **41**, 725 (1995)].
9. O. V. Rudenko, A. Sarvazyan, and S. G. Emilianov, J. Acoust. Soc. Am. **99**, 2791 (1996).
10. Tjotta Sigve, Rept/Dep. Appl. Math. Univ. Bergen, No. 119, 1 (1998).
11. A. V. Krasnoslobodtsev, G. A. Lyakhov, and K. F. Shipilov, Akust. Zh. **45**, 832 (1999) [Acoust. Phys. **45**, 750 (1999)].
12. E. Ya. Kogan and N. E. Molevich, Pis'ma Zh. Tekh. Fiz. **12**, 96 (1986) [Sov. Tech. Phys. Lett. **12**, 40 (1986)].
13. E. Ya. Kogan and N. E. Molevich, Zh. Tekh. Fiz. **56**, 941 (1986) [Sov. Phys. Tech. Phys. **31**, 573 (1986)].
14. N. E. Molevich and A. N. Oraevskiĭ, Tr. Fiz. Inst. im. P. N. Lebedeva, Ross. Akad. Nauk **222**, 45 (1992).

15. T.-Y. Toong, P. Arbeau, C. A. Garris, *et al.*, in *Proceedings of 15th Symposium (International) on Combustion* (The Combustion Inst., Pittsburgh, USA, 1975), p. 87.

16. G. E. Abouseif, T.-Y. Toong, and J. Converti, in *Proceedings of 17th Symposium (International) on Combustion* (Univ. of Leads, England, 1978), p. 1341.

17. N. E. Molevich and A. N. Oraevskiĭ, Akust. Zh. **35**, 482 (1989) [Sov. Phys. Acoust. **35**, 282 (1989)].

18. A. A. Karabutov, O. V. Rudenko, and O. A. Sapozhnikov, Akust. Zh. **34**, 644 (1988) [Sov. Phys. Acoust. **34**, 371 (1988)].

19. O. V. Rudenko, M. M. Sagatov, and O. A. Sapozhnikov, Zh. Éksp. Teor. Fiz. **98**, 808 (1990) [Sov. Phys. JETP **71** (3), 449 (1990)].

20. O. V. Rudenko and S. I. Soluyan, *Theoretical Foundations of Nonlinear Acoustics* (Nauka, Moscow, 1975; Consultants Bureau, New York, 1977).

21. S. A. Akhmanov, A. P. Sukhorukov, and R. V. Khokhlov, Usp. Fiz. Nauk **93**, 19 (1967) [Sov. Phys. Usp. **10**, 609 (1967)].

Translated by M. Lyamshev

Acoustical Physics, Vol. 48, No. 2, 2002, pp. 214–219. Translated from Akusticheskiĭ Zhurnal, Vol. 48, No. 2, 2002, pp. 253–259.

Increase in the Efficiency of the Shear Wave Generation in Gelatin Due to the Nonlinear Absorption of a Focused Ultrasonic Beam

Yu. A. Pishchalnikov, O. A. Sapozhnikov, and T. V. Sinilo

Moscow State University, Vorob'evy gory, Moscow, 119899 Russia

e-mail: oleg@acs366b.phys.msu.su

Received December 18, 2000

Abstract—Experimental results and theoretical estimates are presented to demonstrate the prospects of using the acoustic nonlinearity of a gel-like medium for increasing the efficiency of the shear wave generation in it by a pulsed ultrasonic beam. The experiment is based on the propagation of a focused beam of longitudinal acoustic waves at a frequency of 1.1 MHz in a gelatin sample and on the detection of shear waves by the optical method [1]. It is demonstrated that the amplitude of the shear wave excited by a nonlinear acoustic pulse can be increased by an order of magnitude owing to the formation of shock fronts in the profile of this pulse. © *2002 MAIK "Nauka/Interperiodica".*

An ultrasonic wave that experiences both absorption and scattering in the course of its propagation transfers part of its momentum to the medium. As a consequence, an amplitude-modulated wave produces low-frequency (medium) elastic stresses in the medium, i.e., the radiation pressure [2]. In the case of the ultrasound localization in the form of a beam, the corresponding shear stresses produce a transverse wave propagating in the direction perpendicular to the beam axis (Fig. 1). In common solids, this effect is minor; however, it can become noticeable in gel-like media, where the shear modulus is small and the corresponding shear strain is relatively large. Such media are rubbers, gels, and soft biological tissues. The detection of the amplitude or the propagation velocity of the transverse disturbances provides an opportunity to measure the shear modulus of the medium [1]. This method can be promising for medical applications, e.g., for an early detection of cancer, since the values of the shear moduli for healthy and cancer-affected tissues differ by orders of magnitude [3]. If a focused acoustic beam is used, an efficient generation of shear waves occurs only in the focal region. Thus, it is possible to obtain a local excitation of shear waves in a medium at a large distance from the source of radiation.

The main difficulty in the utilization of this effect is connected with the fact that the excited shear waves are usually very weak, and, therefore, difficult to detect. Hence, it is important to find ways to increase the efficiency of the generation of shear stresses. Here we suggest one such method namely, to use large-amplitude focused ultrasonic pulses whose profiles are nonlinearly distorted in the course of their propagation for increasing the efficiency of the generation of shear-wave signals. Experiments on samples made of gelatin with different concentration (i.e., with different values of the shear modulus) are described. It is demonstrated that, in the case of a constant total energy of the acoustic pulse, it is possible to obtain an amplification of the shear wave by reducing the duration of the excitation pulse and by simultaneously increasing its amplitude to the values at which shock fronts are formed in the wave profile. A theoretical calculation is conducted to compare the efficiencies of the shear wave excitation with and without allowance for the medium nonlinearity and to evaluate the gain.

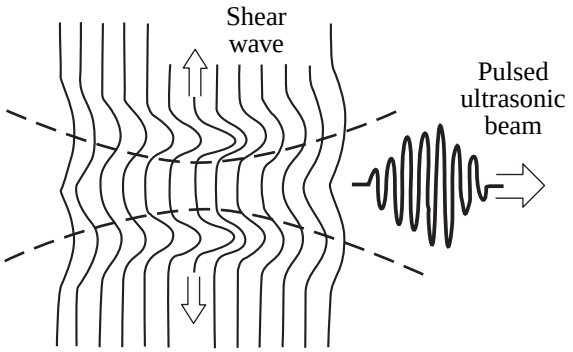

Fig. 1. Excitation of a shear wave due to the absorption of a focused ultrasonic pulse. The dashed lines indicate the boundaries of the ultrasonic beam. The solid lines illustrate the deformation of the medium: in the initial unperturbed state, they formed a family of equidistant vertical straight lines. The absorbed ultrasonic pulse exerts a radiation pressure on the medium, and the shear stress arising in this case produces a quasi-cylindrical shear wave traveling away from the beam axis.

1063-7710/02/4802-0214$22.00

The setup used in the experiments is schematically represented in Fig. 2. An ultrasonic beam was produced by a focusing piezoceramic transducer 10 cm in diameter with a 20-cm curvature radius. The transducer operated at a resonance frequency of 1.1 MHz [4]. The longitudinal and transverse dimensions of the focal region, which were measured according to the zeros of the amplitude distribution of the pressure field, were 87 and 7 mm, respectively. The transducer was excited by an electric signal from an HP33120A generator using an ENI AP400B power amplifier. We used a pulsed regime of excitation with rectangular envelopes of pulses. The pulse duration varied from 40 to 700 μs. The source was submerged into a water basin with the dimensions $20 \times 20 \times 60$ cm^3 and could be moved with the help of a positioning system (Velmex VP9000, USA) in three mutually perpendicular directions. A gelatin sample shaped as a cylinder with a diameter of 80 mm and a generatrix of 65 mm was placed into the focal region of the ultrasonic beam. Figure 3 shows a photograph of the ultrasonic transducer (on the left) and one of the samples (on the right). The sample was positioned in such a way that the cylinder axis coincided with the acoustic axis and the central section of the cylinder lay in the focal plane of the source. An optical system described in [1] was selected to detect the shear waves. The beam of a helium-neon laser was focused at the edge of an opaque particle 60–300 μm in size, which was placed in the medium. On the shear wave arrival, the particle moved and modulated the transmitted energy of the laser beam. The light signal detected further by a photodiode was proportional to the shear displacement. To incorporate such modulator particles into the medium, gelatin samples were manufactured in two stages, which provided an opportunity to put the particles into the central section perpendicular to the cylinder axis.

The purpose of our measurements was to demonstrate that the use of an acoustic wave with shocks in its profile makes the excitation of shear-wave signals much more efficient. Ultrasonic pulses with different amplitudes, but with the same energy (which was attained by the corresponding choice of the pulse duration) were used. If the ultrasonic propagation in the medium were linear, the amplitude of the shear waves excited by acoustic pulses with the same energy would be the same [1]. However, in the presence of nonlinearity, the profile of an ultrasonic wave in the focal region of the beam becomes distorted, and in the case of a rather large amplitude, shock fronts arise, i.e., a sawtooth profile is formed. As a consequence, the wave is absorbed more efficiently and transfers a greater part of its momentum to the medium, as compared to the case of linear propagation. Thus in the nonlinear regime, one can expect a considerable increase in the amplitude of the shear disturbance generated by the ultrasonic wave.

The regime calibration according to the total energy of acoustic pulses was performed by measuring the average radiation force exerted by a periodic sequence

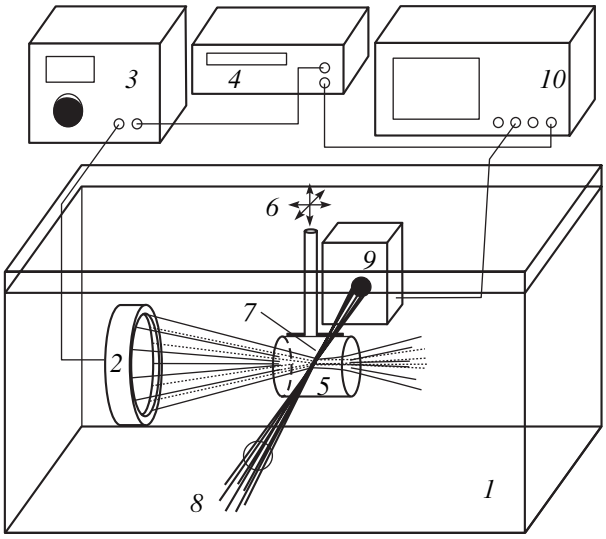

Fig. 2. Experimental setup: (*1*) a water basin, (*2*) an ultrasonic transducer, (*3*) an electric power amplifier, (*4*) a generator, (*5*) a gelatin sample, (*6*) a micropositioning system, (*7*) a shutter particle, (*8*) a beam of a He-Ne laser, (*9*) a photodiode, and (*10*) a digital oscilloscope.

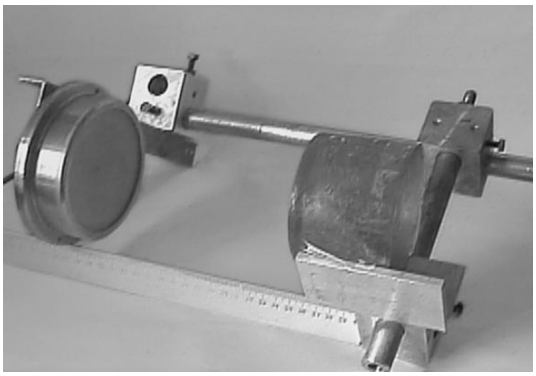

Fig. 3. Photograph of the piezoceramic transducer (on the left) and the gelatin sample (on the right).

of pulses on a wide-aperture target absorber [5]. The target was shaped as a cylinder 12 cm in diameter and 5 cm in height and was made of rubber of the type of an RTV-2 two-component silicon elastomer, which had a large absorption coefficient and an acoustic impedance close to the impedance of water. To measure the radiation force, an acoustic beam was directed to the absorber from below and the absorber was weighted both under the ultrasonic irradiation and immediately after switching off the source of ultrasound [6]. In such measurements, the change in the absorber weight ΔP and the average ultrasonic power W are related as $\Delta P/W = 67$ mg/W [5]. On the basis of these measurements, several regimes of operation with different lengths and amplitudes of pulses were selected for a preset acoustic energy.

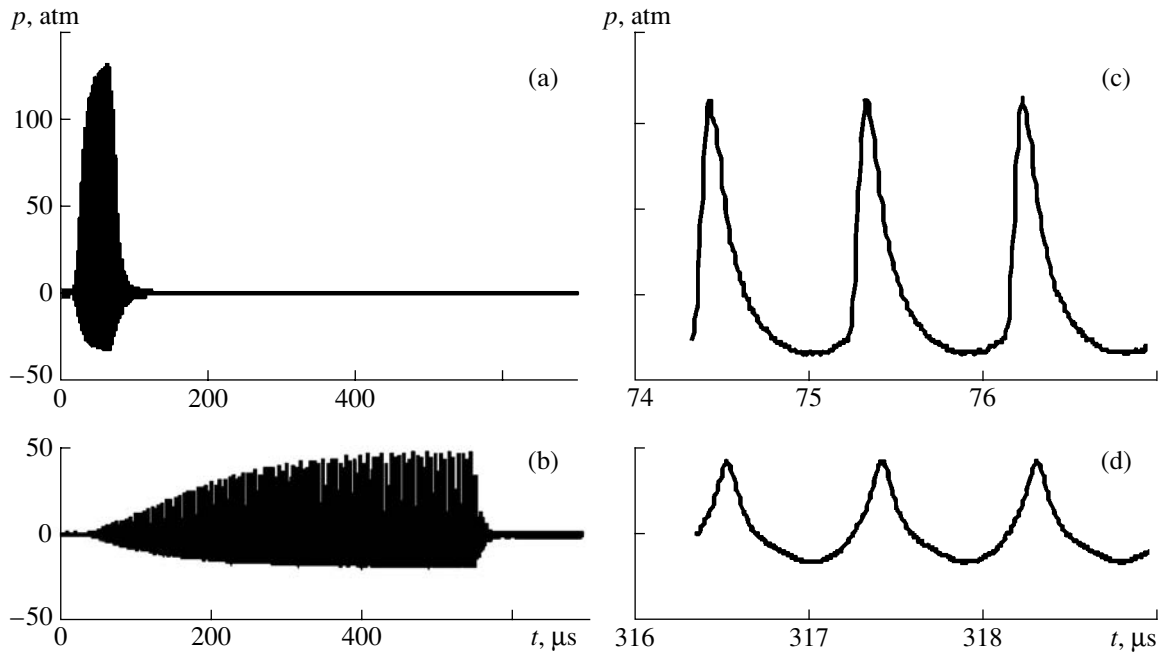

Fig. 4. Shape of an ultrasonic pulse at the focal point in the (a, b) broad and (c, d) narrow time windows: (a, c) a nonlinear regime and (b, d) a quasi-linear regime.

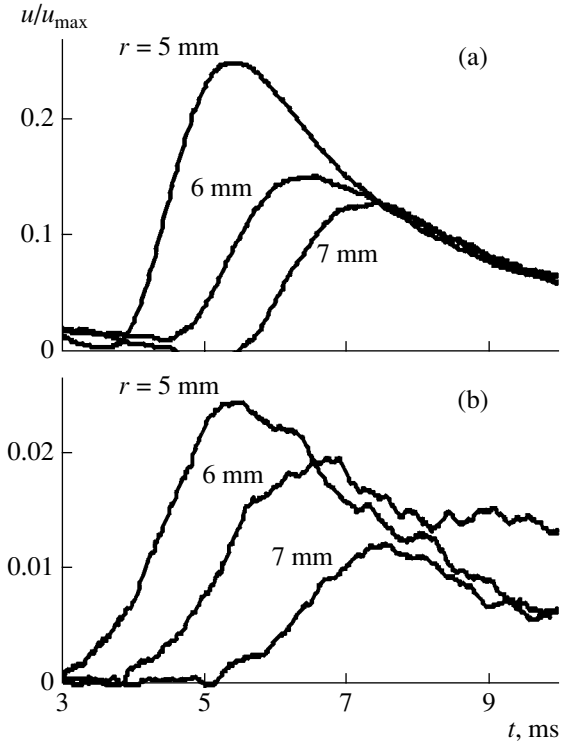

Fig. 5. Time profiles of a shear pulse (the photodiode signal u) measured in the focal plane at three different distances from the acoustic axis r: (a) a nonlinear regime and (b) a quasi-linear regime. The values of the displacement u (for all curves) are normalized to its maximal value in the nonlinear regime u_{max}.

To verify that, in the selected regimes, the acoustic signals were really subjected to nonlinear distortions, the measurements of the wave form in the focal region of the beam were also conducted using a self-made broadband PVDF membrane hydrophone with a sensitive area 0.5 mm in diameter. The rear side of the PVDF film was acoustically loaded by a thick layer of transformer oil, which provided an opportunity to eliminate the stray capacitance and enhance the locality of reception [7]. Figure 4 shows the wave profiles of the shortest and longest pulses in the focal region of the source. Figures 4a and 4b show the whole pulses, and Figs. 4c and 4d, three periods from their central parts. It should be noted that the electric signal at the piezoelectric transducer and, therefore, the ultrasonic wave emitted by it were sinusoidal in both cases. As one can see from Fig. 4, in the focus, the wave is strongly distorted, especially, in the case of a large amplitude: shock fronts are clearly visible in the profile of the first pulse, whereas the second profile is distorted to a lesser extent. Thus, the effect of the acoustic nonlinearity of the medium must manifest itself in the comparison of the efficiencies of the shear wave generation in the two indicated regimes.

Figure 5 demonstrates the experimentally measured profiles of a shear pulse in the focal plane at different distances from the acoustic axis of the beam (5, 6, and 7 mm, respectively). Figure 5a corresponds to the shear wave excitation by a short high-amplitude pulse (a nonlinear regime) and Fig. 5b corresponds to the excitation by a long pulse with a much smaller amplitude (a quasi-linear regime) and with the same total energy $E = 4.2$ mJ.

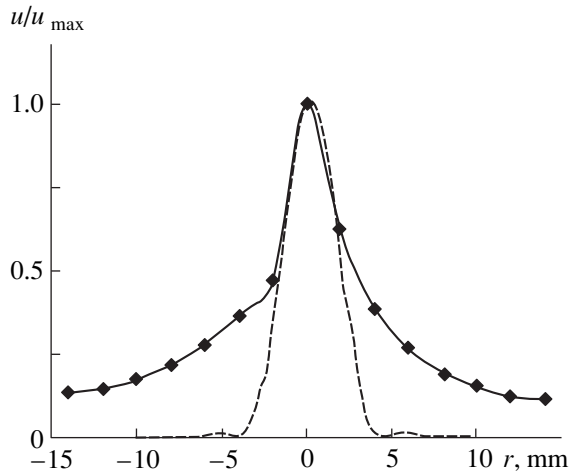

Fig. 6. Transverse distribution of the shear wave amplitude measured in the focal plane of the source in the nonlinear regime (the solid line) and the transverse profile of intensity (the dashed line). The curves are normalized to the corresponding maximal values.

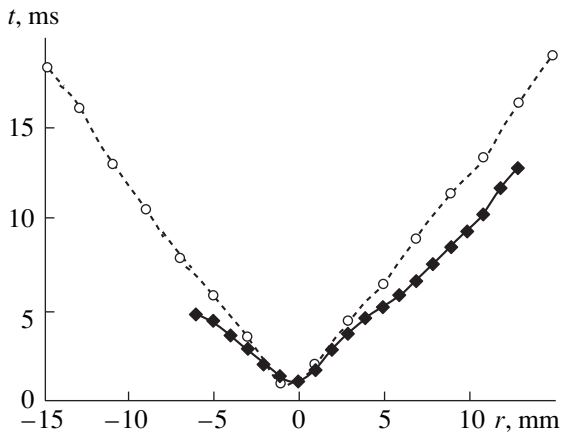

Fig. 7. Delay time of the peak of the shear wave versus the transverse coordinate *r*. The measurements were performed in the nonlinear regime for two gelatin concentrations: 4.5% (the dashed line) and 6.7% (the solid line).

All curves are normalized to the maximal displacement at the beam axis in the nonlinear excitation regime. It is necessary to note that the vertical scales in Figs. 5a and 5b differ by a factor of ten. Thus, although the signal profiles in the nonlinear and quasi-linear regimes look almost the same at the corresponding distances, the amplitudes of shear waves differ essentially. In the quasi-linear regime, the signals were weak and their amplitude was comparable to the noise amplitude. Therefore, the curves were obtained by averaging over 300–400 realizations. Thus, the assumption that the efficiency of the shear wave generation grows when the acoustic nonlinearity of the medium comes into play was confirmed. Similar results were obtained for other regimes of excitation with different pulse energies and for samples with different gelatin concentrations.

It is of interest to know how far from the point of excitation it is possible to detect the shear waves. Figure 6 demonstrates the transverse distribution of the peak displacement in the shear wave excited in the nonlinear regime (with the ultrasonic pulse duration equal to 55 μs and the total energy of a single pulse equal to 4.2 mJ) in a sample with a gelatin concentration of 4.5%. The dashed line in the same figure shows the experimentally measured transverse distribution of the intensity of an acoustic wave in the focal plane, which corresponds to the distribution of the sources of shear waves. Both curves are normalized to the corresponding maximal values. One can see clearly that, although a shear wave decays rapidly, it still propagates to a considerable distance from the acoustic beam. This provides an opportunity to measure the velocity of shear waves c_t with a sufficiently high accuracy and, hence, to determine the shear modulus $\mu = \rho c_t^2$.

Figure 7 presents the detection time of the peak of a shear pulse versus the distance *r* between the detection point and the axis of the ultrasonic beam. The two curves correspond to two different concentrations of gelatin (4.5 and 6.7%) and are obtained using nonlinear acoustic pulses. The slope of these curves is inversely proportional to the propagation velocity of shear waves in the corresponding material. The experimental results shown in Fig. 7 for the gelatin concentrations 4.5 and 6.7% give the values of the velocity $c_t = 0.8$ and 1.2 m/s and the shear modulus $\mu = 690$ and 1450 Pa, respectively. These values coincide with the shear modulus measured by the indentation method using a rigid sphere [8, 9]. Thus, the remote excitation and detection of shear waves provide an opportunity to determine the shear modulus.

Let us proceed to the theoretical description of the observed effects. The shear disturbances can be described in the framework of the linear theory because of their smallness. The displacement **u** of the particles of the elastic medium in the force field **F** can be described by the equation

$$\rho\frac{\partial^2 \boldsymbol{u}}{\partial^2 t} = \left(K + \frac{\mu}{3}\right)\mathrm{graddiv}\mathbf{u} + \mu\Delta\mathbf{u} + \rho\mathbf{F}, \qquad (1)$$

where ρ is the density of the medium; *K* and μ are the bulk modulus and the shear modulus, respectively; **F** is the volume density of forces acting from the side of the ultrasonic beam; and *t* is time. Let a weakly divergent beam of acoustic waves, which has a circular cross section, propagate in the medium. We denote the longitudinal and the transverse coordinates by *z* and *r*, respectively. Then, we can ignore the transverse component F_r of the force **F** because of its smallness in comparison with the longitudinal component F_z.

We note that, if the transverse dimension of the beam is much smaller than the absorption length, the force F_z varies mainly in the transverse direction by decreasing with the distance from the axis, whereas its dependence on the longitudinal coordinate is weak. In the indicated conditions, we can ignore the dependence of the deformation of the medium on the longitudinal coordinate and assume that the displacement of particles occurs only along the z axis. In this case, Eq. (1) takes the form of an inhomogeneous wave equation for a shear cylindrical wave:

$$\frac{\partial^2 u_z}{\partial t^2} - c_t^2 \Delta_\perp u_z = F_z(r, t), \tag{2}$$

where $c_t = \sqrt{\mu/\rho}$ is the velocity of shear waves and $\Delta_\perp = \frac{1}{r}\frac{\partial}{\partial r} + \frac{\partial^2}{\partial r^2}$ is the transverse Laplacian. The form of the solution to the wave equation (2) is determined by the dependence of the volume force F_z on the coordinate and time. If the dependence of the force on time at all space points is described by the same function $\varphi(t)$, the expression $F_z = \Phi(r)\varphi(t)$, where $\Phi(r)$ describes the transverse profile of the acoustic beam, is true. As we demonstrated in our previous paper [1], in the case of a short pulse $\varphi = \delta(t)$ with the transverse profile of the beam in the form $\Phi(r) = F_0(1 + r^2/a^2)^{-3/2}$, the solution to Eq. (2), i.e., the pulsed response, is expressed analytically as

$$h(r, t) = \frac{aF_0}{2c_t}\theta(t)\sqrt{\frac{(\sqrt{A} + \sqrt{B})^2 - 4(1 + r^2/a^2)}{AB}}, \tag{3}$$

where $A = 1 + (r + c_t t)^2/a^2$, $B = 1 + (r - c_t t)^2/a^2$, a is the radius of the sound beam, and $\theta(t)$ is the Heaviside step function. According to Eq. (3), the characteristic duration of the pulsed response coincides with the traveling time of the shear wave through the excitation region $t_a = a/c_t$. In the case of an arbitrary function $\varphi(t)$, the solution has the form of a convolution $u_z = h * \varphi$. If the action duration is $t_0 \ll t_a$, the profile of the shear wave coincides with the profile of the pulsed response: $u_z = t_0 h(r, t)$. As one can see from Eq. (3), the displacement of the medium manifests itself most strongly at the beam axis ($r = 0$), where it depends on time as $u_z = F_0 t/(1+(c_t t/a)^2)$. Hence, the maximal displacement of the medium under the effect of a pulsed radiation force is

$$u_{\max} = \frac{at_0 F_0}{2c_t}. \tag{4}$$

The result given by Eq. (4) corresponds to the following time dependence of the volume force at the beam axis: $F_z(0, t) = F_0$ in the interval $0 \le t \le t_0$ and $F_z = 0$ outside this interval.

To compare the linear and nonlinear regimes of excitation, it is necessary to calculate the volume force. The force of radiation pressure in a viscous heat-conducting medium can be written in the form [10]

$$F_z = \frac{b}{c_l^5 \rho^3}\overline{\left(\frac{\partial p}{\partial t}\right)^2}, \tag{5}$$

where c_l is the velocity of longitudinal waves; p is the acoustic pressure in the ultrasonic beam; $b = \zeta + \frac{4}{3}\eta + \kappa\left(\frac{1}{C_v} - \frac{1}{C_p}\right)$ is the dissipation coefficient; ζ and η are the volume and shear viscosities; κ is the coefficient of heat conductivity; C_p and C_v are the specific heats at constant pressure and at constant volume, respectively; and the overbar means averaging over the period of the ultrasonic wave. When small-amplitude ultrasound is used, the wave form within a pulse is sinusoidal: $p = p_0 \sin\omega t$. In this case, we obtain from Eq. (5):

$$F_0^{\text{lin}} = \alpha p_0^2/\rho^2 c_l^2, \tag{6}$$

where $\alpha = b\omega^2/2\rho c_l^3$ is the ultrasonic absorption coefficient and the superscript "lin" indicates the linear case.

Taking into account the fact that $I = p_0^2/2\rho c_l$ is the wave intensity, from Eqs. (4) and (6) we obtain

$$u_{\max}^{\text{lin}} = \frac{\alpha a}{\rho c_l c_t} t_0 I. \tag{7}$$

As one can see from this expression, the medium displacement under the effect of the radiation force is proportional to the quantity $t_0 I$, i.e., it is determined by the energy of the ultrasonic pulse rather than by its intensity. Therefore, in the linear regime, ultrasonic pulses with different amplitudes p_0 but with the same total energy produce identical shear-wave signals.

Now let us consider the case of the shear wave excitation by an acoustic pulse of the same duration t_0 but with a saw-tooth carrier instead of the sinusoidal one. An ultrasonic wave acquires such a shape as a result of its nonlinear evolution (see Fig. 4c). The wave propagation in a nonlinear dissipative medium is described by the Burgers equation

$$\frac{\partial p}{\partial z} - \frac{\varepsilon}{\rho c_l^3} p \frac{\partial p}{\partial \tau} = \frac{b}{2\rho c_l^3}\frac{\partial^2 p}{\partial \tau^2}, \tag{8}$$

where $\tau = t - z/c_l$ is time in the moving coordinate system and ε is the acoustic nonlinearity parameter of the medium. The profile of a saw-tooth wave within a single period is described by the Khokhlov solution [11]

$$p = \frac{p_s}{2}\left[-\frac{\omega\tau}{\pi} + \tanh\left(\frac{p_s \tau}{2b}\right)\right], \quad -\pi \le \omega\tau \le \pi, \tag{9}$$

where p_s is the value of the pressure jump at the shock front. It depends on the distance as $p_s = 2\pi p_0/(1 + \sigma)$,

where $\sigma = \varepsilon\omega p_0 z/\rho c_l^3$ is the distance from the source divided by the length of the shock formation and p_0 is a certain characteristic value of the wave amplitude. However, the specific form of the function $p_s(z)$ is unimportant for our calculations. We are interested in the case of waves with large amplitudes, $p_s/b\omega \gg 1$. Formally, the consideration of large-amplitude waves corresponds to the transition $b \longrightarrow 0$ in Eq. (9). In this case, a shock is formed in the profile. Substituting Eq. (9) into expression (5) for the force of radiation pressure, performing the averaging, and passing to the limit $b \longrightarrow 0$, we obtain

$$F_0^{\mathrm{nl}} = \frac{\varepsilon f}{6\rho^3 c_l^5} p_s^3. \tag{10}$$

Here, $f = \omega/2\pi$ is the wave frequency. The superscript "nl" indicates that the estimate given by Eq. (10) belongs to the case of the nonlinear ultrasonic propagation. Let us indicate two important features of the nonlinear case (Eq. (10)) that make it different from the linear case (Eq. (6)). First, the radiation force does not depend on the linear absorption coefficient of the medium. Second, the radiation force in the case of a saw-tooth profile is proportional to the third power of the wave amplitude rather than to the second power. The latter fact is fundamental and testifies to the possibility of increasing the efficiency of the shear wave generation in the nonlinear regime. We note that the intensity of a saw-tooth wave is expressed as $I = p_s^2/12\rho c_l$. From Eqs. (4) and (10), we obtain

$$u_{\max}^{\mathrm{nl}} = \frac{\varepsilon f a}{\rho^2 c_l^4 c_t} t_0 I p_s. \tag{11}$$

As one can see, in the case of a fixed wave energy ($t_0 I$ = const), the generation efficiency is directly proportional to the value of the pressure jump p_s at the shock fronts of the saw-tooth wave. Remember that there is no dependence on the amplitude in the linear case (see Eq. (7)). Comparing Eqs. (7) and (11) in the case of the same intensities of the sinusoidal and saw-tooth waves, we obtain the following amplitude ratio of the shear-wave signals:

$$K = \frac{u_{\max}^{\mathrm{nl}}}{u_{\max}^{\mathrm{lin}}} = \frac{\varepsilon f p_s}{\alpha\rho c_l^3}. \tag{12}$$

Thus, we obtain that the factor K is proportional to the amplitude of the acoustic wave p_s, i.e., it can be much greater than unity for a high-intensity ultrasound. The parameters in gelatin have the following characteristic values: $\alpha = 1\ \mathrm{m}^{-1}$, $\varepsilon = 4$, $\rho = 10^3\ \mathrm{kg/m}^3$, and $c_l = 1.5 \times 10^3$ m/s. For ultrasonic waves with the amplitude $p_s = 10^7$ Pa and the frequency $f = 10^6$ Hz used in the experiment, we obtain that, at a given pulse energy, the maximal displacement value observed in a medium with a pronounced nonlinearity is approximately ten times greater than in the case of linear propagation. This estimate is confirmed by the experiment (see Fig. 5).

Therefore, the efficiency of the shear wave generation can be considerably increased by using pulses whose wave profiles contain shock fronts. Certainly, when using saw-tooth signals for medical purposes, it is necessary to be sure that they cause no tissue damage, i.e., there is no cavitation and no overheating of the medium. Such conditions are obtained by using rarely repeated short pulses of the megahertz frequency range. For example, saw-tooth profiles are observed in the course of the operation of some diagnostic ultrasonic devices intended for cardiological applications [12].

ACKNOWLEDGMENTS

We are grateful to V.V. Yakushev for manufacturing the PVDF films and for discussing the characteristic features of the calibration of our acoustic sensors. We are also grateful to D. Cathignol for providing us with the components of the device for measuring the total power of the beam by the radiation force.

The work was supported by the CRDF, project no. RP2-2099, the FIRCA-NIH, project no. DK43881, and the program "Universities of Russia," project no. 1-5286.

REFERENCES

1. V. G. Andreev, V. N. Dmitriev, Yu. A. Pishchal'nikov, *et al.*, Akust. Zh. **43**, 149 (1997) [Acoust. Phys. **43**, 123 (1997)].
2. L. K. Zarembo and V. A. Krasil'nikov, *Introduction to Nonlinear Acoustics* (Nauka, Moscow, 1966), pp. 178–205.
3. A. P. Sarvazyan, O. V. Rudenko, S. D. Swanson, *et al.*, Ultrasound Med. Biol. **24** (9), 1419 (1998).
4. R. O. Cleveland, O. A. Sapozhnikov, V. R. Bailey, and L. A. Crum, J. Acoust. Soc. Am. **107**, 1745 (2000).
5. IEEE Std 790-1989, *IEEE Guide for Medical Ultrasound Field Parameter Measurements (ANSI)* (IEEE, New York, 1990).
6. A. E. Ponomarev, Yu. A. Pishchal'nikov, T. V. Sinilo, and O. A. Sapozhnikov, in *Proceedings of the VII All-Russian School–Seminar on Wave Phenomena in Inhomogeneous Media, Krasnovidovo, Moscow region, May 2000* (Moscow State Univ., Moscow, 2000), Vol. 1, p. 34.
7. J. Tavakkoli, A. Birer, and D. Cathignol, Shock Waves **5**, 369 (1996).
8. N. E. Waters, Br. J. Appl. Phys. **16**, 557 (1965).
9. V. G. Andreev and A. V. Vedernikov, Vestn. Mosk. Univ., Ser. 3: Fiz., Astron., No. 1, 34 (2001).
10. N. S. Bakhvalov, Ya. M. Zhileĭkin, and E. A. Zabolotskaya, *Nonlinear Theory of Sound Beams* (Nauka, Moscow, 1982; AIP, New York, 1987).
11. O. V. Rudenko and S. I. Soluyan, *Theoretical Foundations of Nonlinear Acoustics* (Nauka, Moscow, 1975; Consultants Bureau, New York, 1977).
12. *Output Measurements for Medical Ultrasound*, Ed. by R. C. Preston (Springer, Berlin, 1991).

Translated by M. Lyamshev

Acoustical Physics, Vol. 48, No. 2, 2002, pp. 220–224. Translated from Akusticheskiĭ Zhurnal, Vol. 48, No. 2, 2002, pp. 260–265.

Sound Waves Generated Due to the Absorption of a Pulsed Electron Beam in Gas

A. I. Pushkarev, M. A. Pushkarev, and G. E. Remnev

Research Institute of High Voltages, Tomsk Polytechnical University, pr. Lenina 2, Tomsk, 634050 Russia

e-mail: kedr@ephc.tomsk.ru

Received June 29, 2001

Abstract—The results of an experimental investigation of acoustic vibrations (their frequency, amplitude, and attenuation coefficient) generated in a gas mixture as a result of the injection of a high-current pulsed electron beam into a closed reactor are presented. It is shown that the change in the phase composition of the initial mixture under the action of the electron beam leads to a change in the frequency of the sound waves and to an increase in the attenuation coefficient. By measuring the change in frequency, it is possible to evaluate with sufficient accuracy (about 2%) the degree of conversion of the initial products in the plasmochemical process. Relations describing the dependence of the sound energy attenuation coefficient on the size of the reactor and on the thermal and physical properties of the gases under study are derived. It is shown that a simple experimental setup measuring the parameters of acoustic waves can be used for monitoring the plasmochemical processes initiated by a pulsed excitation of a gas mixture. *© 2002 MAIK "Nauka/Interperiodica".*

INTRODUCTION

The plasmochemical processes that accompany the injection of an electron beam in a gas or the volume gaseous discharges are currently considered as an alternative to thermodynamical-equilibrium chemical processes. Unlike these, in plasmochemical reactions the main part of energy of the source of excitation (up to 80–90%) is delivered to the vibrational degrees of freedom of molecules, which provides a high efficiency of chemical processes [1, 2]. The plasmochemical methods of film deposition from ionized vapor make it possible to fabricate high-quality multilayer structures [3, 4]. In volume gaseous discharges and under an electron beam injection, an efficient dissociation of NO_x and SO_2 molecules is observed [5–7]. Plasmochemical processes find applications in dry etching of Ni, Fe, and other thin films [8] and in sterilization [9]. For monitoring the plasmochemical processes, optical methods (emission and absorption spectroscopy, Rayleigh scattering, and so on) and mass spectrometry methods are used [10]. These methods require complicated equipment and optical access to the reaction zone.

When the energy of a pulsed source of excitation (a pulsed microwave discharge, a pulsed high-current electron beam, a gaseous discharge, and so on) dissipates in a closed plasmochemical reactor, the radiation-acoustic effect [11] leads to the generation of acoustic vibrations, which are determined by the nonuniformity of excitation (and, accordingly, of heating) of the reagent gases. The measurement of the parameters of sound waves does not require complicated equipment but provides ample data on the processes that occur in the plasmochemical reactor.

EXPERIMENTAL SETUP

This paper presents the results of investigation of the sound waves generated in one-, two-, and three-component gas mixtures as a result of the dissipation of the energy of a pulsed high-current electron beam in a closed plasmochemical reactor (PCR). A Temp accelerator [12] operating in an electron mode was used as a source of a high-current electron beam (HCEB) with the following parameters: the maximal electron energy 300 keV, the current of the beam at the maximum 12 kA, and the pulse width at the half-amplitude level 60 ns. The PCR had the form of a tube. Electrons were injected in the tube at its end through a titanium foil.

Two reactors with different dimensions were used in the experiments: one with a diameter of 6 cm and a length of 11.5 cm and the other with a diameter of 9 cm and a length of 30 cm. The sound waves were detected by a differential pressure transducer capable of measuring pressure variations in the reactor with frequencies up to 3.5 kHz. The gases studied in the experiment were as follows: argon, nitrogen, oxygen, methane, silicon tetrachloride, tungsten hexafluoride, and their mixtures.

INVESTIGATION OF THE SOUND WAVE FREQUENCY

In a closed reactor with rigid walls, after the dissipation of a pulsed electron beam, standing waves are generated whose frequency in an ideal gas is [13]

$$f_n = \frac{n}{2l}\sqrt{\frac{\gamma RT}{\mu}}, \qquad (1)$$

1063-7710/02/4802-0220$22.00 © 2002 MAIK "Nauka/Interperiodica"

where n is the serial number of harmonic ($n = 1, 2, \ldots$), l is the length of the reactor, γ is the adiabatic exponent, R is the universal gas constant, and T and μ are the temperature and molar mass of gas in the reactor.

In the experiments, we recorded the sound vibrations corresponding to the generation of standing waves along and across the reactor. For our investigations, we chose the lowest component of the sound waves with the fundamental frequency of waves propagating along the reactor ($n = 1$ in Eq. (1)).

The dependences of the frequency of sound vibrations in the PCR on the parameter $(\gamma/\mu)^{0.5}$ for the one-component gases in the reactors 11.5 and 30 cm long are shown in Fig. 1. The dots correspond to experimental data and the lines correspond to calculations by Eq. (1) for l = (*1*) 11.5 and (*2*) 30 cm. As seen from this figure, in the investigated frequency range, the sound vibrations are adequately described by the relation for ideal gases.

The measurement of the frequency of sound vibrations generated due to the dissipation of energy of the pulsed source of excitation makes it possible to monitor the plasmochemical reactions resulting in the formation of solid products, e.g., $CO_2 \longrightarrow C + O_2$, $WF_6 \longrightarrow W + 3F_2$, etc. The minimal degree of conversion of the initial gas that can be detected by the change in frequency does not exceed 2% for the attained accuracy of the frequency measurement. The low attenuation of sound waves makes it possible to measure the vibration frequency accurate to 0.5%.

In actual plasmochemical reactions, multicomponent gas mixtures are used, and the products of reactions are also gas mixtures. In calculating the frequency of sound vibrations, one has to take into account the weight coefficient of every component of the gas mixture and perform the calculation by the formula [14]

$$f_{sw} = \frac{\sqrt{RT}}{2l\sqrt{m_0}}\sqrt{\sum_i \frac{\gamma_i m_i}{\mu_i}}, \qquad (2)$$

where m_0 is the total mass of all components of the gas mixture and m_i, γ_i, and μ_i are the mass, the adiabatic exponent, and the molar mass of the ith component, respectively. Taking into account that the mass of the ith component is

$$m_i = 1.66 \times 10^{-27}\mu_i N_i = K\mu_i \frac{P_i V}{P_0},$$

where N_i is the number of molecules of the ith component, P_i is its partial pressure, V is the volume of the PCR, P_0 = 760 torr, and K is a constant, Eq. (2) can be written in the form that is more convenient for data processing

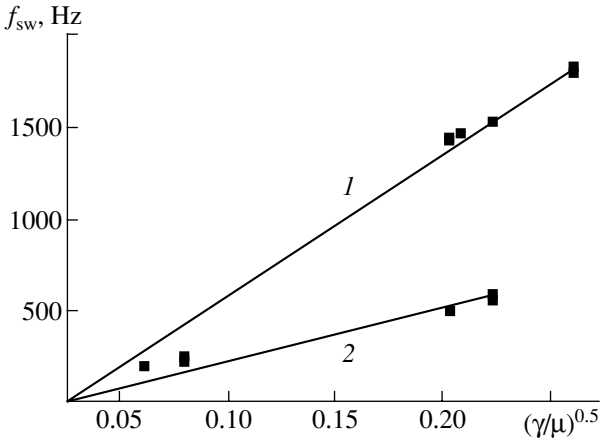

Fig. 1. Frequency of sound vibrations in the PCRs (*1*) 11.5 and (*2*) 30 cm long as a function of the ratio of the adiabatic exponent to the molar mass for single-component gases.

$$f_{sw} = \frac{\sqrt{RT}\sqrt{\sum_i \gamma_i P_i}}{2l\sqrt{\sum_i \mu_i P_i}}. \qquad (3)$$

The measurements of the frequency of sound vibrations excited in the PCR due to the injection of an HCEB in two- and three-component mixtures showed that the discrepancy between the values calculated by Eq. (3) and the experimental values did not exceed 10%, and at the frequencies lower than 400 Hz the discrepancy was less than 5%. The dependence of the frequency of sound vibrations generated in the PCR due to the injection of an electron beam in two- and three-component mixtures on the parameter φ,

$$\varphi = \sqrt{\sum_i \gamma_i P_i} \Big/ \sqrt{\sum_i \mu_i P_i},$$

is shown in Fig. 2. The dots correspond to experimental data and the line corresponds to the calculation by Eq. (3).

By simple calculations, it is possible to show that, for a chemical reaction in which the initial mixture of reagents and the final mixture obtained in the reaction, are gases, the frequency of sound vibrations measured after the reaction is equal to the vibration frequency in the initial mixture. However, if solid or liquid products are obtained in the reaction, the frequency of the sound waves will change.

The proposed technique for monitoring the plasmochemical reaction by the change in frequency of sound vibrations was used in studying the direct reduction of tungsten from tungsten hexafluoride under the action of an HCEB [15]. The results were in good agreement with the data obtained by weighing the substrate placed in the reactor.

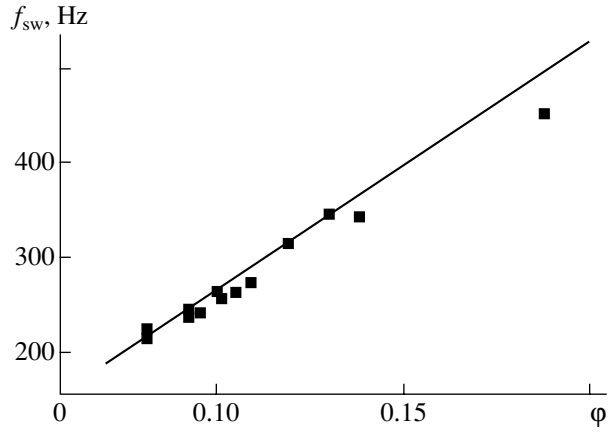

Fig. 2. Frequency of sound vibrations in the 30-cm-long PCR as a function of the parameter φ for a gas mixture.

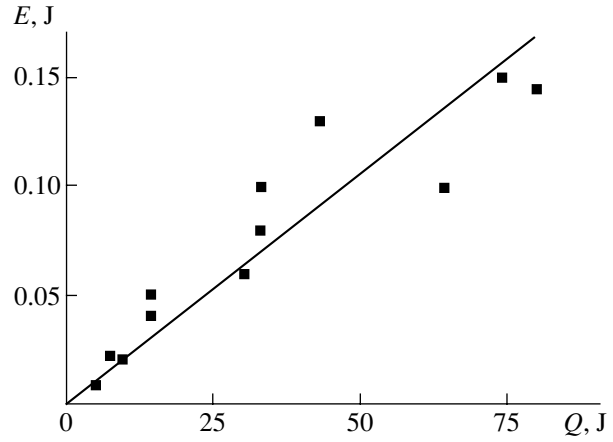

Fig. 3. Energy of sound vibrations in the PCR as a function of the energy of the electron beam absorbed in a gas.

INVESTIGATION OF THE SOUND WAVE ENERGY

In a closed volume of the PCR, with the injection of an electron beam, standing waves are generated, the form of which is in our case nearly sinusoidal. Then, the energy of the sound vibrations is described by the expression [13]

$$E = 0.25\beta\Delta P_{sw}^2 V,$$

where β is the compressibility of the medium, ΔP_{sw} is the amplitude of the sound waves, and V is the volume of the reactor. When the degree of compression is low ($\Delta P_{sw} \ll 1$) and the law of momentum conservation is valid (a low attenuation), the compressibility of the medium can be calculated by the formula [13]

$$\beta = (\rho c_{sw}^2)^{-1},$$

where ρ is the gas density and c_{sw} is the sound velocity in gas.

The dependence of the energy of sound vibrations in the reactor on the energy of the electron beam absorbed in gas is shown in Fig. 3. The energy of the HCEB absorbed by the gas was measured by the change in pressure in the reactor after the injection of the HCEB (as in [16]). The pressure was measured by the same differential pressure transducer that was used for detecting the sound waves.

For nitrogen and argon, a good correlation between the energy of sound vibrations and the energy contribution of the electron beam to gas was observed in a wide range of pressures (and, accordingly, in a wide range of energy contributions of the beam to gas), which makes it possible to evaluate the energy contribution of the electron beam to gas by the sound wave amplitude. The energy of sound waves was about 0.2% of the energy of the electron beam absorbed in the gas.

INVESTIGATION OF THE SOUND WAVE ATTENUATION

Since the form of sound vibrations generated in the reactor due to the injection of the HCEB is nearly sinusoidal, the change in the energy of sound waves due to the absorption is described by the relation [13]

$$E(t) = E_0 e^{-\alpha t},$$

where α is the absorption coefficient.

When a sound wave propagates in a tube closed at both ends, the absorption coefficient equals

$$\alpha = \alpha_1 + \alpha_2 + \alpha_3 + \alpha_4,$$

where α_1 is the sound absorption coefficient for the propagation in an unbounded gas, α_2 is the absorption coefficient due to the reflection from the side walls of the tube for the propagation along the tube, α_3 is the absorption coefficient due to the reflection from the tube ends, and α_4 is the absorption coefficient due to the friction at the tube walls.

The absorption coefficient of the sound wave energy in gas due to the heat conduction and the shear viscosity of gas can be determined by the Stokes–Kirchhoff formula [13]

$$\alpha_1 = \frac{(2\pi f_{sw})^2}{2\rho c_{sw}^2}\left[\frac{4}{3}\eta + \chi\left(\frac{1}{C_v} - \frac{1}{C_p}\right)\right], \qquad (4)$$

where η is the coefficient of shear viscosity of gas (g/cm s), χ is the coefficient of heat conduction (cal/cm s deg), and C_v and C_p are the heat capacities of gas at constant volume and at constant pressure, respectively.

For a low-frequency sound wave propagating along a circular tube, when the condition $\lambda > 1.7d$ (where λ is the wavelength and d is the tube diameter) is satisfied, the wave front is plane and the sound energy attenuation coefficient for the propagation along a tube with

ideally heat-conducting walls can be calculated by the Kirchhoff formula [17]

$$\alpha_2 = \frac{1}{r_0}\sqrt{\frac{\pi f_{sw}}{\rho}}\left[(\gamma-1)\sqrt{\frac{\chi}{\gamma C_p}} + \sqrt{\eta}\right], \quad (5)$$

where r_0 is the tube radius.

Taking into account that $\rho = \rho_0 P/P_0$, where P is the pressure of gas in the reactor, ρ_0 is the gas density at normal conditions, and $P_0 = 760$ torr, we obtain from Eq. (5):

$$\alpha_2 = \frac{K_1}{r_0}\sqrt{\frac{f_{sw}}{P}},$$

where

$$K_1 = \sqrt{\frac{\pi P_0}{\rho_0}}\left[(\gamma-1)\sqrt{\frac{\chi}{\gamma C_p}} + \sqrt{\eta}\right]. \quad (6)$$

It can be shown that the temporal absorption coefficient for the sound wave energy in a closed reactor with multiple reflection from its ends is equal to

$$\alpha_3 = \frac{c_{sw}}{l}\ln(1-\delta), \quad (7)$$

where l is the length of the reactor and δ is the energy absorption coefficient of a sound wave at a single reflection.

For normal incidence of a plane sound wave on a metal wall, which is a good heat conductor, the energy absorption coefficient equals [17]

$$\delta = 4(\gamma-1)\sqrt{\frac{\pi f_{sw}\chi}{\gamma C_p P}}. \quad (8)$$

However, if we consider only normal incidence of a sound wave on the ends of the reactor, we should neglect the absorption of the sound wave energy at reflection from the side walls of the reactor (i.e., $\alpha_2 = 0$). In this case, the sound absorption will be determined only by the heat conduction and the gas viscosity (Eq. (4)) and by the absorption at reflection from the reactor ends (Eqs. (7) and (8)). As will be shown below, the experimentally measured sound energy absorption coefficients in the reactor are several times greater than the values calculated by formulas (4), (7), and (8). Consequently, in the reflection from the ends of the reactor, it is necessary to take into account the dependence of the absorption coefficient on the angle of incidence and perform calculations by the formula [17]

$$\delta = \sqrt{\frac{f_{sw}}{\gamma P}}\left[0.39(\gamma-1)\sqrt{\frac{\chi}{C_p}} + 0.37\sqrt{\eta}\right]. \quad (9)$$

Taking into account that, for $\delta \ll 1$, $\ln(1-\delta) \approx \delta$, from Eqs. (9) and (7) we derive

$$\alpha_3 = \frac{K_2}{l}\sqrt{\frac{f_{sw}}{P}},$$

where

$$K_2 = c_{sw}\left[0.39(\gamma-1)\sqrt{\frac{\chi}{\gamma C_p}} + 0.37\sqrt{\frac{\eta}{\gamma}}\right]. \quad (10)$$

The inclusion of the sound wave energy loss due to the friction at the walls is important when the diameter of the tube is comparable with the mean free path of gas molecules, i.e., for capillary tubes. In our case, we can assume that $\alpha_4 \approx 0$.

Numerical estimates of the contributions of various mechanisms of sound absorption in the reactor show that the influence of volume absorption (due to the heat conduction and gas viscosity) is insignificant. For example, for sound waves generated in a 30-cm PCR filled with nitrogen at a pressure of 500 torr, we have $\alpha_1 = 1.8 \times 10^{-3}$ s^{-1}, $\alpha_2 = 5.9$ s^{-1}, and $\alpha_3 = 7.7$ s^{-1}.

The summary absorption coefficient taking into account only the normal incidence of sound waves (i.e., $\alpha_2 = 0$, $\alpha_3 = 1.2$ s^{-1}) is much smaller than the experimentally measured coefficient of sound absorption for these conditions (14.7 s^{-1}). Then, the expression for the summary absorption coefficient of the sound wave energy in a closed reactor can be written as

$$\alpha = \left(\frac{K_1}{r_0} + \frac{K_2}{l}\right)\sqrt{\frac{f_{sw}}{P}}, \quad (11)$$

where K_1 and K_2 are calculated by Eqs. (6) and (10), r_0 and l are the radius and length of the reactor in centimeters, f_{sw} is measured in hertz, and P is in torrs.

The values of the coefficients K_1 and K_2 for the investigated gases are given in the table.

It is important to note that, for the propagation of sound waves in a closed reactor, the main contribution (60–80%) to the absorption is made by the gas viscosity. The magnitude of the second term in Eqs. (5) and (9) is 3–9 times greater (for various gases) than the magnitude of the first term. The contributions of the side walls and ends of the reactor to the absorption of the sound wave energy are approximately equal for a large reactor.

The dependence of the sound energy absorption coefficient in the reactor on the pressure for various gases is shown in Fig. 4. For the comparison of the attenuation coefficients observed in different plasmochemical reactors (with the lengths 11.5 and 30 cm) and in various gases, the value of the attenuation coefficient

Table

Gas	K_1	K_2
N_2	25	218
O_2	27	189
Ar	32	254
WF_6	6.5	52

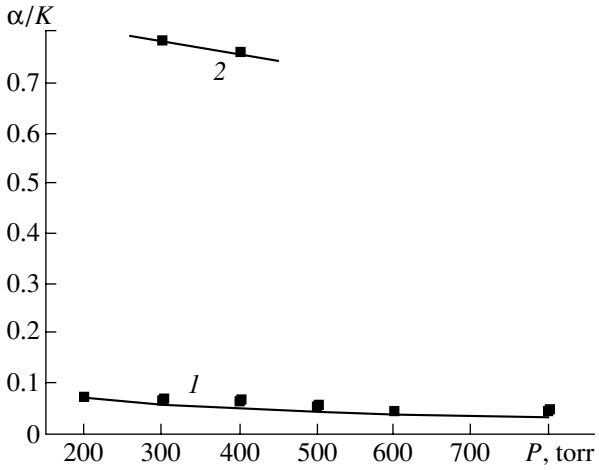

Fig. 4. Normalized coefficient of sound absorption in the reactor as a function of pressure.

was normalized to the coefficient K calculated by the formula

$$K = \sqrt{f_{sw}}\left(\frac{K_1}{r_0} + \frac{K_2}{l}\right).$$

The dots in Fig. 4 correspond to experimental measurements, and curve *1* is calculated by Eq. (11). For nitrogen, argon, and oxygen, the discrepancy between the calculated and experimental values of the absorption coefficient does not exceed 30%.

For sound waves generated due to the dissipation of a pulsed electron beam in the WF_6 vapor (curve *2* in Fig. 4), the experimentally obtained values of the absorption coefficient far exceed (by a factor of 14–15) the values calculated by Eq. (11). This may be caused by the formation of clusters in the reactor with the injection of the electron beam. The presence of large particles in the volume of gas leads to an increase in the absorption of sound waves. At the injection of the HCEB in WF_6, the direct reduction of tungsten in the form of nano-sized particles take place, which results not only in an increase in the frequency of sound waves [15], but also in a considerable growth of the sound energy absorption.

CONCLUSION

The described investigations of the sound waves generated in a closed reactor due to the dissipation of the energy of a pulsed electron beam show that a simple experimental setup detecting acoustic vibrations makes it possible to monitor with a high accuracy the plasmochemical process that is accompanied by a change in the phase composition of the initial reagent mixture. The formation of clusters in the volume of the reactor leads to a change in the frequency of sound waves and to a considerable increase in the attenuation of the vibration amplitude. Thus, the sound-wave diagnostics can be used for monitoring plasmochemical processes.

REFERENCES

1. V. D. Rusanov and A. A. Fridman, *Physics of a Chemically Active Plasma* (Nauka, Moscow, 1984).
2. A. A. Ivanov and T. K. Soboleva, *Nonequilibrium Plasma Chemistry* (Atomizdat, Moscow, 1978).
3. *Ionized Physical Vapor Deposition*, Ed. by Jeffrey A. Hopwood (San Diego, CA, Academic, 2000).
4. P. Czuprynski, O. Joubert, L. Vallier, and N. Sadeghi, J. Vac. Sci. Technol. A **17** (5), 2572 (1999).
5. Mak Yong Sun, IEEE Trans. Plasma Sci. **27** (4), 1188 (1999).
6. G. V. Denisov, Yu. N. Novoselov, and R. M. Tkachenko, Pis'ma Zh. Tekh. Fiz. **26** (16), 30 (2000) [Tech. Phys. Lett. **26**, 710 (2000)].
7. T. Ikegaki, S. Seino, Y. Oda, *et al.*, in *Proceedings of 13th International Conference BEAMS 2000* (Nagaoka, Japan, 2000), p. 934.
8. H. Cho, K. B. Jang, and D. C. Hays, Appl. Surf. Sci. **140** (1–2), 215 (1999).
9. S. Yu. Socovnin, Yu. A. Kotov, and M. E. Balesin, in *Proceedings of 12th Symposium on High Current Electronics* (Tomsk, 2000), Vol. 2, p. 512.
10. V. K. Zhivotov, V. D. Rusanov, and A. A. Fridman, *Diagnostics of Nonequilibrium Chemically Active Plasma* (Energoatomizdat, Moscow, 1985).
11. L. M. Lyamshev, *Radiation Acoustics* (Nauka, Moscow, 1996).
12. G. E. Remnev, I. F. Isakov, M. S. Opekunov, *et al.*, Izv. Vyssh. Uchebn. Zaved., Fiz., No. 4, 92 (1998).
13. M. A. Isakovich, *General Acoustics* (Nauka, Moscow, 1973).
14. B. M. Yavorskiĭ and A. A. Detlaf, *A Handbook on Physics* (Nauka, Moscow, 1968).
15. G. E. Remnev, A. I. Pushkarev, M. A. Pushkarev, *et al.*, Izv. Vyssh. Uchebn. Zaved., Fiz., No. 5, 33 (2001).
16. Yu. F. Bondar', S. I. Zavorotnyĭ, A. L. Ipatov, *et al.*, Fiz. Plazmy (Moscow) **8**, 1192 (1982).
17. B. P. Konstantinov, *Hydrodynamic Sound Formation and Propagation in a Bounded Medium* (Nauka, Moscow, 1974).

Translated by A. Svechnikov

Acoustical Physics, Vol. 48, No. 2, 2002, pp. 225–234. Translated from Akusticheskiĭ Zhurnal, Vol. 48, No. 2, 2002, pp. 266–276.

Diffraction of Sound by an Elastic Cylinder Near the Surface of an Elastic Halfspace

E. L. Shenderov[†]

Morfizpribor Central Research Institute, Chkalovskiĭ pr. 46, St. Petersburg, 197376 Russia

Received September 25, 2000

Abstract—Diffraction of an acoustic wave by an elastic cylinder near the surface of an elastic halfspace is considered. The solution relies on a Helmholtz-type integral equation and uses the Green function of an elastic halfspace. The latter function is represented in the form of an integral over the Sommerfeld contour on the plane of a complex variable that has the meaning of the angle of the wave incidence on the halfspace boundary. An integral equation for the sound pressure distribution over the cylinder surface is derived. This equation is reduced to an infinite system of equations for the Fourier-series expansion coefficients of this distribution. The results obtained are valid for the diffraction of a cylindrical wave and a plane wave. They also describe the diffraction of a spherical wave when the transmitter and receiver are far from the cylinder and lie in one plane that is orthogonal to the cylinder axis. © *2002 MAIK "Nauka/Interperiodica".*

If a body is located near a sound-reflecting boundary, an emitted or diffracted sound experiences multiple reflections between the body and the boundary, which can significantly change the pattern of the acoustic field. The sound diffraction by bodies located near a planar boundary has been extensively studied. The *T*-matrix method combined with the summation of multiply reflected waves was used to study the scattering from particular bodies located near a liquid halfspace [1, 2]. A cylinder with rounded ends and an elastic spherical shell were considered. In [3–5], the problem was solved by replacing the reflecting boundary with the object image symmetric about this boundary. Such a replacement leads to a problem of diffraction by two bodies, which is solved using the summation theorem for the special functions involved in the sound field expansions and is reduced to an infinite system of equations. The methods for solving such problems can be found in [6–8]. However, the replacement of the boundary with a symmetric object image is only valid for a perfect (acoustically hard or soft) boundary. In the case of an elastic or impedance boundary, this method is inapplicable. The situation is the same as in the classical problem of the spherical wave reflection from an impedance plane, whose solution is described in [9].

This paper addresses the diffraction by an elastic cylinder located near an elastic or impedance halfspace. The halfspace may be stratified or covered with an elastic plate. The dependence of the reflection coefficient or the input impedance of the halfspace surface on the incidence angle is assumed to be known.

[†] Deceased.

The solution presented below is a rigorous solution to the two-dimensional problem, i.e., to the problem of diffraction of a cylindrical acoustic wave by an elastic cylinder when the cylinder axis and the axes of the cylindrical source and the receiver are parallel to each other and to the surface of the halfspace. However, as shown in the appendix, the results obtained are valid for the diffraction of the cylindrical wave and for the diffraction of the spherical wave when the receive and transmit points lie in one plane that is orthogonal to the cylinder axis and the distance from one of these points to the cylinder is large in terms of the wavelength. In this case, the only difference in the solutions for the incident cylindrical and spherical waves is that, for the cylindrical wave, the amplitude of the wave scattered from the cylinder (and, therefore, the radius of the equivalent sphere) is by a factor of $\sqrt{2}$ greater than that for the spherical wave. This fact was noted earlier in [10].

Let us derive a system of equations for the coefficients of the Fourier series expansion of the total acoustic field on the cylinder surface.

The coordinate system is illustrated in Fig. 1. Let a line source M_0 oriented normally to the plane of the drawing emit the cylindrical wave

$$p_i(\mathbf{r}_1) = -ik\rho cQG_0(\mathbf{r}_0, \mathbf{r}_1), \qquad (1)$$

where $k = \omega/c$ is the wave number; ρ and c are the density of the upper halfspace and the acoustic velocity in it, respectively; Q is the source strength; and $G_0(\mathbf{r}_0, \mathbf{r}_1) = iH_0^{(1)}(k|\mathbf{r}_1 - \mathbf{r}_0|)/4$ is the Green function for a free space.

1063-7710/02/4802-0225$22.00 © 2002 MAIK "Nauka/Interperiodica"

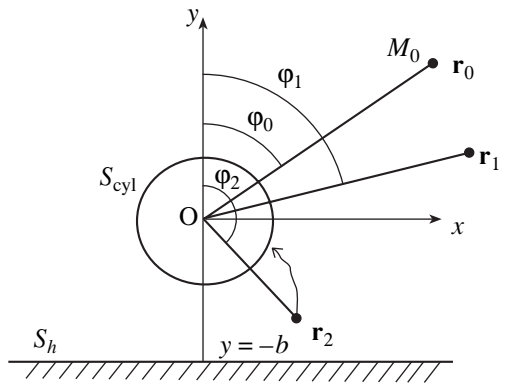

Fig. 1. Coordinate system.

In the upper halfspace, the total acoustic field satisfies the Helmholtz-type integral equation

$$p(\mathbf{r}_1) = -ik\rho cQG(\mathbf{r}_1, \mathbf{r}_0) + \int\limits_{S = S_h + S_{cyl}} \left[p(\mathbf{r}_2)\frac{\partial G(\mathbf{r}_1, \mathbf{r}_2)}{\partial n_2} - \frac{\partial p(\mathbf{r}_2)}{\partial n_2} G(\mathbf{r}_1, \mathbf{r}_2) \right] dS. \quad (2)$$

Here, the surface of integration, S, consists of the surface of the cylinder and the surface of the halfspace. The derivation of Eq. (2) can be found in [11] (appendix). The subscript 2 indicates that the derivative is taken along the normal at the point $\mathbf{r}_2$, which lies at the surface of the cylinder in the integral over the surface S_{cyl} and at the surface of the halfspace in the integral over the halfspace surface S_h. As the Green function $G(\mathbf{r}_1, \mathbf{r}_2)$, any Green function of the Helmholtz differential equation can be used. To eliminate the integration over the infinite surface, we choose the Green function for the upper halfspace so as to satisfy the boundary conditions at the surface (see [11]):

$$G(\mathbf{r}_1, \mathbf{r}_2) = \frac{i}{4\pi}\int\limits_{-\infty}^{\infty} \exp(iku(x_1 - x_2)) \times [\exp(ik\gamma|y_1 - y_2|) + A_h' \exp(ik\gamma(y_1 + y_2))]\frac{du}{\gamma}, \quad (3)$$

where $\gamma = \sqrt{1 - u^2}$, $A_h' = \exp(i2kb\gamma)A_h$, $A_h(u) = (w_h\gamma - 1)/(w_h\gamma + 1)$, $w_h = Z_h/(\rho c)$, and Z_h is the input impedance of the elastic halfspace. The change of variables $u = \sin\theta$ transforms the expression for $A_h(u)$ into the formula

$$A_h(\theta) = \frac{w_h\cos\theta - 1}{w_h\cos\theta + 1}, \quad (4)$$

which gives the reflection coefficient for the plane wave incident on the boundary of the elastic halfspace at the angle θ. Note that, for a locally responding surface (i.e., a surface whose properties are described by the normal impedance), the impedance w_h is independent of the incidence angle, whereas, for an elastic surface, the impedance depends on this angle. The following expression for this impedance is presented in [9]:

$$w_h = w_l\frac{\cos^2 2\theta_t}{\cos\theta_l} + w_t\frac{\sin^2 2\theta_t}{\cos\theta_t}. \quad (5)$$

Here, $w_l = (\rho_1 c_l)/(\rho c)$ and $w_t = (\rho_1 c_t)/(\rho c)$ are the wave impedances of the lower halfspace normalized by ρc. The subscripts l and t refer to longitudinal and shear waves, respectively; c_l and c_t are the velocities of these waves; and ρ_1 is the density of the medium. The angles of refraction θ_l and θ_t satisfy the Snell law: $\sin\theta_l = \sin\theta(c_l/c)$ and $\sin\theta_t = \sin\theta(c_t/c)$.

Let us write the distributions of the sound pressure and of the normal component of the particle velocity over the surface of the halfspace as the Fourier integrals representing the expansions in the wave numbers:

$$p(x_2) = \int\limits_{-\infty}^{\infty} P(u)\exp(ikux_2)du, \quad (6)$$

$$v_n(x_2) = \frac{1}{i\omega\rho}\frac{\partial p}{\partial n_2} = \int\limits_{-\infty}^{\infty} V(u)\exp(ikux_2)du. \quad (7)$$

In these expressions, x_2 denotes a point on the surface of the halfspace. For each plane wave, the complex amplitudes of the sound pressure and particle velocity are related as $P(u) = -Z_h(u)V(u)$. These expressions yield the formula for the normal derivative of the sound pressure at the surface of the halfspace, which enters into Eq. (2):

$$\frac{\partial p(\mathbf{r}_2)}{\partial n_2} = -ik\int\limits_{-\infty}^{\infty} \frac{P(u)}{w_h(u)}\exp(ikux_2)du. \quad (8)$$

Substituting Eqs. (3), (6), and (8) into Eq. (2), we obtain that the integral over the halfspace surface S_h is zero and only the integral over the cylinder surface S_{cyl} is left. Thus, the use of the Green function given by expression (3) eliminates the integration over the infinite surface.

Expression (3) can be represented as $G = G_0 + G_1$, where G_0 is the Green function for a free space and the term G_1 determines the field reflected from the boundary of the halfspace, i.e.,

$$G_0(\mathbf{r}_1, \mathbf{r}_2) = \frac{i}{4}H_0^{(1)}(k|\mathbf{r}_1 - \mathbf{r}_2|) = \frac{i}{4}\sum_{n=-\infty}^{\infty} \begin{Bmatrix} J_n(kr_1)H_n^{(1)}(kr_2) \\ J_n(kr_2)H_n^{(1)}(kr_1) \end{Bmatrix} \exp(in(\varphi_1 - \varphi_2)), \quad \begin{matrix} r_2 > r_1, \\ r_1 > r_2, \end{matrix} \quad (9)$$

$$G_1(\mathbf{r}_1, \mathbf{r}_2) = \frac{i}{4\pi}\int\limits_{-\infty}^{\infty} A_h' \exp[ik(u(x_1 - x_2) + \gamma(y_1 + y_2))]\frac{du}{\gamma}. \quad (10)$$

Expression (9) represents the summation theorem for the cylindrical functions. Using the change of variables $u = \sin\theta$ and $\gamma = \cos\theta$ and switching to the cylindrical coordinates $x_1 = r_1\sin\varphi_1$, $y_1 = r_1\cos\varphi_1$, $x_2 = r_2\sin\varphi_2$, and $y_2 = r_2\cos\varphi_2$, we obtain

$$G_1(\mathbf{r}_1, \mathbf{r}_2) = \frac{i}{4\pi}\int_\Gamma A_h'(\theta) \times \exp[ikr_1\cos(\varphi_1 - \theta)]\exp[ikr_2\cos(\varphi_2 + \theta)]d\theta. \quad (11)$$

Here, Γ is the Sommerfeld contour: $-\pi/2 + i\infty$, $\pi/2 - i\infty$. Using the expansion of a plane wave in cylindrical functions

$$\exp(ikr\cos\alpha) = \sum_{m=-\infty}^{\infty} i^m J_m(kr)\exp(im\alpha), \quad (12)$$

we obtain

$$G_1(\mathbf{r}_1, \mathbf{r}_2) = \frac{i}{4}\sum_{n=-\infty}^{\infty}(-i)^n J_n(kr_1)\exp(in\varphi_1) \times \sum_{m=-\infty}^{\infty}(-i)^m J_m(kr_2)\exp(-im\varphi_2) f_{m+n}, \quad (13)$$

where f_{m+n} are the coefficients defined as

$$f_s = \frac{(-i)^s}{\pi}\int_\Gamma A_h(\cos\theta)\exp[i2kb\cos\theta + is\theta]d\theta. \quad (14)$$

For an acoustically hard or acoustically soft surface of the halfspace, $A_h = 1$ or -1, respectively. Then, expression (14) takes the form of an integral representation of the Hankel function, which yields $f_s = \pm H_s^{(1)}(2kb)$, where the plus and minus signs refer to the acoustically hard and acoustically soft surfaces, respectively. Applying the summation theorem twice, one can show that, in these particular cases, the term G_1 is expressed by the formula $G_1 = iH_0^{(1)}(kR')/4$, which describes the field of the image line source; in this case, $R' = \sqrt{(x_1 - x_2)^2 + (y_1 + y_2)^2}$.

Let us represent the unknown distribution of the total sound pressure on the surface of the cylinder as the expansion

$$p(r, \varphi)|_{r=a} = \sum_{q=-\infty}^{\infty} p_q\exp(iq\varphi), \quad (15)$$

where p_q are the unknown coefficients. The normal component of the particle velocity in the medium at the surface of the cylinder is equal to the radial component of the particle velocity of the cylinder and can be represented as the expansion

$$v(\varphi) = \sum_{q=-\infty}^{\infty} v_q\exp(iq\varphi) = \frac{1}{i\omega\rho}\frac{\partial p}{\partial n}\bigg|_{r=a}.$$

The coefficients p_q and v_q are related as $v_q = -p_q/Z_q$, where Z_q are the mode impedances of the elastic cylinder oscillations, which are given by Eq. (A.3) of the appendix. Therefore, we obtain

$$\frac{\partial p}{\partial n}\bigg|_{r=a} = -ik\sum_{q=-\infty}^{\infty}\frac{p_q}{w_q}\exp(iq\varphi). \quad (16)$$

Here, $w_q = Z_q/(\rho c)$ are the mode impedances normalized by the wave impedance of the medium.

Let us place the observation point at the surface of the cylinder, substitute the above expressions into integral relationship (2), and take into account that, with the Green function chosen above, the integration can be performed only over the cylinder surface. The following transformations are simple, but cumbersome. Therefore, we only describe their main stages:

(a) Substitute expansion (15) at $\varphi = \varphi_1$ in Eq. (2) on its left-hand side.

(b) Substitute the Green function with Eqs. (9) and (13) it involves into the first term on the right-hand side by replacing r_2 and φ_2 with a and φ_0.

(c) Substitute expansions (15) and (16) of the distributions of the sound pressure and its normal derivative over the surface of the cylinder into the integrand.

(d) Substitute the Green function into the integrand by performing the differentiation along the normal with respect to the variable r_2. After completing the differentiation, set $r_1 = r_2 = a$. When calculating the derivative in Eq. (9), one should first let the point r_2 tend to the surface, i.e., assume that $r_1 > r_2$ and use the lower line of formula (9); take the derivative with respect to r_2; and then set $r_1 = r_2 = a$.

(e) Integrate with respect to φ_2 with allowance for the orthogonality relationships for the exponential factors. As a result, the sums over m and n involved in the integrand and containing φ_2 vanish except for the terms with $n = q$ or $m = q$.

(f) Change the order of the summation in the double sums, i.e., use the change of variables $n \longleftrightarrow q$, to obtain the factors $\exp(iq\varphi_2)$ in all their terms. Since all the sums over q are Fourier series, the equation obtained must be satisfied for each term of the sum over q.

(g) Using the well-known identity $J_n'(ka)H_n^{(1)}(ka) = J_n(ka)H_n^{(1)'}(ka) - 2i/(\pi ka)$, obtain the system of equations for the coefficients p_q:

$$p_q + \sum_{n=-\infty}^{\infty} p_n z_{qn} = b_q, \quad q = -\infty \ldots \infty, \quad (17)$$

where

$$z_{qn} = \frac{w_q}{w_n}(-1)^{q+n}\frac{J_n(ka) - iw_nJ_n'(ka)}{H_q^{(1)}(ka) - iw_qH_q^{(1)'}(ka)}f_{q+n}, \quad (18)$$

$$b_q = \frac{\rho cQ}{2\pi a}\frac{w_q}{H_q^{(1)}(ka) - iw_qH_q^{(1)'}(ka)} \times\left(H_q^{(1)}(kr_0)\exp(-iq\varphi_0)\right. \quad (19)$$

$$\left. + \sum_{m=-\infty}^{\infty}(-1)^{m+q}J_m(kr_0)\exp(-im\varphi_0)f_{m+q}\right).$$

Note that the coefficients z_{qn} of the matrix depend on neither the source position nor the position of the observation point. The free terms b_q depend on the source position but are independent of the position of the observation point.

To find the sound pressure p at the observation point M_1, we again resort to Eq. (2) and represent it, using Eqs. (9) and (13), as a sum of the incident cylindrical wave p_i, the wave p_r reflected from the halfspace boundary, and the wave p_s scattered by the cylinder (with allowance for the multiple scattering between the cylinder and the halfspace):

$$p = p_i + p_r + p_s, \quad (20)$$

where

$$p_i = k\rho cQH_0^{(1)}(k|\mathbf{r}_1 - \mathbf{r}_0|)/4, \quad (21)$$

$$p_r = \frac{k\rho cQ}{4}\sum_{n=-\infty}^{\infty}(-i)^nJ_n(kr_1)\exp(in\varphi_1) \times\sum_{m=-\infty}^{\infty}(-i)^mJ_m(kr_0)\exp(-im\varphi_0)f_{m+n}, \quad (22)$$

$$p_s = \int_{S_{\text{cyl}}}\left[p(\mathbf{r}_2)\frac{\partial G(\mathbf{r}_1, \mathbf{r}_2)}{\partial n_2} - \frac{\partial p(\mathbf{r}_2)}{\partial n_2}G(\mathbf{r}_1, \mathbf{r}_2)\right]dS. \quad (23)$$

First, consider Eq. (22). Substitute representation (14) into it and, in each sum, expand the plane wave in cylindrical functions. As a result, we obtain the integral representation for the reflected wave:

$$p_r = \frac{k\rho cQ}{4\pi}\int_\Gamma A_{\text{h}}(\theta)\exp[ik(2b\cos\theta + r_1\cos(\varphi_1 + \theta) + r_0\cos(\varphi_0 - \theta)]d\theta. \quad (24)$$

This expression differs from Eq. (11) in the constant factor and in the subscripts that indicate the positions of the source and the observation point with the coordinates (r_0, φ_0) and (r_1, φ_1), respectively. Expression (24) is an expansion of the reflected cylindrical wave similar to the Weyl–Brekhovskikh integral [9] in the classical problem of the spherical wave reflection from an elastic halfspace.

To find the scattered field, substitute expansion (15) and the Green function, written as the sum of expressions (9) and (13), into formula (23). Assume that the point $\mathbf{r}_2$ resides on the cylinder surface, i.e., $r_2 = a$. Since, in this case, $r_1 > r_2$, we should use the lower line in formula (9). Then, we obtain

$$p_s = -\frac{\pi ka}{2} \times\left[\sum_{q=-\infty}^{\infty}p_qs_qH_q^{(1)}(kr_1)\exp(iq\varphi_1) + \sum_{q=-\infty}^{\infty}p_qs_qu_q\right], \quad (25)$$

where

$$u_q = \sum_{n=-\infty}^{\infty}(-1)^{n+q}J_n(kr_1)\exp(in\varphi_1)f_{n+q}, \quad (26)$$

$$s_q = (J_q(ka) - iw_qJ_q'(ka))/w_q. \quad (27)$$

System of equations (17) and expression (25) determine the scattering field in terms of the coefficients of the Fourier series expansion of the total field on the cylinder surface. Therefore, when the radius of the cylinder decreases, these coefficients tend to the expansion coefficients of the sum of the incident and scattered fields rather than to zero. Hence, it is reasonable to transform these coefficients so as to extract the coefficients of expansion of the scattered field, which tend to zero as the radius of the cylinder decreases. To this end, we introduce new expansion coefficients a_q, which are related to the coefficients p_q as

$$p_q = -a_q\frac{2}{\pi ka}\frac{w_q}{J_q(ka) - iw_qJ_q'(ka)}. \quad (28)$$

Then, the system of equations (17)–(19) will have the form

$$a_q + \sum_{n=-\infty}^{\infty}a_nD_{nq} = E_q, \quad q = -\infty \ldots \infty, \quad (29)$$

$$D_{nq} = -a_q^{(0)}(-1)^{q+n}f_{q+n}, \quad (30)$$

$$E_q = a_q^{(0)}\frac{k\rho cQ}{4}\left[H_q^{(1)}(kr_0)\exp(-iq\varphi_0) + \sum_{m=-\infty}^{\infty}(-1)^{m+q}J_m(kr_0)\exp(-im\varphi_0)f_{m+q}\right], \quad (31)$$

and the scattered field (25) will take the form

$$p_s = \sum_{q=-\infty}^{\infty} a_q \Big[H_q^{(1)}(kr_1)\exp(iq\varphi_1) + \sum_{n=-\infty}^{\infty} (-1)^{n+q} J_n(kr_1)\exp(in\varphi_1) f_{n+q} \Big]. \quad (32)$$

In Eqs. (30) and (31), the coefficients $a_q^{(0)}$ are determined by formulas (A.2).

To obtain an asymptotic expression for the case when the receiver and transmitter are far from the cylinder, we first consider the field reflected from the plane. If at least one of the wave distances, kr_1 or kr_0, is much greater than unity, the integral in Eq. (24) can be calculated by the saddle-point method. Poles of the function $A_h(\theta)$ that may be crossed in the course of the deformation of the integration path can be neglected, because the residues at these poles produce surface waves, which decay exponentially with distance from the surface. In the exponent, we can single out the term $ik(h_0 + h_1)\cos\theta$, where $h_0 = b + r_0\cos\theta$ and $h_1 = b + r_1\cos\theta$ are the distances from the transmitter and the observation point to the surface, respectively. Therefore, the calculation of the residues gives rise to the factor $\exp(-k(h_0 + h_1)\mathrm{Re}(\cos\theta))$. The amplitude of the surface wave thus depends on the sum $h_0 + h_1$ rather than on each distance individually. Hence, if the distance from at least one of these points to the surface is longer than the wavelength, the contribution of the residue can be neglected. This fact has been noted in relation to the problem of the spherical wave reflection from a halfspace [9].

The value of the variable of integration corresponding to the saddle point is determined as

$$\tan\theta_0 = \frac{r_0\sin\varphi_0 - r_1\sin\varphi_1}{2b + r_0\cos\varphi_0 + r_1\cos\varphi_1}. \quad (33)$$

As follows from Fig. 2, θ_0 is equal to the angle of incidence of sound at the point corresponding to the specular reflection. After calculating the integral, we obtain

$$p_r \approx A_h(\theta_0)\frac{k\rho cQ}{4}\sqrt{\frac{2}{\pi kl}}\exp(ikl - i\pi/4), \quad kr_1 \gg 1, \quad k(h_0 + h_1) \gg 1, \quad (34)$$

where $l = r_1\cos(\varphi_1 + \varphi_0) + 2b\cos\theta_0 + r_0\cos(\varphi_0 - \theta_0)$ is the total distance M_0SM_1 (Fig. 2). The first, second, and third terms of the expression for l are the lengths of the segments $M_1'A$, AB, and BM_0, respectively. Thus, in the far-field region, the reflected field is expectedly formed as a result of the emission of a cylindrical image source with the amplitude that is proportional to the reflection coefficient of sound at the angle of incidence corresponding to the geometrical optics reflection.

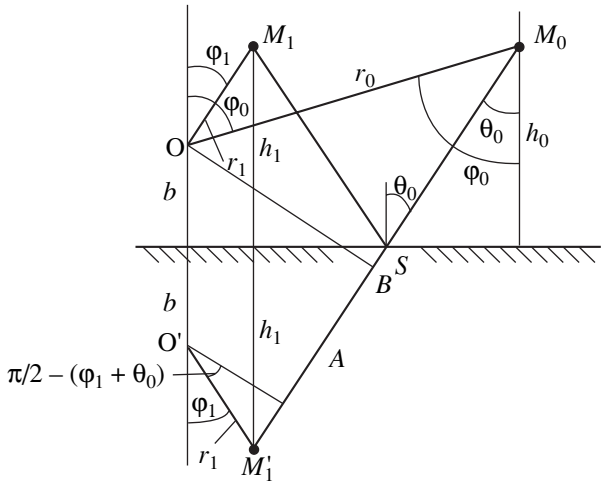

Fig. 2. To the derivation of Eqs. (33) and (34).

If the source is at a long distance from the cylinder, i.e., $kr_0 \gg 1$, Eq. (31) can be simplified. To this end, we represent the sum that appears in this expression as

$$\sum_{m=-\infty}^{\infty} = \frac{i^q}{\pi}\int_\Gamma A_h(\theta) \times \exp(ik(2b\cos\theta + r_0\cos(\theta - \varphi_0)) + iq\theta)d\theta. \quad (35)$$

When $kr_0 \gg 1$, this integral can be calculated by the saddle-point method. If $r_0 \gg b$ and $kr_0 \gg q$, the saddle point is $\theta_0 \approx \varphi_0$. When transforming the integration path into the steepest descent path, it can cross the poles of the function $A_h(\theta)$. The residues at these poles determine the surface waves near the halfspace boundary. However, since the contributions of these poles decrease exponentially with the distance from the boundary, they can be ignored when calculating the field produced by a distant source. Note that all contributions of the poles and the corresponding surface waves produced by the interaction between the closely spaced cylinder and boundary are taken into account rigorously, because they are described by the coefficients f_{q+m}, which enter into the matrix coefficients z_{qm}.

After calculating the integral, we obtain the system of equations

$$a_q + \sum_{n=-\infty}^{\infty} a_n D_{qn} = F_q, \quad q = -\infty \ldots \infty, \quad (36)$$

where the coefficients of the matrix coincide with the coefficients given by Eq. (30) and the right-hand sides are written as

$$F_q \approx p_i^{(0)} a_q^{(0)}(-i)^q \times [\exp(-iq\varphi_0) + (-1)^q A_h'(\varphi_0)\exp(iq\varphi_0)]. \quad (37)$$

Here, $p_i^{(0)}$ represents the sound pressure in a free space at a point lying on the cylinder axis, i.e.,

$$p_i^{(0)} \approx \frac{k\rho cQ}{4}\sqrt{\frac{2}{\pi kr_0}}\exp(ikr_0 - i\pi/4).$$

For the diffraction of a unit-amplitude plane wave, one should set $p_i^{(0)} = 1$ and replace the sign of approximate equality with the sign of exact equality.

Let us calculate the sound pressure in the scattered wave at the observation point located far from the cylinder when $kr_1 \gg 1$. The sum over n in Eq. (32) can be represented as

$$\sum_{n=-\infty}^{\infty} = \frac{i^q}{\pi}\int_\Gamma A_h(\theta) \times \exp[ik(2b\cos\theta + r_1\cos(\varphi_1 + \theta)) + iq\theta]d\theta. \quad (38)$$

In the far-field region, i.e., under the constraints imposed when calculating integral (35), integral (38) can also be calculated by the saddle point method. The saddle point is determined as $\theta_0 = -\varphi_1$. Then, we obtain the scattered field as

$$p_s = \sqrt{\frac{2}{\pi kr_1}}\exp(ikr_1 - i\pi/4)\Phi_s(\varphi_1), \quad (39)$$

where

$$\Phi_s(\varphi_1) \approx \sum_{q=-\infty}^{\infty} a_q(-i)^q \times [\exp(iq\varphi_1) + (-1)^q\exp(-iq\varphi_1)A_h'(\varphi_1)]. \quad (40)$$

The system of equations (36) and expressions (39) and (40) completely determine the scattered field formed in the far zone as a result of the diffraction of a plane wave and also of a cylindrical wave by an elastic cylinder located near a boundary of an elastic halfspace.

In system of equations (36), the indices assume positive and negative values, whereas the existing programs for solving systems of linear equations handle only positive indices. If the variables are renumbered through shifting their indices by a constant value, the most significant terms (for example, a_0 and a_1) will occur in the middle of the system, which is inconvenient when an infinite system of equations is solved by the reduction method. It is therefore reasonable to rearrange the system so as to make all indices positive and place the most significant terms at the beginning of the system. It is also useful to separate the solution into the symmetric and antisymmetric parts about $\varphi_1 = 0$. The system of equations can thus be split into two systems, each of them being twice as small as the original system, which reduces the computation time when the dimension of the system is large. The manipulations and final formulas are omitted here for brevity.

Consider the calculation of coefficients f_{n+q} defined by integral (14). Let us split this integral into integrals over the segments $(-\pi/2 + i\infty, -\pi/2)$, $(-\pi/2, \pi/2)$, and $(\pi/2, \pi/2 - i\infty)$. In the first and third of these integrals, we change the variables $\theta = -\pi/2 + i\alpha$ and $\pi/2 - i\alpha$, respectively. Denoting $A_h(\theta)$ at $\theta = \pm(\pi/2 - i\alpha)$ as $A_h^{(1)}(\alpha)$, we obtain $f_s = (-i)^s(I_1 - iI_2)/\pi$, where

$$I_1 = \int_0^{\pi/2} A_h(\theta)\exp(i2kb\cos\theta)\cos(n\theta)d\theta, \quad (41)$$

$$I_2 = \int_0^{\infty} A_h^{(1)}(\alpha)\exp(-2kb\sinh\alpha) \times [\exp(i\pi n/2 + n\alpha) + \exp(-(i\pi n/2 + n\alpha))]d\alpha, \quad (42)$$

$$A_h^{(1)}(\alpha) = \frac{iw_h\sinh\alpha - 1}{iw_h\sinh\alpha + 1}, \quad (43)$$

and the refraction angles θ_l and θ_t, which enter into Eq. (5), are written as

$$\sin\theta_l = (c_l/c)\cosh\alpha, \quad \sin\theta_t = (c_t/c)\cosh\alpha. \quad (44)$$

The function $A_h(\theta)$ does not have any poles on the real axis of the complex plane of θ. Therefore, the integral I_1 is calculated in a straightforward manner. When the medium is lossless, the function $A_h^{(1)}(\alpha)$ can increase without limit at certain points of the integration path, which corresponds to the condition of the generation of surface waves. In this case, a residue at the pole should be added. The pole is however found as a solution to an intricate transcendental equation. It is therefore simpler to assume that the reflecting halfspace is always lossy and that the velocities of the longitudinal and transverse waves are complex-valued.

Integral (42) converges fast, the integrand starting to decrease rapidly when $\sinh\alpha > n\alpha(2kb)$. Note that, due to the sharp maxima in the integrand, in order to decrease the computation time, it is reasonable to split the integration interval into a number of shorter intervals and calculate each of these integrals using a quadrature formula rather than integrate over the entire interval at once. In this study, we used the Gaussian quadrature formula with the automatic selection of the number of nodes.

The system of equations was solved by reduction. To obtain the result with at least three true decimal digits, it was sufficient to retain $1.2k\alpha + 3$ terms in the series and, accordingly, the same number of equations in the system. The convergence of the system depends on the distance between the cylinder and the surface of the halfspace and persists until the cylinder touches the boundary.

When calculating the bistatic scattering patterns produced by the elastic cylinder (Fig. 3), we took into

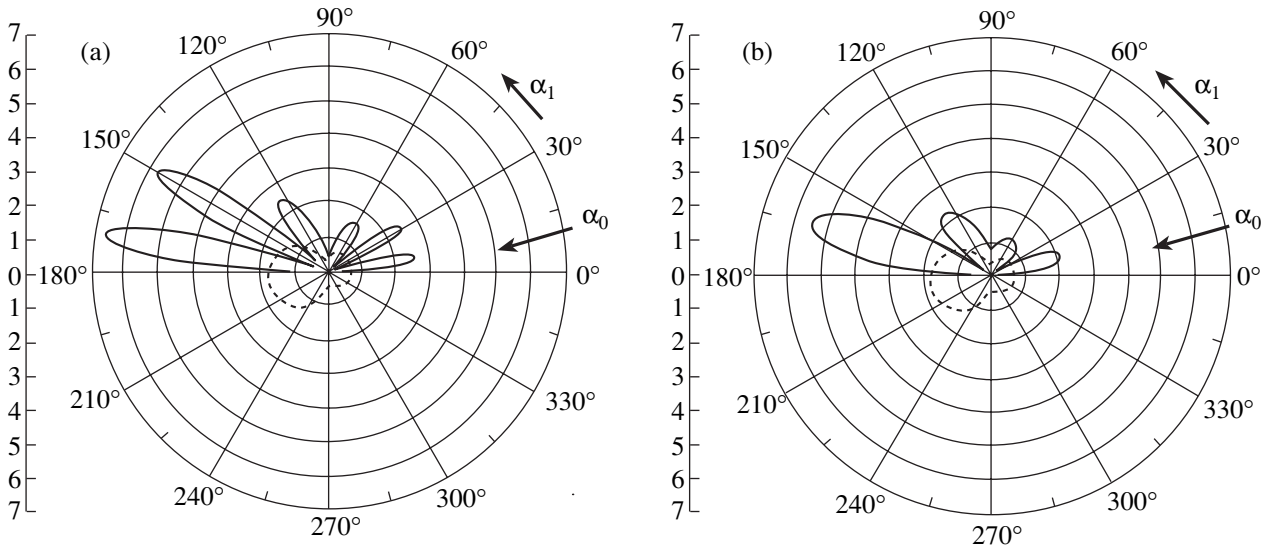

Fig. 3. Bistatic scattering patterns for an elastic cylinder located near the surface of a liquid halfspace (the solid lines) and in a free space (the dotted lines): kb = (a) 7.0 and (b) 3.0, ρ_m = 2000 kg/m^3, ka = 3.0, $c_l^{(\mathrm{cyl})}$ = 2000 m/s, $c_t^{(\mathrm{cyl})}$ = 300 m/s, $\varepsilon_l^{(\mathrm{cyl})}$ = 0.1, $\varepsilon_t^{(\mathrm{cyl})}$ = 0.2, ρ_1 = 1800 kg/m^3, c_l = 2000 m/s, ε_l = 0.01, and $\varphi_0 = 80°$ ($\alpha_0 = 10°$).

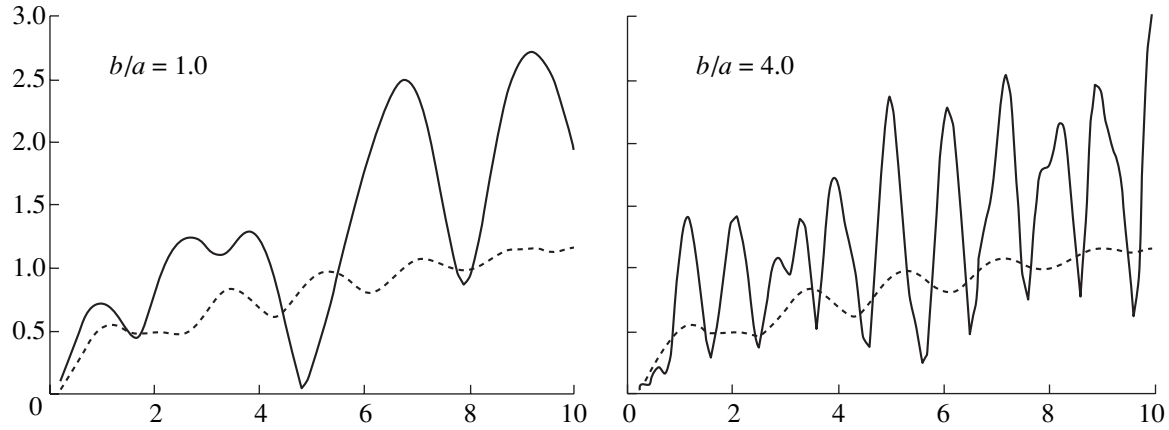

Fig. 4. Relative amplitude of the backscattered field for a cylinder located near the boundary of a halfspace (the solid lines) and in a free space (the dotted line) versus the wave radius for different distances between the cylinder and the surface: ρ_m = 2000 kg/m^3, ka = 3.0, $c_l^{(\mathrm{cyl})}$ = 2000 m/s, $c_t^{(\mathrm{cyl})}$ = 300 m/s, $\varepsilon_l^{(\mathrm{cyl})}$ = 0.1, $\varepsilon_t^{(\mathrm{cyl})}$ = 0.2, ρ_1 = 1800 kg/m^3, c_l = 2000 m/s, ε_l = 0.01, and $\varphi_0 = 45°$.

account the active loss in the cylinder material. The coefficients that characterize the sound attenuation for the transverse waves were assumed to be twice as large as those for the longitudinal waves, which is typical of elastic media (rubber-like materials). In Fig. 3 and the subsequent figures, the plots are constructed versus the angular coordinate $\alpha_1 = 90° - \varphi_1$.

As compared to the scattering patterns in a free space, the patterns produced by a cylinder located near a boundary are more nonuniform. The additional maxima and minima in the patterns occur due to the multiply reflected waves and the interference between them. The longer the distance between the cylinder and the boundary is, the smaller the angular spacing between the extrema of the plots. At certain directions, the amplitude of the wave scattered by the cylinder located near the halfspace boundary was found to be 2–3 times greater than the amplitude of the wave scattered by the cylinder located in a free space.

The dependence of the scattering amplitude on the wave radius of the cylinder exhibits an oscillatory behavior (Fig. 4). Oscillations of two types are observed here. One of them is associated with the resonance oscillations of the cylinder, and the other is produced by the interference of the waves multiply scattered between the cylinder and the plane. The frequency of the oscil-

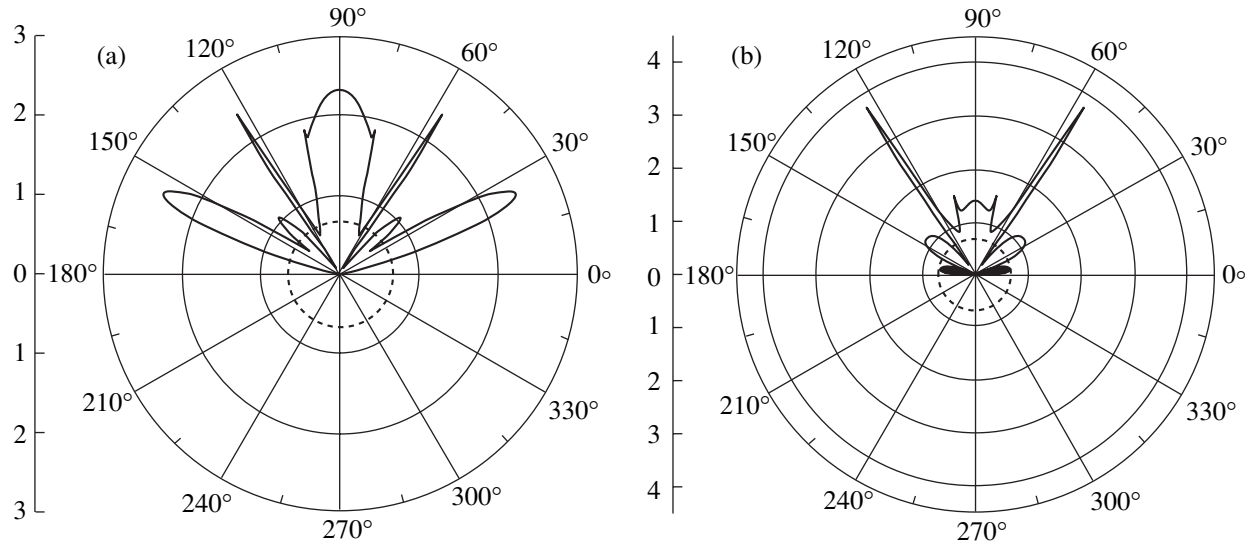

Fig. 5. Backscattering patterns for a cylinder located near the surface of an elastic halfspace (the solid lines) and in a free space (the dotted lines): kb = (a) 7.0 and (b) 3.0, ρ_m = 2000 kg/m^3, ka = 3.0, $c_l^{(\mathrm{cyl})}$ = 1800 m/s, $c_t^{(\mathrm{cyl})}$ = 300 m/s, $\varepsilon_l^{(\mathrm{cyl})}$ = 0.1, $\varepsilon_t^{(\mathrm{cyl})}$ = 0.2, ρ_1 = 2700 kg/m^3, c_l = 6100 m/s, c_t = 3050 m/s, ε_l = 0.001, and ε_t = 0.002.

lations increases with the distance between the cylinder and the halfspace surface.

The above results refer to a cylinder located near a liquid halfspace. Figure 5 shows the backscatter (monostatic) pattern for the elastic halfspace. The backscatter patterns exhibit sharp maxima due to the excitation of the longitudinal and transverse waves. The angles at which these maxima occur satisfy the conditions $\sin\varphi_1 \approx c/c_l$ and $\sin\varphi_1 \approx c/c_t$. In Fig. 5, these angles correspond to $\alpha_1 = \pi/2 - \varphi_1$ of 57° and 123° for the shear waves and 76° and 104° for the longitudinal waves.

ACKNOWLEDGMENTS

This work was supported by the Russian Foundation for Basic Research, project no. 00-02-17840.

APPENDIX

RELATION BETWEEN THE SOLUTIONS TO THE PROBLEMS OF THE DIFFRACTION OF CYLINDRICAL AND SPHERICAL WAVES BY A CYLINDER

Paper [12] was the first to consider the diffraction of a plane wave by an elastic cylinder. Later, similar problems in various formulations were solved in a number of works (see, e.g., [13, 14]). The diffraction of a spherical acoustic wave by an elastic cylinder was first considered in [15]. However, as it is indicated above, the solution is expressed in terms of rather intricate complex integrals of cylindrical functions of a complex argument, which are very difficult to calculate. Therefore, in this paper, we use an exact solution to the two-dimensional problem, while a solution for the spherical incident wave is obtained for the asymptotic case when the transmitter and receiver are far from the cylinder.

Let a cylinder of radius a be centered at the origin of coordinates and r_1, φ_1 and r_0, φ_0 be the coordinates of the observation point and of a line source of a cylindrical wave, respectively. The diffracted field is given by the well-known expansion (see, e.g., [10])

$$p_s^{(\mathrm{cyl})} = \frac{k\rho c Q}{4} \times \sum_{n=-\infty}^{\infty} a_n^{(0)} H_n^{(1)}(kr_0) H_n^{(1)}(kr_1) \exp(in(\varphi_1 - \varphi_0)), \tag{A.1}$$

where

$$a_n^{(0)}(ka) = -\frac{J_n(ka) - iw_n J_n'(ka)}{H_n^{(1)}(ka) - iw_n H_n^{(1)\prime}(ka)}. \tag{A.2}$$

Here, $w_n = Z_n/\rho c$ are the mode impedances of the elastic cylinder normalized by ρc. Expressions for the impedances Z_n can be found in [7]:

$$Z_n = \frac{i\rho_m c_t^{(\mathrm{cyl})}}{k_t a} \times \frac{F_1(k_l a)F(k_t a) - 2F_3(k_l a)F_2(k_t a)}{nJ_n(k_t a)F_1(k_l a) - k_l J_n'(k_l a)F_2(k_t a)}, \tag{A.3}$$

where $k_l = \omega/c_l^{(\mathrm{cyl})}$ and $k_t = \omega/c_t^{(\mathrm{cyl})}$ are the wave numbers of the longitudinal and shear waves in the material

of the cylinder, ρ_m is the density of the material of the cylinder, and

$$F_1(x) = 2n(xJ_n'(x) - J_n(x));$$
$$F_2(x) = x^2J_n''(x) - xJ_n'(x) + n^2J_n(x); \quad \text{(A.4)}$$
$$F_3(x) = x^2[J_n''(x) + (1 - (c_l^{(cyl)}/c_t^{(cyl)})^2/2)J_n(x)].$$

In expression (A.3), a misprint present in [7] is corrected.

When $kr_0 \gg 1$ and $kr_1 \gg 1$, we use asymptotic expressions for the Hankel functions and normalize the scattered field by the sound pressure of the incident wave at the cylinder axis, i.e., by

$$p_0^{(cyl)} = \frac{k\rho cQ}{4}H_0^{(1)}(kr_0)$$
$$\approx \frac{k\rho cQ}{4}\sqrt{\frac{2}{\pi kr_0}}\exp(ikr_0 - i\pi/4),$$

to obtain the ratio of the sound pressure amplitude of the scattered wave to the amplitude of the incident wave at the origin

$$\frac{p_s^{(cyl)}}{p_0^{(cyl)}} = \sqrt{\frac{2}{\pi kr_1}}\exp(ikr_1 - i\pi/4)\Phi_s(ka), \quad \text{(A.5)}$$

where

$$\Phi_s(ka) = \sum_{n=-\infty}^{n=\infty}(-1)^n a_n^{(0)}(ka)\exp(in(\varphi_0 - \varphi_1)). \quad \text{(A.6)}$$

Assume that the sound is radiated by a spherical source and the distance between the source and the cylinder axis is r_0. Then, the sound pressure in a free space at a point located at this distance will be

$$p_0^{(sph)} = -ik\rho cQ\frac{\exp(ikr_0)}{4\pi r_0}. \quad \text{(A.7)}$$

To derive an expression for the scattered field in the three-dimensional case, i.e., for a spherical wave, we use the following familiar technique [10, 16]: we replace k with $\sqrt{k^2 - \xi^2}$ everywhere; multiply by $\exp[i\sqrt{k^2 - \xi^2}(z_1 - z_0)]/(2\pi)$, where z_1 and z_0 are the coordinates of the observation point and the source along the cylinder axis (Fig. A); and integrate with respect to ξ between the infinite limits. As a result, we obtain

$$p_s^{(sph)} = \frac{-i\rho cQ}{4\pi^2\sqrt{r_0r_1}}$$
$$\times\int_{-\infty}^{\infty}\exp[i\sqrt{k^2 - \xi^2}(r_1 + r_0) + i\xi(z_1 - z_0)] \quad \text{(A.8)}$$
$$\times\Phi_s(\sqrt{k^2 - \xi^2}a)d\xi.$$

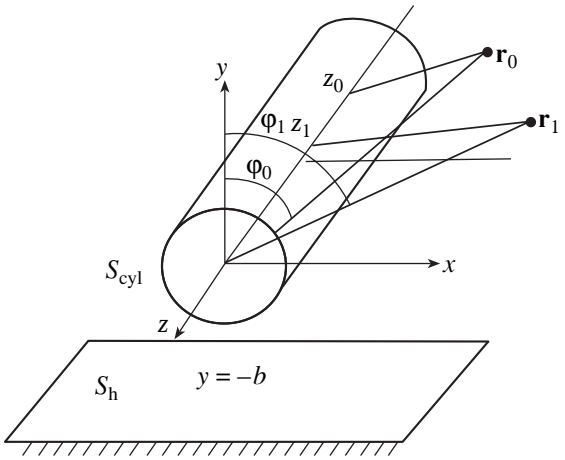

Fig. A. Coordinate system for the three-dimensional problem.

Since we consider the case when $kr_0 \gg 1$ and $kr_1 \gg 1$, the integral can be calculated by the stationary phase method. For simplicity, assume that the source and the receiver are located in one plane that is orthogonal to the axis, i.e., $z_1 = z_0$. Then, we obtain

$$p_s^{(sph)} = -\frac{\rho cQ}{(2\pi)^{3/2}}\sqrt{\frac{k}{r_0r_1(r_1 + r_0)}} \quad \text{(A.9)}$$
$$\times\Phi_s(ka)\exp(ik(r_1 + r_0)).$$

We normalize this quantity by the sound pressure at the axis in a free space (i.e., in the absence of the cylinder), which is given by Eq. (A.7). As a result, we arrive at the expression

$$\frac{p_s^{(sph)}}{p_0^{(sph)}} = \sqrt{\frac{2r_0}{\pi kr_1(r_1 + r_0)}}\exp(ikr_0)\Phi_s(ka). \quad \text{(A.10)}$$

The comparison of expressions (A.5) and (A.10) yields that the function $\Phi_s(ka)$, which depends on the radius of the cylinder and its elastic characteristics and on the scattering angles, is the same for the cylindrical and spherical sources, whereas the distance dependence of the scattering amplitudes are different. In a particular case when the source and the receiver are at the same point, i.e., $r_1 = r_0$, we have

$$\frac{p_s^{(sph)}}{p_0^{(sph)}} = \sqrt{\frac{1}{\pi kr_1}}\exp(ikr_1)\Phi_s(ka). \quad \text{(A.11)}$$

Contrasting this expression with formula (A.6), we obtain that, for the spherical source, the scattering amplitude is $\sqrt{2}$ times smaller than that for the line source. As was noted in [10], this fact can be explained as follows. When the spherical wave is diffracted by a cylinder, the Fresnel zones, i.e., antiphase regions whose contributions partly compensate for each other, occur on the surface of the cylinder along its axis. The

radius of the equivalent sphere for the diffraction of the spherical wave by an infinite cylinder can be obtained through the comparison of expression (A.11) with a similar expression for the acoustically hard or acoustically soft sphere of radius a_{equiv} that is large in terms of the wavelength. In this case, the following well-known expression is valid:

$$\left|\frac{p_s^{(\text{sph})}}{p_0^{(\text{sph})}}\right| = \frac{a_{\text{equiv}}}{2r_1}. \tag{A.12}$$

Equating expressions (A.11) and (A.12), we obtain the radius of the equivalent sphere for the spherical wave incident on the cylinder:

$$a_{\text{equiv}} = 2\sqrt{\frac{r_1}{\pi k}}|\Phi_s(ka)|. \tag{A.13}$$

To obtain the radius of the equivalent sphere for the backscattered field, we should set $\varphi_1 = \varphi_0$ in the expressions for Φ_s. Note that, in [7], the positive angular direction is opposite to that accepted in this paper; therefore, in the tables given there in the appendix, the values associated with the backscatter are denoted as $\Phi_s(\pi)$.

The radius of the equivalent sphere for the incidence of a cylindrical or plane wave on a cylinder can be found by equating expressions (A.5) and (A.12), which yields

$$a_{\text{equiv}} = 2\sqrt{\frac{2r_1}{\pi k}}|\Phi_s(ka)|. \tag{A.14}$$

Thus, the radius of the equivalent sphere for a plane or cylindrical wave incident on an infinite cylinder is found to be $\sqrt{2}$ times greater than that for a spherical incident wave.

As follows from Eqs. (A.13) and (A.14), the radius of the equivalent sphere for an infinite cylinder depends on the distance between the source and the cylinder. This property is also associated with the Fresnel zones that occur along the cylinder axis (see, e.g., [10]). The size of the first zone, which makes the greatest contribution to the scattered field, increases with the distance. Since the radius of the equivalent sphere increases with the distance between the cylinder and the source and receiver position as $r_1^{1/2}$, the amplitude of the scattered field decreases by the cylindrical law $r_1^{-1/2}$ rather than by the spherical law r_1^{-1}.

REFERENCES

1. G. C. Bishop and J. Smith, J. Acoust. Soc. Am. **101**, 767 (1997).
2. G. C. Bishop and J. Smith, J. Acoust. Soc. Am. **105**, 130 (1999).
3. J. C. Bertrand and J. W. Young, J. Acoust. Soc. Am. **60**, 1265 (1976).
4. G. C. Gaunaurd and H. Huang, IEEE Trans. Ultrason. Ferroelectr. Freq. Control **43**, 690 (1996).
5. G. C. Gaunaurd and H. Huang, J. Acoust. Soc. Am. **96**, 2526 (1994).
6. V. Tversky, J. Appl. Phys. **23** (3), 407 (1952).
7. E. L. Shenderov, *Wave Problems in Hydroacoustics* (Sudostroenie, Leningrad, 1972).
8. E. A. Ivanov, *Electromagnetic Wave Diffraction by Two Bodies* (Nauka i Tekhnika, Minsk, 1968).
9. L. M. Brekhovskikh, *Waves in Layered Media*, 1st ed. (Nauka, Moscow, 1957; Academic, New York, 1960).
10. E. L. Shenderov, *Radiation and Scattering of Sound* (Sudostroenie, Leningrad, 1989).
11. E. L. Shenderov, Akust. Zh. **46**, 816 (2000) [Acoust. Phys. **46**, 716 (2000)].
12. J. J. Faran, J. Acoust. Soc. Am. **23**, 405 (1951).
13. L. M. Lyamshev, Akust. Zh. **2**, 358 (1956) [Sov. Phys. Acoust. **2**, 382 (1956)].
14. W. H. Lin and A. C. Raptis, J. Acoust. Soc. Am. **73**, 736 (1983).
15. Tao-bao Li and Mitsuhiro Ueda, J. Acoust. Soc. Am. **87**, 1871 (1990).
16. L. B. Felsen and N. Marcuvitz, *Radiation and Scattering of Waves* (Prentice-Hall, Englewood Cliffs, NJ, 1973; Mir, Moscow, 1978), Vols. 1, 2.

Translated by A. Khzmalyan

Acoustical Physics, Vol. 48, No. 2, 2002, pp. 235–238. Translated from Akusticheskiĭ Zhurnal, Vol. 48, No. 2, 2002, pp. 277–280.

SHORT COMMUNICATIONS

Resonance Absorber for Flexural Waves in Beams and Plates

A. D. Lapin

Andreev Acoustics Institute, Russian Academy of Sciences, ul. Shvernika 4, Moscow, 117036 Russia

e-mail: bvp@akin.ru

Received March 15, 2001

In practice, a vibration insulation for flexural waves in beams and plates is obtained with the use of resonators [1–7]. The simplest resonator is a spring–mass system [8–10]. When such a resonator is positioned normally to a plate and attached to it by a spring, it provides effective scattering of flexural waves propagating in the plate. The vibration insulation occurs because of the scattering (reflection) of flexural waves from the resonators [3, 4, 6]. A dissipative loss in a resonator reduces the efficiency of its operation as a scatterer for flexural waves. Earlier [11], it was shown that, at a certain value of the dissipation factor, the power absorbed by a resonator reaches its maximum and becomes equal to the power scattered by this resonator. The latter property of resonators with dissipation can be used for designing efficient absorbers of flexural waves propagating in beams and plates. Wide-band absorbers consisting of several resonant elements were studied in [12].

Consider a thin semi-infinite cantilever beam coincident with the semiaxis $x > 0$ so that its fixed end is at $x = 0$. A harmonic flexural wave propagating along the beam is characterized by the displacement

$$w^{(i)}(x, t) = \exp[-i(kx + \omega t)],$$

where k and ω are the wave number and the circular frequency, respectively. The reflection from the fixed end gives rise to two waves one of which is homogeneous and the other inhomogeneous. The reflected field has the form

$$w^{(r)}(x, t) = \{ie^{ikx} - (1 + i)e^{-kx}\}e^{-i\omega t}.$$

The total field in the beam is expressed as

$$\begin{aligned} w^{(0)}(x, t) &= w^{(i)}(x, t) + w^{(r)}(x, t) \\ &= (1 + i)\{\cos(kx) - \sin(kx) - e^{-kx}\}e^{-i\omega t}. \end{aligned} \quad (1)$$

In this standing field, the antinodes occur at the points

$$x_n \approx \frac{(4n - 1)\pi}{4k},$$

where n represents any arbitrary positive integer. At some of the antinodes of the field $w^{(0)}$ (e.g., at $x = x_q \equiv H$), we attach a resonator to the beam and assume that the resonator has a mass m and an elastic coefficient $\kappa(1 - i\varepsilon)$, where ε is the dissipation factor. Under the effect of the field $w^{(0)}(x, t)$, the resonator is excited and generates a field $w^{(1)}(x, t)$. The total field w in the beam with the resonator is equal to the sum $w^{(0)} + w^{(1)}$. Let us show that, at the resonance frequency, at a certain value of the dissipation factor ε, the travelling flexural wave $\exp[i(kx - \omega t)]$ propagating in the total field $w(x, t)$ in the region $x > H$ is absent.

Denote the displacement of the resonator mass by $w'(t)$. The equation of motion of this mass has the form

$$m\frac{d^2w'}{dt^2} = -F(t), \quad (2)$$

where the force F is determined by the formula

$$F(t) = \kappa(1 - i\varepsilon)[w'(t) - w(H, t)]. \quad (3)$$

The equation of motion of the beam connected with the resonator can be written as

$$\rho\frac{d^2w}{dt^2} + G\frac{d^4w}{dx^4} = F(t)\delta(x - H), \quad (4)$$

where ρ and G are the linear density and flexural rigidity of the beam, respectively, and $\delta(x)$ is the delta function. The wave number of the flexural wave is equal to $\left(\frac{\rho}{G}\omega^2\right)^{\frac{1}{4}}$. Since $w^{(i)}$ and $w^{(r)}$ are free waves, we can replace w by $w^{(1)}$ on the left-hand side of Eq. (4). The displacement $w^{(1)}$ satisfies the boundary condition

$$w^{(1)} = \frac{dw^{(1)}}{dx} = 0 \text{ at } x = 0. \quad (5)$$

The scattered field in the beam can be derived as follows. We calculate the displacement produced in a semi-infinite beam by a harmonic point force $F(t) = F_0\exp(-i\omega t)$, where F_0 is a complex amplitude. In an infinite beam, this point force causes the displacement

$$\begin{aligned} w^{(2)}(x, t) = \frac{iF_0}{4Gk^3}\{&\exp[ik|x - H|] \\ &+ i\exp[-k|x - H|]\}\exp(-i\omega t). \end{aligned}$$

1063-7710/02/4802-0235$22.00

Taking into account the waves reflected from the fixed end $x = 0$, we obtain the following expressions for $w^{(1)}$:

$$0 < x < H, \quad w^{(1)}(x,t) = \frac{iF_0}{4Gk^3}\{\exp[ik(H-x)] + i\exp[-k(H-x)] + [ie^{ikH} - (1+i)e^{-kH}]e^{ikx} + [e^{-kH} - (1+i)e^{ikH}]e^{-kx}\}\exp(-i\omega t), \tag{6}$$

$$x > H, \quad w^{(1)}(x,t) = \frac{iF_0}{4Gk^3}\{[e^{-ikH} + ie^{ikH} - (1+i)e^{-kH}]e^{ikx} + [ie^{kH} + e^{-kH} - (1+i)e^{ikH}]e^{-kx}\}\exp(-i\omega t). \tag{7}$$

We select the force amplitude F_0 so as to satisfy Eq. (3). According to Eq. (2), the displacement of the mass will have the form

$$w'(t) = \frac{F_0}{m\omega^2}\exp(-i\omega t). \tag{8}$$

Substituting Eqs. (1), (6), and (8) in Eq. (3), we obtain the desired force amplitude

$$F_0 = i\omega w_0^{(0)}(H)\left\{\left[\mathrm{Re}Y + \frac{\varepsilon\omega}{\kappa(1+\varepsilon^2)}\right] + i\left[\mathrm{Im}Y + \frac{1}{m\omega} - \frac{\omega}{\kappa(1+\varepsilon^2)}\right]\right\}^{-1}, \tag{9}$$

where

$$w_0^{(0)}(H) = w^{(0)}(H,t)\exp(i\omega t),$$

$$Y = \frac{-i\omega w^{(1)}(H,t)}{F(t)}$$

is the compliance of the semi-infinite beam with respect to the point force. Neglecting small quantities of the order of $\exp(-kH) \equiv \exp\left[-(4q-1)\frac{\pi}{4}\right]$, we obtain the approximate expressions

$$w_0^{(0)}(H) = 2\exp(-ikH), \quad Y = \frac{\omega}{4Gk^3}(2+i).$$

The scattered field $w^{(1)}$ is calculated by substituting F_0 in Eqs. (6) and (7).

The resonance scattering occurs at the frequency ω_0 determined from the equation

$$\mathrm{Im}Y + \frac{1}{m\omega} - \frac{\omega}{\kappa(1+\varepsilon^2)} = 0. \tag{10}$$

At the resonance frequency, the force amplitude is

$$F_0 = i\omega w_0^{(0)}(H)\left[\mathrm{Re}Y + \frac{\varepsilon\omega}{\kappa(1+\varepsilon^2)}\right]^{-1} \approx i4Gk^3e^{-ikH}\left[1 + \frac{2\varepsilon Gk^3}{\kappa(1+\varepsilon^2)}\right]^{-1}.$$

Let us separate the wave travelling along the x axis from the total field $w = w^{(0)} + w^{(1)}$. According to Eqs. (1) and (7), the amplitude of this wave is expressed as

$$A = i + \frac{iF_0}{4Gk^3}[e^{-ikH} + ie^{ikH} - (1+i)e^{-ikH}].$$

At the frequency $\omega = \omega_0$, we approximately obtain

$$A = i\left\{1 - 2\left[1 + \frac{2\varepsilon Gk^3}{\kappa(1+\varepsilon^2)}\right]^{-1}\right\}.$$

When the dissipation factor ε is approximately equal to $\kappa/(2Gk^3)$, the amplitude A becomes zero. This means that the resonator completely absorbs the incident wave.

A similar consideration is possible for a plate. Let a semibounded plate lie in the upper xy half-plane and be rigidly clamped along the boundary $y = 0$. A harmonic flexural wave incident on this boundary is characterized by the displacement

$$w^{(i)}(x,y,t) = \exp[i(k_x^0x - k_y^0y - \omega t)],$$

where k_x^0 and $-k_y^0$ are the projections of the wave vector of the incident wave on the x and y axes, respectively. The total field $w^{(0)}$ in the plate is equal to the sum of the incident and reflected waves:

$$w^{(0)}(x,y,t) = -i2\{\sin(k_y^0y - \varphi^0) + \sin\varphi^0\exp(-\alpha^0y)\}\exp[i(k_x^0x - \varphi^0 - \omega t)], \tag{11}$$

where

$$\alpha^0 = \sqrt{k^2 - (k_x^0)^2} \quad \text{and} \quad \sin\varphi^0 = \frac{k_y^0}{\sqrt{2}k}.$$

In this field, the antinodes occur on the lines $y_n \approx \frac{\pi(2n-1) + 2\varphi^0}{2k_y^0}$, where n is any integer. We attach identical resonators with masses m and elastic coefficients $\kappa(1 - i\varepsilon)$ to the plate along one of these lines (e.g., $y = y_q \equiv H$) at the points $x = x_s \equiv sL$, where $s = 0, \pm1, \pm2, \ldots$. The resonators are excited by the field $w^{(0)}$ and generate the field $w^{(1)}$. The total field in the plate with the resonators is $w = w^{(0)} + w^{(1)}$.

Let us denote the displacement of the mass of the sth resonator [which is attached to the plate at the

point (x_s, H)] by $w_s'(t)$. The equation of motion of this mass has the form

$$m\frac{d^2w_s'}{dt^2} = -F_s(t), \tag{12}$$

where the force F_s is determined by the formula

$$F_s(t) = \kappa(1-i\varepsilon)[w_s'(t) - w(x_s, H, t)]. \tag{13}$$

The equation describing the motion of the plate connected with the resonators can be written in the form

$$\rho\frac{dw^2}{dt^2} + G\Delta^2 w = \sum_{s=-\infty}^{s=\infty} F_s(t)\delta(x-x_s)\delta(y-H),$$

where ρ and G are the surface density and the flexural rigidity of the plate, respectively, and Δ is the Laplacian. On the left-hand side of this equation, the quantity w can be replaced by $w^{(1)}$.

The structure of the scattered field is determined by the period of the scattering array (chain) of resonators, and the quantity $w^{(1)}(x, y, t)\exp(-ik_x^0 x)$ is a periodic function of x with a period L. Then, in the presence of the exciting field given by Eq. (11), the force $F_s(t)$ can be represented in the form

$$F_s(t) = F\exp[(k_x^0 x_s - \omega t)],$$

where F is the force amplitude at $s = 0$. The scattered field in the plate is obtained in the same way as the scattered field in a beam. In an unbounded plate, the chain of point forces $F_s(t)$ generates the field

$$w^{(2)}(x, y, t) = \sum_{n=-\infty}^{n=\infty} \frac{iF}{4LGk^2}\left\{\frac{1}{k_y^n}\exp(ik_y^n|H-y|) + \frac{i}{\alpha^n}\exp(-\alpha^n|H-y|)\right\}\exp[i(k_x^n x - \omega t)],$$

where

$$k_x^n = k_x^0 + \frac{2\pi}{L}n,$$

$$k_y^n = \sqrt{k^2 - (k_x^n)^2}, \quad \text{and} \quad \alpha^n = \sqrt{k^2 + (k_x^n)^2}.$$

Taking into account the waves reflected from the clamped boundary $y = 0$, we obtain the following expression for $w^{(1)}$ at $y \geq H$:

$$w^{(1)}(x, y, t) = \sum_{n=-\infty}^{n=\infty} \frac{iF}{4LGk^2}\left\{\frac{1}{k_y^n}[1 - \exp(i2k_y^n H - i2\varphi^n)] \times \exp[i(k_x^n x - \omega t) + ik_y^n(y-H)] + i\left[\frac{1}{\alpha^n} - \frac{2}{k_y^n}\sin\varphi^n \exp(ik_y^n H - i\varphi - \alpha^n H)\right] \times \exp[i(k_x^n x - \omega t) - \alpha^n(y-H)]\right\}, \tag{14}$$

where $\sin\varphi^n = \dfrac{k_y^n}{\sqrt{2}k}$. In Eq. (14), the first term in the braces represents a homogeneous plane wave for $|k_x^n| < k$ and an inhomogeneous plane wave for $|k_x^n| > k$, and the second term in the braces always represents an inhomogeneous wave.

We select the force amplitude F so as to satisfy Eq. (13). The displacement of the plate at the point of the resonator attachment is understood as the displacement averaged over the contact area between the plate and the resonator. According to Eq. (12), the displacement $w_s'(t)$ is equal to $\dfrac{F_s(t)}{m\omega^2}$. Substituting $w^{(0)}$, $w^{(1)}$, and w_s' in Eq. (13), we derive the desired force amplitude

$$F = i\omega w_0^{(0)}(0, H)\left\{Y + i\left[\frac{1}{\omega m} - \frac{\omega}{\kappa(1-i\varepsilon)}\right]\right\}^{-1},$$

where

$$w_0^{(0)}(0, H) = w^0(0, H, t)\exp(i\omega t) \approx 2\exp(-ik_y^0 H),$$

$$Y = \frac{-i\omega w^{(1)}(x_s, H, t)}{F_s(t)} \approx \sum_{n=-\infty}^{n=\infty} \frac{\omega\varepsilon_n}{4LGk^2k_y^n}\left\{1 - \exp[i2(k_y^n H - \varphi^n)] + i\frac{k_y^n}{\alpha^n}\right\},$$

$$\varepsilon_n = \frac{\sin(k_x^n a)}{(k_x^n a)}\frac{\exp(ik_y^n a) - 1}{(ik_y^n a)}.$$

Averaging is performed over a square area whose side $2a$ is small compared to the flexural wavelength; $\varepsilon_n \approx 1$ when $k_x^n a \ll 1$.

The scattered field is obtained from Eq. (14) by substituting F into it. The resonance scattering occurs at the frequencies determined from the equation

$$\mathrm{Im}\,Y + \frac{1}{m\omega} - \frac{\omega}{\kappa(1+\varepsilon^2)} = 0.$$

This dispersion equation is identical in form to Eq. (10). However, because of the complex dependence of Y on frequency, it may have several solutions. At the resonance frequency, the amplitude of the nth scattered

homogeneous spectrum (i.e., scattered homogeneous plane wave) has the form

$$A_n = -\frac{\omega}{2LGk^2k_y^n}\left\{Y_1 + \frac{\varepsilon\omega}{\kappa(1+\varepsilon^2)}\right\}^{-1} \times \exp[-i(k_y^0 + k_y^n)H]\{1 - \exp[i2(k_y^n H - \varphi^n)]\}, \quad (15)$$

where

$$Y_1 = \mathrm{Re}\,Y = \sum_s{}' \frac{\omega}{4LGk^2k_y^s}\{1 - \cos[2(k_y^s H - \varphi^s)]\}. \quad (16)$$

Here, the prime denotes the summation over all s at which k_y^s is real.

When the period of the chain is smaller than $\lambda(1 + \sin\theta)^{-1}$, where $\theta = \arcsin\frac{k_x^0}{k}$ is the angle of the wave incidence and $\lambda = \frac{2\pi}{k}$, only the "zeroth" spectrum is homogeneous in the scattered field given by Eq. (14). Then, from Eqs. (15) and (16), we derive the expressions

$$Y_1 = \frac{\omega}{2LGk^2k_y^0},$$

$$A_0 = 2\exp(-i2\varphi^0)\left[1 + \frac{2\varepsilon LGk^2k_y^0}{\kappa(1+\varepsilon^2)}\right]^{-1}.$$

Combining the homogeneous reflected wave with the zeroth scattered spectrum, we obtain a travelling homogeneous wave with the amplitude A equal to

$$[-\exp(-i2\varphi^0) + A_0] = -\exp(-i2\varphi^0)\left\{1 - 2\left[1 + \frac{2\varepsilon LGk^2k_y^0}{\kappa(1+\varepsilon^2)}\right]^{-1}\right\}.$$

When the dissipation factor ε is approximately equal to $\frac{\kappa}{2LGk^2k_y^0}$, the amplitude A becomes zero. This means that the chain of resonators completely absorbs the incident wave.

REFERENCES

1. I. I. Klyukin, Akust. Zh. **6**, 213 (1960) [Sov. Phys. Acoust. **6**, 209 (1960)].
2. I. I. Klyukin and Yu. D. Sergeev, Akust. Zh. **10**, 60 (1964) [Sov. Phys. Acoust. **10**, 49 (1964)].
3. M. A. Isakovich, V. I. Kashina, and V. V. Tyutekin, in *Marine Instrument Making, Ser. Acoust.* (Inst. of Acoustics, USSR Acad. Sci., Moscow, 1972), Issue 1, pp. 117–125.
4. M. A. Isakovich, V. I. Kashina, and V. V. Tyutekin, USSR Inventor's Certificate No. 440509, Byull. Izobret., No. 31 (1974).
5. M. A. Isakovich, V. I. Kashina, and V. V. Tyutekin, Akust. Zh. **23**, 384 (1977) [Sov. Phys. Acoust. **23**, 214 (1977)].
6. L. S. Tsil'ker, Akust. Zh. **26**, 606 (1980) [Sov. Phys. Acoust. **26**, 336 (1980)].
7. R. J. Nagem, I. Velikovik, and G. Sandri, J. Sound Vibr. **207**, 429 (1997).
8. *Acoustics Handbook*, Ed. by Malcolm J. Crocker (Wiley, New York, 1997).
9. M. Gurgoze and H. Batan, J. Sound Vibr. **195**, 163 (1996).
10. M. Gurgoze, J. Sound Vibr. **223**, 667 (1999).
11. A. D. Lapin, Akust. Zh. **33**, 278 (1987) [Sov. Phys. Acoust. **33**, 164 (1987)].
12. V. V. Tyutekin and A. P. Shkvarnikov, Akust. Zh. **18**, 441 (1972) [Sov. Phys. Acoust. **18**, 369 (1972)].

Translated by E. Golyamina

Acoustical Physics, Vol. 48, No. 2, 2002, pp. 239–242. Translated from Akusticheskiĭ Zhurnal, Vol. 48, No. 2, 2002, pp. 281–284.

SHORT COMMUNICATIONS

Statistical Properties of the Sidelobe Level of an Acoustic Parametric Antenna

D. B. Ostrovskiĭ

Morfizpribor Central Research Institute, Chkalovskiĭ pr. 46, St. Petersburg, 197376 Russia

e-mail: mfp@mail.wplus.net

Received May 14, 2001

An advantage of a parametric transmitting antenna (PTA) is that it has lower sidelobes than traditional antennas [1], which provides a low level of interferences created by the surface and volume reverberation and also enhances hiding of the transmission. The angular pressure dependence $P(\theta, \beta)$ at the difference frequency can be written as

$$P(\theta, \beta) = P_{f1}(\theta, \beta)P_{f2}(\theta, \beta)\Psi, \quad (1)$$

where (θ, β) are the angular coordinates; $P_{f1,2}(\theta, \beta)$ is the pressure produced by the source at the partial pumping frequencies f_1 and f_2, respectively; and Ψ is a function independent of angles (θ, β), which is different for different PTA models [1–5].

Since the directional pattern determines only the angular antenna characteristics, the PTA factor [6], or the nonnormalized directional pattern, can be written as

$$R(\theta, \beta) = R_{f1}(\theta, \beta)R_{f2}(\theta, \beta), \quad (2)$$

where $R_{f1,2}(\theta, \beta)$ are the partial patterns at the frequencies f_1 and f_2.

As for real sources, the parameters of their elements are spread; therefore, $R_{f1}(\theta, \beta)$, $R_{f2}(\theta, \beta)$, and, hence, $R(\theta, \beta)$ are random variables. The statistical characteristics of $R(\theta, \beta)$ are determined by the statistical characteristics of $R_{f1}(\theta, \beta)$ and $R_{f2}(\theta, \beta)$. The only known work on the statistical characteristics of PTA [7] studies only the pressure at the difference frequency at the maximum of the directional pattern versus the spread in the partial pumping frequencies. Therefore, it is of interest to study the statistic of PTA's sidelobes.

Consider the statistical characteristics of a random PTA's pattern in the general case, as this is customary in the statistical theory of antennas [6, 8]; i.e., with allowance for errors in the excitation amplitude and phase, for errors in element settings, and for element failures. We will normalize function (2) by its mean value; then the magnitude of the normalized pattern is

$$|R(\theta, \beta)| = A|R_{f1}(\theta, \beta)R_{f2}(\theta, \beta)|, \quad (3)$$

where

$$1/A = \overline{|R_{f1}(\theta, \beta)|}\,\overline{|R_{f2}(q, \beta)|}. \quad (4)$$

For simplicity sake, we denote $|R_{fi}(\theta, \beta)| = R_i$, $i = 1, 2$.

The pumping signal can be applied to the antenna in a two-channel or one-channel excitation mode [1]. In the first mode, the source array is divided into two equal, though statistically independent, overlapping subarrays. In the one-channel excitation mode, the beat signal between the pumping frequencies is applied to each element of the source.

First, consider the two-channel excitation mode. Since the subarrays that constitute the PTA pumping source are statistically independent, the mean value and variance of the pattern at the difference frequency are expressed in terms of the mean values and variances of the partial directional patterns:

$$\overline{R} = \overline{R_1}\,\overline{R_2}, \quad D_R = D_{R1}D_{R2} + \overline{R_1}^2 D_{R2} + \overline{R_2}^2 D_{R1}.$$

As shown in [8], the functions R_1 and R_2 are described by the Rician distribution:

$$f(R_i) = \frac{R_i}{\sigma_i^2}\exp\left(-\frac{R_i^2 + Q_i^2}{2\sigma_i^2}\right)I_0\left(\frac{R_i Q_i}{\sigma_i^2}\right), \quad (5)$$

where Q_i and σ_i $(i = 1, 2)$ are the distribution parameters.

For a traditional antenna representing the source, i.e., when $Q/\sigma > 3$–4, the Rician distribution (5) goes over into the Gaussian distribution; when $Q/\sigma < 0.5$, it changes to the Rayleigh distribution [9]

$$f(R) = \frac{R}{\sigma^2}\exp\left(-\frac{R^2}{2\sigma^2}\right), \quad (6)$$

whose mean value and variance are

$$M[R] = \sigma\sqrt{\pi/2}, \quad D[R] = \sigma^2(2 - \pi/2). \quad (7)$$

Since our primary interest is in low sidelobe levels, we assume that the magnitude of the directional pattern

1063-7710/02/4802-0239$22.00

is characterized by distribution (6). In this case, the partial patterns are independent and, therefore, the magnitude of the normalized pattern at the difference frequency is characterized by the two-dimensional Rayleigh distribution

$$f(x, y) = \frac{xy}{\sigma_1^2\sigma_2^2}\exp\left(-\frac{x^2 + y^2}{2\sigma_1\sigma_2}\right), \quad (8)$$

where the parameters $\sigma_{1,2}$ of the distribution correspond to the random variables X and Y, i.e., to R_1 and R_2.

Let us express σ in terms of the statistical characteristics of fluctuations of the antenna elements. The array factor $R(\theta, \beta)$ is

$$R(\theta, \beta) = \sum_{m=1}^{N_0} A_{m0}\Delta_m \exp[i(\mathbf{k} - \mathbf{k}_0)\mathbf{r}_{m0}], \quad (9)$$

where A_{m0} is the nominal excitation coefficient of the mth element, N_0 is the nominal number of elements, $\mathbf{k}$ is the wave vector, and $\mathbf{r}_{m0}$ is the nominal position vector of the array element.

Summarizing the data presented in [6, 8, 10], we represent the scatter coefficient Δ_m for the parameters of the mth element as

$$\Delta_m = a_m(1 + \delta_m)\exp(i\varphi_m)\exp[i(\mathbf{k} - \mathbf{k}_0)\delta\mathbf{r}_m], \quad (10)$$

where a_m is the failure parameter, which equals unity with a probability p when the element is operable and zero with probability $1–p$ when it fails; δ_m is the relative amplitude error; and $\delta\mathbf{r}_m$ is the fluctuation in the element position.

Let us assume for definiteness sake that the fluctuations possess the following properties:

(i) elements and fluctuations of different types are statistically independent;

(ii) fluctuations are uniformly distributed over the antenna aperture;

(iii) elements are statistically indistinguishable;

(iv) phase errors and adjustment errors have the Gaussian distribution with zero mean values; standard deviations of the amplitude, phase, and adjustment errors are σ_Δ, σ_φ, and σ_d, respectively.

As follows from [8], the parameter σ of distribution (6) subject to these assumptions has the form

$$\sigma_i^2 = \frac{1 + \sigma_\Delta^2 - p\exp(-\sigma_\varphi^2 - k_i^2\sigma_d^2)}{2p\exp(-\sigma_\varphi^2 - k^2\sigma_d^2)} \times R_{\mathrm{el}}^2(\theta, \beta, f_i)\sum_{m=1}^{M} A_{m0}^2 \Big/ \left(\sum_{m=1}^{M} A_{m0}\right)^2, \quad (11)$$

where R_{el} is the directional pattern of one element (in the case of a planar antenna and complete compensation [6]); M is the number of elements (for the two-channel mode, $M = N_0/2$); N_0 is the nominal number of elements in the source; and $k_i = 2\pi f_i/c$.

As follows from Eq. (11), the quantities dependent on the frequency f_i are the element pattern R_{el} and the wave number k. Since the condition $f_i/F \approx 10$ (F is the difference frequency) is usually met and, therefore, $f_1 \approx f_2 \approx f_0 = (f_1 + f_2)/2$, we can assume that $\sigma_1 = \sigma_2 = \sigma(f_0)$. Replacing $\sigma_{1,2}$ in Eq. (8) with σ, we obtain the distribution density of PTA's pattern in the form of the product of independent random variables [11]:

$$f(R) = RK_0(R/\sigma^2)/\sigma^4, \quad (12)$$

where $K_0(z)$ is the Macdonald function, whose mean value and variance are

$$M[R] = \pi\sigma^2/2, \quad D[R] = \sigma^4(4 - \pi^2/4). \quad (13)$$

Figure 1a shows the histogram and distribution (12), which approximates it. We performed simulations for an antenna with the average pumping frequency f_0 = 50 kHz, difference frequency F = 5 kHz, and total number of elements $N_0 = 18 \times 18$. The levels of partial directional patterns were 0.0266 and 0.0264. The numerical characteristics of the fluctuations obtained from n = 1000 realizations were as follows: $p = 0.9$, $\sigma_\Delta = 0.7$, $\sigma_\varphi = 0.3$, and $\sigma_d = 2$ mm. The solid curve refers to the parameter σ obtained from formula (13); the dashed curve, from formula (11). The two curves virtually coincide and approximate with statistical confidence the directional pattern distribution of the parametric radiator excited in the two-channel mode.

Consider the one-channel excitation mode. As follows from the expressions that describe the models of the parametric radiator, in the one-channel excitation mode, the pressures P_{f1} and P_{f2} are created by the whole antenna aperture. Accordingly, the partial directional patterns R_1 and R_2 are formed by all elements of the source. The PTA pattern is calculated by formula (3), but, in this case, the partial patterns R_1 and R_2 are not independent.

Each of the partial patterns is a random (in general, nonstationary) process in frequency. At the same time, at $f/F \gg 1$, in the theory of the parametric radiator [4, 5], the product of pressures at the frequencies f_1 and f_2 in formula (1) is replaced by the squared pressure at the frequency f_0: $P_{f1}P_{f2} \cong P_{f0}^2$. Then, PTA pattern (3) goes over into

$$|R(\theta, \beta)| = A|R_{f0}(\theta, \beta)|^2, \quad 1/A = \overline{|R_{f0}(\theta, \beta)|}^2,$$

i.e., becomes equal to a squared directional pattern of the source at the frequency f_0.

The original directional pattern of the source has Rician distribution (5). The square of this random vari-

Table

Mode	Mean value		Variance	
	formula	ζ_M	formula	ζ_D
Linear	$\sigma\sqrt{\pi/2}$	1	$\sigma^2(2-\pi/2)$	1
Two-channel	$\pi\sigma^2$	$\sigma\sqrt{2\pi}$	$4\sigma^4(4-\pi^2/4)$	$2\sigma^2(4+\pi)$
One-channel	$2\sigma^2$	$2\sigma\sqrt{2\pi}$	$4\sigma^4$	$8\sigma^2/(4-\pi)$
$X(2)/X(1)$	–	$\pi/2 > 1$	–	$4-\pi^2/4 > 1$

able, i.e., the directional pattern of the parametric antenna, will have the distribution

$$f(R) = \frac{1}{2\sigma^2}\exp\left(-\frac{R+Q^2}{2\sigma^2}\right)I_0\left(\frac{\sqrt{R}Q}{\sigma^2}\right), \qquad (14)$$

where the parameter $Q = |R_0(f_0)|$ is the nominal pattern of the source and σ is determined by formula (11) at $M = N_0$.

If $Q/\sigma > 3$, the directional pattern of the PTA is distributed as a squared Gaussian variable

$$f(R) = \frac{1}{2\sigma\sqrt{2\pi R}}\exp\left[-\frac{(\sqrt{R}-Q)^2}{2\sigma^2}\right].$$

When $Q/\sigma < 0.5$, the directional pattern of the PTA operating in the one-channel mode has the distribution

$$f(R) = \frac{1}{2\sigma^2}\exp\left(-\frac{R}{2\sigma^2}\right).$$

The results of simulations shown in Fig. 1b refer to the same source antenna as in the two-channel mode. In this case, we consider the direction, in which $Q/\sigma \approx 1$; therefore, the approximating curve is calculated by formula (14).

Let us compare the parametric radiator operating in different excitation modes and the traditional (linear acoustic) antenna in terms of their stability to fluctuations of the statistical characteristics at the same number of elements N_0 and at the same fluctuation parameters σ_Δ, σ_φ, σ_d, and p. We consider small directional pattern levels satisfying the condition $Q/\sigma < 0.5$. The table summarizes the formulas for the mean value and variance and for the ratios of the PTA's statistical characteristics to similar characteristics of the linear antenna. In the table, ζ_M is the ratio of the mean value of the PTA pattern in the two-channel (one-channel) excitation mode to that of the linear antenna, and ζ_D is the variance ratio. As the parameter σ, we use the parameter of the linear antenna, which is taken into account in the respective formulas for the two-channel mode. The bottom row of the table compares the two excitation modes of the parametric radiator, $X(2)$ and $X(1)$.

The parameter σ is on the order of $1/N_0$; therefore, the sidelobe level of the PIA directional pattern is more stable to random fluctuations both in mean value and in variance, i.e., it has a lower average level and a smaller

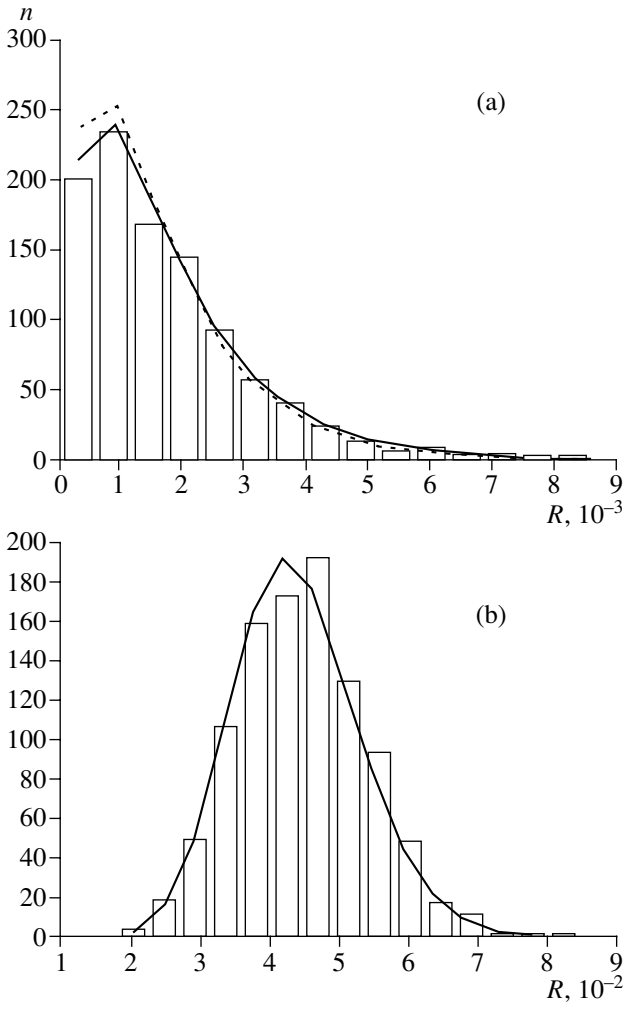

Fig. 1. Distribution histograms and the approximating functions: (a) the two-channel mode and (b) the one-channel mode.

spread. The one-channel excitation mode is more stable to element parameter fluctuations than the two-channel mode.

REFERENCES

1. B. K. Novikov and V. I. Timoshenko, *Parametric Antennas in Underwater Detection and Ranging* (Sudostroenie, Leningrad, 1989).
2. J. N. Tjøtta, S. Tjøtta, and E. H. Vefring, J. Acoust. Soc. Am. **88**, 2859 (1990).
3. V. B. Zheleznyĭ, Prikl. Akust. (Taganrog), No. 11, 23 (1985).
4. M. B. Moffett and R. H. Mellen, J. Acoust. Soc. Am. **61**, 325 (1977).
5. R. L. Rolleigh, J. Acoust. Soc. Am. **58**, 964 (1975).
6. M. D. Smaryshev and Yu. Yu. Dobrovol'skiĭ, *Hydroacoustic Antennas* (Sudostroenie, Leningrad, 1984).
7. V. N. Zuev and N. I. Kalyagin, Prikl. Akust. (Taganrog), No. 9, 47 (1983).
8. V. B. Zhukov and D. B. Ostrovskiĭ, *Parametric Reliability of Hydroacoustic Antennas* (Sudostroenie, Leningrad, 1980).
9. P. Beckmann, J. Res. Natl. Bur. Stand., Sect. D **66** (3), 231 (1962).
10. V. M. Khrustalev, Tr. Taganrog. Radiotekh. Inst., Issue 22, 107 (1971).
11. D. B. Ostrovskiĭ, Sudostroit. Prom., Ser. Obshchetekh., No. 37, 49 (1992).

Translated by A. Khzmalyan

Acoustical Physics, Vol. 48, No. 2, 2002, pp. 243–245. Translated from Akusticheskiĭ Zhurnal, Vol. 48, No. 2, 2002, pp. 285–287.

CHRONICLE

Yuriĭ Mikhaĭlovich Sukharevskiĭ (On His 95th Birthday)

Professor Yuriĭ Mikhaĭlovich Sukharevskiĭ—a doctor of engineering, a laureate of the USSR State Award, and a prominent scientist whose activity has been closely connected with the development of Russian hydroacoustics—turned ninety-five.

Sukharevskiĭ was born in Moscow on September 8, 1906. In 1930, he graduated from the Moscow Power Institute, where he specialized in electrical engineering. Simultaneously, he studied music at the Piano Faculty of the Moscow Conservatory. After receiving his master's degree in music in 1931, he became a post-graduate student and continued his studies at the conservatory until 1935.

Sukharevskiĭ's first research project dates back to 1929, when he was still a student. His first publication appeared in 1930. At that time, he was already working at the Moscow Electrical Plant. Later that same year, he became a researcher at the Acoustic Laboratory of the Central Research Institute of the People's Commissariat of Communication. There, his attention was directed toward the problems of using electroacoustic equipment for reception and high-fidelity reproduction of speech and music produced in broadcasting studios and concert halls. The change in the scientific interests of Sukharevskiĭ was explained by his natural desire to combine his two professions—engineering and music. In 1931–1935, he published a number of papers on electroacoustics and architectural acoustics and, in 1936, he published a monograph entitled *Modern Electroacoustics and Wire Broadcasting.* Another book written in collaboration with A.V. Rabinovich entitled *Broadcasting Studios and Microphones* appeared in 1938.

Sukharevskiĭ was also involved in the problems of electroacoustic metrology. In 1934, at the Central Research Institute of the People's Commissariat of Communication, he developed and designed Russia's first test bench for the absolute calibration of microphones and for testing loudspeaker characteristics, including nonlinearity. In 1936, he completed Russia's first acoustic test site for powerful sound sources, where he performed extensive studies of the directional characteristics of acoustic horns. The results of these studies were published in 1938 in *Elektrosvyaz'*. At that time, Sukharevskiĭ was working on the development of acoustical systems for the All-Union agricultural exhibition in Izmailovo Park, Moscow. There, he supervised the installation of the first outdoor anechoic distributed system of loudspeakers, which simulated the effect of large concert hall reverberation.

In 1938, Sukharevskiĭ became a senior researcher at the Physical Institute of the Academy of Sciences of the USSR. In 1939–1940, he performed theoretical and experimental studies of acoustic feedback that restricted the possibilities of sound amplification in sound-amplifying systems. The results of these studies were published in *Doklady Akademii Nauk SSSR.*

In 1939, Sukharevskiĭ received his candidate degree, and, in 1940, he became a doctor of engineering. His doctoral dissertation was entitled *Methods for Calculating Sound-Amplification Systems.* One of his official reviewers was N.N. Andreev.

Upon the German invasion of the USSR in World War II, Sukharevskiĭ began working on military acoustical problems. The research and development projects carried out by Sukharevskiĭ and his colleagues during the war were described in his paper in *Acoustical Physics* in 1996. Specifically, Sukharevskiĭ described his work in collaboration with D.I. Blokhintsev on the improvement of sound-detecting horns used in anti-aircraft artillery in 1942 and the full-scale experiments

1063-7710/02/4802-0243$22.00

performed in collaboration with V.S. Grigor'ev in the Pacific Ocean in 1944. These experiments dealt with the characteristics of sonars used on Russian and foreign naval vessels and submarines. Simultaneously, Sukharevskiĭ studied sound reflection from the hulls of ships and the acoustic parameters of the ocean that determine the operating range of sonars.

For his contribution to the defense potential of the USSR, Sukharevskiĭ was awarded an Order of the Red Banner of Labor.

The experience gained by Sukharevskiĭ during his work in the Pacific determined his continued career in hydroacoustics. The program proposed by Sukharevskiĭ for extensive studies in this area was the impetus for organizing an experimental hydroacoustic base for the Physical Institute of the Academy of Sciences of the USSR, namely, a marine research station with a coastal laboratory, stationary transmitting–receiving antennas, and research ships. The idea of organizing such a station was approved by S.I. Vavilov, director of the Physical Institute. During the next fifteen years, Sukharevskiĭ worked on the realization of this idea.

In 1945–1948, using the ships of the Black Sea Fleet, Sukharevskiĭ continued his studies (including those of sea reverberation) that were started during his work in the Pacific. The results of these studies were published in *Doklady Akademii Nauk SSSR* (1948). Sukharevskiĭ was authorized to select the optimal location for the marine station. The main criterion was that the station should be near a deep-water region. The Caucasian coastal region of the Black Sea satisfied this requirement. In addition, the warm climate allowed full-scale investigations year-round in any weather condition. The region could also be considered as a 1 : 2–1 : 3 scale model of the northwestern Pacific. The final choice was Cape Sukhumi, with a bottom slope of 35°. This place was most convenient because of the nearby port facilities for research ships.

In 1948, Sukharevskiĭ organized an expedition to the Black Sea. With a small group of researchers and the support of the Black Sea Fleet, he established a temporary marine station at Cape Sukhumi equipped with hydroacoustic antennas, which he designed, and mock-ups of the electronic and recording systems installed at the Sukhumi lighthouse. Using this equipment, he conducted investigations of sound reflection from ships and submarines. The newly developed stationary equipment was also used for studying the acoustic parameters of the marine environment: the sound absorption in sea water and the sound scattering from the sea bottom and surface.

In 1953, studies of the sound propagation through the sea began and, specifically, the studies of sound fields in the regions of geometric shadow. In 1954, these studies resulted in the discovery of the far zones of underwater insonification, or the so-called convergence zones. Describing this effect in 1956, Sukharevskiĭ suggested that it could open up possibilities for long-range underwater detection and ranging in the audio frequency range. He proposed the 3/2 power law to describe the frequency dependence of sound absorption in the sea.

In 1954, the Acoustical Laboratory of the Physical Institute of the Academy of Sciences of the USSR was reorganized into the Acoustics Institute of the Academy of Sciences of the USSR. Simultaneously, the Sukhumi expedition received the title of the Sukhumi Marine Research Station of the Acoustics Institute. At that time, the capital construction of the marine research station was in progress and new equipment was installed. The program of studying the far zones of insonification was extended, and other hydroacoustic investigations were carried out. They included the sound reflection from wakes of ships, the sound fluctuations caused by the inhomogeneity and dynamics of the marine environment (in relation to underwater communication and target indication), and the static characteristics of sea reverberation.

In 1959, Sukharevskiĭ proposed a method to increase the operating range of existing hydroacoustic equipment by more than an order of magnitude using the effect of far zones of insonification. He calculated the parameters of the corresponding shipborne hydroacoustic systems that allowed such long-range operation. He initiated and supervised the development of the first Russian long-range hydroacoustic system for mass production. For this work, Sukharevskiĭ received a USSR State Award.

Sukharevskiĭ combined his scientific work with the education of two research groups in Moscow and Sukhumi. His friend and colleague, theoretical physicist G.D. Malyuzhinets, assisted him in his work. Together, they contributed largely to the development of the theoretical studies of sound scattering from thin-walled elastic shells, hydrodynamic cavitation, and sound scattering from the sea surface.

In 1959, Sukharevskiĭ supervised the Soviet–China marine expedition on hydroacoustics.

In 1961–1966, Sukharevskiĭ held the office of Deputy Director of the Acoustics Institute. While performing his administrative duties, he continued his collaboration with industrial institutes, design offices, and naval institutions in developing new hydroacoustic equipment. Using his experience in studying different aspects of hydroacoustic problems, Sukharevskiĭ undertook the complex investigation of the triad represented by a hydroacoustic system, the environment, and a ship with the aim to optimize the operating frequency. In contrast to the conventional deterministic representation of marine environment parameters, he considered the statistics of the main parameters for a global set of various acoustic conditions in the ocean and studied the operating range of a hydroacoustic system as a probabilistic quantity.

The probabilistic approach developed by Sukharevskiĭ for describing the operating range of hydroa-

coustic systems and the new technique he proposed for range estimation offered the possibility of making the operation of hydroacoustic systems more reliable. This possibility is based on the fact that the parameter indicating the efficiency of a hydroacoustic system, i.e., the operating range, is guaranteed with a given integrated probability. The approach proved to be of dramatic significance for this area of research. The main results of these studies were published by Sukharevskiĭ in *Acoustical Physics* in 1995. Throughout the years, Sukharevskiĭ investigated the prospects of hydroacoustic science and engineering. During a ten-year period, he gave lectures on hydroacoustics at the Institute of the Improvement of Professional Skills for the leading specialists of the shipbuilding industry. At the present time, Sukharevskiĭ is a principle researcher at the Acoustics Institute.

Sukharevskiĭ's achievements in various fields of acoustics, as well as his entire career in science, testify to his outstanding abilities. Sukharevskiĭ is a prominent and far-seeing scientist. He made a significant contribution to the introduction of scientific results into modern engineering.

Sukharevskiĭ is the author of more than 150 scientific publications. He is not only a talented researcher but also an excellent teacher of young scientists. His scientific school is well known as the one of top-level acousticians. The ability to select and educate students is one of the most remarkable skills of Sukharevskiĭ. He educated more than 30 doctors and candidates of science, including some members and corresponding members of the Academy of Sciences, honored scientists and engineers, and honored inventors. Some of his students hold leading posts at various research institutes and design offices.

Sukharevskiĭ carries authority with broad circles of acoustical physicists, designers of hydroacoustic equipment, and Navy specialists. For his services to the country, Sukharevskiĭ was awarded two Orders of the Red Banner of Labor, an Order of the October Revolution, a Badge of Honor, a Valiant Labor during the Patriotic War Medal, and other medals.

Sukharevskiĭ is a man of duty, responsibility, and exceptional, enduring capabilities. In 1996, he became a laureate of the competition among the best publications of 1995 appearing in the journals of the Russian Academy of Sciences. Sukharevskiĭ was awarded a special grant from the President of the Russian Federation as a prominent scientist of Russia.

The interests of Sukharevskiĭ reach far beyond his professional occupation in science. His friends and colleagues enjoy his musical performances at parties held at the Acoustics Institute.

We wish Yuriĭ Mikhaĭlovich Sukharevskiĭ good health and many happy years to come.

Translated by E. Golyamina

Acoustical Physics, Vol. 48, No. 2, 2002, p. 246. Translated from Akusticheskiĭ Zhurnal, Vol. 48, No. 2, 2002, p. 288.

CHRONICLE

In Memory of Evgeniĭ L'vovich Shenderov (June 1, 1935–September 1, 2001)

Evgeniĭ L'vovich Shenderov—Honored Scientist and Engineer of the Russian Federation, Doctor of Engineering, Professor, and Head of the Research Sector of the Morfizpribor Central Research Institute—passed away after a brief illness.

Shenderov started working at the Morfizpribor Central Research Institute immediately after his graduation from the Leningrad Elecrotechnical Institute in 1957. For more than 44 years, his work was related to the formation and development of one of the most important areas of modern underwater acoustics: the study of the effect of sonar domes on the parameters of hydroacoustic arrays. He developed techniques for calculating the acoustic permeability of sonar domes and proposed new designs of sound-transparent parts of domes, which have found practical application in the design of naval ships and submarines. Shenderov was a talented scientist and outstanding engineer. He founded a scientific school, the work of which made a critical contribution to the development of underwater acoustics. The scope of Shenderov's scientific interests was rather wide. He published a number of fundamental works devoted to the diffraction of sound waves by elastic plates and shells, the optical visualization of sound fields diffracted by complex-shaped bodies, and the theoretical methods of analyzing the sound fields and sound wave diffraction by ship hulls. Shenderov is the author of more than 100 scientific publications and 50 inventions. Many of his papers were published in *Acoustical Physics* and in the *Journal of the Acoustical Society of America* (*JASA*). Shenderov wrote two fundamental monographs on theoretical acoustics: *Wave Problems of Underwater Acoustics* (1972) and *Radiation and Scattering of Sound* (1989). He was also involved in tutorial activities and was known as an excellent lecturer. In different higher educational institutes of St. Petersburg, he gave lectures on sound radiation, wave propagation, and oscillation of mechanical systems. Shenderov presented his papers at many scientific conferences. The last paper he prepared was presented by his colleagues at the 17th International Congress on Acoustics in Rome, two days after his death.

Shenderov was a member of the Scientific Council on Acoustics of the Russian Academy of Sciences and a member of the Editorial Council of *Acoustical Physics.* For years, he was a co-chairman of the Leningrad (now, St. Petersburg) seminar of the Scientific Council on Acoustics of the Russian Academy of Sciences.

Shenderov was a charming and benevolent person. Being a true intellectual, he was fairly democratic and friendly toward other people. He carried indisputable authority with all who knew him not only in his profession but also in other areas. Shenderov had a wide variety of hobbies: he was a yachtsman, tourist, downhill skier, free diver, underwater photographer, cabinetmaker, gardener, and oven maker.

This outstanding scientist, talented engineer, and good friend has passed away. The shining memory of Evgeniĭ L'vovich Shenderov will forever remain in the hearts of those who were lucky enough to have known this wonderful person.

Translated by E. Golyamina

1063-7710/02/4802-0246$22.00 © 2002 MAIK "Nauka/Interperiodica"